UNIVERSITÀ
DEGLI STUDI
DI PADOVA

Sede Amministrativa: Università degli Studi di Padova

Centro di Ateneo di Studi e Attività Spaziali "Giuseppe Colombo" (CISAS)

SCUOLA DI DOTTORATO DI RICERCA IN: SCIENZE TECNOLOGIE E MISURE SPAZIALI
INDIRIZZO: MISURE MECCANICHE PER L'INGEGNERIA E LO SPAZIO
CICLO: XXVIII

INNOVATIVE TECHNOLOGIES FOR THE ACTUATION OF SPACE MANIPULATORS

Direttore della Scuola: Ch.mo Prof. Giampiero Naletto
Coordinatore d'indirizzo: Ch.mo Prof. Stefano Debei
Supervisore: Ch.mo Prof. Alessandro Francesconi

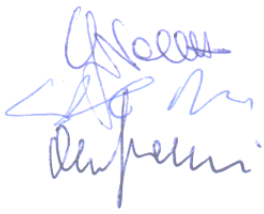

Dottorando: Ing. Francesco Branz

a G. che rende tutto più leggero

Abstract

The thesis objective is to evaluate innovative actuation technologies for space robotics; the main output is the feasibility proof of a robotic space system based on low-TRL devices. The activity focused on double-cone Dielectric Elastomer Actuators (DEAs).

The research motivation comes from the wide interest on robotics that recently grew among the space community. A large variety of space missions can benefit from the implementation of automated systems. On-Orbit Servicing (OOS) missions, for example, are based on robotic servicing vehicles that perform complex tasks on client objects.To date, a considerable number of relevant robotic systems have been operated in space; main tasks include assembly of complex structures, manipulation of client vehicles and support to astronauts activities. Besides conventional DC drives, innovative technologies, like smart materials, are sometimes adopted as space actuators. The most notable are: piezo-electric actuators and motors; shape memory devices; bimetallic actuators; Electro-Active Polymers (EAPs). The latter have not been employed in space systems yet, and their TRL is currently 2-3. Dielectric Elastomer are arguably the best performing EAPs and have been selected to be investigated in this work.

An example mission scenario is conceived and simulated in order to determine preliminary requirements for the robotic system and the single actuator. An Active Debris Removal (ADR) mission is selected as a key OOS application of robotic systems. The selected device configuration is the double-cone actuator, which is based on two circular, pre-stretched membranes of elastomer coated with compliant electrodes. Proper electromechanical models are identified for the selected actuator. Numerical simulations are performed in order to collect a large number of actuator performance data from which interpolating relations are obtained allowing to estimate the steady-state performances of the device. Transfer function (TF) based models are developed on the basis of time dependent data from long term tests. TF models are validated by comparison with experimental results. The developed models, both static and dynamic, are suitable for the implementation of control algorithms and for robotic applications. The capability to control the actuator is proven by means of laboratory tests conducted to evaluate the step response of actuators. Finally, a multi-body application of DEAs is designed and manufactured along with a proper control algorithm. The prototype is tested in laboratory environment and the control algorithms and numerical models are experimentally validated.

Summary

In this work, innovative technologies for the actuation of space robotic systems are investigated as possible alternative to traditional motors. The research activity focused on double-cone Dielectric Elastomer Actuators (DEAs). The most notable results achieved are predictive models for the static and dynamic performances estimation of the mentioned devices and experimental validation of both single actuators and a robotic arm prototype.

The general objective of the thesis is to evaluate innovative actuation technologies for space robotics; the main expected output of the research is the feasibility proof of a robotic space system based on low-TRL (Technology Readiness Level) devices. This objective is achieved by fulfilling two secondary goals:

1. development of models to predict the actuator performances and validation of ready-to-use design tools;
2. experimental evaluation of a multi-body manipulator prototype in laboratory environment.

The motivation on which this work is based, comes from the wide interest on robotics that recently grew among the space community. A large variety of space missions can benefit from the implementation of automated systems reducing risks, costs, delays and errors deriving from human interaction (i.e. astronauts or ground operators) with space vehicles and structures. On-Orbit Servicing (OOS) missions, in particular, are based on robotic servicing vehicles that perform complex tasks on client objects enabling unprecedented scenarios of improved accessibility to space. Future effective and efficient exploitation of space is strongly dependent on the development of key technologies to support existing and planned orbital assets, aiming to extend spacecraft operational life and to boost mission flexibility. Investigation on innovative actuation technologies is critical to improve space robotics performances and enable new applications. The TRL advancement of young technologies is at the basis of the development of new systems.

To date, a considerable number of relevant applications of robotics have been operated in space; main tasks include assembly of complex structures, manipulation of client vehicles and support to astronauts activities. Five human operated manipulators have equipped the Space Shuttle or the International Space Station (ISS), along with a variety of other experimental demonstrators; three examples of humanoid robotic astronauts have been tested and reached different levels of development; a wide range of autonomous demonstrative OOS missions

have been conceived and designed, are currently under development or, in some cases, have been flown with success; several planetary probes and (partially) autonomous rovers have been operated on the surface of extraterrestrial bodies like the Moon or Mars. These missions and others constitute the solid background on which this work is based and consolidate the motivation behind the research. The past and present trend in the space sector is to seek improved capabilities, flexibility and autonomy of vehicles, assigning a prominent role to robotics as a key enabling technology.

By far the most common actuators in space systems are conventional DC drives like stepper motors and brushless motors: the first are used in robotic arms for control simplicity and positioning accuracy, the second are the standard option in reaction wheels. In some cases brushed DC motors (in sealed or planetary environment) and, less often, voice coil motors have been used. Innovative technologies, like smart materials, are rarely adopted mainly due to reliability and heritage reasons. In general, the space community is very conservative and new technologies have to be proven fail safe and robust, and, for this reason, well-known solutions are often preferred. Nevertheless, implementation examples of smart technologies in space exist and they performed particularly well in off-nominal conditions, where traditional solutions show limitations. It is worth mentioning the most notable: piezo-electric actuators and motors, used in micro-positioning and precision pointing; shape memory devices, employed in release mechanisms; bimetallic actuators, implemented in single-shot systems and thermal control; Electro-Active Polymers (EAPs). The latter have not been extensively employed in space systems yet, although interest is growing around them on the basis of the appealing capabilities proved in many laboratory tests. A wide choice of alternative EAP materials and configurations have been proposed, with ample performance ranges. Dielectric Elastomer Actuators are a promising branch of EAPs family, whose space TRL is currently 2-3. Dielectric Elastomers are arguably the best performing EAPs and, for this reason, very appealing. DEAs have been selected to be investigated in this work for three main reasons:

1. good compromise performances in terms of stroke/deformation, force/torque and time response;
2. interesting characteristics like low mass and low power consumption, possibility to improve performances through design flexibility and modularity, multi-DoF configurations, simple manufacturing process, low costs, solid state actuation (no friction), self-sensing capability;
3. highly innovative technology with low TRL.

Double-cone actuators are selected for their flexibility and multi-DoF architecture.

An example mission scenario is conceived and simulated in order to determine preliminary requirements for the robotic system and the single actuator. An Active Debris Removal (ADR) mission is selected as a key OOS application of robotic systems. In the considered scenario a large piece of debris ($1400\,\mathrm{kg}$) is captured by a small spacecraft by means of a multi-DoF manipulator. The debris is spinning with respect to the servicing spacecraft which is equipped

with a robotic arm composed by a variable number of joints (1-3). The capture interface is rigid and guarantees the mechanical connection between the manipulator and the client object. Several simulations are performed with different initial conditions and capture strategies, including the options of a rigidly controlled or free flying spacecraft. The requirements have been defined in terms of forces/torques and rotations at the robot joints. The maximum angular deflection required to the entire robotic arm is 90 deg; torque and forces are strongly dependent on the initial debris (relative) angular momentum, thus it is possible to relax the joint requirement imposing stricter constraints to the target selection or relative navigation system of the servicer.

The double-cone DE actuator is based on two circular, pre-stretched membranes of elastomer coated with compliant electrodes on both sides. By applying high voltage to the electrodes, electrostatic forces squeeze the membrane reducing its thickness and, consequently, expanding the material in the plane. Such material deformation is exploited to displace the actuator shaft. Multiple DoF are obtained by selecting a proper electrode layout; a 2-DoF (one rotational, θ, and one translational, y) configuration is selected in view of the proposed robotic application. On the basis of the results available in literature, the commercial polyacrylic elastomer called 3M^{TM} VHB^{TM} 49XX is chosen. Proper electromechanical models are identified for the mentioned polymer.

Once a set of geometrical and manufacturing parameters are defined, numerical simulations based on literature as well as newly developed FEM models are performed in order to collect a large number of performance data. Interpolating relations are obtained from the collected data and allow to estimate the steady-state performances of the actuator. Torque/force and rotation/stroke are proportional to the squared value of applied high-voltage. The mentioned relations allow to compute the gain to which squared voltage has to be multiplied to estimate the desired quantity. The mean error on estimations is 6.1% for angular rotation, 10.6% for torque, 22.5% for linear stroke and 11.8% for force.

A different approach is adopted to model the dynamic behavior of DEAs: transfer function (TF) based models are developed from time dependent data collected through long term tests. The elastomeric material adopted in the device manufacturing shows a relevant viscoelastic behavior that considerably affects the time response of actuators. The TF approach is chosen to simplify the estimation of the transient behavior of DEAs and to provide a practical design tool for robotic applications. The prediction capabilities of TF models are evaluated by comparison with experimental step response. The mean error on the 70% rise time is 15% for angular rotation, 9.5% for torque, 14% for linear stroke and 14% for force; the mean error on amplitude for $t > t_r$ is 4% for angular rotation, 4% for torque, 9% for linear stroke and 11% for force.

The developed models, both static and dynamic, are suitable for the implementation of control algorithms and, consequently, for robotic applications. The capability to control the actuator is experimentally proven by testing Single Input / Single Output compensators to actuate both DoF independently. Laboratory tests are conducted in order to evaluate the step response

of double-cone actuators. Good accordance is obtained between the simulated and the experimentally measured time response with errors compatible with the prediction inaccuracies of the mentioned models.

Finally, a multi-body application of double-cone actuators is designed, manufactured and tested along with a proper control algorithm. The robotic arm is composed by two double-cone DEAs mounted in series. Each actuator has two DoFs and the manipulator moves in the horizontal plane. Two degrees of kinematic redundancy are achieved in the manipulator by controlling only the in-plane position of the end-effector. The arm prototype is suspended by an inextensible cable that reduces the effects of gravity on the motion. The experimental task is the tracking of simple linear and arc trajectories. A vision system monitors the position of the end-effector (optical marker) and feeds the position information to a control computer that commands the voltage actuation to the joints through a properly designed control algorithm. The kinematic redundancy is exploited by the controller to optimize the end-effector trajectory to achieve a given objective: several control schemes with alternative optimization functions are designed and simulated numerically in order to select the best performing option. The chosen control algorithm aims at the minimization of joint variables in order to reduce the risk of actuators saturation. The system performs well and the maximum position error norm is 6.4% of total path length for linear trajectory and 6.8% for arc trajectory.

Sommario

In questo lavoro si studiano tecnologie innovative per l'attuazione di sistemi robotici spaziali come possibili alternative ai motori elettrici tradizionali. Le attività di ricerca si sono focalizzate su attuatori ad elastomeri dielettrici (Dielectric Elastomer Actuators - DEA) a doppio cono. I risultati più importanti che si sono ottenuti sono modelli numerici per la predizione delle prestazioni statiche e dinamiche dei dipositivi citati e la validazione sperimentale sia dei singoli attuatori che di un prototipo di braccio robotico.

L'obbiettivo generale della tesi è di valutare tecnologie innovative per attuatori robotici spaziali; il principale prodotto della ricerca è la prova di fattibilità di un sistema robotico spaziale basato su dispositivi a basso TRL (Technology Readiness Level). Questo fine è raggiunto dal compimento di due obbiettivi secondari:

1. sviluppo di modelli per la predizione delle prestazioni dell'attuatore e di strumenti matematici per il dimensionamento dello stesso;
2. valutazione sperimentale del prototipo di un manipulatore in ambiente di laboratorio.

La motivazione alla base del lavoro deriva dall'ampio interesse per la robotica dimostrato recentemente dalla comunità scientifica del settore spaziale. Una grande varietà di missioni spaziali beneficia dall'implementazione di sistemi automatici per la riduzione di rischi, costi, ritardi ed errori derivanti dall'interazione umana (i.e. astronauti e operatori da terra) con veicoli e strutture spaziali. Le missioni di On-Orbit Servicing (OOS), in particolare, sono basate su veicoli robotici di servizio che eseguono compiti complessi su oggetti orbitanti consentendo la realizzazione di scenari senza precedenti. Il futuro sfruttamento efficiente ed efficace dello spazio dipende fortemente dallo sviluppo di tecnologie chiave in supporto di risorse orbitali esistenti o pianificate, con lo scopo di estendere la vita operativa dei satelliti e di incrementarne la flessibilità di missione. Lo studio di tecnologie innovative per l'attuazione è fondamentale per migliorare le prestazioni di sistemi robotici spaziali e consentire nuove applicazioni. L'avanzamento di TRL di giovani tecnologie sta alla base dello sviluppo di nuovi sistemi.

Ad oggi un numero considerevole di rilevanti applicazioni robotiche sono state realizzate nello spazio; i compiti principali includono l'assemblaggio di strutture complesse, manipolazione di veicoli e supporto all'attività di astronauti. Cinque bracci robotici hanno equipaggiato lo Space Shuttle o la Stazione Spaziale Internazionale (ISS), oltre ad una varietà di dimostratori

sperimentali; tre esempi di astronauti robotici umanoidi sono stati testati ed hanno raggiunto diversi livelli di sviluppo; svariate missioni autonome di OOS sono state concepite e progettate, sono attualmente in sviluppo o, in alcuni casi, hanno volato con successo; varie sonde e veicoli di superficie hanno operato su corpi celesti extraterrestri come la Luna o Marte. Queste ed altre missioni costituiscono il contesto su cui si basa questo lavoro e ne consolidano le motivazioni. La tendenza passata e presente nel settore spaziale è quella di ricercare il miglioramento delle capacità, della flessibilità e dell'autonomia dei veicoli, assegnando un ruolo prominente alla robotica come tecnologia fondamentale.

Gli attuatori di gran lunga più utilizzati in sistemi spaziali sono i motori a corrente continua come i motori passo-passo e senza spazzole: i primi sono utilizzati nei bracci robotici per la semplicità di controllo ed accuratezza di posizionamento, mentre i secondi sono l'opzione standard per le ruote di reazione. In alcuni casi sono stati utilizzati anche motori a spazzole a corrente continua (con involucro sigillato o in ambiente planetario) e, meno di frequente, motori voice coil. Tecnologie innovative, come i 'materiali intelligenti', sono adottate di rado principalmente per motivi di affidabilità e di scarsa storia di utilizzo. In generale la comunità scientifica spaziale è molto conservativa e le nuove tecnologie devono dimostrarsi robuste ed a prova di fallimento, e vengono spesso preferite ad esse soluzioni meglio conosciute. Ciononostante, esistono esempi di implementazione di tecnologie intelligenti nello spazio che hanno operato bene in condizioni non nominali, dove sistemi tradizionali hanno mostrato dei limiti. Se ne citano i più significativi: attuatori e motori piezoelettrici, utilizzati nel posizionamento e puntamento di precisione; dispositivi a memoria di forma, impiegati in meccanismi di rilascio; attuatori bimetallici, utilizzati in sistemi a singolo azionamento e nel controllo termico; Electro-Active Polymers (EAP). Gli ultimi non sono ancora stati utilizzati estensivamente in sistemi spaziali, sebbene un grande interesse stia crescendo attorno ad essi a causa delle interessanti capacità che sono state provate in molti test di laboratorio. In letteratura è stata proposta un'ampia scelta di materiali e configurazioni EAP, per un ampio ventaglio di prestazioni. Gli attuatori ad elastomeri dielettrici (DEA) sono un ramo promettente della famiglia degli EAP, il cui TRL spaziale è attualmente 2-3. Gli elastomeri dielettrici sono probabilmente gli EAP con prestazioni migliori e, per questo motivo, i più interessanti. I DEA sono stati scelti per essere studiati in questo lavoro per tre ragioni principali:

1. sono un buon compromesso in termini di movimento/deformazione, forza/coppia e risposta temporale;
2. presentano caratteristiche interessanti come leggerezza e basso consumo di potenza, possibilità di migliorarne le prestazioni grazie alla flessibilità di impiego e la modularità, configurazioni a molti gradi di libertà, semplicità costruttiva, costi ridotti, attuazione a stato solido (nessun attrito), capacità di self-sensing;
3. sono una tecnologia altamente innovativa con basso TRL.

Gli attuatori a doppio cono sono stati scelti per la loro flessibilità operativa e la configurazione a molti gradi di libertà.

Per la determinazione dei requisiti preliminari del sistema robotico e del singolo attuatore, è stato concepito e simulato uno scenario di missione esemplificativo. Si è scelta una missione di rimozione attiva di detriti spaziali in quanto si tratta di un'importante applicazione dei sistemi robotici per OOS. Nello scenario considerato un grosso detrito ($1400\ \mathrm{kg}$) viene catturato da un piccolo satellite tramite un manipolatore a più gradi di libertà. Il detrito è dotato di velocità di rotazione relativa rispetto al satellite di servizio il quale è equipaggiato con un braccio robotico composto da un numero variabile di giunti (1-3). L'interfaccia di cattura è rigida e garantisce la connessione meccanica tra il manipolatore ed il detrito. Sono state eseguite varie simulazioni con differenti condizioni iniziali e strategie di cattura, compresa l'opzione di un satellite rigidamente controllato o libero di muoversi. I requisiti sono stati definiti in termini di forze/coppie e rotazioni ai giunti. La massima deflessione angolare richiesta all'intero braccio è $90\ \mathrm{deg}$; coppie e forze dipendono molto dal momento angolare (relativo) iniziale del detrito ed è quindi possibile rilassare i requisiti sui giunti imponendo requisiti più stringenti alla selezione del detrito target o al sistema di navigazione relativa del veicolo di servizio.

L'attuatore ad elastomeri dielettrici a doppio cono è basato su due membrane di elastomero circolari, pre-deformate ricoperte da elettrodi deformabili su entrambi i lati. Applicando alta tensione agli elettrodi, si generano forze elettrostatiche che schiacciano la membrana riducendone lo spessore ed espandendola nel piano. Questa deformazione del materiale viene sfruttata per muovere l'albero centrale dell'attuatore. Gradi di libertà multipli sono ottenuti selezionando uno schema di elettrodi appropriati; considerando l'applicazione robotica proposta è stata scelta una configurazione a due gradi di libertà (uno rotazionale ed uno traslazionale). Sulla base dei risultati disponibili in letteratura, è stato selezionato l'elastomero poliacrilico commerciale denominato 3M^{TM} VHB^{TM} 49XX. Sono stati identificati dei modelli elettromeccanici appropriati per il polimero considerato.

Dopo aver identificato dei parametri di progetto, si eseguono simulazioni numeriche basate su modelli disponibili in letteratura e modelli ad elementi finiti in maniera tale da raccogliere un consistente mole di dati prestazionali. Delle relazioni interpolanti vengono ottenute dai dati raccolti e consentono di stimare le performance statiche dell'attuatore. Coppia/forza e rotazione/traslazione sono proporzionali al valore al quadrato della tensione applicata. Con le relazioni ricavate si calcola il guadagno per il quale deve essere moltiplicata la tensione al quadrato per stimare la grandezza desiderata. L'errore medio sulle stime è 6.1% per la rotazione angolare, 10.6% per la coppia, 22.5% per la traslazione e 11.8% per la forza.

Un approccio differente è stato adottato per la modellazione del comportamento dinamico dell'attuatore: sono stati sviluppati dei modelli basati su funzioni di trasferimento ricavate da dati di test a lungo termine. L'elastomero considerato mostra un comportamento viscoelastico che influenza significativamente la risposta temporale degli attuatori. Il modello con funzioni di trasferimento è stato adottato per semplificare la stima della risposta tempovariante dell'attuatore e per fornire uno strumento pratico per la progettazione di applicazioni robotiche. Le capacità predittive delle funzioni di trasferimento sono state valutate confrontandole con

dati sperimentali della risposta al gradino. L'errore medio sul tempo di salita al 70% è 15% per la rotazione, 9.5% per la coppia, 14% per la traslazione e 14% per la forza; l'errore medio in ampiezza per $t > t_r$ è 4% per la rotazione, 4% per la coppia, 9% per la traslazione e 11% per la forza.

I modelli sviluppati, sia statici che dinaimci, sono adatti alla progettazione di algoritmi di controllo e, quindi, di applicazioni robotiche. La capacità di controllare l'attuatore è provata sperimentalmente testando compensatori Singel Input / Single Output per l'attuazione indipendente di entrambi i gradi di libertà. La risposta al gradino degli attuatori a doppio cono controllati è valutata sperimentalmente tramite test di laboratorio. Si è ottenuto una buona corrispondenza tra la risposta temporale simulata e quella misurata, con errori compatibili alle inaccuratezza dei modelli descritti.

In fine, si è progettata, realizzata e testata un'applicazione robotica degli attuatori a doppio cono in parallelo ad un algoritmo di controllo appropriato. Il braccio robotico è composto da due attuatori montati in serie. Ogni attuatore possiede due gradi di libertà ed il manipolatore si muove nel piano orizzontale. Si ottengono due gradi di ridondanza cinematica controllando solo la posizione nel piano dell'end-effector. Il prototipo di braccio è sospeso da un cavo inestensibile che riduce gli effetti della gravità sul moto. Il task sperimentale è quello di percorrere una semplice traiettoria lineare o ad arco. Un sistema di visione è utilizzato per monitorare la posizione dell'end-effector (marcatore ottico) e fornisce l'informazione di posizione at un computer di controllo che comanda la tensione di attuazione ai giunti tramite un algoritmo di controllo. La ridondanza cinematica è sfruttata per ottimizzare la traiettoria e raggiungere un obbiettivo dato: diversi schemi di controllo sono stati progettati e simulati numericamente per selezionarne il più performante. L'algoritmo selezionato ha lo scopo di minimizzare le variabili di giunto per ridurre il rischio di saturazione degli attuatori. Il sistema dà buoni risultati e il massimo errore sulla norma del vettore posizione è 6.4% della lunghezza totale per la traiettoria lineare e 6.8% per quella ad arco.

Acknowledgement

I would like to express my gratitude to my supervisor, Prof. Alessandro Francesconi, for his precious guidance and advice, for his inspiring visions that pose constant challenges to my research.

I am thankful to Prof. Ruggero Carli, Andrea Carron and Diego Romeres for the collaborative efforts put in the development of this very work.

My appreciation goes to Alberto Dalla Libera and Nicola Tarraran for their help, and to the FELDs and POLARIS teams for the success that I accidentally shared.

A special thought goes to the ARCADE and ARCADE-R2 teams, for the results that finally came: the best proof that everything is possible.

Many fellow Ph.D. students shared with me the struggles and the satisfaction of research. I want to thank Francesco, Livia, Lorenzo, Riccardo, Andrea, Sebastiano, Laura, Matteo, Mattia: we will reach for the stars!

Finally, I am grateful to my friends, in Padova and Trento, and to my family who listen to my chatter about obscure topics, support me in bad times and help me downsize my ego.

Contents

1 Introduction

In this introductory chapter the objective of the research is stated and the motivation that pushed the activities is explained (Sec. 1.1). In addition, the layout of the thesis is schematically described (Sec. 1.2).

1.1 Objective and motivation

The aim of this work is to evaluate innovative actuation technologies, like smart materials, for space robotic systems. The primary objective is to prove the feasibility of a robotic arm specifically designed for spacecraft operations and based on a low-TRL (Technology Readiness Level) actuator. The main goal articulates in two secondary objectives, the first focusing on the actuator as a single device, the second relative to the implementation of a relevant robotic application; on one hand, the research aims at the identification (or development) of static/dynamic performance models that allow the controlled motion of the actuator, while, on the other hand, seeks the experimental validation of a multi-body system prototype. The conceptual process flow of this work is to review existing actuation technologies, select the most promising solution to implement improved space manipulators and assess its suitability to operate in complex systems in the framework of an orbital mission.

Automatic systems have historically played a prominent role in space technologies, due to their fitness to the orbital scenario where the limits, risks and costs of human action are amplified. Robotic systems, in particular, are becoming more and more appealing since they allow the execution of complex tasks and operations reducing the presence of human operators in the loop. Among the missions that most profitably benefit from robotic systems are those involving On Orbit Servicing (OOS) operations, where one or more servicing vehicles automatically perform tasks of variable complexity on client objects. It is a shared opinion among the space community that future missions will strongly rely on OOS to limit costs, improve capabilities and extend operational life of existing and prospective assets; the exploitation of robotic systems in space will presumably see an incremental growth over the next decades.

Spacecraft and orbital systems employ very consolidated technologies, mainly for reliability reasons. Robotic systems are no exception and only two or three traditional electric motor types see a wide use as actuators in space mechanisms. Although many unconventional technologies offer alternative options for actuation, few of them find a (limited) application to the space scenario. Nevertheless, when extremely strict requirements, peculiar constraints or specific tasks come into play, unconventional technologies, like smart materials, have been forcedly selected and successfully employed. The advantages of innovative solutions allow the

implementation of unprecedented applications that enable key capabilities in space vehicles. For this reason, the effort to evolve the TRL of promising technologies generally pays back with advancements in space systems that finally result in improved performances. These general considerations motivate and lead the research activities presented in this work.

1.2 Thesis approach and structure

In this section the approach followed in the research as well as the thesis layout are presented. Fig. 1.1 schematically presents the flow of the main work packages with reference to the pertaining sections.

Ch. 2 presents the technical background in which the work is set. In particular, Sec. 2.1 reviews literature in the field of space robotics, mentioning all the relevant examples of robotic applications, like manipulators or other automated systems, at various stages of development. Sec. 2.2 presents an overview of existing technologies for space mechanisms actuators, particularly focusing on less conventional devices; in addition, low-TRL solutions with potential space application, like Electro Active Polymers, are mentioned and, among them, a large number of Dielectric Elastomer Actuators (DEA) geometries are referenced. A trade-off analysis is performed in Sec. 2.2.2 and the selection of the DEA technology is explained.

In Ch. 3 a space manipulator application scenario is simulated in order to provide preliminary requirements for the actuator and manipulator design. On the basis of the growing interest around OOS missions, a debris capture operation is simulated to estimate dynamic loads on the gripping robotic arm. The double-cone actuator geometry is selected among other candidates.

Ch. 4 explains in detail the DE double-cone actuator working principle, the notable features and the modeling approach adopted in the research activities. The main design challenges of DEs are presented from the mechanical, electrical and thermal points of view; a brief bibliographic assessment of the compatibility of DEs with the space environment is also reported.

Ch. 5 focuses on the definition of design-oriented, static and dynamic performance models of double-cone actuators and their experimental validation. Steady-state and transient behavior models have been developed aiming at the feedback controlled motion of DE actuators. Laboratory tests have been performed for the validation of developed tools.

Ch. 6 describes the design, development and testing of a multi-body robotic arm prototype to prove the feasibility of a DE based manipulator. The system is tested in laboratory with some level of reduced gravity simulation.

Finally, in Ch. 7 the conclusions of the work are presented along with some possible future developments of the research.

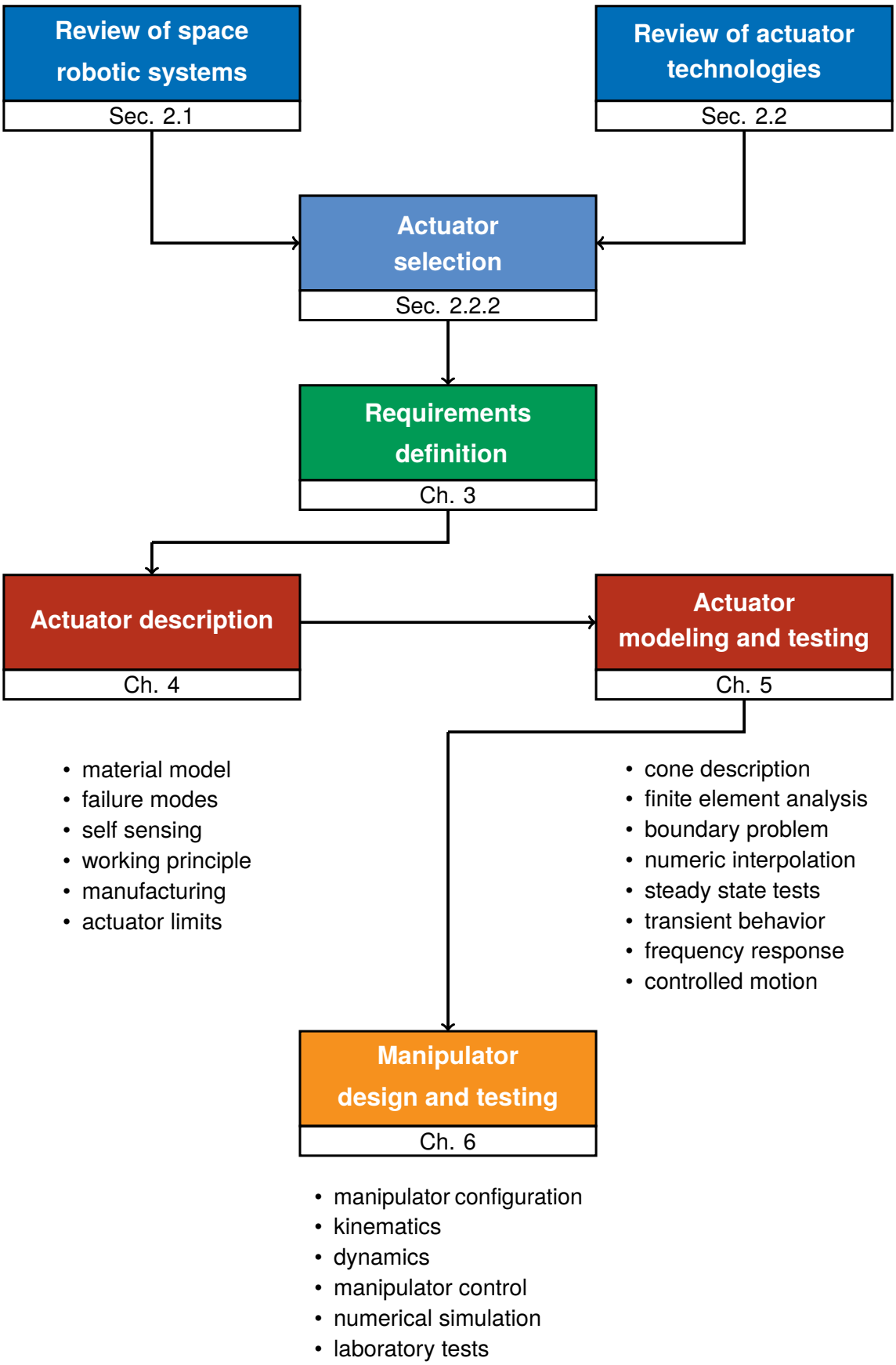

Fig. 1.1: Thesis logic

2 Background

This chapter provides an overview of the background in which this thesis work is set. The most notable space robotics examples are referenced in Sec. 2.1. Different technologies employed in actuators for space mechanisms are reviewed in Sec. 2.2, with specific focus on the so-called smart materials systems. A trade-off between the mentioned actuator technologies and geometries is briefly presented in Sec. 2.2.2.

2.1 Space robotics

The use of robotic systems in space is becoming more and more appealing to improve the performances of space systems and extend their operational life through maintenance. On-Orbit Servicing (OOS) refers to a vast field of operations performed on orbital objects after their deployment. Possible tasks of OOS include assembly, repair, updating, re- or deorbiting, spacecraft release and retrieve, astronaut activities support, inspection, refueling. The interest in OOS motivated the development of several robotic systems and experiments for space operations. Flores-Abad *et al.* [1] provide an exhaustive review of space robotic technologies and applications to OOS.

In 1981 the 6-DoF Shuttle Remote Manipulator System (SRMS, see Fig. 2.1a), developed by the Canadian Space Agency (CSA), equipped for the first time a Space Shuttle mission and marked a key milestone in the development of space robotics [2]. Further developments led to the Space Station Remote Manipulation System (SSRMS, see Fig. 2.1b) which is an updated, 7-DoF version of the arm specifically designed to equip the International Space Station (ISS). SSRMS is part of the ISS Mobile Servicing System (MSS) which is completed by the Special Purpose Dexterous manipulator (SPDM) [3] and the Mobile Remote Services Base System (MRSBS). The first is an add-on to the main robotic arm that allows to execute many delicate tasks previously performed by astronauts, while the second is a movable platform for SSRMS and SPDM that translates along the ISS main structure.

Two more robotic systems equip the ISS: the Japanese Experiment Module Remote Manipulator System (JEMRMS, see Fig. 2.2a) [4] build by the Japan Aerospace Exploration Agency (JAXA) and the European Robotic Arm (ERA, see Fig. 2.2b) [5] provided by the European Space Agency (ESA). JEMRMS is a servicing tool to support the scientific experiments mounted externally on the Japanese Experiment Module (JEM). It is composed by two 6-DoF manipulators: the main arm and the fine arm that allows to perform dexterous tasks. ERA is a 7-DoF arm equipped with a repositionable base that can be mounted on the Russian modules of the ISS.

(a) SRMS operating in support to EVAs on Space Shuttle

Courtesy of NASA

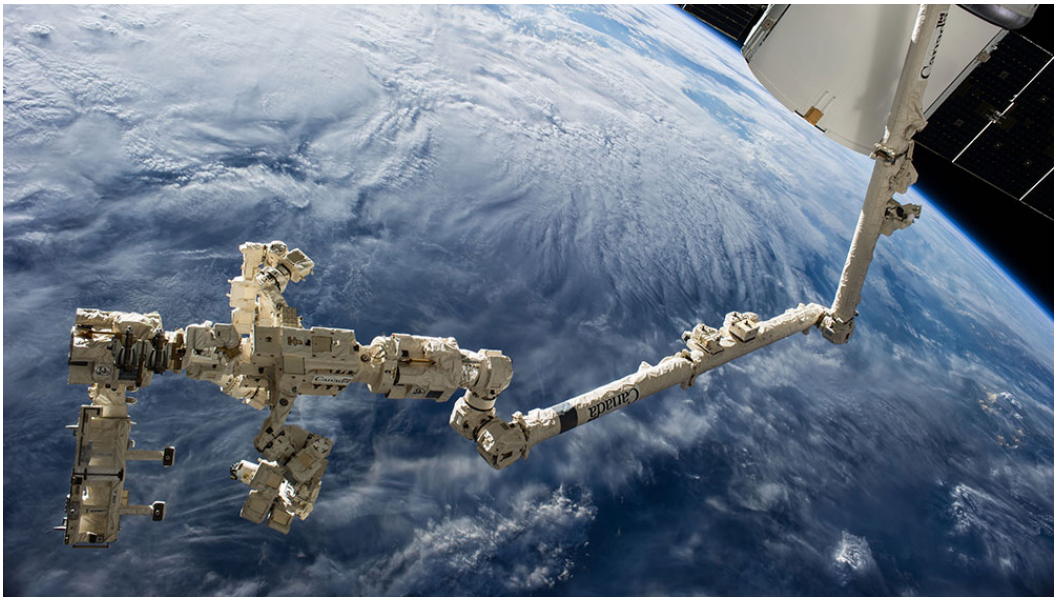

(b) SSRMS and DEXTRE attached to ISS with SpaceX Dragon cargo ship on the background

Courtesy of NASA

Fig. 2.1: Canadian space manipulators on Space Shuttle and ISS

Several robotic experiments have been conducted or are under development by the German Space Center (DLR). The Robot Technology Experiment (ROTEX) [6] was intended to test robotic technologies in teleoperation aboard the Space Shuttle. The Robotics Component Verification (ROKVISS) experiment [7] also aimed at the validation of robotic technologies and was tested on the ISS. DLR is also developing a humanoid robot called Space Justin [8] which is intended to perform complex repair tasks in teleoperation while mounted on a spacecraft (see Fig. 2.3a).

(a) JEMRMS working on the Japanese Experiment Module

Courtesy of NASA/JAXA

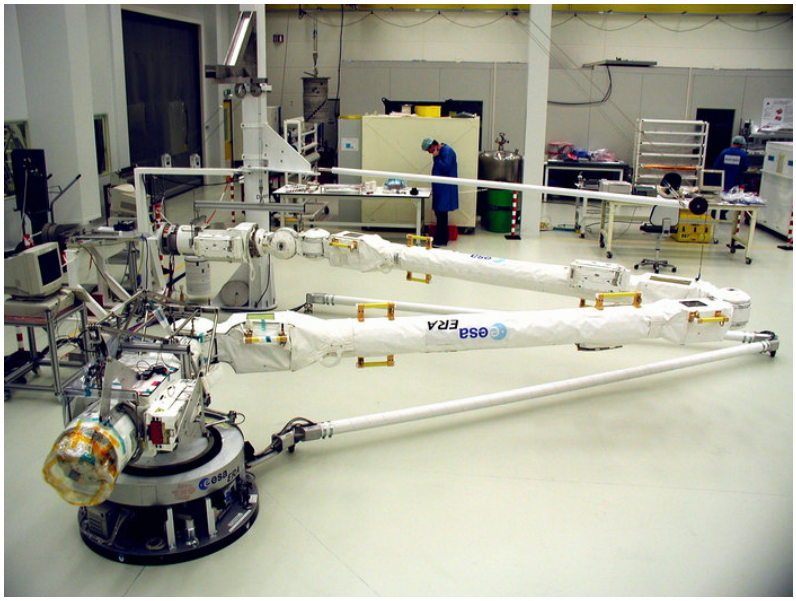

(b) ERA during flat floor testing

Photo: ESA

Fig. 2.2: Examples of space manipulators on board the ISS

National Aeronautics and Space Administration (NASA) has developed some experiments similar to Justin: Robonaut 1 (R1, see Fig. 2.3b) [9] and its updated version, Robonaut 2 (R2, see Fig. 2.3c) [10]. These systems are anthropomorphic robots that assist astronauts during Extra Vehicular Activities (EVA) and represent the state-of-the-art of space servicing robotics. R2 is capable to operate with standard EVA tools nominally designed for human operators and is currently operated on the ISS.

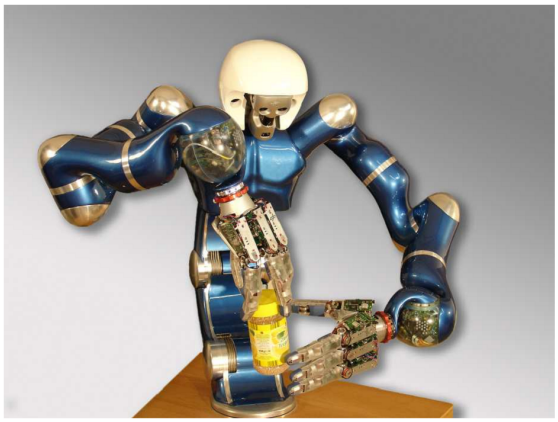

(a) DLR Justin [8]

Reprinted with permission from [8], ©2007 IEEE

(b) Robonaut

Courtesy of NASA

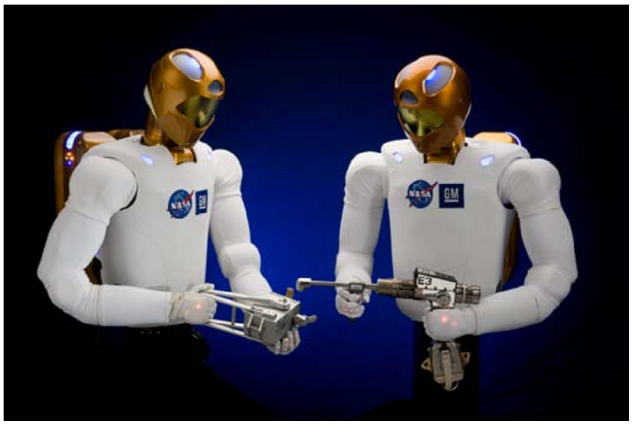

(c) Robonaut 2

Courtesy of NASA

Fig. 2.3: Humanoid robots developed by DLR and NASA

Aside from the manipulators operated on the Space Shuttle or the ISS, much effort was recently put in the development of OOS demonstrative missions. The first of such missions was carried out by JAXA and is called Experimental Test Satellite VII (ETS-VII, see Fig. 2.4a) which was an unmanned spacecraft equipped with a 6-DoF arm [11][12]. Launched in 1997, it performed a number of complex operations in teleoperation (component replacing, deployment of a space structure, spacecraft berthing, etc.).

Another example of robotic demonstrative mission is Orbital Express launched in 2007 by the Defense Advanced Research Projects Agency (DARPA) and Boeing [13] [14]. During this mission a servicing spacecraft performed rendez-vous, docking and servicing operations on a client vehicle expressly designed for that purpose.

DARPA worked also on the Front-end Robotics Enabling Near-term Demonstration (FREND) aiming at laboratory testing of full-scale experiments of autonomous rendez-vous and docking procedures with spacecraft not specifically designed to enable robotic servicing [15][16].

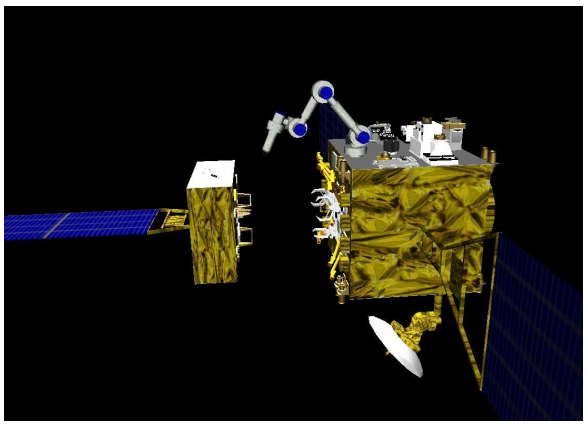

(a) Artist's impression of ETS-VII

Courtesy of JAXA

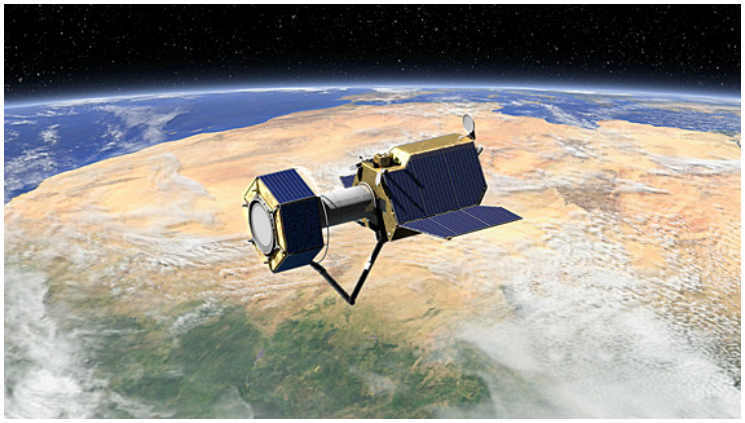

(b) Artist's impression of DEOS

Photo: DLR, CC-BY 3.0

Fig. 2.4: Notable OOS missions

Currently FREND, a 7-DoF manipulator, is being employed in the DARPA program named PHOENIX whose objective is to interact with decommissioned GEO satellites.

The United States Air Force Research Laboratory (USAFRL) operated the Experimental Satellite System 11 (XSS-11) in 2002 in order to test accurate detection, tracking and pose estimation strategies to enable docking procedures. Rendez-vous enabling technologies have been tested also in the framework of the NASA Demonstration for Autonomous Rendezvous Technology (DART) program launched in 2005 [17].

The German (DLR) effort to develop OOS systems is recently focusing on the development of the Deutsche Orbital Servicing (DEOS, see Fig. 2.4b) mission [18]. The objective of DEOS is to validate procedures and techniques to capture a slowly tumbling and non-cooperative satellite. The target vehicle is specifically designed to be serviced by the main spacecraft. At the end of the mission, after capture and coupling of the two satellites, the joint system will perform a controlled re-entry maneuver.

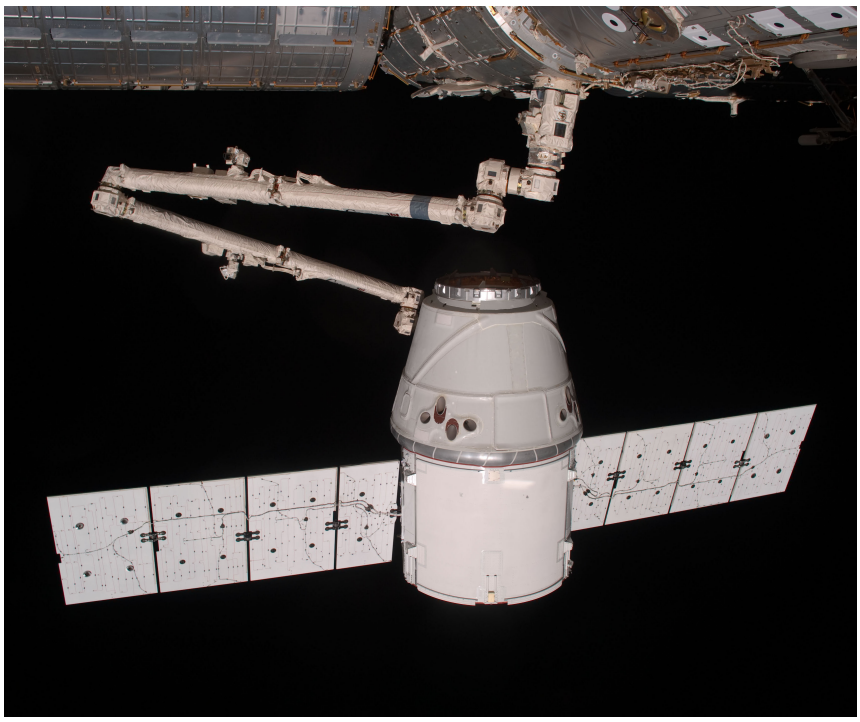

Fig. 2.5: Dragon cargo ship by SpaceX berthed on ISS by SSRMS
Courtesy of NASA

It is worth mentioning two programs carried on by commercial companies. First, the ConeXpress Orbital Life Extension Vehicle (CX-OLEV) developed by Obital Recovery Limited (ORL) to perform life-extension procedures on geostationary satellites [19]. Second, is the ISS cargo and crew servicing system program developed by Space Exploration Technologies (SpaceX, see Fig. 2.5).

Although this work focuses mainly on orbital applications, attention must be paid also to planetary robotic systems [20]. The first examples of robotic systems on extraterrestial bodies were the Lunokhod-1 and Lunokhod-2 rovers developed by USSR. More effort was put in the robotic exploration of Mars, starting with Viking-1 and Viking-2 landers by NASA which are equipped with robotic arms to perform scientific analysis (Fig. 2.6a). For similar purposes, the NASA's Phoenix lander also exploited a 4-DoF manipulator (Fig. 2.6b). NASA operated a number of rovers on Mars surface, the first of whom was Sojourner in the framework of the Mars Pathfinder mission (Fig. 2.6c). The Mars Exploration Rovers (Spirit and Opportunity) by NASA were remarkably successful and set a milestone in robotic exploration of extraterrestrial planets (Fig. 2.6d). The state of the art of planetary rovers is represented by the Curiosity rover by NASA (Fig. 2.13c). The european effort in planetary robotic exploration is represented by the planned ExoMars rover by ESA (Fig. 2.7b). The China National Space Administration (CNSA) developed the Yutu lunar rover lunched and operated in 2014.

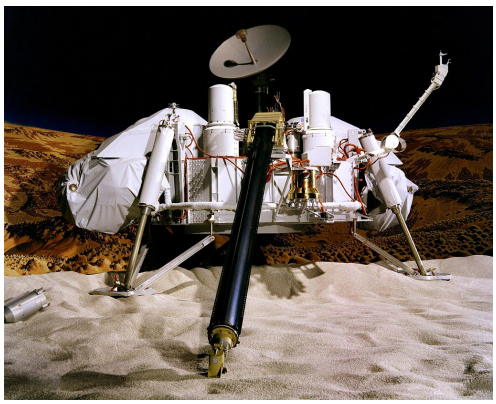

(a) Viking martian lander

Courtesy of NASA

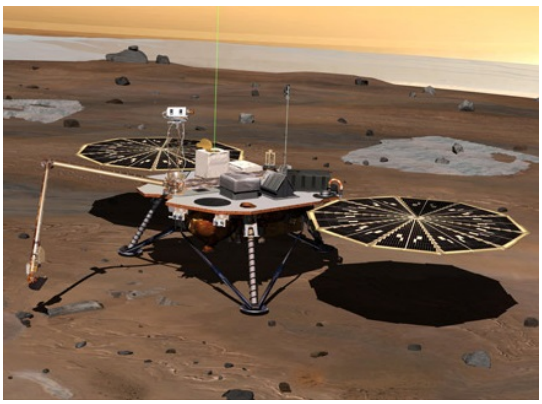

(b) Phoenix martian lander

Courtesy of NASA

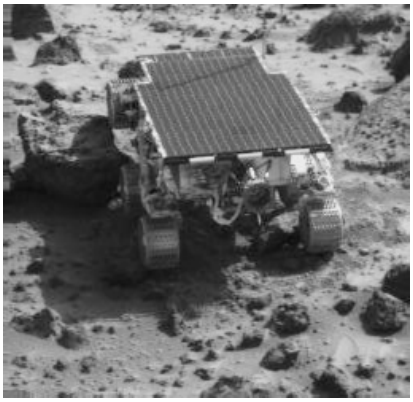

(c) Sojourner martian rover

Courtesy of NASA

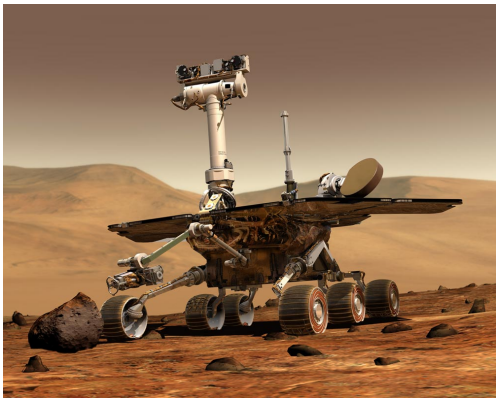

(d) Mars Exploration Rover

Courtesy of NASA

Fig. 2.6: Robotic missions on extraterrestial bodies - 1

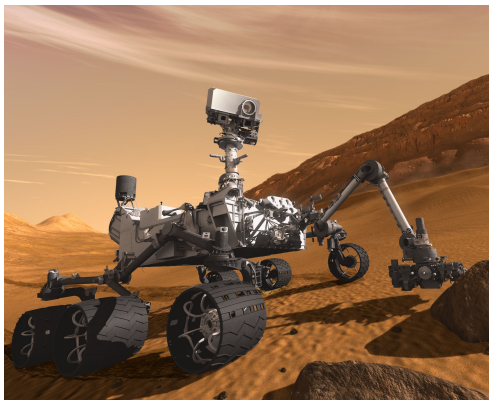

(a) Curiosity martian rover

Courtesy of NASA

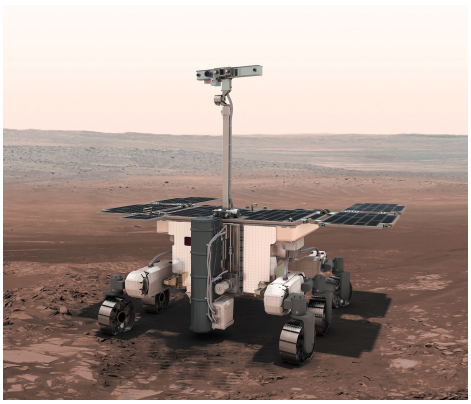

(b) ExoMars rover

Photo: ESA

Fig. 2.7: Robotic missions on extraterrestial bodies - 2

2.2 Space mechanism actuators

The actuation of space mechanisms, including robotic systems, is most often performed by means of traditional DC electric motors, mainly for heritage and reliability reasons [21]. Very

commonly DC stepper motors in combination with harmonic drives are used for structure deployment or pointing applications. Stepper motors are controlled in position and often selected due to their simple control electronics, the possibility to drive them in open loop and the intrinsic unpowered holding torque. An example of the mentioned actuator architecture called Harmonic Drive Rotary Actuator (HDRA) has been developed by Sener, Spain, with the support of ESA [21]. The standard actuators employed in reaction wheels are brushless DC motors for their smooth and wearless motion (see Fig. 2.8a). Brushless motors require a more complex commutation electronics, but offer the best durability for continuous operations as well as lower cog torque: they are often used when high speed is required. In some cases brushed motors are employed, especially when a pressurized environment is available (e.g. planetary atmosphere or sealed casing) to avoid arching and accelerated wear out (see Fig. 2.8b). Finally, voice coil motors can be employed in space applications, although they are far less common (see Fig. 2.8c).

(a) Reaction wheel with brushless motor

Courtesy of Clyde Space

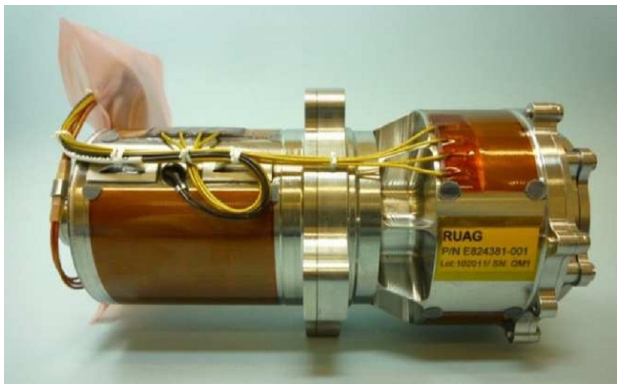

(b) Sealed Brushed Gear Motor

courtesy of RUAG Schweiz AG, RUAG Space

(c) Voice Coil Motor

Courtesy of Cedrat Technologies.

Fig. 2.8: Examples of traditional space actuators

This work focuses on innovative actuation technologies and their application to robotics or space systems in general.

2.2.1 Smart materials actuators

Although the definition of the expression *smart materials* is sometimes controversial, it generally refers to materials that are capable to react to external stimuli in a controllable way. Such stimuli are of various nature, thus allowing to classify the different types of materials accordingly. Several devices exploit smart materials for diverse purposes including actuation, sensing, self healing or memory.

The use of smart materials actuators is still very limited in the space sector due to objective challenges in bringing new technologies to satisfactory levels of readiness, as well as to the strong conservativeness of the space community which broadly prefers robust, well-known and risk-safe solutions. A brief overview of most notable smart actuation technologies in space follows, including: piezoelectric actuators and motors, shape memory actuators, bimetallic actuators and Electro-Active Polymers (EAP) actuators. Tab. 2.1 provides a schematic comparison between the main smart actuator technologies.

Tab. 2.1: Smart actuator technologies comparison

Technology	Force	Stroke	Velocity	Mass density	Issues
piezo-actuators	large	small	high	high	constant power
piezo-motors	large	large	low	high	complex electronics
shape memory	large	large	very low	high	discrete actuation
bimetallic	small	small	very low	high	basic applications
EAPs (DEAs)	small	large	low	low	high voltage

2.2.1.1 Piezoelectric actuators and motors

The direct piezoelectric effect is a reversible process found in many natural crystals, such as quartz or topaz, which generate an electric charge in response to an applied mechanical stress. It is also called sensor effect and converts mechanical energy into electrical energy. The converse piezoelectric effect, or actuator effect, causes a change in the length of these materials when an electrical voltage is applied, converting electrical energy into mechanical energy. This phenomenon (Fig. 2.9) is due to the non-centrosymmetric structure of the crystals (rombohedral or tetragonal), which allows ions to move more easily along one axis than the others. In fact, when a stress is applied to the material the crystalline structure is disturbed and there is a variation in the direction of the polarization, P, of the electric dipoles. The change in P appears as a variation of surface charge density upon the crystal faces, corresponding to a variation of the electric field between the faces. A linear relation links stress and voltage, the higher the mechanical stress, the bigger the change in polarization and the more charge displacement is produced. Piezoelectric materials exhibit their effect only below a certain temperature, called Curie temperature. Above the Curie point, the crystal present cubic symmetrical structure, having no dipole moment. Below the Curie point, the crystal

has a tetragonal or rhombohedral symmetry, hence a dipole moment. The increment of the temperature results in a progressive degradation of the piezoelectric effect.

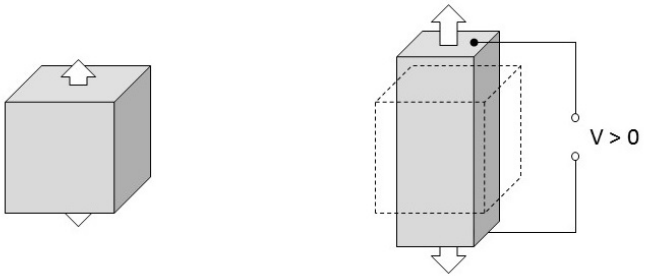

(a) Direct effect (sensor)

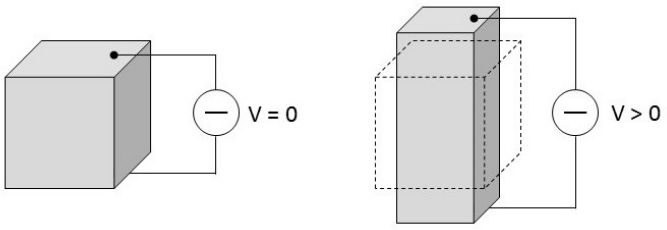

(b) Converse effect (actuator)

Fig. 2.9: Piezoelectric effect

The output produced by natural materials is relatively small. Industrial applications employ synthetic crystals (like gallium orthophosphate, $GaPO_4$), ceramics (like barium titanate, $BaTiO_3$, and lead zirconate titanate, PZT) or polymers (like polyvinylidene fluoride) which exhibit larger displacements or induce larger electric voltages [22].

Among all smart materials, piezoelectrics represent the most mature and consolidated technology for space mechanisms and, thanks to their high accuracy, they are widely used as actuators in general. The major advantages of piezo-actuators are their magnetic cleanliness, high operating frequency, easiness of control, and repeatability. In addition they can be operated from cryogenic temperatures to a maximum of $150\ ^{\circ}\mathrm{C}$ without showing a degradation of the piezoelectric effect. Major disadvantages of this technology include low deformations and the need for continuous power to maintain a certain position, which could be problematic for many space applications because of the limited power available.

Depending on their task, different configurations have been proposed for solid-state actuators, like Multi-Layer Actuators (MLA), stripe actuators or piezoelectric motors. An MLA is made of a stack of thin piezoelectric ceramic layers (usually PZT) with an electrode placed between each layer. The application of a voltage (usually the maximum voltage is $150\ \mathrm{V}$) produce an expansion deformation up to about 0.1% of length. For example a stack of $100\ \mathrm{mm}$ in length and of $1\ \mathrm{cm}^2$ in section provides a free stroke of $100\ \mu\mathrm{m}$ and a blocking force of about $30\ \mathrm{N}$. The small stroke limits the applicability of such actuators. In addition, the ceramics used have a low tensile strength which can lead to failure in vibrational environment. To

overcome these limits, Amplified Piezo Actuators (APA) have been developed by Cedrat Technologies [23]. To overcome the tensile stress limit a compressive pre-stress is applied on the ceramic, which also improves the deformation of the material. The pre-stress is obtained by inserting the stacks in an elliptical metallic shell. This structure offers mechanical protection, while allowing deformation. The expansion of the active material along the shell major axis produces an amplified contraction of the minor axis. These devices (Fig. 2.10a) achieve a deformation of $0.5 \div 1\%$ of length while still producing high forces. The obtained response time for these actuators to reach the full stroke is $200\ \mu s$. This result has been achieved with a good reproducibility leading to a total of 10^{10} cycles with no failure. Amplified piezoelectric actuators have no hinges or sliding parts so they do not require lubrication making them suitable for cryogenic applications, where traditional lubricants may freeze, and for vacuum applications, where lubricants might outgas.

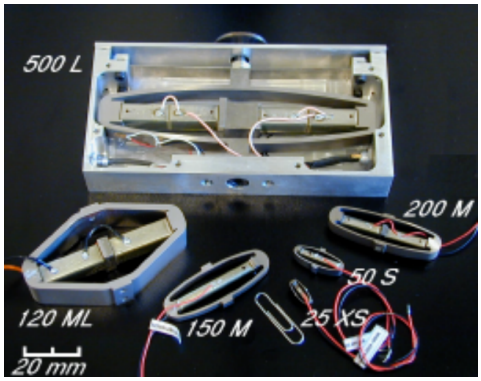

(a) Amplified Piezo Acutators [23]

Reprinted from [23]. Courtesy of Cedrat Technologies.

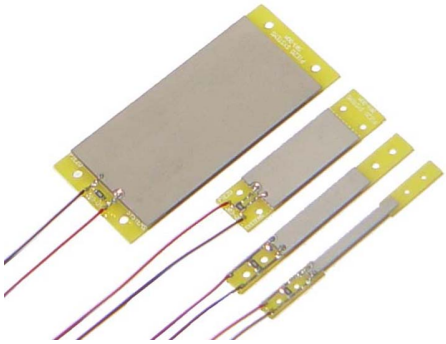

(b) Bending piezo actuators

Courtesy of Piezo Systems.

Fig. 2.10: Common piezoelectric actuators

Stripe actuators, also called bending actuators, are designed to produce a relatively large mechanical deflection in response to a electric input (see Fig. 2.10b). They present a rectangular structure, where an end is fixed and the other is free to deflect. This bending offers a large stroke and, if the deflection is constrained, a very limited blocking force when compared to stack actuators. Stripe actuators are composed by layers of different materials attached together and two basic structure are possible: monomorph and bimorph. The monomorph actuators are made of a piezoelectric layer and a passive material, generally metallic, with an electrode attached on the active surface. When voltage is applied the fibers of the active layer tend to stretch while the passive metal does not react and block the expansion. This bond induces the bending of the actuator. The bimorph actuators consist of two layers of piezoelectric ceramic bonded together with a central electrode. In this configuration the two layers present an opposite direction of polarization, and are electrically connected in series. When a voltage input is applied, one ceramic layer tends to expand and the other to contract, causing the bending of the actuator. Stripe actuators are primarily used as small pumping devices and for opening or closing valves. Nevertheless, MLA actuators are often preferred

to strip actuators because of their combination of accurate displacement with high blocking force.

Piezoelectric motors are based on a large number of small deformable piezo elements that exploit friction to actuate the moving part which can either be a rotor or a linear rod. The active elements deform and apply a centipede-like, push-pull force on the moving part (see Fig. 2.11). The use in space system can be interesting due to their non-magnetic nature, the fine resolution and the holding torque/force at rest.

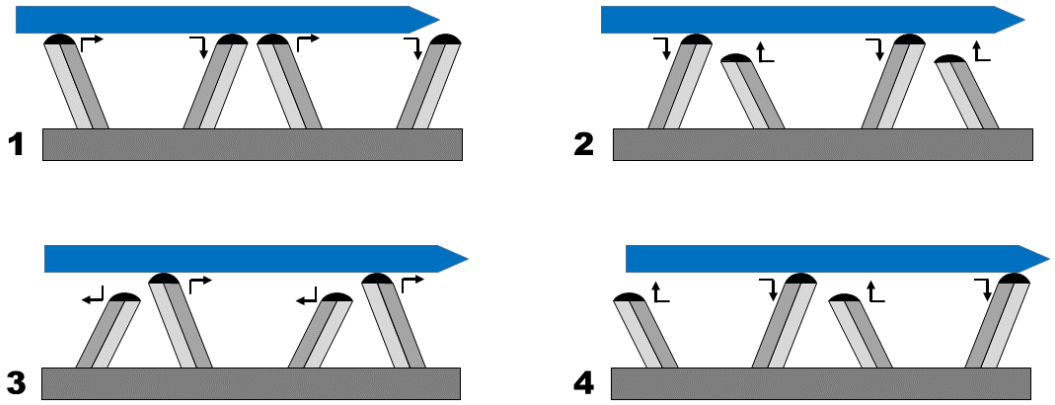

Fig. 2.11: Working principle of piezoelectric motors: movable part (blue) is pushed forward by a large number of synchronized (1-4) piezo legs (two-colored gray)

Several piezo mechanisms using multilayer actuators have been designed to meet requirements for space applications. They present high output energy to mass ratio and they are able to withstand large external forces and intense vibrations. They are widely used for active cancellation of micro vibration, high precision pointing mechanisms or other types of instrumentation. One of the first applications of piezo actuated instruments was used in 2003 for a scanning device on the MIDAS mechanism of ROSETTA mission [24]. It uses an atomic force microscope to study the dust resulting from the 67P/Churyumov-Gerasimenko comet. The microscope utilizes a piezoelectric stage to achieve fine adjustments. It is made of eight APAs placed in the x and y directions that can achieve strokes of $100\ \mu\mathrm{m}$ for scanning along both directions. The x and y axis are decoupled by flexural hinges. There is also an actuator to produce a stroke of $8\ \mu\mathrm{m}$ along the z direction. However in case of failure the system is not centered. To overcome the problem a symmetric stage was developed, so even without any power supply the mechanism is normally centered. This is an xy stage which uses two pairs of APAs working in a push-pull mode, so that the non-energized and energized zero positions are almost equal. An application of this device can be found on the LASCO telescope aboard of the SOHO spacecraft [25]. A three degree-of-freedom tilt mechanism was developed by Cedrat Technologies. This device is based on two pairs of amplified piezo actuators exhibiting $35\ \mu\mathrm{m}$ of stroke each, arranged in cross configuration. The mechanism allows an independent tilt movement of $\pm 2\ \mathrm{mrad}$ around both the x and y axis and a stability better than $1\ \mu\mathrm{rad}$. It presents a high frequency bandwidth of $1\ \mathrm{kHz}$, which can be useful for precise and fast optical applications like optical switches and spectrometry. Finally, it is typically three to five times

lighter than a voice coil actuator. A set of ten of these mechanisms are integrated in the space atomic clock PHARAO, installed on the ISS. They guarantee stability and control of the angle of incidence of laser beams in front of an optical fiber [26].

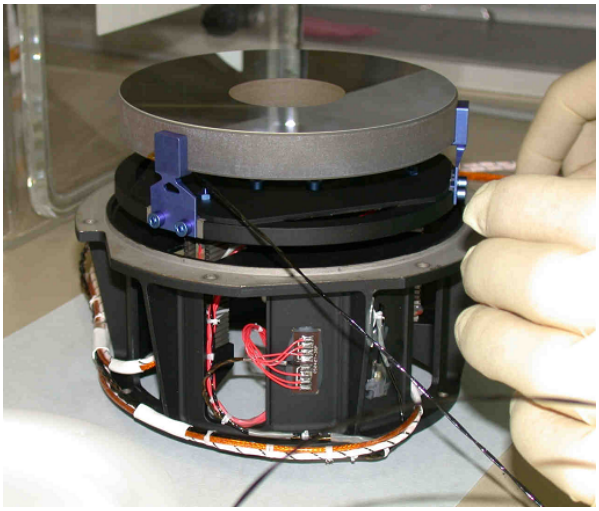

Fig. 2.12: PICARD/SODISM mechanism [27]

Another mechanism using APAs was developed to be mounted on telescopes for earth observation [28]. It is a 5-DoF mechanism which is able to move a mirror of a maximum weight of $3\ \mathrm{kg}$, in order to compensate thermal deformation of the satellite structure. The focusing and tilts movements are produced by three vertical actuators placed at $120\ \mathrm{deg}$ on a circle. The transverse movements are produced by three horizontal actuators made of pairs mounted in series and constituting the sides of an equilateral triangle set inside a circle. The device is able to provide a maximum translation of about $100\ \mu\mathrm{m}$ and a rotation of $200\ \mu\mathrm{rad}$. A similar device is used on SODISM optical system of PICARD mission, where three piezoelectric actuators are used to move the primary mirror, enabling the rotation around x and y axes and a translation along z (see Fig. 2.12) [27].

More space applications of piezoelectric actuators include the Point Ahead Angle Mechanism of the proposed eLISA mission [29], the Beam Steering Mechanism of ATLID instrument on ErathCARE mission [30], the Cold Gas Proportional Thruster valves developed by Selex Galileo [32], the piezoelectric CheMin instrument sieving mechanism on board Curiosity rover [31], and others (see Fig. 2.13).

Piezoelectric actuators are also capable of suppressing micro vibrations on board spacecraft. Typical vibrations for a spacecraft on orbit are within 50 and $150\ \mathrm{Hz}$ and are mainly due to internal moving parts like flywheels. Stripe and patch piezo actuators have been proposed for vibration suppression on sensible instrumentation [33]. Piezo-actuated 6-DoF Stewart platforms can be employed for holding scientific instruments and compensate the vibration transmitted to them by the vehicle structure. Stewart platforms have been proposed also for the control of vibrations in space truss structures [34]. Fine mechanical stability in a free-floating

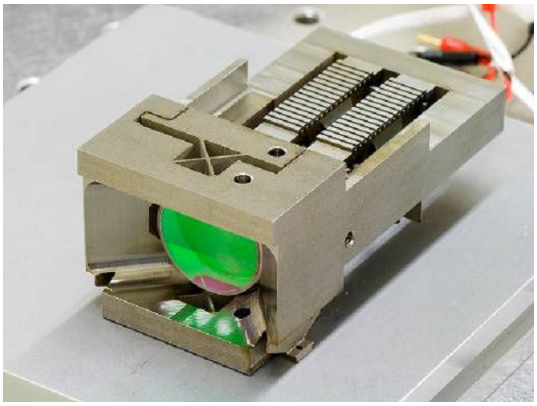

(a) LISA/PAAM mechanism [29]

Reprinted from [29] ©2010 SPIE

(b) ATLID Beam Steering Mechanism [30]

Reprinted with permission from [30]. ©ESA 2013. Cedrat Technologies.

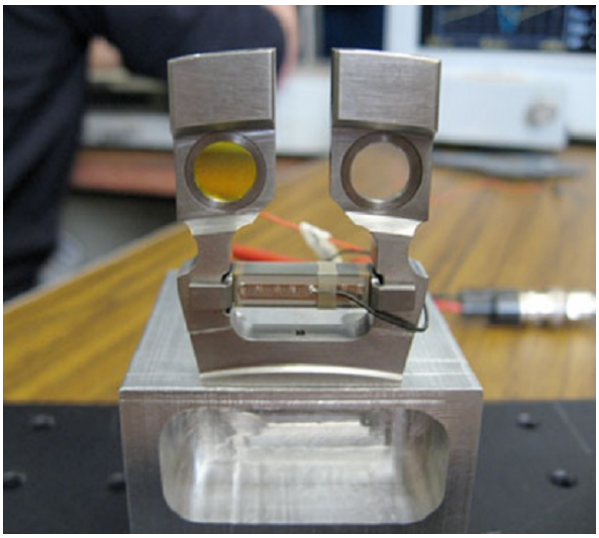

(c) CheMin sieving mechanism [31]

©2012 by the autors of [31]

Fig. 2.13: Space piezoelectric actuators

space truss is difficult to achieve because this kind of structures are generally large, flexible and subject to a wide variety of static and dynamic perturbations (i.e. thermal loads, attitude control and reaction-wheels vibrations). A second technique for vibration control consists of replacing some bars of the truss with active bars controlled by piezo actuators. This method was investigated using CASTOR experiment [35] mounted on the MIR space station in 1997. Another technique consists of adding actuated cables (active tendon concept) between various points of the truss. The advantage of this method is that the truss mechanical properties are not modified and that the implementation of active tendons can be performed at a later development stage of the truss. Micro vibration cancellation is employed on the infrared interferometers mounted on MetOp satellites and on DARWIN mission [23]. Concluding, also piezoelectric motors have been developed to be used in space systems. One notable example is the Grabbing, Positioning and Release Mechanism (GPRM) on board the LISA Pathfinder

mission [36]. In this application a linear piezoelectric motor (see Fig. 2.14) is used to hold, release and reposition a free-floating test mass for gravitational studies.

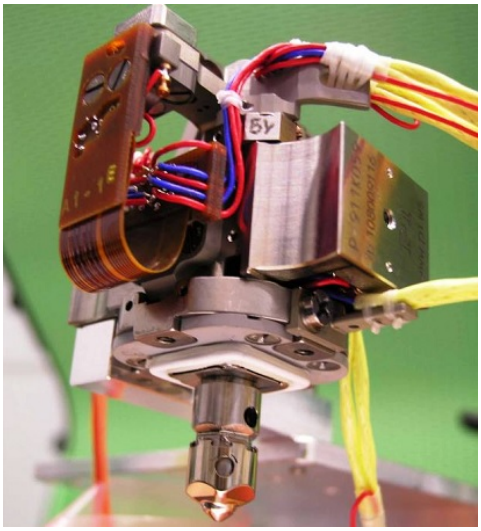

Fig. 2.14: GPRM on LISA Pathfinder mission [36]
Courtesy of RUAG Schweiz AG, RUAG Space. ©2009 ESA

Tab. 2.2: Piezoelectroc actuators PROs and CONs

Device	PROs	CONs
APA	large force	small stroke
	high actuation frequency	complex electronics
	high precision	high mass density
	high reliability	
	flight heritage	
bending actuator	large deflection	small force
	high actuation frequency	low accuracy
piezo-motor	large forces	complex control & electronics
	large stroke	low velocity

2.2.1.2 Shape memory actuators

Shape Memory Alloys (SMAs) are metallic alloys that are capable of memorizing and restoring the original shape, after being deformed and exposed to an appropriate thermal treatment. Thanks to this property, SMAs can be used to generate motion and force, making them an alternative for actuators in mechanism, also in space applications. Only few of these materials are of commercial relevance: Nitinol (Ni-Ti) and some copper-based alloys (Cu-Al-Ni and Cu-Zn-Al) or their combinations with small quantities of other elements. Other alloys are not suited for industrial manufacturing either because the constituent elements are too expensive

or because they cannot be used unless they are in the form of single crystals. The properties of Nitinol and copper alloys are fairly different due to their different micro-structure. Since Nitinol alloys have much higher strength, larger recoverable strain, better corrosion resistance and, most importantly, higher reliability than copper alloys, they are the standard SMA choice for use in space and several other applications.

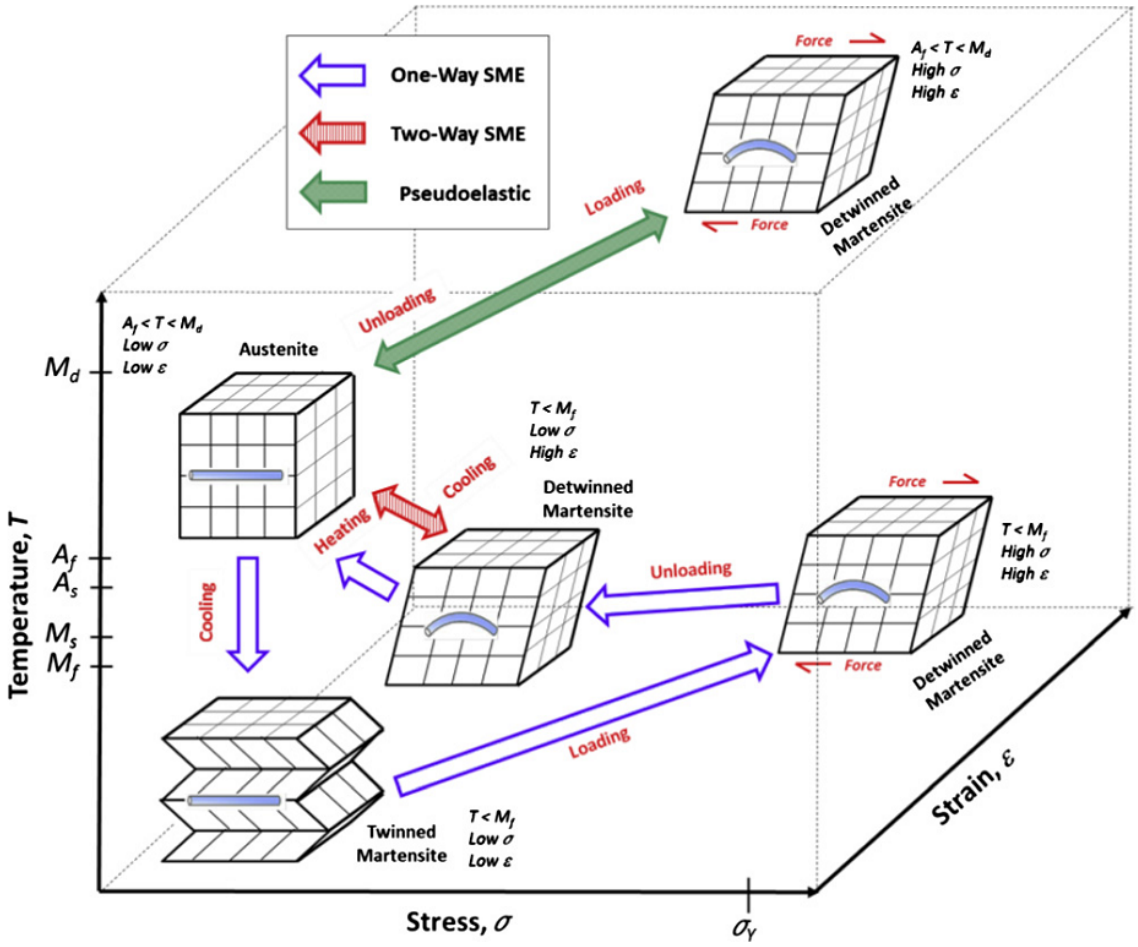

Fig. 2.15: Shape memory alloy structure transformations [37]

The SMAs characteristic behavior is related to the ability of the material to change its crystal structure, i.e. mutate from one crystal structure to another. It is a phase transformation, called martensitic transformation, which occurs between the high temperature parent phase, austenite, and the low temperature phase, martensite. Martensitic transformation in shape memory alloys is defined as a displacive (or diffusionless) transformation, since the chemical bonds between atoms are restructured instead of broken, so that the chemical composition matrix is intact. Such transformation can be induced by a temperature variation, which changes the free energy of the material. The temperature at which shape transitions occur can be adjusted by slight changes in the alloy composition and through heat treatment. SMAs can exist mainly in two different phases with three different crystal structures (twinned martensite,

detwinned martensite and austenite) and six possible transformations can occur between these structures (see Fig. 2.15); the operating temperature and applied stresses are the drivers of the structure transformation. The austenite structure is stable at high temperatures and is characterized by cubic crystalline structure, whereas martensite is steady at low temperatures, presenting a tetragonal or monoclinic crystalline structure; moreover, martensite has a low yield limit and it is easily deformable. The transition from austenite to martensite can result in twinned martensite if any internal and external shear stress is present, or detwinned martensite if such stresses develop up to a sufficient level. If sufficient stress is applied, the reorientation of twinned martensite into detwinned martensite can occur [38]. The peculiar behavior of SMAs is summarized by two features:

- Shape Memory Effect (SME), which is the capability of restoring the original undeformed shape after an inelastic deformation (at low temperature) by increasing the temperature (One-Way Shape Memory Effect, OWSME) or to regain the deformed shape through cooling (Two-Way Shape Memory Effect, TWSME);
- pseudoelasticity (or superelasticity), which is the ability to recover a considerable deformation at high temperature.

OWSME is the simplest shape memory effect and it is often exploited in actuators (see violet-outlined arrows in Fig. 2.15). At the beginning of the loading path the alloy is in its austenitic configuration; at the time of cooling (form martensite-start-temperature, M_s, to martensite-finish temperature, M_f) the SMA transforms into the twinned martensitic configuration without any strain applied. Applying stress on the structure causes a reorientation of martensite into a fully detwinned state and a macroscopic plastic deformation of the material. During unloading, while the elastic strain is fully recoverable, the inelastic part, caused by the detwinning process, persists due to the stability of detwinned martensite. When the alloy is heated, the transformation process proceeds and gradually recovers the original austenitic structure and undeformed shape between the austenite start temperature, A_s, and the austenite finish temperature, A_f.

When TWSME is present, the material structure can change between austenite and detwinned martensite only through heating/cooling (see red arrow in Fig. 2.15). TWSME is obtained by means of material training processes, such as thermal cycles with different imposed shapes at high and low temperature. Although TWSME alloys show a more sophisticated memory effect, they are commercially less interesting, because they need special material training requirements and with the same amount of material they provide half of the recovery strain generated by OWSME alloys [39] and are more affected by fast deterioration.

The SMA alloy shows a considerable non-linear elastic behavior at high temperature (in the A_f - M_d range, see green arrow in Fig. 2.15): if an external load is applied to the material in the austenitic state, the internal structure changes to detwinned martensite (Stress-Induced detwinned Martensite, SIM) showing large macroscopic deformations. The original austenite and external shape is recovered upon unloading without any temperature change needed. This

behavior is called pseudoelasticity (or superelasticity) and it is a non-linear property, meaning that Young's modulus is strictly dependent on the temperature and deformation.

Compared to traditional actuation solutions, shape memory actuators offer some advantages: mass and volume saving, simple design, noiseless operations (low vibrations), no shock loadings when used as a replacement of pyrotechnic devices. Nevertheless, SMAs present also limitations which include a relatively small usable strain, low actuation frequency, low controllability, low long-term performances, low accuracy and low energy efficiency. Different factors influence the long-term performance and reliability of SMA actuators such as operative temperature, stress, strain and the number of transformation cycles accumulated. Maybe the main drawback of these materials is the low operational frequency due to the heating/cooling process time constants: while electric heating by Joule effect can be fast, the cooling is often much slower and less predictable. The best way to mitigate this issue is to provide active cooling of the SMA component, although this contributes to the increase of cost, weight, physical volume and mechanical / control complexity of the device. A simpler solution is passive cooling, which is not controllable and strongly dependent on environment conditions.

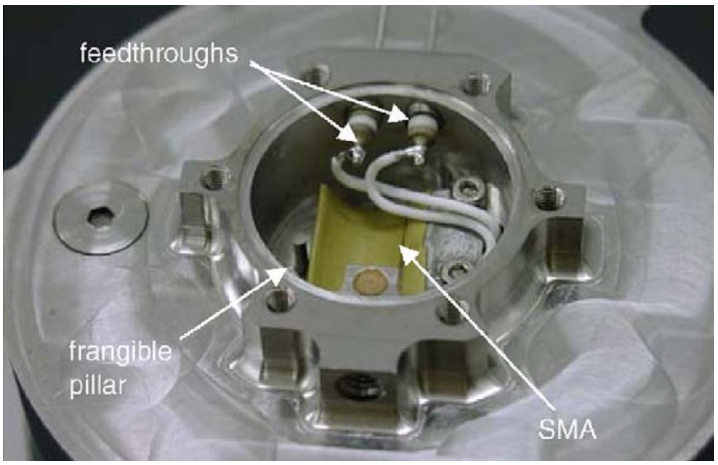

Fig. 2.16: SMA actuator in Ptolemy/Rosetta [40]

Shape-memory actuators in space are primarily used as non-explosive actuators for deployment and release mechanisms. Spacecraft require a variety of release devices to accomplish mission-related functions like separation from the launch vehicle or deployment of solar arrays and other appendages. The traditional employment of pyrotechnic charges exhibit numerous drawbacks like: the extremely high cost of handling, storage and transportation during ground operations and integration; the propagation of high shocks to the spacecraft structure, subsystems and payload; the possible ejection of contaminants which are detrimental to lenses and electronics; the impossibility to guarantee the flight model reliability due to the disposable nature of these devices. Low-shock, non-pyrotechnic spacecraft release devices are a safe alternative that allow to mitigate the hazards connected to the use of pyrotechnic devices.

SMA low-shock release devices are Frangibolts® by TiNi Aerospace and pin-pullers. Frangibolts® are devices designed for the deployment of a wide variety of stowed appendages, like solar panels or antennas. They are composed by a Nitinol hollow cylinder wrapped with an electric heater, and a pre-notched titanium bolt. The TiNi cylinder is pre-compressed at low temperature to martensitic phase (up to 5% of length) and secured with the bolt that holds the compression load. When the release is required, an electric current heats the actuator up triggering the martensite-to-austenite transformation. The increased load in the bolt reaches the ultimate stress causing the fracture at predetermined locations and releasing the loads; the SMA element recovers the original shape. Frangibolts® are cost-efficient, easy to install, eject no gas / particles, produce no shock loads, can be actuated and reloaded several times in order to verify proper operation of the system. Two potential limitations affect Frangibolts® : the long response time of the device due to the slow heating process of the SMA actuator ($20 \div 70$ s); the limit to maximum temperature allowable near the actuator (~ 100 °C), since the Nitinol transition temperature cannot be much higher than 120 °C. Frangibolts® are used in several space missions: on the Clementine spacecraft they were used to deploy the solar panels [41]; the REXIS/OSIRIS-REx spectrometer contains a deployable cover that was held closed by the bolt for several years in cold storage [42]; the Solar Orbiter mission will mount three release mechanism which will be opened in sequence to release its antenna [43].

SMA actuated pin-pullers are used to hold, lock or secure deployable or moving parts on spacecrafts during launch. Pin retraction is achieved by using a Nitinol wire which triggers the release of the elastic energy stored in a compressed spring. By directly passing current through the Nitinol element, the release mechanism can be triggered in milliseconds. SMA pin-pullers design is inherently simple, small and safe, they require very low power to be actuated and do not pose any outgassing concerns.

Shape-memory alloys and polymers can also be used as hinges to deploy folded structures. For example, the Lightweight Flexible Solar Array (LFSA) experiment incorporated a thin SMA strip at the hinge location which, when actuated, opened a previously folded solar array. Deployment has been shown to take approximately 30 s [44].

SMA are also used for applications different from release devices. A SMA actuator is mounted on the Ptolemy instrument of the Rosetta comet lander, which is an advanced gas analyzer. The instrument relies on a supply of pure helium, which is stored in a pair of titanium gas tanks. The use of a conventional valve to seal the tanks would have led to a high loss of helium through leakage over the long period of inactivity involved in this mission (fitfteen years from filling to use). Instead, the tanks are sealed with a hollow frangible pillar, which was broken with a SMA actuator to release the gas after reaching the comet (Fig. 2.16). The actuator is made of a Nitinol strip with a deformed buckled shape that, upon heating, recovers its original planar shape fracturing the pillar [40].

Fig. 2.17: SMA actuator for hopping robots [45]

Space robotics applications have been also conceived, like the SMA actuators proposed by Montminy et al. [45] for the mobility of small planetary exploration robots (see Fig. 2.17) or the dust cover SMA actuated arm on board the Mars Pathfinder rover [46].

Tab. 2.3: Shape-memory actuators PROs and CONs

Device	PROs	CONs
Frangibolt® & pinpuller	large force high reliability non-explosive	single-shot actuation strict temperature ranges slow actuation
custom actuator	large deflection large force repeatable	discrete actuation slow actuation

2.2.1.3 Bimetallic actuators

Bimetallic strip actuators are simple devices which are used to convert a temperature change into mechanical displacement. The strips present a bimorph structure, consisting of two bands of different metals. The strips are bonded together along their surfaces by riveting, brazing or welding. The materials are chosen to have very different thermal expansion coefficients, so the different expansions force the flat strip to bend one way if heated, and in the opposite direction if cooled below its initial temperature. The metal with the higher coefficient of thermal expansion is known as the active material and is on the outer side of the bend when the strip is heated, the metal with the smaller thermal expansion is known as the passive element. The passive element is often an iron-nickel alloy, having an almost zero thermal expansion (between

10^{-7} and 10^{-6} K^{-1}) and the active element is chosen considering operating environment and costs. In addition a third metallic layer can be introduced consisting of either copper or nickel sandwiched between the active and passive elements to increase both thermal and electrical conductivity of the actuator.

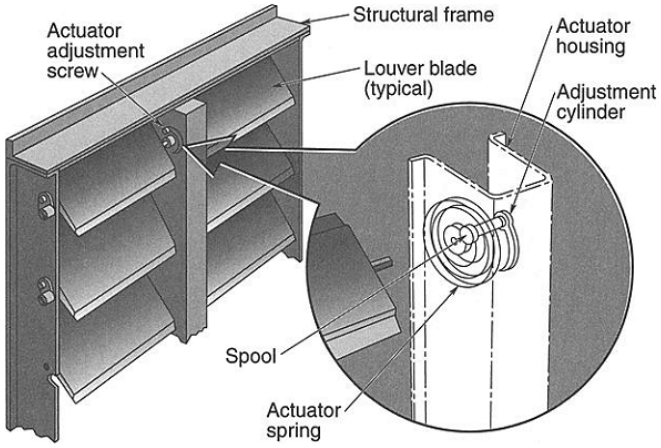

Fig. 2.18: Louvers for thermal control [47]

There are two general classes of bimetallic actuators: creep elements, which exhibit a gradual change in shape in response to a temperature change and are employed in smooth movement applications, and snap-action devices, which jump from one position to another at a specific temperature. The first type is used for satellites thermal control, as in louver radiator systems, shown in Fig. 2.18. These systems consist of different elements: baseplate, blades and the actuators. The baseplate is a surface that has low absorptance and emittance and covers a critical set of components whose temperature has to be controlled. The blades are the louver elements that give variable-radiation characteristics to the baseplate. They are highly polished to reduce emittance and their rotation is actuated by the expansion or contraction, according to the perceived baseplate temperature, of a spiral bimetallic actuator. The actuators drive the blades from fully closed to fully open over only a $1\ ^{\circ}C$ temperature change. The louver begins to open passively (by conduction from the mounting plate to the bimetallic spring) at about $10\ ^{\circ}C$. These types of louver assemblies have been used for several space missions, such as Pegasus, the Hubble Space Telescope, Nimbus, the Earth Resources Technology Satellite, SolarMax, Cassini, Seasat and the Global Positioning System (GPS) satellites [47].

In space application bimetallic actuators are used for the actuation of micro-machined valves and pumps. Excellent performances can be obtained, including high deflections and large actuation forces under relatively low bias voltages. An application can be found on ExoMars Pasteur/MOMA, where is mounted a hermetically sealed gas tank which is used for a gas analyzer. A configuration similar to the one mounted on Rosetta could not be used since the system is subjected to temperatures of $130\ ^{\circ}C$ during the sterilization process mandatory for planetary missions, while the SMA actuator activation point is $76\ ^{\circ}C$. A single-shot bimetallic

snap-disc valve was developed. It is electrically actuated by an ohmic heater that is very thin and lightweight and can heat up to a temperature of $200\ °C$. On the top of the snap-disc a needle pin is attached. When the actuator is heated the pin pierces a metallic membrane, thereby opening the valve. The design of this single-shot valve is such that it allows it to withstand a temperature of $130\ °C$ and a pressure of $50\ \mathrm{bar}$. The valve is also lightweight ($6.62\ \mathrm{g}$) and it requires $90\ \mathrm{s}$ of powering at $9\ \mathrm{W}$ to operate [48].

Tab. 2.4: Bimetallic actuators PROs and CONs

Device	PROs	CONs
bimetallic spring for radiator louvers	large deflection active control without electronics	repeatable strict temperature ranges slow actuation
custom actuator	large deflection high reliability	discrete actuation slow actuation single-shot actuation basic applications

2.2.1.4 Dielectric Elastomers

A large family of versatile materials are the so-called Electro Active Polymers (EAPs), which have been intensively investigated over the last decades while several applications have been proposed to exploit their potentialities. The two main families of EAPs are ionic EAPs and electronic EAPs [49]. The first family includes:

- carbon nanotubes;
- conductive polymers;
- electrorheological fluids;
- ionic polimer-metallic composites;
- ionic polymer gels.

The second family includes:

- liquid crystalline elastomers;
- ferroelectric polymers;
- electro-viscoelastic elastomers;
- electrostrictive paper
- electrostrictive graft polymers;
- dielectric elastomers.

Among EAPs, a number of studies have proven the impressive properties of Dielectric Elastomers (DE) like high energy densities ($> 1000\ \mathrm{J/m^3}$) and large actuation strains ($> 100\%$) [50]. DEs are a promising family of materials that can be employed in solid-state actuators and

devices. They show several advantages over other concurrent solutions: they are suitable to both actuation and power generation applications in various geometries [51], easy to manufacture and suitable for 3-D printing [52], employable in multiple degrees of freedom systems [53] and capable of self sensing functionalities [54].

Thanks to their distinguishing capabilities, these devices can satisfy the strict requirements of very specific applications (e.g. space systems) and, at the same time, improve the performances of existing solutions. For example, space robotics can take advantage from the employment of DE actuators, since they enable relevant features like:

- distributed actuation;
- compactness and simplicity (i.e. many DoFs with few actuators);
- low mass;
- low power consumption;
- absence of vibration and wear.

Nevertheless, no space application of these technologies has been brought to a Technology Readiness level (TRL) higher than a preliminary feasibility investigation (TRL 2-3). Work needs to be done in order to bring DEs to space, mainly due to environment compatibility issues (see Sec. 4.3.1); current limits affect the employed materials (outgassing, radiation compatibility, degradation), the power supply systems (high voltage) and manufacturing process (lack of reliability and repeatability).

A remarkable number of geometries have been proposed for DE-based actuators, including cylindrical and rolled actuators [55][53], planar actuators [56], folded actuators [57], lozenge-shaped actuators [58], thin rotary motors [59] and several cone or double-cone assemblies [60][61][62]. Many of the cited geometries feature multiple DoFs actuation considerably improving the operational flexibility. The double-cone configuration shows as many as five independent DoFs [63], thus making it a good candidate for compact and light-weight applications. DEAs can be split in two main categories depending on the tensional state imposed to the material before actuator manufacturing. In some applications the elastomer is uni- or bi-axially pre-stretched in order to impose positive stresses in the material, while in some other geometries such preliminary deformation is not necessary. The pre-stretch generally increases the performances on the device, increasing the energy density, the actuation strains and reducing the risk of membrane instabilities. Nevertheless, some drawbacks are connected with pre-stretching, like the increased complexity of the manufacturing process or the need to properly constrain the material when stretched in order to support the internal stresses. Acrylic elastomers are usually pre-stretched while silicones often do not need this preconditioning process.

Arguably the simplest DEA geometry is the planar actuator [64]. In this configuration the pre-stretched material is mounted on a rigid ring structure and a concentric circular electrode is laid in the middle of the circular membrane (see Fig. 2.19a). The electrodes expand radially when high voltage is applied; more than 12.5% radial deformation was observed after 175 s

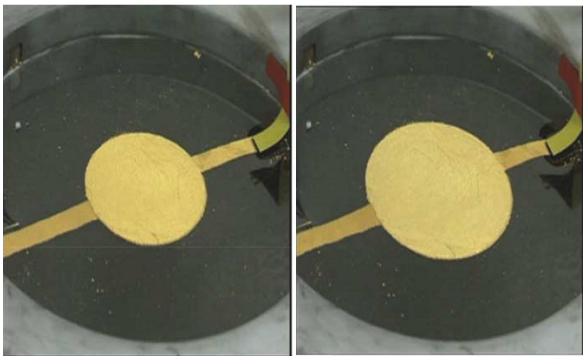

(a) Planar actuator [64]

Reprinted from [64] ©2005, with permission from Elsevier.

(b) Diaphragm actuator [65]

Reprinted from [65] ©2007 SPIE

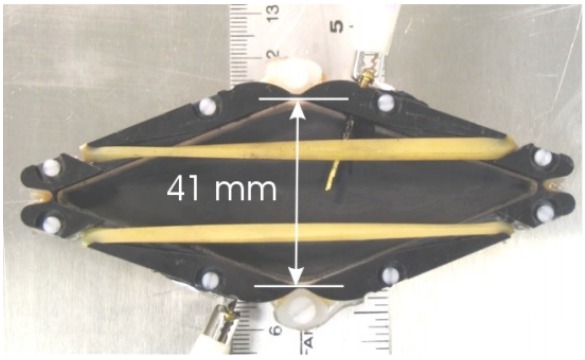

(c) Lozenge shaped actuator [66]

Reprinted from [66] with permission from the author ©2007 SPIE

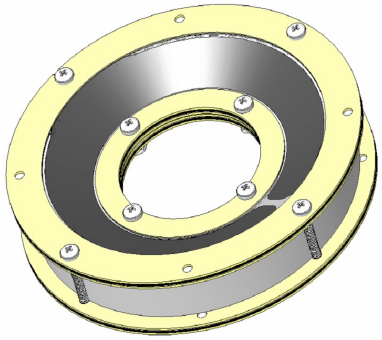

(d) Universal muscle actuator [67]

Reprinted from [67] with permission from the author ©2006 SPIE

Fig. 2.19: Dielectric Elastomer Actuators geometries - 1

under $3.5\ \mathrm{kV}$ of applied voltage. This actuator will unlikely find a real world application, but it is a key demonstrative experiment, very useful to understand the behavior of DE devices in detail.

A somewhat similar application of DE are diaphragm actuators [65]. These devices are conceived as pump prototypes (see fig. 2.19b). A circular elastomer membrane makes up the wall of a pressurized chamber. The chamber internal pressure inflates the membrane that bulges out of the rigid structure. The membrane is fully covered by compliant electrode; voltage application causes a variation of internal pressure. Both silicone and polyacrylate have been tested. The pressure variation available in a $13\ \mathrm{cm}^3$ diaphragm actuator is approximately $1.2\ \mathrm{kPa}$ under $3\ \mathrm{kV}$ of applied voltage.

Lozenge shaped actuators are an example of 1-DoF linear actuator [66]; a planar elastomer membrane is uniaxially stretched and mounted on a deformable structure composed by four rigid elements connected by hinges. The rigid elements are assembled to form a diamond shape; the material uniaxial prestretch is parallel to the minor diagonal. The membrane internal stress tends to collapse the diamond along the pre-stretch direction (i.e. reduce the minor diagonal), while elastic elements (e.g. elastic hinges or rubber bands) counteract the membrane loads until an equilibrium condition is reached. The membrane is fully covered by compliant electrode; when voltage is applied, the membrane stress relaxes and the actuator

reaches a new equilibrium position with different diagonal lengths. The stroke along the minor diagonal is the useful DoF. Following optimal design procedures [58], this actuator is capable of an almost constant actuation force through the whole stroke. Example performance figures for a four-layer actuator are 2.2 to 2.9 N of force over a 60 mm stroke under 4.8 kV of applied voltage.

The so-called universal muscle actuator is another option of linear actuator [67]. This actuator is composed by two annulus shaped membranes deformed to truncated cones, mounted mirrored to each other, with coincident minor bases and the major bases fixed (see Fig. 2.19d). The output shaft is concentric to the mebranes. Both membranes are completely coated by electrodes and when high voltage is applied the height of the truncated cone increases; by differential actuation of either one membrane or the other, it is possible to obtain positive or negative stroke.

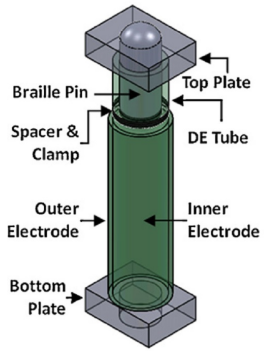

(a) Cylindrical actuator [68]

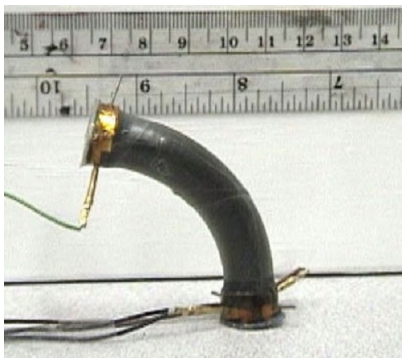

(b) Spring rolled actuator [53]

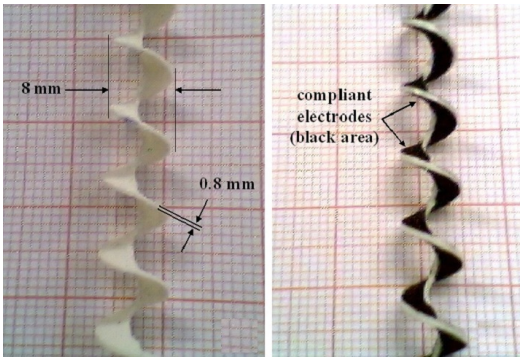

(c) Helical actuator [69]

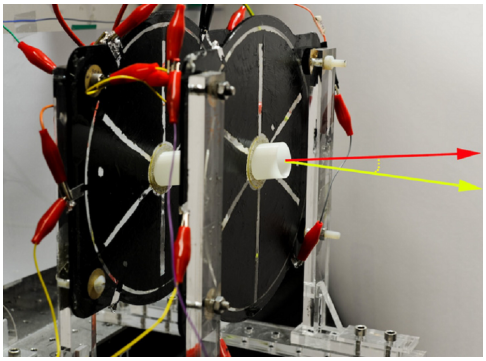

(d) Thin rotary motor [59]

Fig. 2.20: Dielectric Elastomer Actuators geometries - 2

A simple geometry proposed for DEA is cylindrical [55]. The dielectric membrane is rolled up to cylindrical shape, possibly in multiple layers (see Fig. 2.20a). A single electrode is applied to the cylindric membrane. By applying high voltage to the electrodes, the actuator elongates axially. Few millimeters long silicone cylindric actuators (diameter 2 mm) can reach 5% elongation under 19.5 N of applied voltage. Refreshable braille pads based on cylindrical DEAs have been conceived [68].

An alternative cylindrical actuator is provided with a core spring for pre-load [53]. Mechanically, the actuator is an improved version of the cylindrical architecture, the only difference being that the membrane is rolled around a compressed spring. In addition, the electrodes are multiple (two or four), longitudinal and each of them spans only for a limited angular width (180 deg for two electrodes, 90 deg for four electrodes). Depending on the number of electrodes, this actuator features more than one DoF: two (one translational, one rotational) in the two-electrode case or three (one translational, two rotational) in the four-electrode case. The rotational DoFs are perpendicular to the cylinder axis (see Fig. 2.20b). A 2-DoF rolled actuator (length 68 kV, diameter 14 mm) is capable of 90 deg of maximum bending angle and 0.7 N of maximum lateral force under 6 kV of applied voltage.

Also helical actuators occupy a cylindrical envelope and provide a 1-DoF linear actuation [69]. Unstretched silicone is employed in this application. Elastomer helices are cut out of tubes and the electrodes are deposited on the cutting planes thus being connected throughout the actuator length (see Fig. 2.20c). The helical element is later coated within a cylindrical protective envelope. By applying voltage to the electrode, the actuator contracts along the cylinder axis; a 5% contraction (4 mm in a 80 mm actuator) can be reached under 11 kV of applied voltage.

A thin rotary motor based on DE was proposed by Anderson *et al.* [59]. Two acrylic, circular membranes (diameter 200 mm) are pre-stretched, mounted on rigid frames, concentric and parallel to each other at a fixed distance (85 mm); both the membranes are coupled to a central shaft by means of a special deformable gear. The circular membranes are divided in six sectors and wedge shaped compliant electrodes are applied on them (see Fig. 2.20d). By alternatively applying high voltage to the electrodes in proper sequence and symmetrically on both membranes, a wobbling and rotational motion of the central shaft is generated. A maximum rotation speed of 0.16 rad/s was achieved under 2.5 kV of applied voltage at 2.5 Hz of electrodes commutation frequency.

Stack actuators are made of un-stretched silicone [70]. A large number of small circular or square pads of silicone are coated on both sides with compliant electrodes and piled one on top of the other to form a stack of layers (see Fig. 2.21a). Voltage application to the electrodes causes the thickness reduction of each silicone pad and the overall contraction of the actuator. Prototypes capable of 18% of contraction strain (4 mm for a 23 mm long actuator) or up to 32 N of force under 4.2 kV of applied voltage.

A comparable architecture are folded actuators [57]. A strip of dielectric elastomer is coated with compliant electrode on both sides and than folded several times obtaining a geometry very similar to stack actuators (see Fig. 2.21b). By applying high voltage the elastomer thickness is reduced and the actuator is compressed. For a 40-mm long example actuator with squared section (25×25 mm) it is possible to achieve 16% of axial compression (6.4 mm) or 2.7 N of force under 6 kV of applied voltage.

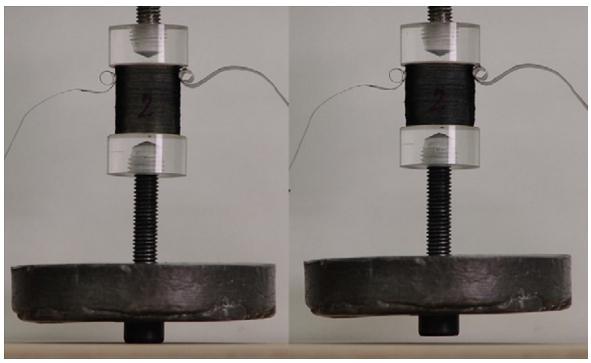

(a) Stacked linear actuator [70]

Reprinted from [70] ©2009, with permission from Elsevier.

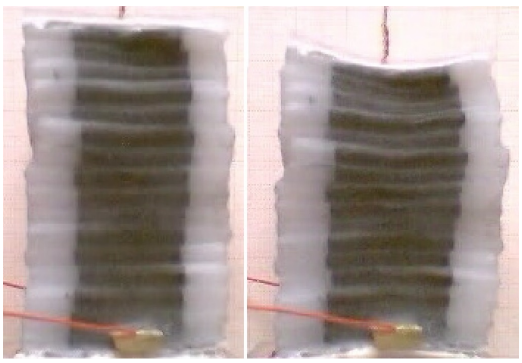

(b) Folded actuator [57]

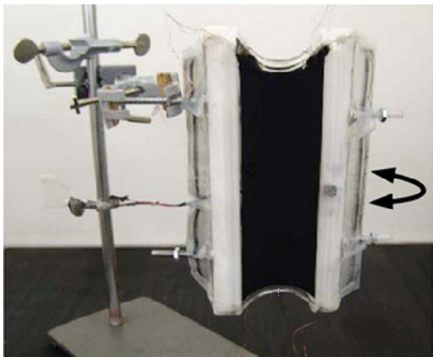

(c) Actuated hinge [71]

Reprinted from [71] ©2008, with permission from Elsevier.

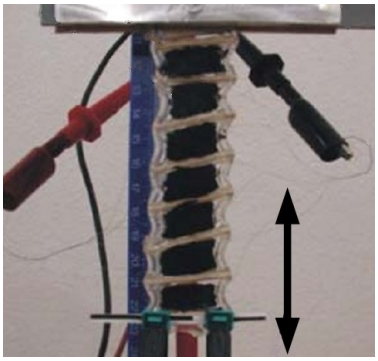

(d) Chainlike flat linear actuator [72]

Reprinted from [72] ©2006, with permission from the author.

Fig. 2.21: Dielectric Elastomer Actuators geometries - 3

A flexural actuator based on two pre-stretched DE membranes mounted on a hinge structure has been proposed by Lochmatter *et al.* [71]. The DE membranes are constrained at two sides and free at the other two (see Fig. 2.21c). Both surfaces of each membrane is coated with a single compliant electrode; when voltage is applied to one membrane it extends allowing the other to contract under internal stresses, thus rotating the hinge structure. Example performance values for a single layer actuator (width $190\ \mathrm{mm}$, length $62\ \mathrm{mm}$) are: $32\ \mathrm{deg}$ of angular displacement and $1.2\ \mathrm{N}$ of blocking force under $4\ \mathrm{kV}$ of applied voltage.

Chainlike actuators are another actuator option [72]. These actuators are composed by a linear series of small squared membranes coated with compliant electrode, resulting in a flexible strip-like structure (see Fig. 2.21d). A 95-mm long, 30-mm wide actuator showed 10.5% elongation $(10\ \mathrm{mm})$ under $4.5\ \mathrm{kV}$ of applied voltage.

Conic actuators are an interesting solution for 1-DoF to 5-DoF actuators (see Fig. 2.22). There are different options for the implementation of DE cone actuators, but all of them share the active element geometry. A circular membrane is biaxially stretched, coated with compliant electrodes and deformed to conical shape. A pre-load is required to keep the cone shape and it can be provided in several different ways like: lozenge spring (Fig. 2.22a), flexural springs (Fig. 2.22b), tensional rubber band (Fig. 2.22c). All the mentioned configurations are 1-DoF linear actuators; by applying high voltage to the electrodes, the cone height increases. For

(a) Single-cone linear actuator with lozenge spring [73]

(b) Single-cone linear actuator with flexural springs (not visible) [74]

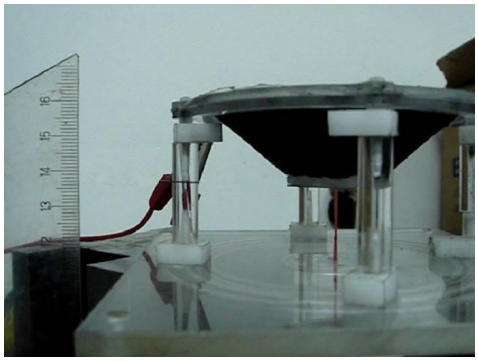

(c) Single-cone linear actuator with pre-load rubber band [75]

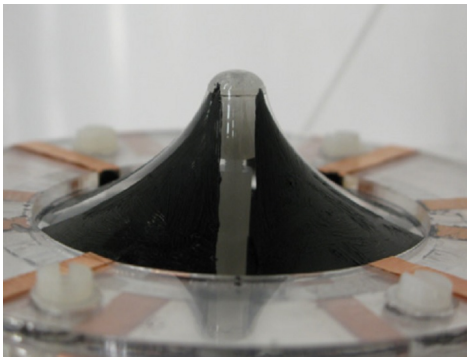

(d) 5-DoF double-cone actuator with rigid pre-load pivot [63]

Fig. 2.22: Dielectric Elastomer cone actuators

example, blocking force can reach 0.55 N and the linear stroke can reach 4.2 mm under 3 kV of applied voltage (actuator total diameter $80 \div 100$ mm). The geometry shown in Fig. 2.22d proposed by Conn *et al.* is composed by two DE cones mounted concentric, one-mirrored to the other with a rigid shaft that keeps them separated and deformed. This device provided multi-DoF capabilities (up to 5 DoFs) and a very promising behavior.

To overcome the issue of limited loads that DEAs can usually withstand and to amplify linear or angular stroke, bi-stable structures have been coupled with DE elements to develop stronger actuators. In all cases, the actuation of the DE element by means of high voltage determines the relaxation of the material internal stresses and the reduction of loads to the pre-loaded structure that snaps to a new equilibrium position; intermediate positions can not be held. Due to this peculiar on/off behavior, these actuators are also called binary actuators. Fig. 2.23 shows four different options: Fig. 2.23a-2.23b depict two antagonistic configurations, the first being a linear actuator and the second a rotational actuator; Fig. 2.23c is the bistable version of the lozenge-shaped actuator; Fig. 2.23d is the bistable version of the cone actuator. Performance figures are the following: linear antagonistic actuators (dimensions: $200 \times 75 \times 6$ mm) are capable of 0.7 N of force and 16 mm of stroke; rotational antagonistic (dimensions: $130 \times 60 \times 37$ mm) can reach 0.02 Nm of torque and 80 deg of angular deformation; diamond actuators (dimensions:

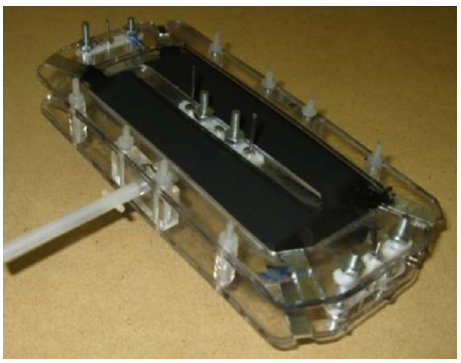

(a) Bistable linear actuator [76]

Reprinted with permission from [76], ©2011 IEEE

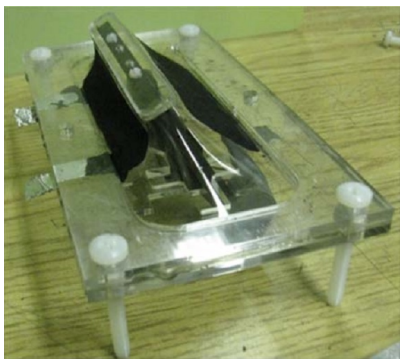

(b) Bistable rotating actuator [76]

Reprinted with permission from [76], ©2011 IEEE

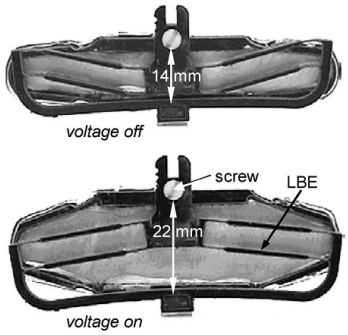

(c) Large-stroke bistable linear actuator [77]

Reprinted with permission from [77], ©2006 IEEE

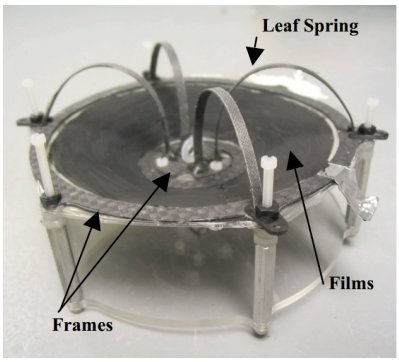

(d) Bistable cone actuator [66]

Reprinted from [66] with permission from the author ©2007 SPIE

Fig. 2.23: Bistable Dielectric Elastomer Actuators

80×30 mm) provide 0.33 N of force and 25 mm of stroke; cone actuators (diameter 100 mm, height 25 mm) output 0.75 N of force and 13 mm of stroke.

Robotic applications of DEAs exist; a few examples are shown in Fig. 2.24-2.25. A 12-DoF walking robot equipped with six 2-DoF spring roll actuators have been proposed by Pei *et al.* [53] (see Fig. 2.24a). An electro-adhesive end-effectors is shown in Fig. 2.24b; it is capable to comply to a 80-g egg by means of DE fingers and to hold it by means of the electrostatic forces generated by the high voltage in the electrodes [78]. Worm-like robots, like those shown in Fig. 2.24c-2.24d, are a typical bio-inspired application of soft robotics [79][80].

Two interesting DEAs applications for planetary exploration are shown in Fig. 2.25. The first (Fig. 2.25a) is a hopping spherical robot based on a linear bi-stable cone actuator [66]. The system is intended to move on the surface of extraterrestial planets avoiding obstacles by jumping over them. The second (Fig. 2.25b) is a spherical rolling robot that is capable to deform its shape by means of DE active areas on the external surface. The sphere has a rigid structure that supports a DE skin, which is divided in four wedge sectors that can be activated independently. Pressurized air inside the sphere keeps the membrane in tension. By applying voltage to one sector, it bulges slightly and deforms the sphere changing the position of its center of mass. Therefore, the system is unbalanced and rolls to reach an equilibrium position [81].

(a) 12-DoF robot based on rolled actuators [53]

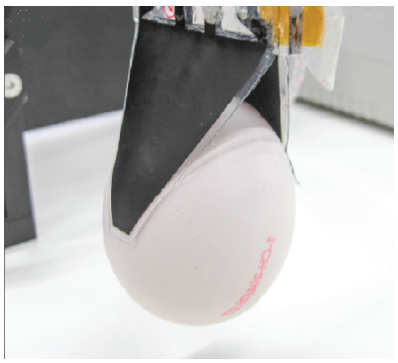

(b) DE electroadhesive gripper [78]

(c) Inchworm robot [79]

(d) Inchworm micro-robot [80]

Fig. 2.24: DEA robotic systems - 1

(a) Bistable DEA hopping robot [66]

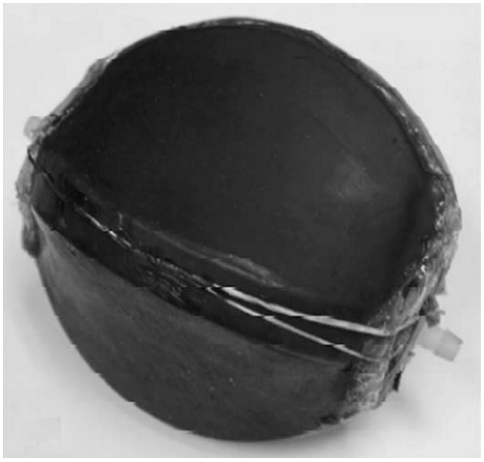

(b) Rolling robot [81]

Fig. 2.25: DEA robotic systems - 2

Some additional space applications of DEs have been published at different stages of development: windscreen wiper [82], satellite pointing system [83], distributed actuation solutions for mass transport systems [84], space structures oscillation damping with DEAs [85].

Tab. 2.5: Dielectric Elastomer Actuators PROs and CONs

Device	PROs	CONs
alternative configurations	large deflection	small forces
	controllable	slow actuation
	suitable for robotics	high-voltage
	self-sensing	low TRL
	compliance	
	multi-DoF	

2.2.2 Technology and geometry selection

All the mentioned smart actuator technologies show advantages and are finding applications in space. The trade-off between candidate technologies for the manipulator actuation aims to achieve a good balance between different functional performances like force/torque, stroke and frequency. Piezoelectric actuators are very strong and fast but show extremely small actuation strokes. Shape memory alloys/polymers can be designed to achieve large deformations or forces, but are very slow and strongly dependent on external temperature for actuation. Bimetallic actuators present a similar behavior, thus making them not suitable for the desired robotic application. Dielectric Elastomers show promising characteristics like large deformations, simple design and no vibration, while achievable forces are, in general, lower compared to concurrent technologies. DE actuators are a very attractive option due to their versatility and other useful characteristics like smooth motion, low power consumption, low mass density, manufacturing simplicity and possibility to easily obtain multi-DoF devices. Furthermore, EAP actuators applications in space are very few, making the choice of DE actuators even more appealing though challenging for the proposed robotic arm. DEAs are the selected technology for the development of the prototype manipulator in this work. The two main families of DEs, polyacrylates and silicones, show different behaviors; in particular, silicones appear to better sustain the environment issues posed by space applications (see Sec. 4.3.1), while only acrylic elastomers allow actuation strains above 10%. This work focuses mainly on actuator performances, rather than survivability, thus leading the material choice to polyacrylates.

A large variety of DEAs have been developed featuring different geometries and behavior. Multiple DE options suitable for manipulator implementation exist and have been mentioned in Sec. 2.2.1.4. Three alternatives are preselected to be employed in a prototype space manipulator: (#1) cylindrical, (#2) planar and (#3) double-cone geometries. Fig. 2.26 depicts them in a simplified view, both in relaxed and actuated state. In option #1 the dielectric membrane is wrapped in a cylindrical shape and can be supported by an internal compression spring. This geometry allows both linear axial displacement and rotation perpendicular to the actuator axis for a maximum of 3 DoF. The device can easily be manufactured in a multi-layer

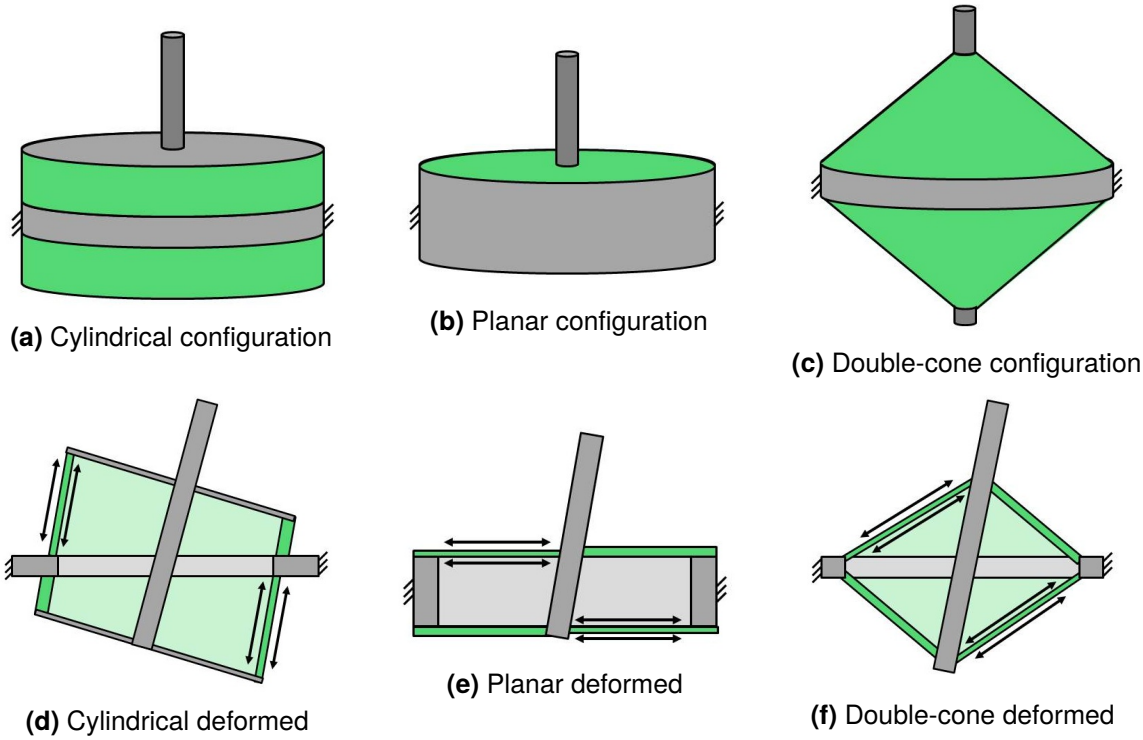

Fig. 2.26: Concurrent actuator geometries considered for space manipulator application (a, b, c). Section views of deformed geometries (d, e, f)

configuration, thus proportionally increasing available force. The main flaw of this option is the risk of local instability in the membrane if the stress state turns to compressive. Option #2 is more stable and extremely easy to manufacture; it allows radial linear displacement and rotation perpendicular to the actuator axis. However, both linear and angular strokes are too small for the proposed robotic application. Option #3 is somehow a trade-off between previous geometries; it features up to 5 DoF (i.e. radial and axial linear displacement, and rotation perpendicular to actuator axis). Axial stroke and rotation values are larger and manufacturing is easy also for multi-layer prototypes. All these architectures, or similar versions, have been described in literature [55][59][63].

Requirements definition

3

Once the technical background is clear, the first step in the development of the DE manipulator technology is the definition of requirements. The system requirements depend on the application scenario selected. The proposed technologies for the actuation of multi-body systems can, in general, be employed in a variety of different scenarios, included a large number of OOS missions. On a theoretical basis, DEAs suit well in many manipulation tasks like berthing of orbital modules, pointing of antennae, solar panels or sensors, and capture of space debris. As mentioned in Sec. 2.1, interest grew considerably over the last decades around the orbital debris problem. An example debris capture scenario is analyzed (Sec. 3.1) and simulated to provide force/torque and stroke/deflection requisites to the robotic system and, consequently, to the actuators. A preliminary analysis has been presented [86].

3.1 Example mission scenario

The example mission selected is an Active Debris Removal (ADR) mission in which a small ($< 200\,\mathrm{kg}$) servicing spacecraft performs rendezvous, approach and capture on a relevant debris object; finally, once the whole system attitude is stabilized, de-orbiting is performed. The capture system is intended as the combination of a DE manipulator with some sort of gripping end-effector that ensures the mechanical connection with the target object. The forces that arise at the interface are the design driver for both the manipulator and the gripping mechanism. Two different capture strategies have been identified in order to assess the minimum achievable capture forces, referring to the pre- and post-capture desired motion of the whole system.

The first strategy focuses on the pre-capture sequence: if the supporting robotic arm is capable of following the desired capture point on the target surface during approach, the impulsive forces at the moment of contact are considerably reduced. This type of maneuver requires the chaser vehicle to have the capability to determine the motion of the target and guide the gripper towards the designated docking point, thus minimizing the relative velocity between the two interface surfaces. Lower loads are applied to the contact interface at the cost of more resources required to the chaser platform.

The second considered strategy refers to post-capture control. The aim to damp or store the residual angular momentum carried by the debris can be achieved with two opposite approaches:

1. the servicing S/C is kept fixed at nominal attitude by means of its Attitude Control System (ACS) and the angular momentum can be properly distributed to the different ACS actuators (e.g. reaction wheels) of the satellite

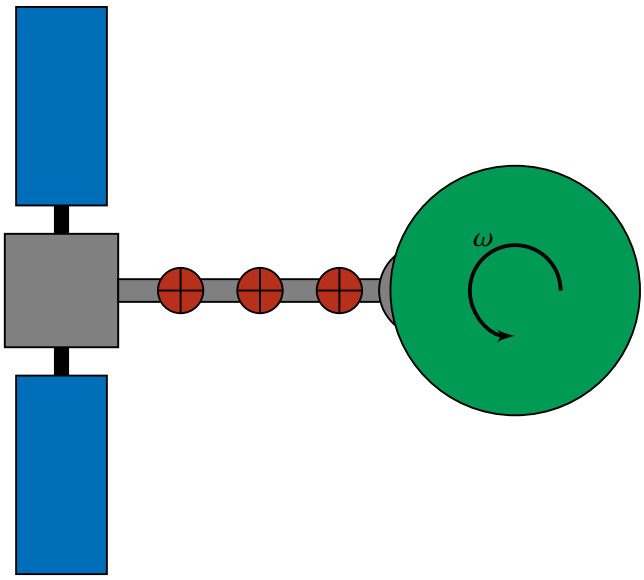

Fig. 3.1: Schematics of the multi-body system considered for the simulated ADR mission: servicing spacecraft (left), robotic arm with joints (red circles), spinning debris (green, right)

2. the servicing S/C can be completely uncontrolled and allowed to follow the motion of the debris; the capture system dampens the relative motion between the S/C and the debris until the satellite-debris system rotates rigidly

Since the mass of the servicing S/C is considerably lower compared to that of the debris, the second approach determines lower capture forces. The second approach requires less forces at manipulator joints and more relaxed control performances to the chaser ACS.

With broad consensus among the international space community [87][88], the most interesting targets for active debris removal are identified as large, intact objects located in highly populated regions of space, since they are a potential source of a large number of debris. In particular, rocket launcher upper stages appear to be good candidates for ADR missions for several reasons [89]. First, these objects are characterized by large mass and, if destroyed by an impact, would generate countless dangerous fragments. Second, they usually have a regular shape and, consequently, capture is easier. Third, they do not present any fragile appendage or structure protruding from the main body; such features could collide with the servicing S/C during approach/capture or detach from the main body and become a new piece of debris. Fourth, they are numerous and similar to each other allowing to employ the same capture system over a number of different missions with no or minor modifications. Fifth, some particular objects in this class (e.g. russian KOSMOS-3M second stages) are fairly uniformly distributed on a large variety of orbital bands, making a distributed removal action possible with few mission scenario differences.

For the example mission proposed here, the mentioned KOSMOS-3M rocket second stage is selected as possible target. The object mass (~ 1400 kg) is representative of a large variety of

objects of the same class (i.e. Vostok, Ariane 1 & 4). The object shape is roughly cylindrical (diameter $2.4\ \mathrm{m}$, length $6.5\ \mathrm{m}$) and the external surface is pretty regular and solid.

A key aspect of debris capture is the determination and management of the object attitude motion. The capture system requirements are strongly dependent on the object angular rate at the moment of connection, both in terms of impulsive capture forces as well as angular momentum management. In general, the objects spin rate is unknown and, although studies exist aiming to determine it in order to ease the ADR procedures [90], different values of possible residual angular velocities have to be considered during simulation. In this work, to identify a realistic range of possible angular rates, different scenarios are considered. The KOSMOS-3M second stage is nominally not spinned, but on some missions a small solid rocket motor placed toward aft fires within seconds after payload separation and gives the spent stage a rotational motion that increases the distance from the released payload. A rough estimate of the residual angular rate in this case is $< 10^{-2}\ \mathrm{rad/s}$ assuming $1\ \mathrm{s}$ of burning time, $20\ \mathrm{N}$ of thrust and $2\ \mathrm{m}$ of moment arm. In the case that no rocket is fired to ease payload separation, a possible motion condition for the object is the oscillation around the gravity gradient equilibrium position; a simple long term simulation has been performed to determine the maximum angular velocity under gravity gradient torques for a KOSMOS second stage on a $80\ \mathrm{deg}$ inclined, $700\ \mathrm{km}$ LEO orbit. The resulting maximum angular velocity is $< 10^{-4}\ \mathrm{rad/s}$.

The general idea is to keep the ADR mission as simple and low-cost as possible, in order to increase the effectiveness and sustainability of the debris remediation technique. For this reason, in the hypothetical mission scenario a S/C in the micro/small satellite range is selected. A preliminary sizing of the servicing vehicle was conducted in order to determine its geometric and inertial properties. The de-orbiting system adopted is based on electric propulsion and was sized as suggested by Savioli *et al.* [91]. Historical data and preliminary design relations [92] were employed for the spacecraft bus sizing that included the following main subsystems: structure, power, ADCS and communication. The breakdown of masses of the satellite bus, the re-entry system and the capture system is presented in Tab. 3.1. The overall vehicle mass is $107\ \mathrm{kg}$ including 20% of contingency, resulting in a cubic shaped S/C body with a side length of approximately $0.7\ \mathrm{m}$.

Tab. 3.1: Preliminary estimation of servicing S/C mass breakdown

System	Mass [kg]
Spacecraft bus	50
Re-entry system	51
Capture system	6

The simulations performed assess the dynamics of the combined debris-chaser system starting at the moment of capture. The implemented equations of robotics account for the multi-body

dynamics of the system. The system is modeled as a combination of a variable number of bodies (i.e. debris, S/C, actuators) connected to each other by means of two-axis rotational joints that represent the actuators degrees of freedom. A control torque is applied to each actuator.

In order to determine the actuator required torque, a control law has to be selected. For simplicity a PD control is implemented in this preliminary phase. The proportional and derivative gains are sized by imposing an appropriate rising time to the system step response in order to avoid an arm deflection greater than $90\ \mathrm{deg}$. Also, to ensure that the controlled system is stable, a minimum $45\ \mathrm{deg}$ phase margin is imposed. With this approach the control law gains are dependent on the initial value of angular momentum carried by the debris.

Different simulation approaches are adopted to account for the different capture strategies conceived. To simulate the first strategy where the satellite is nominally fixed, the S/C body is constrained to having no motion allowed. The second strategy is simulated assuming that the debris motion is not modified by the connection with the servicing spacecraft. These two simulation approaches introduce a simplification to the system and, therefore, accuracy is somewhat affected. Nevertheless, the simulations are for extreme situations which represent the worst load case scenarios. In addition, all simulations are performed twice, assuming that initially the robotic arm is both able and unable to follow the motion of the debris during the approach.

A number of simulations are performed with variable values for the initial debris angular momentum. From the estimations presented previously, the variability range of the angular velocity, ω_{db}, is selected between 10^{-4} and $10^{-1}\ \mathrm{rad/s}$ (including confidence margin). Tab. 3.2 summarizes the simulation most important results. Columns #1 to #3 give information on the type of simulation executed. The first column indicates the capture strategy adopted: if the servicing vehicle is kept fixed or if it is free to move together with the debris. The second column reports the number of actuators in the robotic arm. The third column indicates if the arm is initially still or follows the debris rotation. The last three columns give the actual results T_{max}, S_{max} and N_{max} which is the force required in the direction normal to the capture interface. The values in the table are computed with an initial debris angular velocity $\omega_{\mathrm{db}} = 0.1\ \mathrm{rad/s}$ resulting in an initial debris angular momentum equal to $H_{\mathrm{db}} = 1567\ \mathrm{Nms}$.

The simulations provided interesting and useful results to understand the capture problem boundary conditions, particularly focusing on the maximum loads applied to the robotic system during and immediately after the joining sequence. The torque, T_{max}, required by the single robotic actuator in order to brake the debris rotation and the shear load, S_{max}, on the gripper

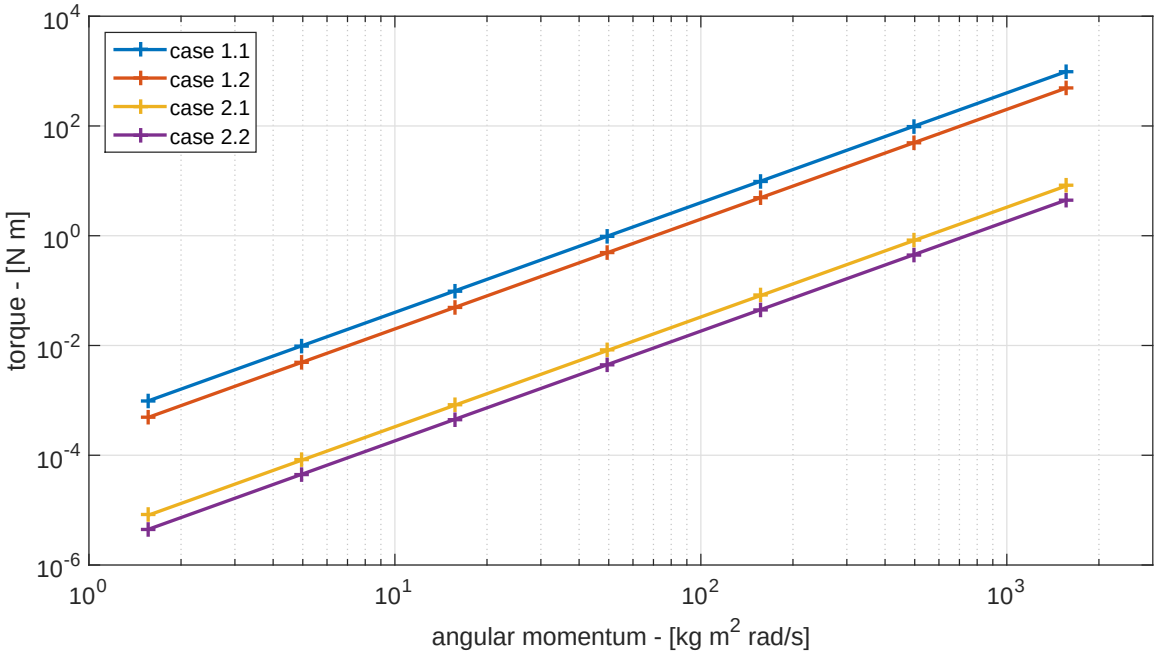

Fig. 3.2: Maximum joint torque load (two actuators) as a function of angular momentum. Different colors for different capture strategies: fixed S/C and still arm (case 1.1), fixed S/C and following arm (case 1.2), free S/C and still arm (case 2.1), free S/C and following arm (case 2.2)

interface are strongly dependent on the initial angular momentum of the debris, $H = I_{\text{db}}\omega_{\text{db}}$. The first approximation on the relations between H and T_{max} or S_{max} is shown in Eq. 3.1

$$\begin{aligned} T_{\text{max}} &= a_2 H^2 \\ N_{\text{max}} &= b_2 H^2 \\ S_{\text{max}} &= c_2 H^2 \end{aligned} \tag{3.1}$$

where a_2, b_2 and c_2 are proper coefficients that depend on the type of simulation executed (i.e. capture strategy, number of robotic actuators and robotic arm approach control). Fig. 3.2-3.4 are graphic representations of the relations in Eq. 3.1 drawn in logarithmic axes; all capture strategies combinations are presented as lines of different colors. Although the results presented in Tab. 3.2 are relative to a worst case scenario, the design focus for the DE actuators and manipulator is to maximize available torque and forces. Literature [63] shows that reasonable values for double-cone actuators are around 1 N for axial force and 10^{-2} Nm for torque; this work will focus on finding ways to improve actuator performances and identify an adequate range of boundary conditions (e.g. lower debris angular rate or inertias) that allow the capture strategy proposed.

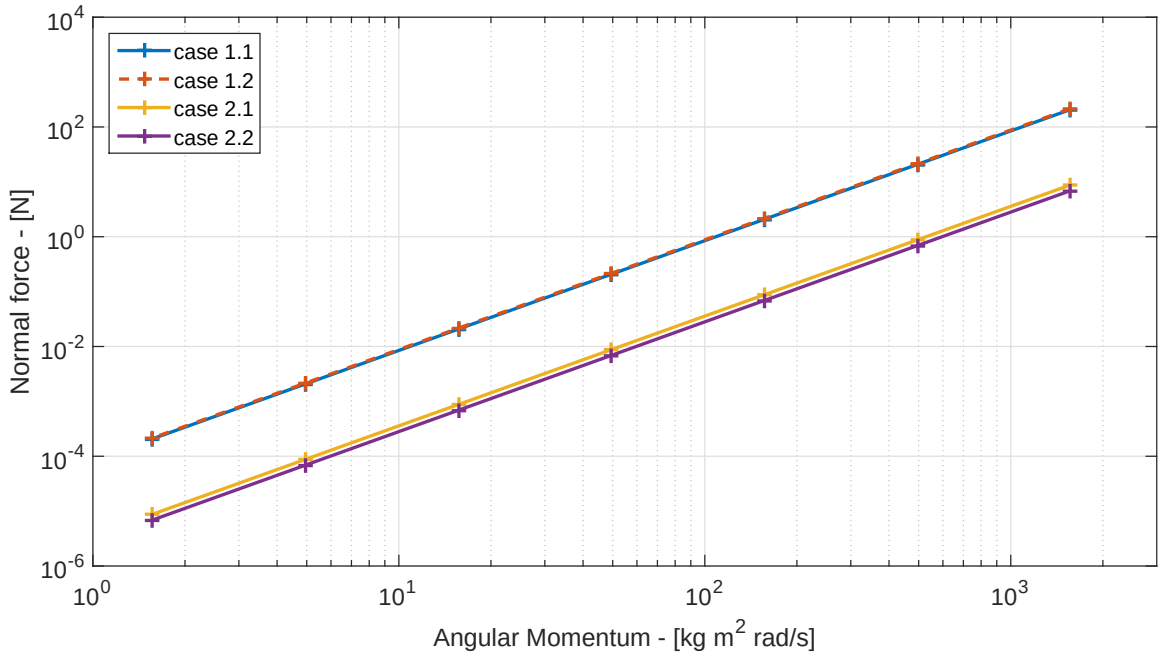

Fig. 3.3: Maximum normal force load on capture interface (two actuators) as a function of angular momentum. Different colors for different capture strategies: fixed S/C and still arm (case 1.1), fixed S/C and following arm (case 1.2), free S/C and still arm (case 2.1), free S/C and following arm (case 2.2)

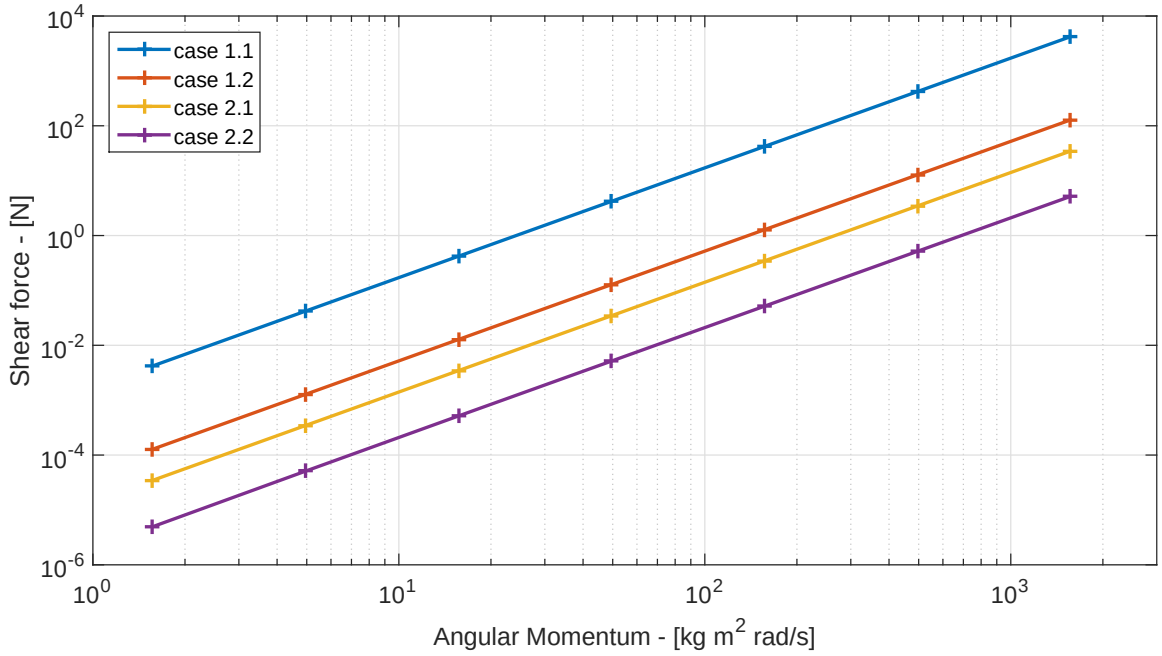

Fig. 3.4: Maximum shear force load on capture interface (two actuators) as a function of angular momentum. Different colors for different capture strategies: fixed S/C and still arm (case 1.1), fixed S/C and following arm (case 1.2), free S/C and still arm (case 2.1), free S/C and following arm (case 2.2)

Tab. 3.2: Maximum actuation on the robotic arm ($T_{\max}$) and loads on the capture interface ($S_{\max}$, $N_{\max}$)

S/C attitude	Act. number	Arm motion	$T_{\max}$ [Nm]	$S_{\max}$ [N]	$N_{\max}$ [N]
fixed	1	still	492	129	224
fixed	2	still	984	4197	208
fixed	3	still	1476	6534	201
fixed	1	follow	492	129	224
fixed	2	follow	492	128	216
fixed	3	follow	492	127	213
free	1	still	4.1	5.4	7.5
free	2	still	8.1	34.6	8.8
free	3	still	12.2	53.9	9.5
free	1	follow	4.1	5.4	7.5
free	2	follow	4.5	5.2	6.9
free	3	follow	4.7	5.1	6.7

Double-cone actuator

4

In this chapter the main characteristics of DE materials and actuators are described. The material mechanical and electromechanical model (Sec. 4.1-4.2), the main DE devices failure modes and their self-sensing capabilities (Sec. 4.3-4.4), as well as the double-cone actuators working principle (Sec. 4.5), manufacturing process (Sec. 4.6) and stroke limits (Sec. 4.7).

4.1 Material mechanical model

The material selected in the present work is the commercial polyacrylic elastomer called 3M^{TM} VHB^{TM} 49XX (the -XX suffix refers to the nominal thickness of the material in tenths of millimeter, e.g. for 3M^{TM} VHB^{TM} 4910 thickness is 1 mm). It is a commonly used material for DE applications. It shows large non-linear elastic deformations and a stress-strain relation that is strongly dependent on the deformation rate (see Fig. 4.1a). Although a permanent deformation appears in data sets (see Fig. 4.1b), it is actually fully recoverable over a long period of time. The material time behavior can be modeled by means of a viscoelastic model; in this work, the actuator behavior is modeled by means of transfer functions, focusing the design on the control problem. The material model is a core aspect of DE actuators modeling.

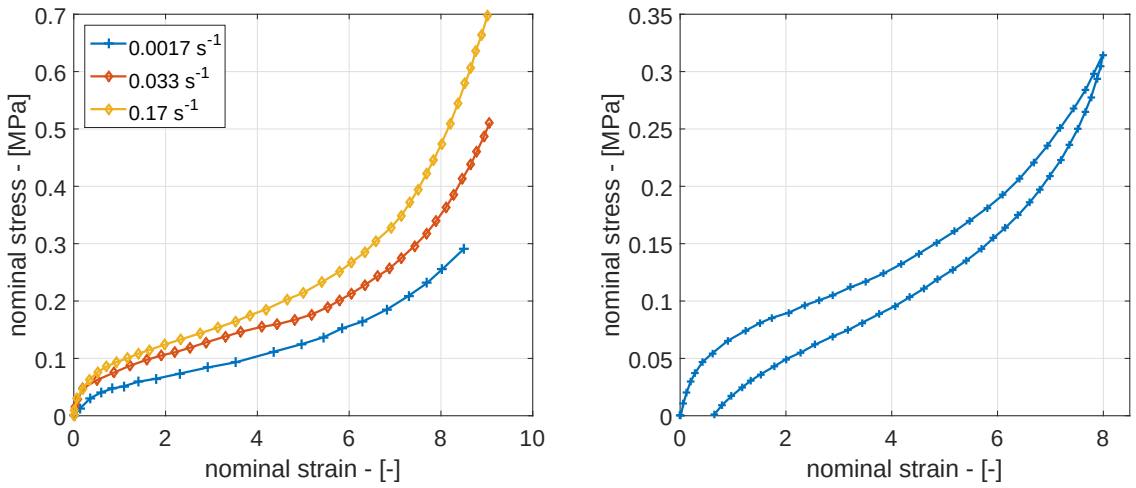

(a) Strain rate effects on stress-strain

(b) Mechanical hysteresis

Fig. 4.1: Viscoelasticity effects on stress strain relations for 3M^{TM} VHB^{TM} 4910; data from [93]

4.1.1 Strain and stress tensors

A brief recap of the continuum theory as proposed by Holzapfel [94] is presented here.

The reference frame of right-handed, rectangular coordinate axes at fixed origin O with orthonormal basis vectors, $\vec{e}_a,\ a = 1,2,3$, is defined. A continuous solid body $\mathcal{B}$ is composed by an infinite number of material points $\mathrm{P} \in \mathcal{B}$. As the body $\mathcal{B}$ moves in space over time it occupies a continuous sequence of geometrical regions denoted by $\Omega_0, \ldots, \Omega$. Every particle $\mathrm{P} \in \mathcal{B}$ corresponds to a geometrical point in regions $\Omega_0, \ldots, \Omega$, which are the configurations of $\mathcal{B}$ at different instants of time. The configuration, Ω_0, at the initial instant of time, t_0, is called reference (or undeformed) configuration. The reference position vector of the generic particle P in Ω_0 is denoted by $\vec{X}$. The configuration, Ω, at the current instant of time, $t > 0$, is called current (or deformed) configuration. In Ω, the particle P is located by the current position vector denoted by $\vec{x}$. The position vectors in the undeformed and deformed configurations are related by a vector field, χ, called motion of $\mathcal{B}$:

$$\begin{aligned} \vec{x} &= \chi(\vec{X}, t) \\ \vec{X} &= \chi^{-1}(\vec{x}, t) \end{aligned} \tag{4.1}$$

The motion χ carries points $\vec{X}$ located at Ω_0 to places $\vec{x}$ in the current configuration Ω. The particle trajectory is the curve composed by all its successive position points. The motion of a body will, in general, change its shape (if the body is deformable), position and orientation. The deformation χ of a body is defined as a motion that is independent of time.

Two possible descriptions of continuum mechanics are possible. The material (or Lagrangian) description is a characterization of the motion w.r.t. the material coordinates (X_1, X_2, X_3) and time t; in this configuration the attention is paid to what happens to a single particle as it moves. The spatial (or Eulerian) description is a characterization of the motion with respect to spatial coordinates and focuses on what happens at a given point in space as time changes. In the following, capital letters will denote entities in the reference configuration, while lowercase letters will denote entities in the current configuration.

The displacement field $\vec{U}$ of a given particle relates its reference position $\vec{X}$ to its postion $\vec{x}$ at current time t. The Lagrangian form is

$$\vec{U}(\vec{X}, t) = \vec{x}(\vec{X}, t) - \vec{X} \tag{4.2}$$

A primary measure of deformation in nonlinear continuum mechanics is the deformation gradient $\mathbf{F}$ which is defined as

$$\mathbf{F}(\vec{X}, t) = \frac{\partial \chi(\vec{X}, t)}{\partial \vec{X}} \tag{4.3}$$

and denotes the deformation gradient of the material field χ. The determinant of $\mathbf{F}$ is denoted by J and describes the change in a volume element from the reference configuration dV to the current configuration dv

$$J(\vec{X},t) = \det F(\vec{X},t) > 0$$
$$dv = J(\vec{X},t)dV \tag{4.4}$$

and $J = 1$ if the deformation is isochoric or the material is incompressible.

The length between two neighboring points $\vec{X}$ and $\vec{Y}$ in the reference configuration is defined as

$$\vec{Y} = \vec{X} + d\vec{X} \tag{4.5}$$

with

$$d\vec{X} = d\epsilon\vec{a}_0$$
$$d\epsilon = |\vec{Y} - \vec{X}| \quad \text{and} \quad \hat{a}_0 = \frac{\vec{Y} - \vec{X}}{d\epsilon} \tag{4.6}$$

where $\hat{a}_0$ is the unit vector of the distance between the two points in the reference position.

After motion the points are displaced to their current positions $\vec{x} = \chi(\vec{X},t)$ and $\vec{y} = \chi(\vec{Y},t)$; through Taylor's expansion it is possible to write that

$$\vec{y} - \vec{x} \approx \mathbf{F}(\vec{X},t)(\vec{Y} - \vec{X}) \tag{4.7}$$

The stretch vector $\vec{\lambda}_{a_0}$ is defined by

$$\vec{\lambda}_{a_0}(\vec{X},t) = \mathbf{F}(\vec{X},t)\vec{a}_0 \tag{4.8}$$

the stretch ratio is simply $\lambda = |\vec{\lambda}_{a_0}|$ and is a measure of how much the unit vector $\hat{a}_0$ has stretched. Then, the distance between $\vec{x}$ and $\vec{y}$ can be expressed as

$$|\vec{y} - \vec{x}| = \lambda d\epsilon \tag{4.9}$$

$\mathbf{F}$ is a measure of the stretch of the material; in an uniaxial tensile test, stretch is defined as current length L over initial length L_i: $\lambda = \dfrac{L}{L_i}$.

An important strain measure in material coordinates is the right Cauchy-Green deformation tensor and is derived from the computation of the squared value of λ

$$\mathbf{C} = \mathbf{F}^{\mathrm{T}}\mathbf{F} \tag{4.10}$$

The spatial counterpart of $\mathbf{C}$ is the left Cauchy-Green deformation tensor defined as

$$\mathbf{b} = \mathbf{F}\mathbf{F}^{\mathrm{T}} \tag{4.11}$$

For the deformation gradient $\mathbf{F}$, the following unique polar decomposition can be defined:

$$\begin{aligned} \mathbf{F} &= \mathbf{R}\mathbf{U} = \mathbf{v}\mathbf{R} \\ \mathbf{R}^{\mathrm{T}}\mathbf{R} &= \mathbf{I}\,, \quad \mathbf{U} = \mathbf{U}^{\mathrm{T}}\,, \quad \mathbf{v} = \mathbf{v}^{\mathrm{T}} \end{aligned} \tag{4.12}$$

In Eq. 4.1.1 $\mathbf{U}$ and $\mathbf{v}$ are the material (or right) stretch tensor and the spatial (or left) stretch tensor, respectively. They are a measure of the local shape change and are in relation with $\mathbf{C}$ and $\mathbf{b}$ through Eq. 4.13

$$\mathbf{U}^2 = \mathbf{U}\mathbf{U} = \mathbf{C} \quad \text{and} \quad \mathbf{v}^2 = \mathbf{v}\mathbf{v} = \mathbf{b} \tag{4.13}$$

The change of local orientation is measured by $\mathbf{R}$, which is called rotation tensor with $\det \mathbf{R} = 1$. The volume change J relates to the described tensors as follows

$$\begin{aligned} \det \mathbf{C} &= \det \mathbf{b} = J^2 \\ \det \mathbf{U} &= \det \mathbf{v} = J \end{aligned} \tag{4.14}$$

A useful relation between left and right Cauchy-Green tensors is

$$\mathbf{b} = \mathbf{v}^2 = \mathbf{R}\mathbf{U}^2\mathbf{R}^{\mathrm{T}} = \mathbf{R}\mathbf{C}\mathbf{R}^{\mathrm{T}} \tag{4.15}$$

The mutually orthogonal and normalized set of eigenvectors $\{\hat{N}_a\}$ and their corresponding eigenvalues λ_a of the material tensor $\mathbf{U}$ are defined as follows with $a = 1, 2, 3$

$$\mathbf{U}\hat{N}_a = \lambda_a \hat{N}_a \tag{4.16}$$

and from Eq. 4.13

$$\mathbf{C}\hat{N}_a = \mathbf{U}^2\hat{N}_a = \lambda_a^2 \hat{N}_a \tag{4.17}$$

The eigenvectors of $\mathbf{U}$ and $\mathbf{C}$ are the same and are called the principal referential directions; the eigenvalues of $\mathbf{U}$ are λ_a called the principal stretches, while the eigenvalues of $\mathbf{C}$ are λ_a^2. Similarly in spatial coordinates

$$\begin{aligned} \mathbf{v}\hat{n}_a &= \mathbf{v}(\mathbf{R}\hat{N}_a) \\ &= \mathbf{R}\mathbf{U}\hat{N}_a \\ &= \lambda_a(\mathbf{R}\hat{N}_a) \end{aligned} \tag{4.18}$$

$$\begin{aligned}\mathbf{b}\hat{n}_a &= \mathbf{b}(\mathbf{R}\hat{N}_a)\\ &= \lambda_a^2(\mathbf{R}\hat{N}_a)\end{aligned} \tag{4.19}$$

The principal spatial directions are defined as the mutually orthonormal and normalized eigenvectors $\hat{n}_a$. The eigenvalues of $\mathbf{U}$ and $\mathbf{v}$, as well as those of $\mathbf{C}$ and $\mathbf{b}$ are the same.

From the uniaxial deformation of a body along one axis (e.g. the x_1 axis) follows

$$x_1 = \lambda_1 X_1 \tag{4.20}$$

Biaxial deformation occurs when two stretches (e.g. λ_1 and λ_2) can be chosen arbitrarily and the other follows from the isochoric condition given by $J = \lambda_1\lambda_2\lambda_3 = 1$. The following relations are valid

$$x_1 = \lambda_1 X_1\ , \quad x_2 = \lambda_2 X_2\ , \quad x_3 = \frac{1}{\lambda_1\lambda_2} X_3 \tag{4.21}$$

In addition, if $\lambda_1 = \lambda_2$, then equibiaxial deformation occurs.

The deformable continuum body $\mathcal{B}$, which occupies the arbitrary region of space Ω with boundary surface $\partial\Omega$ at time t, is under the action of external and internal forces. An imaginary plane surface cuts the body in two parts and passes any given point $\vec{x}$ at time t with spatial coordinates x_a. Focusing only on one part, the unit vector $\hat{n}$ is defined as the outward normal to the infinitesimal surface $\mathrm{d}s$ that surrounds the point $\vec{x}$. An infinitesimal resultant force $d\vec{f}$ acts on the surface element $\mathrm{d}s$. Eq. 4.22 follows

$$\begin{aligned}\mathrm{d}\vec{f} &= \vec{t}\mathrm{d}s = \vec{T}\mathrm{d}S\\ \vec{t}(\vec{x},t,\vec{n}) &= \boldsymbol{\sigma}(\vec{x},t)\vec{n}\\ \vec{T}(\vec{X},t,\vec{N}) &= \mathbf{s}(\vec{X},t)\vec{N}\end{aligned}$$

where $\vec{t}$ is the true (or Cauchy) traction vector and $\boldsymbol{\sigma}$ is the true (or Cauchy) stress tensor, while $\vec{T}$ is the nominal (or first Piola-Kirchhoff) traction tensor and $\mathbf{s}$ is the nominal (or first Piola-Kirchhoff) stress tensor. An important relation between the defined entities is

$$\boldsymbol{\sigma} = J^{-1}\mathbf{P}\mathbf{F}^{\mathrm{T}} = \boldsymbol{\sigma}^{\mathrm{T}} \tag{4.22}$$

The three eigenvalues $\lambda_a^\star$ of $\boldsymbol{\sigma}$ are the principal normal stresses and their corresponding orthonormal eigenvectors $\hat{m}_a$ are the principal directions of $\boldsymbol{\sigma}$. If the material is isotropic, $\hat{m}_a$ coincide with the previously defined principal spatial directions $\hat{n}_a$.

The principal invariants I_a of a generic 3×3 scalar-valued tensor $\mathbf{T}$ are

$$\begin{aligned}
I_1(\mathbf{T}) &= \mathrm{tr}\,\mathbf{T} = T_{11}+T_{22}+T_{33} = \Lambda_1+\Lambda_2+\Lambda_3 \\
I_2(\mathbf{T}) &= \frac{1}{2}\left[(\mathrm{tr}\,\mathbf{T})^2-(\mathrm{tr}\,\mathbf{T}^2)\right] \\
&= T_{11}T_{22}+T_{22}T_{33}+T_{11}T_{33}-T_{12}T_{21}-T_{23}T_{32}-T_{13}T_{31} \\
&= \Lambda_1\Lambda_2+\Lambda_2\Lambda_3+\Lambda_1\Lambda_3 \\
I_3(\mathbf{T}) &= \det\mathbf{T} \\
&= T_{11}(T_{22}T_{33}-T_{23}T_{32})-T_{12}(T_{21}T_{33}-T_{23}T_{31})+T_{13}(T_{21}T_{32}-T_{22}T_{31}) \\
&= \Lambda_1\Lambda_2\Lambda_3
\end{aligned} \tag{4.23}$$

where Λ_a are the eigenvalues of the mentioned tensor. These definitions will become useful in the following, in particular applied to $\mathbf{C}$ and $\mathbf{b}$ within the constitutive laws of hyperelastic materials.

Finally, it is useful to recall the relations between true stress σ_a and nominal stress s_a, as well as true strain ε_a and stretch ratio λ_a

$$\begin{aligned}
\sigma_a &= \lambda_a s_a \\
\varepsilon_a &= \ln(\lambda_a)
\end{aligned} \tag{4.24}$$

In an uniaxial tensile test, given initial length L_i and current length L, the true strain is defined with $\varepsilon = \dfrac{L-L_i}{L}$.

A material is elastic if the stress field at time t depends only on the state of deformation (and state of temperature) and not on deformation history. The materials employed in this work for experimental activity are nominally viscoelastic, rather then simply elastic as described in Sec. 4.1.3. Nevertheless, if a steady state is reached after deformation, meaning that $t >> \tau_m$ where τ_m is some time constant typical of the material relaxation behavior, the material can be considered elastic. The transient behavior of DE actuators will be simulated by means of transfer functions that account for the material relaxation.

4.1.2 Hyperelasticity

A hyperelastic material (like elastomers) is a type of constitutive model for ideally elastic material for which the stress-strain relationship derives from a Helmholtz free-energy function Ψ, defined per unit reference volume. In the case Ψ is a function only of the deformation gradient $\mathbf{F}$ or some form of deformation tensor, $\Psi(\mathbf{F})$ is called strain-energy function and it is a scalar-valued function of one continuous tensor variable $\mathbf{F}$. For homogeneous materials

Ψ depends only upon the deformation gradient $\mathbf{F}$. The constitutive (or stress) relation of hyperelastic materials, in both material and spatial coordinates, has the form

$$\begin{aligned} \mathbf{s} &= \frac{\partial \Psi(\mathbf{F})}{\partial \mathbf{F}} \\ \boldsymbol{\sigma} &= J^{-1} \frac{\partial \Psi(\mathbf{F})}{\partial \mathbf{F}} \mathbf{F}^{\mathrm{T}} \end{aligned} \tag{4.25}$$

It is possible to prove for arbitrary $\mathbf{F}$ that $\psi(\mathbf{F}) = \psi(\mathbf{U})$ meaning that stress in a hyperelastic material depends only on the stretching part of the deformation gradient. The relation $\psi(\mathbf{F}) = \psi(\mathbf{C})$ is also true, leading to

$$\begin{aligned} \mathbf{s} &= 2\mathbf{F}\left(\frac{\partial \Psi(\mathbf{C})}{\partial \mathbf{C}}\right) \\ \boldsymbol{\sigma} &= 2J^{-1}\mathbf{F}\left(\frac{\partial \Psi(\mathbf{C})}{\partial \mathbf{C}}\right)\mathbf{F}^{\mathrm{T}} \end{aligned} \tag{4.26}$$

Further, if the material is isotropic, it is possible to represent the strain-energy function in terms of invariants of $\mathbf{C}$ or $\mathbf{b}$

$$\Psi(\mathbf{F}) = \Psi[I_1(\mathbf{C}), I_2(\mathbf{C}), I_3(\mathbf{C})] = \Psi[I_1(\mathbf{b}), I_2(\mathbf{b}), I_3(\mathbf{b})] \tag{4.27}$$

with

$$I_1(\mathbf{C}) = I_1(\mathbf{b}) \,, \quad I_2(\mathbf{C}) = I_2(\mathbf{b}) \,, \quad I_3(\mathbf{C}) = I_3(\mathbf{b}) \tag{4.28}$$

Since the invariant of such tensors can be expressed as functions of their eigenvalues, it follows that Ψ can be regarded as a function of the principal stretches λ_a or their squared form λ_a^2, which are the eigenvalues of $\mathbf{C}$ and $\mathbf{b}$. This leads to the following simple relations

$$\begin{aligned} s_a &= \frac{\partial \Psi}{\partial \lambda_a} \\ \sigma_a &= J^{-1}\lambda_a \frac{\partial \Psi}{\partial \lambda_a} \end{aligned} \tag{4.29}$$

If the material can be considered incompressible (not necessarily isotropic), than $J = 1$. It is possible to reformulate the constitutive relations again assuming p as hydrostatic pressure (determined from equilibrium equations and boundary conditions)

$$\begin{aligned} \mathbf{s} &= -p\mathbf{F}^{-\mathrm{T}} + \frac{\partial \Psi(\mathbf{F})}{\partial \mathbf{F}} \\ \boldsymbol{\sigma} &= -p\mathbf{I} + \frac{\partial \Psi(\mathbf{F})}{\partial \mathbf{F}} \mathbf{F}^{\mathrm{T}} \end{aligned} \tag{4.30}$$

When isotropy is also considered a suitable strain-energy function (for an incompressible isotropic hyperelastic material) is given by

$$\begin{aligned}\Psi &= \Psi[I_1(\mathbf{C}), I_2(\mathbf{C})] - \frac{1}{2}p(I_3(\mathbf{C}) - 1) \\ &= \Psi[I_1(\mathbf{b}), I_2(\mathbf{b})] - \frac{1}{2}p(I_3(\mathbf{b}) - 1)\end{aligned} \tag{4.31}$$

allowing to express the Ψ as a function of principal stretches λ_a obtaining

$$\begin{aligned}s_a &= -\frac{1}{\lambda_a}p + \frac{\partial \Psi}{\partial \lambda_a} \\ \sigma_a &= -p + \lambda_a \frac{\partial \Psi}{\partial \lambda_a}\end{aligned} \tag{4.32}$$

Several forms of the strain-energy function have been proposed in literature. For material modeling purposes, the form proposed by Yeoh [95] is employed in this work and is reported here expressed in terms of strain tensor invariants and principal stretches

$$\begin{aligned}\Psi &= c_1(I_1 - 3) + c_2(I_1 - 3)^2 + c_3(I_1 - 3)^3 \\ &= c_1(\lambda_1^2 + \lambda_2^2 + \lambda_3^2 - 3) + c_2(\lambda_1^2 + \lambda_2^2 + \lambda_3^2 - 3)^2 + c_3(\lambda_1^2 + \lambda_2^2 + \lambda_3^2 - 3)^3\end{aligned} \tag{4.33}$$

where c_1, c_2, c_3 are material constants derived from experimental data.

Exploiting Eq. 4.32 it is possible to derive the expression of true stress for the specified strain-energy function. In the case of uniaxial extension along the first principal axis with no boundary pressure, it is true that $\lambda_2 = \lambda_3 = \dfrac{1}{\sqrt{\lambda_1}}$ and the expression of the first Cauchy stress becomes

$$\sigma_1 = 2\left(\lambda_1^2 - \frac{1}{\lambda_1}\right)\left[c_1 + 2c_2\left(\lambda_1^2 + \frac{2}{\lambda_1} - 3\right) + 3c_3\left(\lambda_1^2 + \frac{2}{\lambda_1} - 3\right)^2\right] \tag{4.34}$$

while $\sigma_2 = \sigma_3 = 0$. In the case of biaxial extension along the first and second principal axes with no boundary pressure, it is true that $\lambda_3 = \dfrac{1}{\lambda_1\lambda_2}$ and the first and second Cauchy stresses are

$$\begin{aligned}\sigma_1 &= 2\left(\lambda_1^2 - \frac{1}{\lambda_1^2\lambda_2^2}\right)\left[c_1 + 2c_2\left(\lambda_1^2 + \lambda_2^2 + \frac{1}{\lambda_1^2\lambda_2^2} - 3\right) + 3c_3\left(\lambda_1^2 + \lambda_2^2 + \frac{1}{\lambda_1^2\lambda_2^2} - 3\right)^2\right] \\ \sigma_2 &= 2\left(\lambda_2^2 - \frac{1}{\lambda_1^2\lambda_2^2}\right)\left[c_1 + 2c_2\left(\lambda_1^2 + \lambda_2^2 + \frac{1}{\lambda_1^2\lambda_2^2} - 3\right) + 3c_3\left(\lambda_1^2 + \lambda_2^2 + \frac{1}{\lambda_1^2\lambda_2^2} - 3\right)^2\right]\end{aligned} \tag{4.35}$$

while $\sigma_3 = 0$. If an external pressure p_e is applied along the out-of-plane direction of the biaxially deformed sample, the true stresses become

$$\begin{aligned}
\sigma_1 &= -p_e + 2\left(\lambda_1^2 - \frac{1}{\lambda_1^2\lambda_2^2}\right)\left[c_1 + 2c_2\left(\lambda_1^2 + \lambda_2^2 + \frac{1}{\lambda_1^2\lambda_2^2} - 3\right) + 3c_3\left(\lambda_1^2 + \lambda_2^2 + \frac{1}{\lambda_1^2\lambda_2^2} - 3\right)^2\right] \\
\sigma_2 &= -p_e + 2\left(\lambda_2^2 - \frac{1}{\lambda_1^2\lambda_2^2}\right)\left[c_1 + 2c_2\left(\lambda_1^2 + \lambda_2^2 + \frac{1}{\lambda_1^2\lambda_2^2} - 3\right) + 3c_3\left(\lambda_1^2 + \lambda_2^2 + \frac{1}{\lambda_1^2\lambda_2^2} - 3\right)^2\right] \\
\sigma_3 &= -p_e
\end{aligned} \tag{4.36}$$

4.1.2.1 Residual stretch

As already mentioned, in this work the Yeoh form of strain-energy function is employed. In particular, the coefficients proposed by Berselli *et al.* [74] are used, as well as the approach based on residual strain proposed in the same work and recalled here briefly. This model is adopted because the work by Berselli featured an actuator geometry similar to that described in this work and showed promising results validated by experimental evidence.

VHB^{TM} 49XX shows a complete recovery of strain after a long period of time, on the order of thousands of seconds. Since, for actuation purposes, this figure is several orders of magnitude larger than practical actuator time constants, a certain amount of deformation can be considered unrecoverable. Such residual stretch λ_r is neglected during computation of stresses and the coefficients of the strain-energy function are computed accordingly. In other words, the long term strain recovery is neglected and the material is considered affected by permanent set. It is useful to provide a practical example. Consider to have a VHB^{TM} 4910 (original thickness $1\ \mathrm{mm}$) sample that undergoes uniaxial extension with $\lambda_1 = \lambda$. If we consider a material with residual stretch λ_r, an effective stretch ratio is defined as $\lambda_1^\star = \dfrac{\lambda}{\lambda_r}$. The value of σ_1 can be computed by means of Eq. 4.34 using the value of $\lambda_1^\star$ instead of λ_1.

The residual stretch is a function of the total stretch. At first approximation such function is assumed to be linear and validated with the data by Berselli (in [74] with pre-stretch ratio $\lambda_0 = 4$ it is measured that $\lambda_r = 1.6$). The following equation can be employed for an approximate computation of the residual stretch in the case of conic shaped membrane (single- or double-cone actuator) assuming that the membrane is initially equibiaxially pre-stretched and later deformed to conic shape

$$\lambda_r = 1 + 0.14 \cdot \left(\overline{\lambda}_\rho - 1\right) \tag{4.37}$$

where $\overline{\lambda}_\rho$ is an average stretch ratio value over the membrane radial coordinate, ρ, after cone stretch and calculated with Eq. 4.38.

$$\begin{aligned}
b &= \frac{d}{2} - \frac{D}{2} \\
\overline{\lambda}_\rho &= \lambda_0 \cdot \frac{\sqrt{a^2 + b^2}}{b}
\end{aligned} \tag{4.38}$$

where d, D and a are geometric parameters defined in Fig. 4.12, λ_0 is the equibiaxial pre-stretch ratio.

For pre-stretch λ_0, the effective stretch ratio λ_e is given by

$$\lambda_e = \frac{\lambda_0}{\lambda_r} \tag{4.39}$$

4.1.3 Viscoelasticity

The viscoelasticity of materials is observed mainly in two behaviors: creep and stress relaxation. The first is the tendency of the material to undergo increasing deformations over time when subjected to constant stresses. The second is the decrease in stress over time when a constant strain is applied. VHB^{TM} 49XX shows both effects and its behavior can be modeled theoretically, for example exploiting the concept of quasilinear viscoelasticity proposed by Fung [96] and applied to VHB^{TM} by Wissler *et al.* [97]. This approach is proposed here briefly, although it was not employed during actuator modeling. As a matter of fact, for the purposes of this work a more control-oriented approach based on transfer functions was implemented (further details in Sec. 5.6).

Viscoelasticity is modeled with time dependent parameters of the strain-energy function. The Yeoh coefficients c_1, c_2 and c_3 mentioned in Sec. 4.1.2 are used to compute the long-term steady state stresses and will be denoted by $c_1^{(\infty)}$, $c_2^{(\infty)}$ and $c_3^{(\infty)}$. The stress computed with these coefficient is asimptotically reached after an infinite time span and, for isotropic hyperelastic material, Eq. 4.29 can be written as

$$\sigma_a^{(\infty)} = J^{-1}\lambda_a \frac{\partial \Psi^{(\infty)}}{\partial \lambda_a} \tag{4.40}$$

The Yeoh coefficients are here modeled as time dependent, with the following relaxation functions (with $j = 1,2,3$)

$$c_j(t) = c_j^{(\infty)}\left(1 + \sum_{i=1}^{n} g_i \ \mathrm{e}^{-\frac{t}{\tau_i}}\right) \tag{4.41}$$

where g_i and t_i are material parameters that characterize the relaxation behavior and are determined from uniaxial relaxation tests. The stress relaxation function has a similar form

$$\begin{aligned}\sigma_a(t) &= \sigma_a^{(\infty)} + \sum_{i=1}^{n} \sigma_{a_i} \ \mathrm{e}^{-\frac{t}{\tau_i}} \\ &= \sigma_a^{(\infty)}\left(1 + \sum_{i=1}^{n} \frac{\sigma_{a_i}}{\sigma_a^{(\infty)}} \ \mathrm{e}^{-\frac{t}{\tau_i}}\right)\end{aligned} \tag{4.42}$$

where σ_i and τ_i are material parameters strictly related to g_i and t_i. The quasi-linear viscoelasticity main assumption is that the relaxation function is independent of the magnitude of the deformation. Defining the function $s^{(\infty)}(t)$ as follows

$$s_\infty(t) = \frac{\sigma_a(t)}{\sigma_a^{(\infty)}} \tag{4.43}$$

a material is quasi-linear viscoelastic when $s_\infty(t)$ is independent of the imposed elongation in relaxation tests. The parameters g_i and t_i are obtained by coefficient comparison from parameters $\sigma^{(\infty)}$, σ_i and τ_i which are directly obtained from tests.

4.1.4 Other effects

Other effects influence the mechanical behavior of DEs and VHB^{TM} in particular. It is worth mentioning here Mullins effect and temperature effects.

The Mullins effect is a progressive damage that affects many rubbery materials including VHB^{TM} . The material elastic response depends on the maximum deformation previously achieved; the stress-strain curve is softened irreversibly when maximum deformation is increased. After a few deformation cycles the mechanical response change sets and an asymptotic condition is reached. Pre-conditioning can be employed to limit the Mullins effect: cycles of preliminary deformation are imposed to the material in order to reach a constant stress-strain behavior. In this work the Mullins effect is neglected since in the DEAs implementation the material is always pre-conditioned.

Another parameter that considerably affect the performances of DEAs is temperature. The mechanical characteristics of DEs, like for the majority of polymers, are strongly affected by the material temperature. As already mentioned silicones are less affected by temperature variation compared to polyarcylates (see Fig. 4.2). Nevertheless, little research has been conducted for the mechanical characterization of VHB^{TM} at variable temperatures; further investigation is certainly needed.

4.1.5 Experimental data from literature

The strain-energy function parameters are computed from stress-strain test data. Several sets of data can be found in literature for VHB^{TM} 49XX and many forms of strain energy functions have been proposed by different authors. In this section, a review of some experimental sets of data found in literature is presented and the related stress-strain curves are compared to the actual Yeoh model employed in this work.

As explained in 4.1.3, the selected material shows a highly strain-rate dependent stress-strain relation. The simple hyperelastic model can be employed for the estimation of the DE actuator behavior at steady state. In order to properly simulate the steady state stresses within a material sample, it is necessary to perform extremely slow tests for the proper computation of

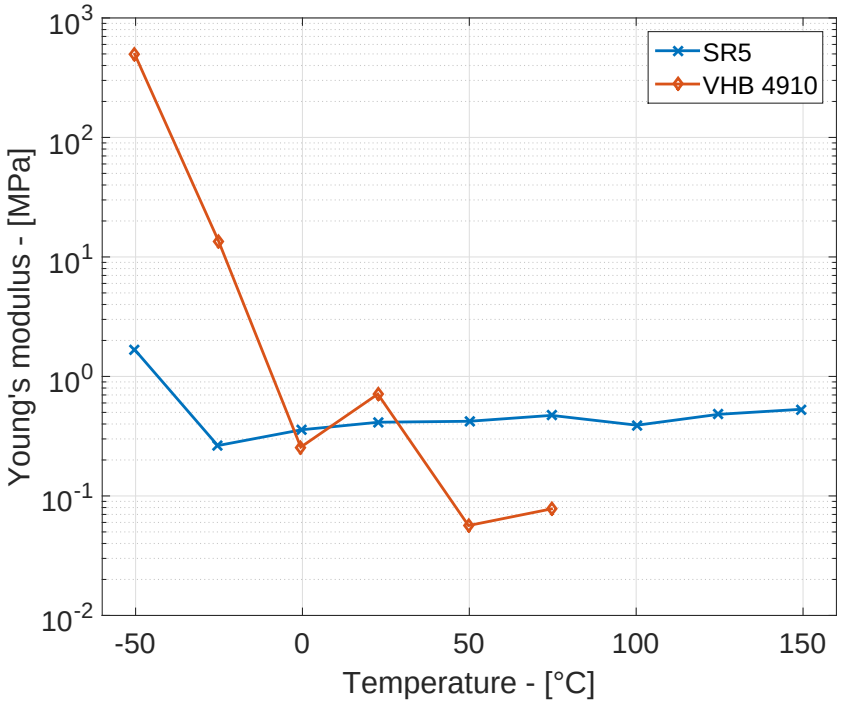

Fig. 4.2: Young's modulus (linear elasticity approximation) as a function of temperature for the silicone SR5 (silicone fluid DC 3481 with 5% of 81-R hardener) and the acrylic elastomer 3M^{TM} VHB^{TM} 4910 (data from [98])

the strain-energy function coefficients. Literature data are often provided along with information about the test conditions, like temperature and strain rate. All the presented data are nominally collected through room temperature tests. Nevertheless, such data show huge discrepancies, possibly not only due to different strain rate or other test conditions (see Fig. 4.3).

The Yeoh strain-energy function proposed by Berselli *et al.* [74] ($c_1 = 15244$ Pa, $c_2 = 75.5$ Pa, $c_3 = 4$ Pa) appears to be a good fit of the data obtained through the slowest tests available in literature (black dashed line in Fig. 4.3). Such fit is obtained applying the residual stretch approach described in Sec. 4.1.2.1. Given these results, the mentioned strain energy function is considered a good choice for steady-state DEA performances estimation.

4.2 Material electromechanical model

The working principle of Dielectric Elastomer devices is based on the combination of hyperelastic nature and the electric insulating properties of such materials.

The elastomeric membrane is coupled with compliant electrodes to form deformable capacitors; the membrane acts as dielectric layer in the capacitor while the electrodes applied to both faces of the membrane are the conductive plates. When a voltage is applied to the electrodes, an attractive Maxwell force arise across the membrane thickness. This force tends to squeeze the membrane and reduce its thickness. A thickness reduction leads to an increase in surface

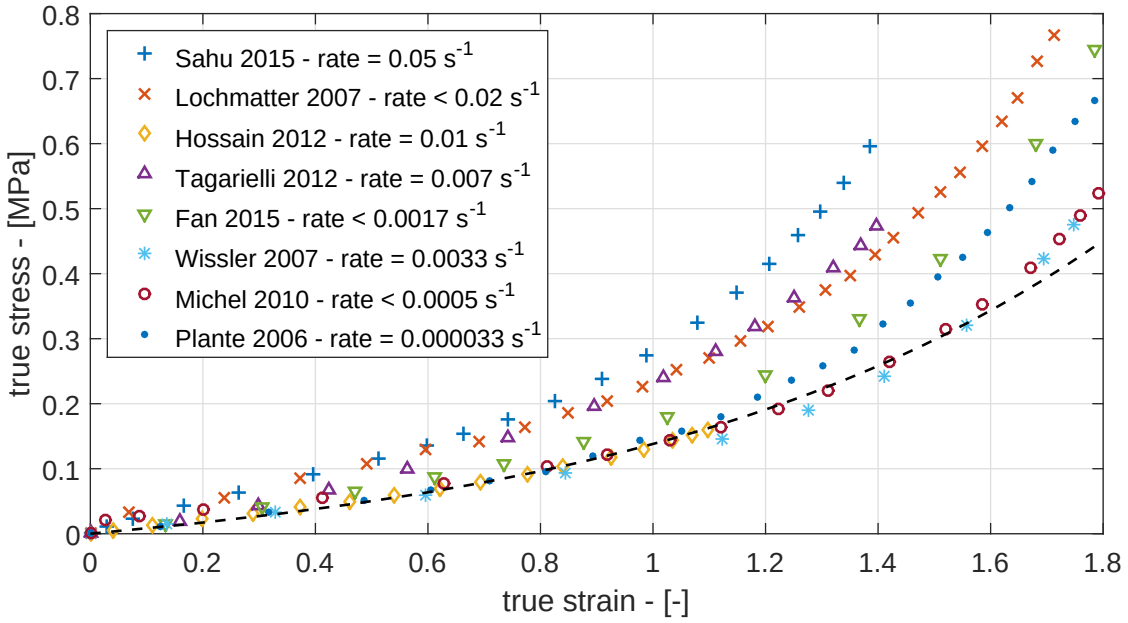

Fig. 4.3: Literature uniaxial test data for VHB^{TM} 49XX: data from Sahu 2015 [99], Lochmatter 2007 [100], Hossain 2012 [101], Tagarielli 2012 [102], Fan 2015 [93], Wissler 2007 [97], Michel 2010 [103] and Plante 2006 [104] (in some case tests are conducted under constant speed rather than constant strain rate and the initial, maximum value of strain rate is presented); fit with Yeoh strain-energy function by Berselli *et al.* [74] (black dashed line)

area in the membrane due to conservation of volume. Fig. 4.4 is a graphic representation of the DE working principle with dielectric material, compliant electrodes and power supply. Particular geometry layouts allow to exploit the planar expansion of the material and obtain the desired actuation.

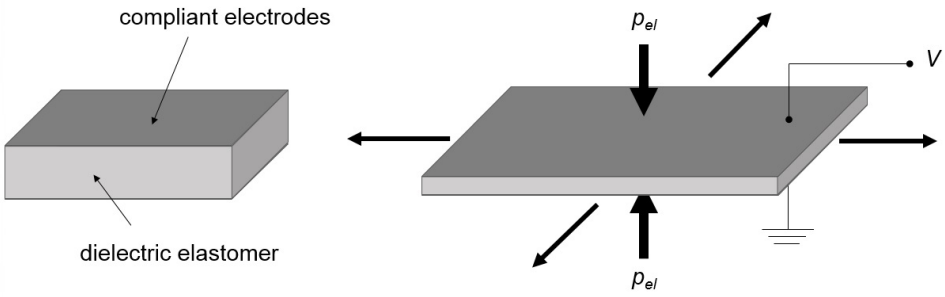

Fig. 4.4: Graphic representation of DEs electromechanical coupling: p_{el} is the pressure due to Maxwell forces under applied voltage V

The electrostatic force per unit area that arise between the electrodes can be computed with Eq. 4.44 initially proposed by Pelrine *et al.* [105]:

$$\begin{aligned} p_{el} &= -\varepsilon_v \varepsilon_r \left(\frac{V}{h}\right)^2 \\ &= -\varepsilon_v \varepsilon_r E^2 \end{aligned} \tag{4.44}$$

where p_{el} is the pressure due to Maxwell forces generated by applied voltage V (negative because compressive), $\varepsilon_v = 8.854 \times 10^{-12}\text{F/m}$ is the vacuum permittivity, ε_r is the relative permittivity of the elastomer, h is the current (deformed) membrane thickness and E is the electric field across the membrane. By combining Eq. 4.44 and Eq. 4.36, it is obtained that the Cauchy stress σ_3 in the third direction is

$$\sigma_3 = -p_{el} \tag{4.45}$$

The dielectric permittivity of VHB™ 49XX is not constant, but depends on voltage application frequency, temperature and pre-stretch conditions. Vu-Cong *et al.* [106] proposed a model to predict the value of ε_r. Although the effects of actuation frequency are significant at low temperatures (below $0°\text{ C}$) or at high frequencies (above 100 Hz), they can be neglected in the most common operating conditions, namely between $0°\text{ C}$ and $100°\text{ C}$ and between 0.1 Hz to 100 Hz. Temperature, on the contrary, plays an important role and can change dielectric permittivity considerably. Above $0°\text{ C}$ the effect of temperature can be described by means of a Debye relation in the form

$$\begin{aligned} \varepsilon_r(T) &= \varepsilon_\infty + \frac{N\mu^2}{3\varepsilon_v kT} \\ &= 2.1 + \frac{960}{T} \end{aligned} \tag{4.46}$$

where ε_∞ is the dielectric permittivity at high values of actuation frequency, N is the dipole density, μ is the dipole moment, k is the Boltzmann constant ($1.3806 \times 10 - 23\text{ m}^2\text{ kg s}^{-2}\text{ K}^{-1}$) and T is the temperature in degrees Kelvin. The second line of Eq. 4.46 is valid for VHB™ . Stretch ratio λ is another parameter that strongly influences the value of dielectric permittivity in VHB™ 4910. In particular, ε_r decreases as λ increases (see Fig. 4.5) and a polynomial relation can be used to describe the phenomenon. Eq. 4.47 describes the complete model by Vu-Cong *et al.* that accounts for temperature and stretch ratio effects.

$$\varepsilon_r(\lambda_1, \lambda_2, T) = \left(\varepsilon_\infty + \frac{N\mu^2}{3\varepsilon_v kT}\right)\left[1 + a(\lambda_1 + \lambda_2 - 2) + b(\lambda_1 + \lambda_2 - 2)^2 + c(\lambda_1 + \lambda_2 - 2)^3\right] \tag{4.47}$$

where λ_i are the in-plane stretches and a, b and c are experimental coefficients ($a = -0.0871$, $b = 0.0121$, $c = -6.285 \times 10^{-4}$).

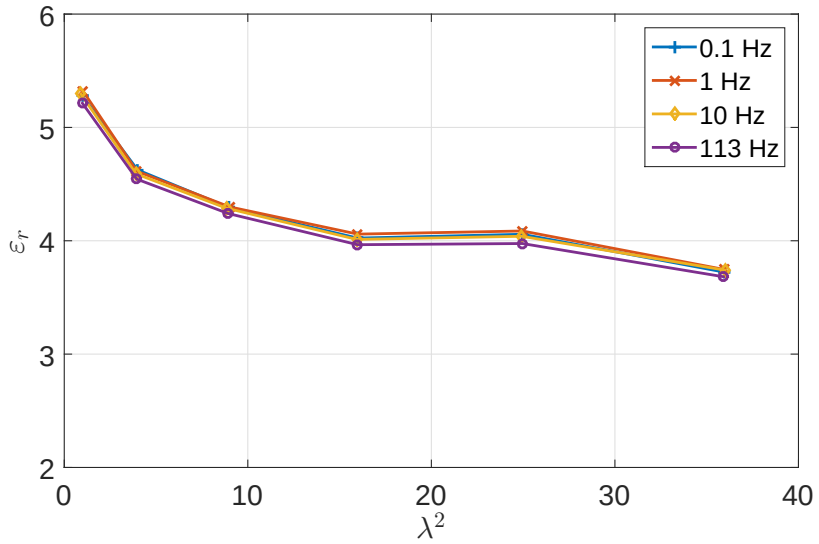

Fig. 4.5: Relation between dielectric permittivity and stretch ratio (curves are parametric w.r.t. actuation frequency; data from [106])

The electromechanical pressure p_{el} acts on the membrane as an external pressure and the expression of true stresses given by Eq. 4.36 becomes

$$\begin{aligned}
\sigma_1 &= -p_{el} + 2\left(\lambda_1^2 - \frac{1}{\lambda_1^2\lambda_2^2}\right)\left[c_1 + 2c_2\left(\lambda_1^2 + \lambda_2^2 + \frac{1}{\lambda_1^2\lambda_2^2} - 3\right) + 3c_3\left(\lambda_1^2 + \lambda_2^2 + \frac{1}{\lambda_1^2\lambda_2^2} - 3\right)^2\right] \\
\sigma_2 &= -p_{el} + 2\left(\lambda_2^2 - \frac{1}{\lambda_1^2\lambda_2^2}\right)\left[c_1 + 2c_2\left(\lambda_1^2 + \lambda_2^2 + \frac{1}{\lambda_1^2\lambda_2^2} - 3\right) + 3c_3\left(\lambda_1^2 + \lambda_2^2 + \frac{1}{\lambda_1^2\lambda_2^2} - 3\right)^2\right] \\
\sigma_3 &= -p_{el}
\end{aligned} \tag{4.48}$$

A more rigorous approach is proposed by [107], and allows to redefine the material strain energy function with three state variables, $\Psi(\lambda_1, \lambda_2, \hat{D})$, in the case of planar biaxial extension (i.e. membrane)

$$\begin{aligned}
\Psi = {} & c_1(\lambda_1^2 + \lambda_2^2 + \lambda_1^{-2}\lambda_2^{-2} - 3) + c_2(\lambda_1^2 + \lambda_2^2 + \lambda_1^{-2}\lambda_2^{-2} - 3)^2 + c_3(\lambda_1^2 + \lambda_2^2 + \lambda_1^{-2}\lambda_2^{-2} - 3)^3 \\
& + \frac{\bar{D}^2}{2\varepsilon_v\varepsilon_r}\lambda_1^{-2}\lambda_2^{-2}
\end{aligned} \tag{4.49}$$

where $\bar{D}$ is the nominal electric displacement or the electric charge on an element of electrode. Knowing that the current membrane thickness, h, is related to the undeformed thickness, t, with $h = \dfrac{t}{\lambda_1\lambda_2}$, the variable $\bar{D}$ is defined as

$$\begin{aligned}
\bar{D} &= \varepsilon_v\varepsilon_r\lambda_1\lambda_2 E \\
&= \varepsilon_v\varepsilon_r\lambda_1\lambda_2\frac{V}{h} \\
&= \varepsilon_v\varepsilon_r\lambda_1^2\lambda_2^2\frac{V}{t}
\end{aligned} \tag{4.50}$$

Partial differentiation of Eq. 4.49 by λ_1 and λ_2 leads to the true stresses that, in view of Eq. 4.50 are equivalent to those of Eq. 4.48

$$\begin{aligned}
\sigma_1 &= 2\left(\lambda_1^2 - \frac{1}{\lambda_1^2\lambda_2^2}\right)\left[c_1 + 2c_2\left(\lambda_1^2+\lambda_2^2+\frac{1}{\lambda_1^2\lambda_2^2}-3\right)+3c_3\left(\lambda_1^2+\lambda_2^2+\frac{1}{\lambda_1^2\lambda_2^2}-3\right)^2\right] \\
&\quad -\varepsilon_v\varepsilon_r\left(\lambda_1\lambda_2\frac{V}{t}\right)^2 \\
\sigma_2 &= 2\left(\lambda_2^2 - \frac{1}{\lambda_1^2\lambda_2^2}\right)\left[c_1 + 2c_2\left(\lambda_1^2+\lambda_2^2+\frac{1}{\lambda_1^2\lambda_2^2}-3\right)+3c_3\left(\lambda_1^2+\lambda_2^2+\frac{1}{\lambda_1^2\lambda_2^2}-3\right)^2\right] \\
&\quad -\varepsilon_v\varepsilon_r\left(\lambda_1\lambda_2\frac{V}{t}\right)^2 \\
\sigma_3 &= -\varepsilon_v\varepsilon_r\left(\lambda_1\lambda_2\frac{V}{t}\right)^2
\end{aligned} \tag{4.51}$$

4.3 Failure modes

A key limiting factor to the application of DEAs to ground and space applications is the intrinsic frailty of the material, this being true for both polyacrilates (e.g. VHB^{TM} 49XX) and silicones. Literature provides analysis of failure modes for VHB^{TM} in works published in the last decade that will be revised here briefly [104] [108]. The elastomer fails either mechanically, by breaking apart, or electricly, by losing its dielectric properties and becoming partially conductive. DE failure modes can be classified in two main groups on the basis of the size scale of the phenomena: local failure modes and large-scale failure modes.

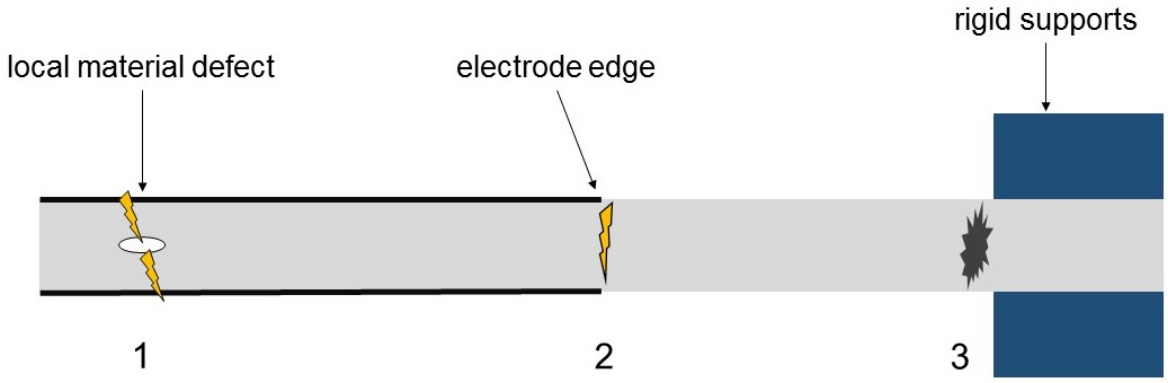

Fig. 4.6: Local failure modes for DE devices: local material defect (1), electric field concetration (2), stress concentration (3)

Local failure modes lead to the DE device failure due to localized causes while the global material condition is safe. Local failure occurs due to three phenomena: local material defects, stress concentration and electric field concentration (see Fig. 4.6). In VHB^{TM} local defects are usually air bubbles or impurities included in the material; in either case, the dielectric material thickness is reduced determining a locally increased electric field. Further, if the included particle is conductive it represents a preferential path for electric current through the material.

Vogan [108] observed that electric field concentration happens at the boundaries of electrodes and, in particular, when these boundaries are sharp. Stress concentration usually takes place at the interface between the elastomer element and the rigid support structures.

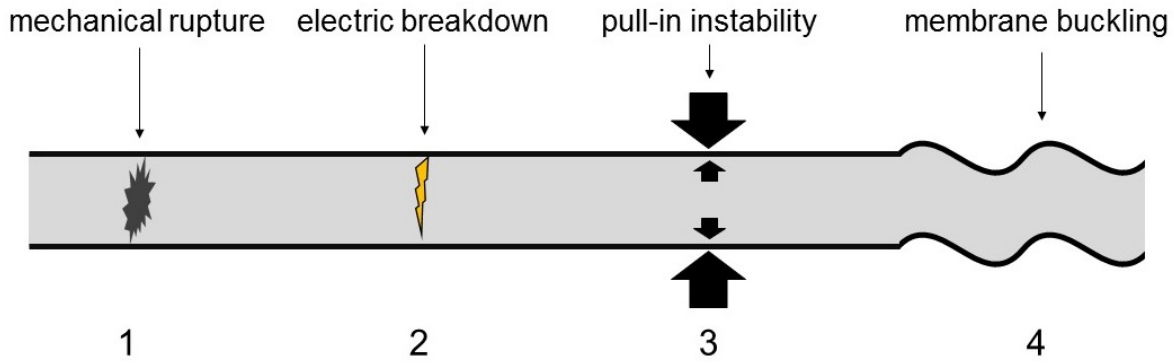

Fig. 4.7: Large-scale failure modes for DE devices: material rupture (1), dielectric breakdown (2), pull-in instability (3), membrane buckling (4).

Large-scale failure modes occur when the entire material or a macroscopic portion of it reaches a critical condition. Four large scale modes can be identified: exceeded material strength, exceeded dielectric strength, pull-in instability and membrane buckling (see Fig. 4.7). If too high stresses are reached inside the material, mechanical rupture can occur; for VHB^{TM} 49XX a failure criterion based on maximum stretch is generally adopted: $\lambda_{max}^2 > 36$. When very large voltage loads are applied to the DEA electrodes, dielectric breakdown can be reached; the limit is posed by a maximum value of electric field which is strongly dependent on the material thickness and, once again, on the stretch ratio. Pull-in instability is typical of DE membranes and consists in the impossibility to reach an equilibrium between the external load due to Maxwell pressure and the material stress that should withstand the boundary load; the Maxwell pressure is always greater than the material stress and the material collapses into complex 3-D wrinkling patterns. The excessive material deformation finally lead either to mechanical or electric rupture. Finally, membrane buckling has been observed in some DEA geometries at low values of pre-stretch; buckling occurs when the planar stresses turn to negative in some areas due to the effect of external loads. Buckling failure is much less likely to occur than the other large-scale failure phenomena. Considering the three main large-scale failure modes, Fig. 4.8 is a graphic representation of the safe operating areas for DEA in terms of pre-stretch ratio λ_{pre} and stretch due to actuation λ_{act}; guidelines are provided to understand which failure mode poses the greater risk in a given DE application. Working loads can considerably increase the risk of failures in DEA and they are considered in Fig. 4.8. Also, the viscoelastic behavior of VHB^{TM} plays an important role and it can considerably affect the failure mechanism; Fig. 4.8a is applicable to high strain rate cases while Fig. 4.8b is applicable to low strain rate cases. In robotic applications, high strain rates are common.

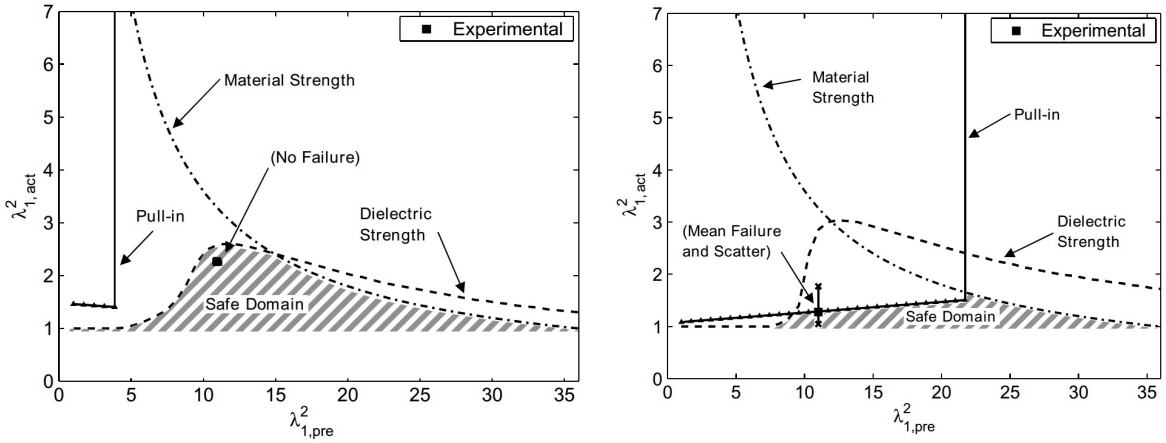

(a) High strain rate ($\dot{\lambda} = 0.064$ s^{-1}) **(b)** Low strain-rate ($\dot{\lambda} = 3.3 \times 10^{-4}$ s^{-1})

Fig. 4.8: Safe operation domain for 3M^{TM} VHB^{TM} DEAs considering large-scale failure modes under working loads [104]

4.3.1 DEAs and space environment

An important aspect to be investigated for any space system is the compatibility with the space environment. Failure of space system components is often triggered by external actions attributable to the harsh space environment. For EAPs and, in particular, DEs the assessment of survivability in space has not been performed exhaustively, yet. Nevertheless, specific information on the interaction of such materials with the environment can be found in literature as well as some applications have been proposed (see Sec. 2.2.1.4). The work by Bonser *et al.* [109] under ESA contract provide a preliminary analysis of the problem taking three main aspects into account: temperature, radiation, pressure.

Thermal loads that act on space systems are huge and the temperature of components varies considerably and rapidly. The lowest temperatures are reached on deep-space interplanetary orbits when the component is in shade (as low as -270° C), while the hottest can be reached on Earth orbits or at inner planets (more than 150° C). Dielectric elastomers, especially silicones, have reasonably large operative temperature ranges and meet the space environment requirement, with modified performances. Furthermore, operating temperature ranges can be extended by thermal insulation from external environment, by internal (possible for conductive materials) or external heating.

Hardly any investigation has been performed on failure risks of EAP systems subjected to highly radiative environment and further work needs to be done. Degradation and failure risks posed by UV radiation and high energy particles can be partly avoided through shielding. DEs could be particularly sensitive to electric charging due to impingement of energized particles, especially considering the presence of HV charged surfaces.

Space vacuum will have a limited effect on EAP materials and mechanisms. Minor changes on performances and mechanical behavior are expected. Out-gassing might be an issue,

although preconditioning processes have been developed in order to mitigate this problem. Actuators design will require minor changes (e.g. venting holes) in order to avoid encapsulation of air bubbles.

4.4 Self sensing capabilities

A peculiar characteristic of DEAs is the possibility to implement the integrated capability to measure the membrane deformation (self-sensing). In this section, the work by Jung *et al.* [54] will be revised briefly by introducing the basic concepts. Each membrane sector coated with deformable electrodes can be modeled as a compliant capacitor whose capacitance is given by

$$C = \varepsilon_v \varepsilon_r \frac{A}{h} \tag{4.52}$$

where A is the electrode area and h is the dielectric membrane deformed thickness; both these parameters vary when the DE system is actuated, therefore leading to a variation of capacitance. In particular, when high voltage is applied to the electrodes they expand in area and reduce in thickness causing an increment of the capacitance.

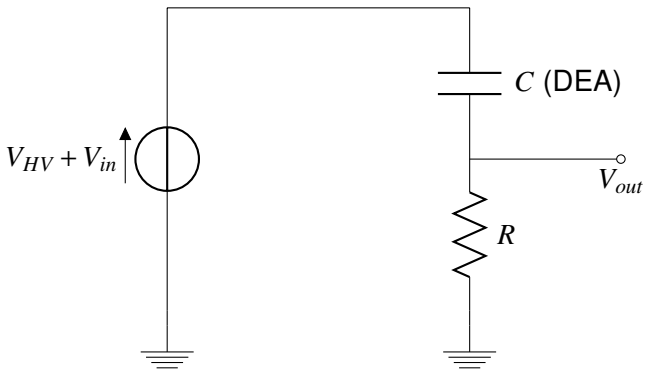

Fig. 4.9: Electric circuit of DEA with additional resistor for self-sensing implementation

The DEA can be included in an electric circuit with an additional resistor, R, obtaining a voltage divider or high-pass filter (see Fig. 4.9). If a low-amplitude, high-frequency voltage signal V_{in} (sensing input) is superimposed to the quasi-static high voltage component used for the DE actuation V_{HV}, the variation of capacitance can be sensed by measuring the amplification of the output voltage V_{out} (sensing output). The capacitive reactance for an input frequency F is given by

$$X_c = \frac{1}{2\pi F C} \tag{4.53}$$

on which depends the amplification of V_{out} measured by the sensing gain G_s as follows

$$\begin{aligned} V_{out} &= \frac{R}{R + X_c} V_{in} \\ &= G_s V_{in} \end{aligned} \tag{4.54}$$

Since V_{in} is alternate, the amplification affects the peaks of the sine wave. Practically, when high voltage is applied to the electrodes, the membrane expands in area and squeezes in thickness increasing the circuit capacitance C, leading to a greater gain G_s and, consequently, to an increased amplitude of the sinusoidal voltage V_{out} which can be measured. In other words, by reading the increment in V_{out}, the amount of deformation in the membrane is measured. Fig. 4.10 shows the conceptual schematics of V_{in} and V_{HV} mixing and extraction of V_{in} for self-sensing measurements in DEAs.

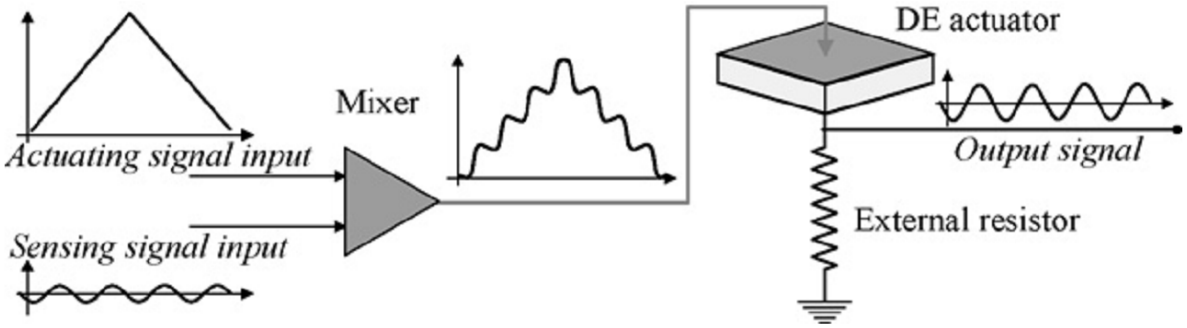

Fig. 4.10: Block diagram of self-sensing measurement implementation [54]

In this work, the self-sensing capability of DE systems has been verified on double-cone actuators, but it has not been adopted for the implementation in feedback control due to the low accuracy obtainable with laboratory-built technology. The experimental verification of a feedback system in double-cone actuators based on self-sensing deformation measurements is under study.

4.5 Double-cone actuator working principle

The double-cone configuration is selected to be investigated a possible robotic actuator for complex manipulators. The double-cone actuator is composed by two planar, circular membranes deformed to conic shape. Deformation is held by rigid supports (two rings and one shaft). The original membrane plane becomes the base of the cone. The cones are than mounted concentric, but mirrored w.r.t. the base plane, forming the double-conic shape.

Each membrane is split in sectors and each of them can be actuated independently. Every sector is coated with conductive grease on both membrane faces forming two electrodes in a sandwich geometry that works as a compliant capacitor. The number of degrees of freedom depends on the number and shape of the membrane sectors (i.e. capacitors). Generally, the sectors are wedges spanning $90\ \mathrm{deg}$ or $180\ \mathrm{deg}$. This geometry allows to reach up to 5 DoFs [63]. In the case considered in this work, each membrane is split in two sectors, $180\ \mathrm{deg}$ wide each. The considered DoFs are one translational along the axis of the actuator and one rotational around an axis lying on the actuator symmetry plane. Each sandwich capacitor has a positive electrode and one grounded electrode. When high voltage load is applied to the

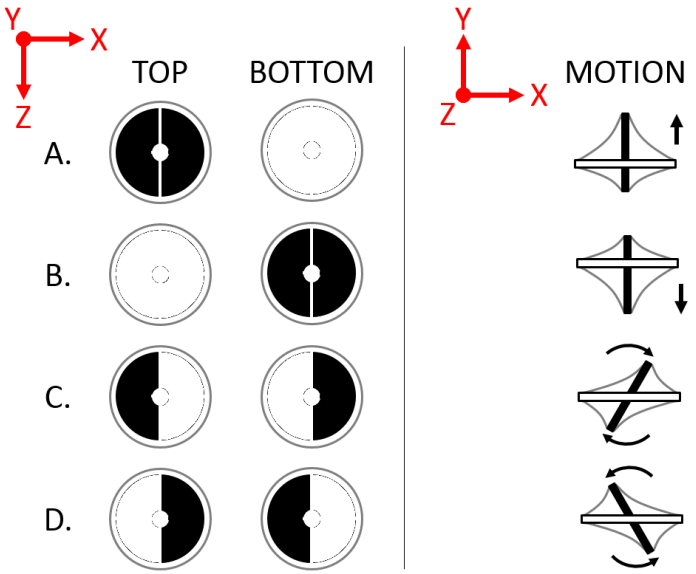

Fig. 4.11: Actuation of the considered DoFs in double-cone actuator: the electrodes are 180-deg wedges, black if high voltage is on, white if high voltage is off. Voltage loads on the top and bottom membrane are shown in the first two columns, while the third shows the motion triggered by the actuation. The four rows list the possible motions: $+y$ and $-y$ translation, $+z$ and $-z$ rotation

compliant capacitor, the Maxwell stress arise inside the membrane and actuation takes place. The compliant electrodes tend to expand in area when actuated. Depending on the shape and number of membrane sectors actuated at the same time, different DoF or a combination of them is actuated. When actuated, the membrane deforms causing the displacement of the central shaft of the actuator. This type of DEA geometry is an antagonistic configuration since the double symmetry (w.r.t. the cone axis and the base plane) provides every capacitor sector with an antagonistic counterpart that exerts the same but opposite force on the shaft. When one electrode is actuated, the membrane stresses in the region relax, the forces on the shaft are unbalanced and the antagonistic sector pulls the shaft. Fig. 4.11 is a schematic view of the possible actuations in the proposed 2-DoF configuration. A second rotational DoF around x-axis of Fig. 4.11, can be easily added to the configuration by manufacturing four 90-deg sectors instead of two; behavior and modeling is equivalent to the $\pm z$ rotation described above.

Fig. 4.12 shows a schematic cut view of the double-cone actuator presenting all the geometric parameters considered in this work: d is the membrane external diameter, D is the membrane inner diameter or the rod diameter, a is the amount of out-of-plane displacement imposed to the membranes, c is half of the rod length. The parameter δ_{re} measures the amount of membrane not covered by electrode in the neighborhood of the central rod: it is expressed in percentage of the total latitudinal coordinate ξ. An acceptable approximation is introduced if the value of δ_{re} is applied to the radial coordinate ρ instead of ξ, meaning that the portion of unstretched membrane not covered by the electrode is an annulus defined by the rod unstretched diameter $\frac{D}{\lambda_0}$ and the diameter $d_{re} = \delta_{re}\frac{d-D}{\lambda_0}$. Other useful parameters not shown in Fig. 4.12 are the

unstretched membrane thickness, t, the number of elastomer layers in the membrane, n, and the mentioned pre-stretch ratio, λ_0.

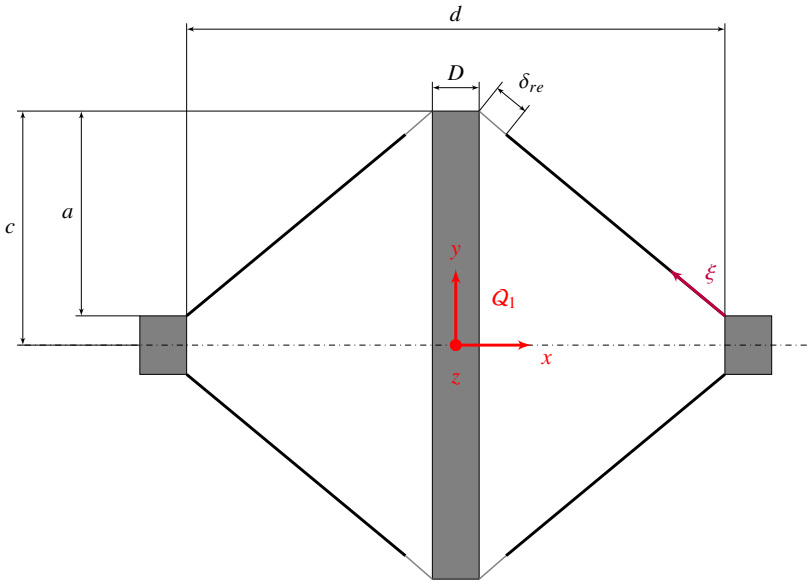

Fig. 4.12: Schematic section view of the actuator with main geometric parameters z-axis points at the reader)

4.6 Manufacturing

The double-cone DE actuators employed in this work have been manufactured manually. A manufacturing procedure have been developed based on literature and a trial-and-error approach. Two membranes compose each actuator; the following describes the manufacturing process for a single membrane and then the assembly of the two halves of the actuator. The manufacturing process of can be subdivided into the following steps:

1. material pre-stretch
2. electrode deposition
3. electric contacts attaching
4. rigid support mounting
5. double cone assembly

As already mentioned, the employed material is 3M^{TM} VHB^{TM} 4910 (1 mm original thickness). It is an adhesive membrane which shows a high bonding effect on polished materials and, in particular, on metals and rigid plastics. The bonding force increases over time: approximately 50% of ultimate bond strength is achieved after 20 minutes, 90% after 24 hours and 100% after 72 hours. On the other hand the elastomer shows a low bonding capability with polyethylene, silicone and neoprene foam, so the latter can be used when adhesion is unwanted.

A simple stretching device was designed and manufactured in order to perform the pre-stretch phase. Such device (see Fig. 4.13) is based on lozenge mechanisms with several diamond

elements. Four arrays of diamonds are assembled in a square structure and their extremities are mounted on two L-shaped support rails. All the components are made of stainless steel (AISI 304). When the system is actuated manually, the lozenge arrays deform and expand in length. The combined deformation effect of the four multiple-diamond systems produces a variable rectangular area at the center (see Fig. 4.14). The maximum area stretch is $\lambda_0^2 = 12.25$.

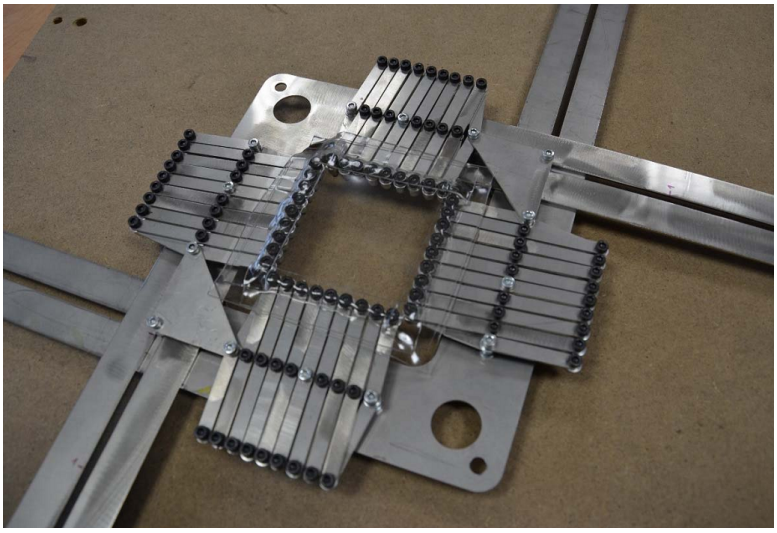

Fig. 4.13: Lozenge mechanism stretching device with unstretched membrane (transparent) attached

A square piece of material (roughly 80×80 mm) is attached on the inner vertexes of the diamonds. A relaxation time of $10 - 15$ minutes is guaranteed to permit a better adhesion. The area expansion of the stretch device is exploited to obtain an equibiaxial stretch of the material. Stresses in the material rise quickly and the adhesive forces need to withstand the increased loading condition. In order to enhance the bonding with the support substrate, pressure can be provided manually pushing the film and easing the adhesion. To perform this operation neoprene foam foil is used. Additional strips of VHB^{TM} can be placed on the four sides, to prevent the film rupture during the stretching. It is once again necessary to press with the neoprene foil to eliminate the air bubbles that can appear between the two films. When the film is biaxially stretched to the desired value of λ_0, it is attached on a large temporary support ring (plastic, see Fig. 4.15) and detached from the stretch device.

Carbon grease (MG Chemicals 846) electrodes are applied on both sides of the membrane in the desired pattern; sectors are separated by an uncoated area, $6 - 8$ mm wide. The grease is spread by means of small brushes or pieces of neoprene foam. This method is simple, but can easily damage the stressed film and grease application has to be very gentle. The conductive layer has to be as uniform as possible to avoid the presence of anomalies that can lead to a non-uniform stretch of the membrane when the voltage is applied or even to the electric failure of the actuator. Paint-brushing does not allow to produce smooth edge electrodes in a controllable and precise manner. Because of that electric charges gather at the electrode

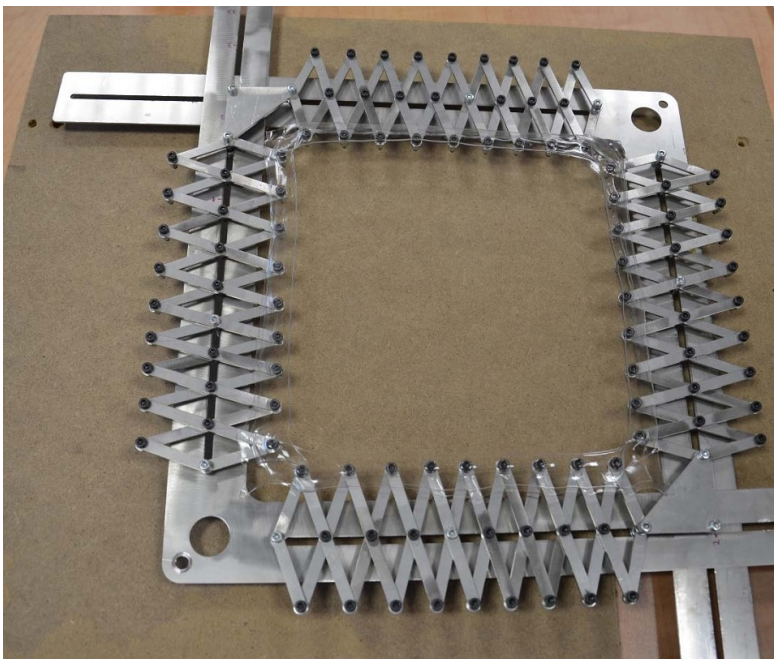

Fig. 4.14: Lozenge mechanism with membrane in stretched state

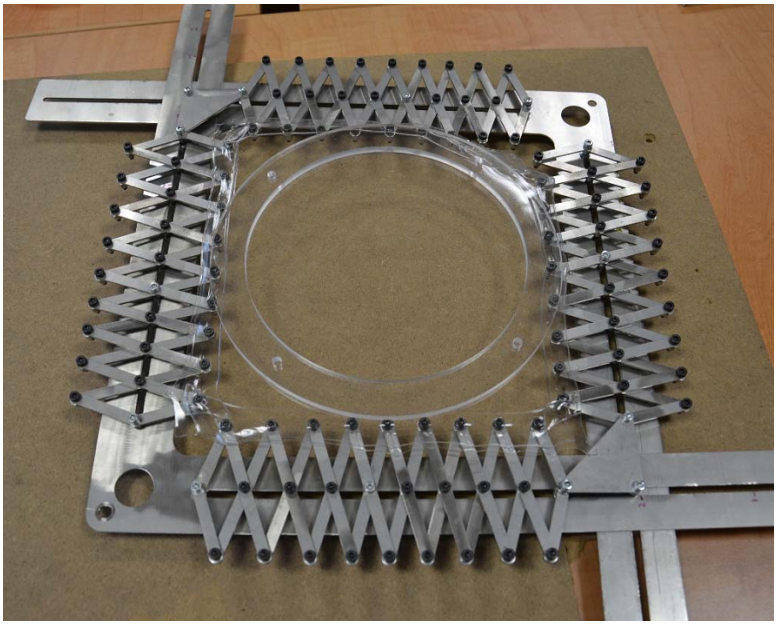

Fig. 4.15: Temporary support ring attached to the elastomer membrane

edges and create unwanted electric field concentration that can cause DEA breakdown even at low voltages.

The single membrane main structure is made of two structural plastic rings (PMMA or PC).

The electric contact is guaranteed by using small strings of adhesive aluminum tape, which are directly applied to the structural ring. The ring is then carefully placed on the membrane (concentric to the temporary ring) and, on the opposite surface, the film is pressed on the ring with neoprene foil to eliminate air bubbles. The aluminum tape is put in contact with

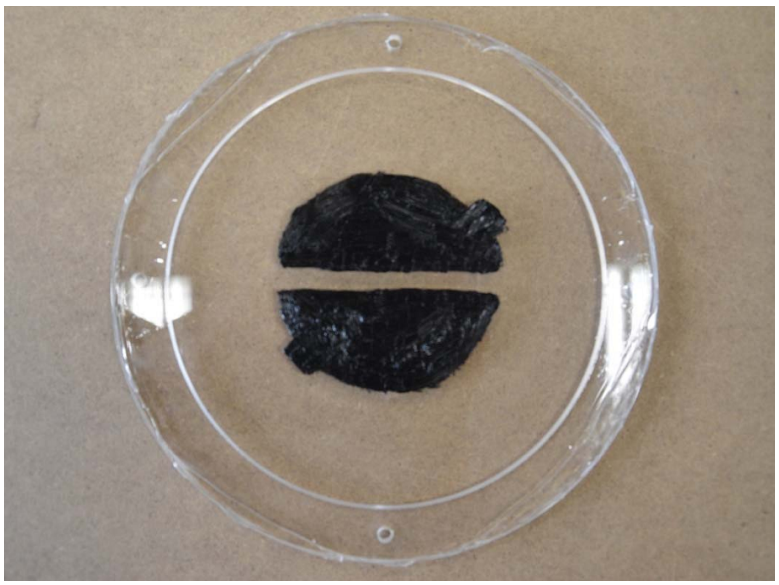

Fig. 4.16: Application of carbon grease electrodes

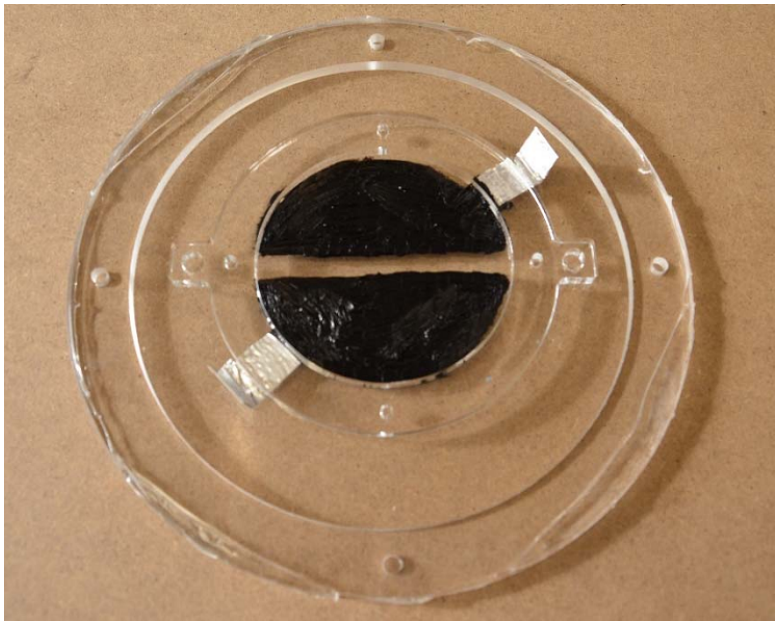

Fig. 4.17: Application of the membrane to the support ring with contacts

the conductive grease, one aluminum string for each electrode. The contacts are placed distant from each other in order to avoid arching when high voltage is applied. A thinner ring is attached on the other side of the film w.r.t. the support ring, forming a sandwich geometry; the second ring is required to keep some distance from the second membrane when the actuator is fully assembled. The membrane is detached from the larger temporary ring and excess material is removed. This completes the manufacturing of one actuator membrane

Two membranes are manufactured with the described procedure. These structures are assembled together and with a 3-D printed (PLA) shaft (see Fig. 4.18). The cylinder is placed at the center of the membrane so that it is perpendicular to the ring plane. The other membrane

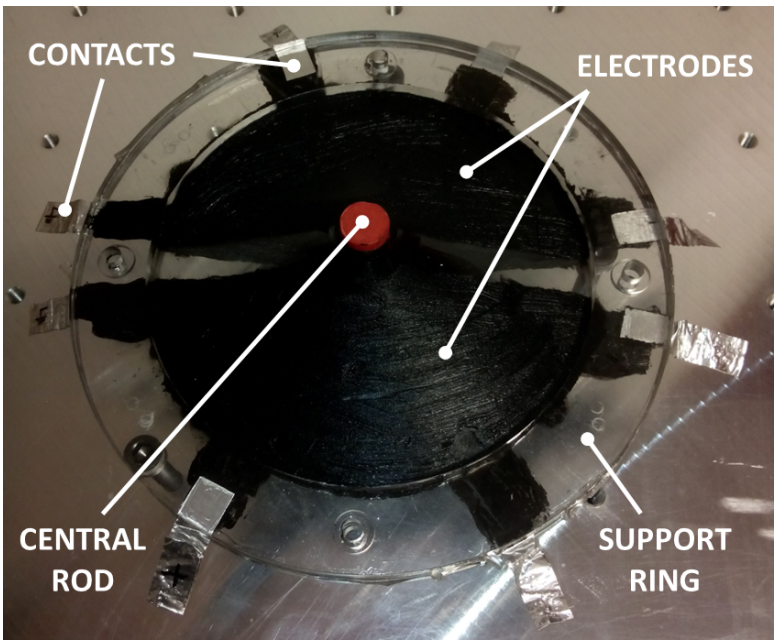

Fig. 4.18: Completed actuator with all functional parts

is pushed on the cylinder so that the grease section are symmetric to those on the first membrane. The two rigid supports are put in contact and connected together with screws, while the membranes assume a conical shape due to the action of the cylinder. Two 3-D printed plastic caps of the same radius of the cylinder are placed on top of the membrane so that during the tests the load cells used for the measures will be in contact with the caps and not directly with the film to prevent damage and arching.

4.7 Actuator kinematic and dynamic limits

DE double cone actuators have limited stroke and rotation. Such limits are mainly of two types (maximum values of stroke and rotation will be denoted here with y_{max} and θ_{max}):

1. Mechanical limits due to geometric and solid mechanics considerations. Geometrically, the axial linear stroke of double-cone actuators cannot exceed the cone height, $y_{max} < a$. On the other hand, the rotation is limited by the maximum local deformation of the DE membrane: above a given value of angular rotation the membrane on side of positive displacement of the actuator rod contracts and tends to deform to complex patterns. In this condition models fail to predict the actuator behavior; a reasonable geometric limit for maximum rotation is $\theta_{max} \leq 45$ deg.
2. Electric limits due to the maximum voltage available from the power supply electronics. The limitation due to a finite value of maximum supply voltage is clear and becomes more critical in the case of multi-DoF systems. In fact, when the same electrodes control more than one DoF (like in double-cone actuators, see Fig. 4.11), the available voltage has to be shared between different DoFs, leading to reduced displacements. For a

given rotation θ and stroke y in a system with combined DoFs, it is possible to define the $\hat{\theta} = \frac{|\theta|}{\theta_{max}}$ and $\hat{y} = \frac{|y|}{y_{max}}$ ratios that allow to develop the following limit formulations

$$\begin{aligned} \theta^{\star}_{max} &= \left(1 - \frac{\hat{y}}{2}\right)\theta_{max} \\ y^{\star}_{max} &= \left(1 - \frac{\hat{\theta}}{2}\right)y_{max} \end{aligned} \tag{4.55}$$

where $\theta^{\star}_{max}$ and $y^{\star}_{max}$ are the deflection limits in the case of combined motion, while θ_{max} and y_{max} are the limits for single DoF actuation. Eq. 4.55 is a rule of thumb inferred from experimental observations; practically, it means that when both rotation and translation DoFs are actuated at maximum voltage at the same time, the rotation and stroke achieved are half the maximum values achievable when each DoF is actuated singularly.

Electric limits are, in general, more strict then mechanical limits, and, for this reason, power electronics design plays an important role in the development of DEA based systems. In robotic systems, the considerations about the rotation/stroke limits in combined motion are of key importance and have to be taken into account when the operational envelope (workspace) of the system is computed.

5 Actuator modeling

A complete modeling of 2-DoF DE double-cone actuators has been performed. Numerical models for the characterization of steady state performances (force/torque and linear/angular stroke) have been developed. Empirical dynamic models based on transfer functions have been interpolated from relaxation tests and verified with sine wave tests at variable frequencies. In addition, a feedback compensator was designed and tested to verify the applicability of the developed models to DEA control problems.

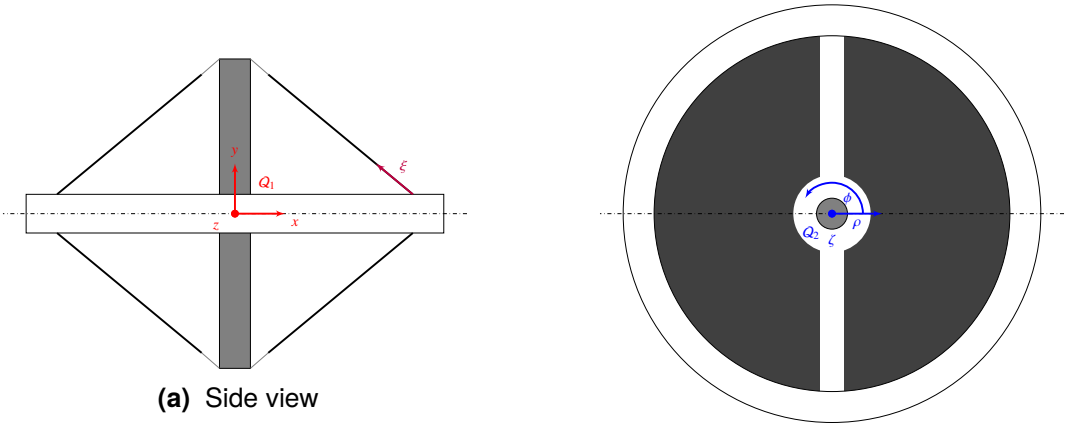

(a) Side view

(b) Top view

Fig. 5.1: Side (a) and top view (b) schematics of the actuator geometry showing circular membranes with electrodes (dark grey), support ring (white w/ black contour) and rigid rod (light gray). Both reference Q_1 (red) and Q_2 (blue) are shown.

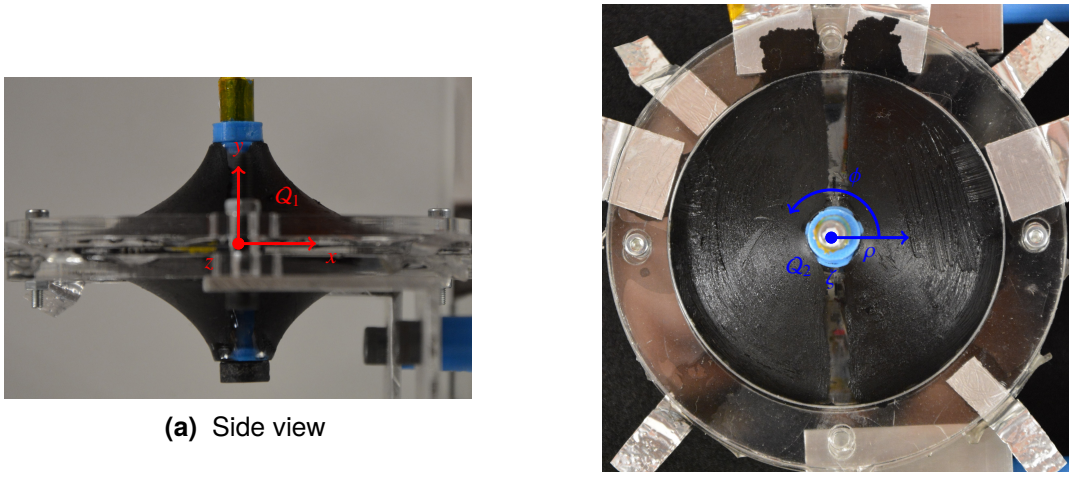

(a) Side view

(b) Top view

Fig. 5.2: Side (a) and top view (b) picture of the double-cone actuator. Both reference Q_1 (red) and Q_2 (blue) are shown.

Define a reference frame on the actuator and call it Q_1 (see Fig 5.27b). The device shows an axial symmetry about the central rod at rest so the y-axis of the frame is parallel to the symmetry axis. The x- and z-axes are perpendicular to each other and to the y-axis forming a right-handed reference frame. The origin of the reference frame is located at the geometrical centre of the actuator, at the midpoint of the central rod on the symmetry axis. The xz plane is the symmetry plane on which the two membranes and their supports are joined (see Fig. 5.27b). The DoFs considered in this work are rotation about the x- and z-axis, and translation along y-axis. In the following the y-axis stroke and force variables are y and F respectively. The z-axis rotation and torque variables are θ and T respectively; x-axis rotation is analogous to z-axis rotation by symmetry.

It is also useful to define a cylindrical coordinate system (Q_2). The origin of Q_2 coincides with the origin of Q_1 and the symmetry axis of Q_2 is parallel to the y-axis of Q_1. The coordinates of Q_2 are the radial distance, ρ, the azimuth angle, ϕ, and the axial position, ζ (see Fig. 5.2b).

5.1 Cone shape mathematical description

In the cone geometry, the stress state is commonly considered planar and the membrane approximation that led to Eq. 4.36 is still valid. In the cylindrical coordinate system, the deformation is described by the meridional (parallel to meridians) stretch ratio, λ_ρ, and the zonal (parallel to latitude circles) stretch ratio, λ_ϕ. These stretches are principal due to axial symmetry, meaning $\lambda_1 = \lambda_\rho$ and $\lambda_2 = \lambda_\phi$. Haddow *et al.* proposed a numerical procedure to determine the shape of one meridian in the problem of a hyperelastic membrane annulus deformed to conic shape, much alike the DE cone actuator geometry. The deformation of the membrane middle surface is described. The reference (undeformed) configuration of the annulus has internal radius P_A, external radius P_B, and is planar with $Z = 0$ and azimuthal coordinate Φ (upper case Greek letters are used to denote the undeformed coordinates: radial coordinate P, azimuthal coordinate Φ and axial coordinate Z). After (effective) pre-stretch λ_e, the current configuration is

$$\begin{aligned} \rho &= \lambda_e P \\ \phi &= \Phi \\ \zeta &= 0 \end{aligned} \tag{5.1}$$

After axially symmetric deformation (cone deformation) the configuration becomes

$$\begin{aligned} \rho &= \rho(P) \\ \phi &= \Phi \\ \zeta &= \zeta(P) \end{aligned} \tag{5.2}$$

with the boundary conditions (see Sec. 4.5 for explanation of parameters D, d and a)

$$\begin{aligned}\rho(P_A) &= \lambda_e P_A = \frac{D}{2}\\ \rho(P_B) &= \lambda_e P_B = \frac{d}{2}\\ \zeta(P_A) &= a\\ \zeta(P_B) &= 0\end{aligned} \tag{5.3}$$

It can be proven that the principal stretches in terms of cylindrical coordinates can be rewritten as

$$\lambda_\rho = \sqrt{\left(\frac{\mathrm{d}\rho}{\mathrm{d}P}\right)^2 + \left(\frac{\mathrm{d}\zeta}{\mathrm{d}P}\right)^2} \qquad \lambda_\phi = \frac{\rho}{P} \tag{5.4}$$

The functional E is defined as

$$E = \int_{P_A}^{P_B} tP\Psi\left(\frac{\rho}{P}, \sqrt{\left(\frac{\mathrm{d}\rho}{\mathrm{d}P}\right)^2 + \left(\frac{\mathrm{d}\zeta}{\mathrm{d}P}\right)^2}\right)\mathrm{d}P \tag{5.5}$$

An approximate solution can be obtained by making the functional E stationary within a set of kinematically admissible deformations like

$$\rho = \lambda_e P \qquad \zeta = \zeta^\star(P) \tag{5.6}$$

with $\zeta^\star(P_A) = a$ and $\zeta^\star(P_B) = 0$. The functional, E, is stationary if

$$\frac{\mathrm{d}}{\mathrm{d}P}\left\{P\frac{\partial\Psi}{\partial\left(\frac{\mathrm{d}\zeta^\star}{\mathrm{d}P}\right)}\left(\lambda_e, \sqrt{\lambda_e^2 + \left(\frac{\mathrm{d}\zeta^\star}{\mathrm{d}P}\right)^2}\right)\right\} = 0 \tag{5.7}$$

leading to the following equation to be solved iteratively

$$\frac{\partial\Psi}{\partial\left(\frac{\mathrm{d}\zeta^\star}{\mathrm{d}P}\right)} = \frac{C}{P} \tag{5.8}$$

where C is a constant to be found to satisfy the boundary conditions (above). Once the solution $\zeta^\star$ and its derivative $\frac{\mathrm{d}\zeta^\star}{\mathrm{d}P}$ are known, it is possible to determine the stretches λ_ϕ and λ_ρ from Eq. 5.4 and, consequently, the true stresses from Eq. 4.36. The knowledge of λ_ϕ and λ_ρ allows to compute the current thickness h of the membrane at each position along ρ. The Maxwell pressure can than be computed with Eq. 4.44.

5.2 Finite Element Analysis model

The actuation of the rotational DoF was modeled by means of an ANSYS® Mechanical parametric model. The model developed for the analysis exploits the intrinsic symmetries of the

actuator (see Fig. 5.1). For the simulations only a quarter actuator is considered (half of a single membrane, see Fig. 5.3) and the geometry is cut at the xy and xz planes.

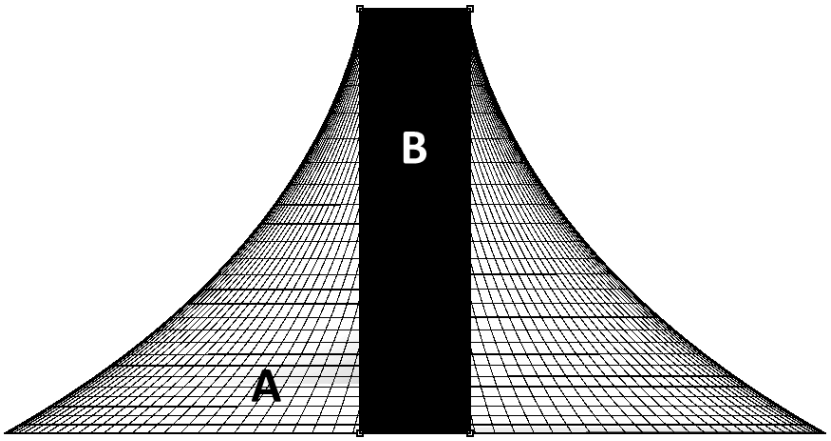

Fig. 5.3: Side view of an example FEM model used in simulations. The geometry is a quarter actuator (i.e. half membrane) and composed by two bodies: the deformable membrane (A, meshed) and the rigid rod (B, black)

Since the purpose of this work is to assess the performances with variable geometric parameters, the model dimensions can be considerably different between simulations. However, in all cases the model is composed by 8-node hexahedra (parallelepipeds) with hyperelastic formulation and the mesh is regular (see Fig. 5.4). The membrane is meshed by a single layer of elements through the thickness. The number of elements ranges between 3000 and 6000 approximately due to variable model dimensions. A sensitivity analysis on the number of elements in the mesh has been performed and a further mesh refinement does not improve the simulation results (see Fig. 5.2.1).

The membrane is modeled by a deformable body (A) shaped like a half disc (cut on the xy symmetry plane) with a central hole. The membrane is radially stretched according to the value of the effective stretch ratio λ_e (see Fig. 4.39); in this phase the membrane is still planar: the bottom nodes ($\zeta = 0$) of the inner and outer edges are free to move only radially, while the top nodes ($\zeta = t$) are allowed to displace also in the ζ direction in order to follow the thickness reduction due to planar stretch. After pre-stretch the external edge of the disc is fixed, while the edge of the central hole is bonded (no slip allowed) to a rigid body (B) that represents the actuator rod.

A rotoidal-translational joint connects B to the fixed reference frame allowing the body to be displaced in order to obtain the out-of-plane deformation of the membrane as well as the operative deformation (i.e. z-axis rotation) due to the actuation. Two types of simulations have been performed: one with blocked z-rotation of B to determine the actuator blocking torque, the other with free z-rotation of B to determine the maximum angular stroke. The body is not deformable and, therefore, it is not meshed, except for the external surface that comes in contact with the elastomer membrane.

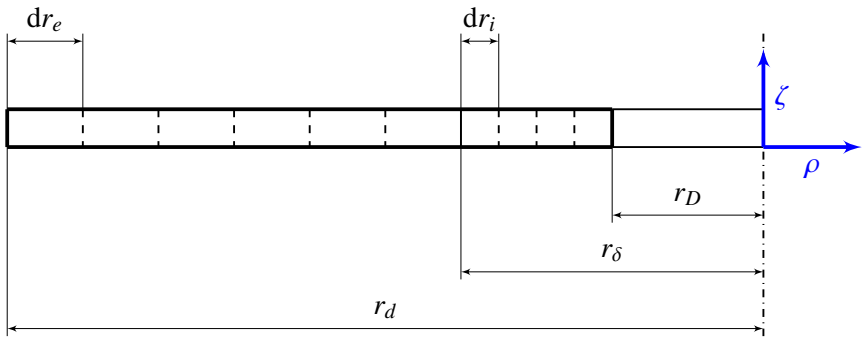

(a) Top view

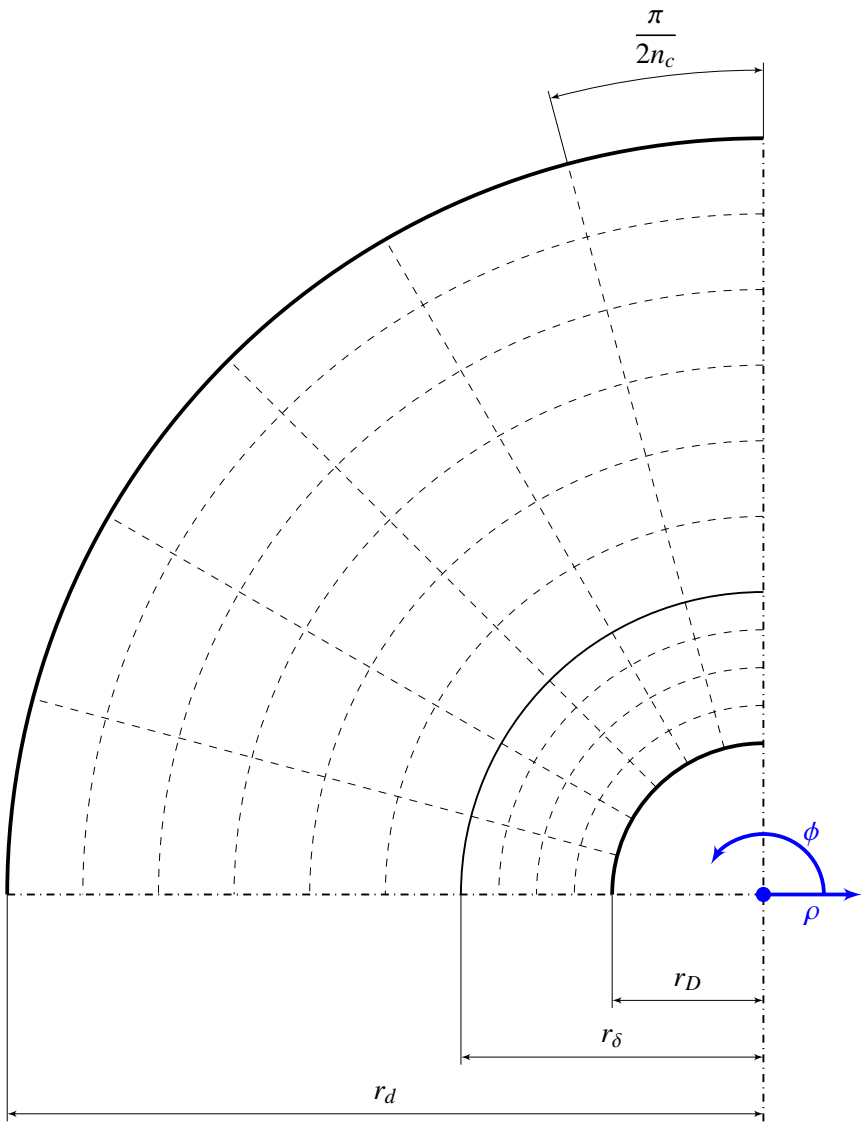

(b) Side view

Fig. 5.4: Graphic representation of the undeformed mesh with the sizing parameters considered for simulations (top and side view): the parameters $\mathrm{d}r_e$, $\mathrm{d}r_i$ and n_c, as well as the reference radii r_d (external), r_D (internal) and r_δ are shown

Fig. 5.4 schematically shows a side and top view of the undeformed mesh and its parameters: the maximum element size, $\mathrm{d}r_e$, along the radius for $r > r_\delta = \frac{\delta_{re}}{2}\frac{d-D}{\lambda_e}$, the maximum element size $\mathrm{d}r_i$ along the radius for $r < r_\delta = \frac{\delta_{re}}{2}\frac{d-D}{\lambda_e}$ and the number of divisions, n_c, in which $90\ \mathrm{deg}$ of angular coordinate ζ are meshed.

The actuation load on the dielectric elastomer is represented by Maxwell pressure due to the applied voltage. For a given value of voltage, the pressure is computed from Eq. 4.44 once the current value of thickness at each location is computed with the procedure described in Sec 5.1.

The FEM model is used to assess the performances of the actuator under the variable parameters mentioned in Sec. 4.5. To achieve this, a Microsoft® Excel® routine is linked to the ANSYS® model and used to compute the model dimensions, Maxwell pressure to be applied to the membrane and effective stretch ratio λ_e for different parameter sets. A parametric study is implemented in the ANSYS® model. The variability ranges of the parameters in the simulations are

$$\begin{gathered} d = \{60\ \ 80\ \ 120\}\ \mathrm{mm} \\ D = \{10\ \ 12\ \ 14\}\ \mathrm{mm} \\ c = \{15\ \ 20\ \ 25\}\ \mathrm{mm} \\ a = c - \mathrm{d}c \quad \text{with} \quad \mathrm{d}c = \{0\ \ 2\}\ \mathrm{mm} \\ \delta_{re} = \{0\ \ 1\ \ 10\}\ \% \\ \lambda_0 = \{3\ \ 3.5\ \ 4\} \end{gathered} \tag{5.9}$$

For each parametric geometry (for a total of 650 simulations), the blocking torque, $T_{\theta=0}$, and the angular stroke, $\theta_{T=0}$, of the actuator are determined.

5.2.1 Mesh sensitivity analysis

The mesh reliability in FEA simulations have been verified by analyzing the sensitivity of results to mesh parameters. The percentage change of the simulation output w.r.t. a change in the main sizing parameters is shown in Fig. 5.5.

The parameters at nominal value are used to generate the mesh used for the simulations. To assess the quality of the mesh the sizing parameters are varied around the nominal value and results are compared with those obtained at nominal values. If the variation between the results at nominal and those at finer mesh sizing (smaller values of $\mathrm{d}r_i$ and $\mathrm{d}r_e$, larger values of n_c) is negligible, the obtained results are considered reliable. Fig. 5.5 shows that a further refinement of mesh beyond the nominal values of the parameters is not necessary, since the percentage variation in the results is below 1%. Sensitivity of the results to an improvement of the mesh is negligible and the results obtained at nominal values of the sizing parameters are considered reliable.

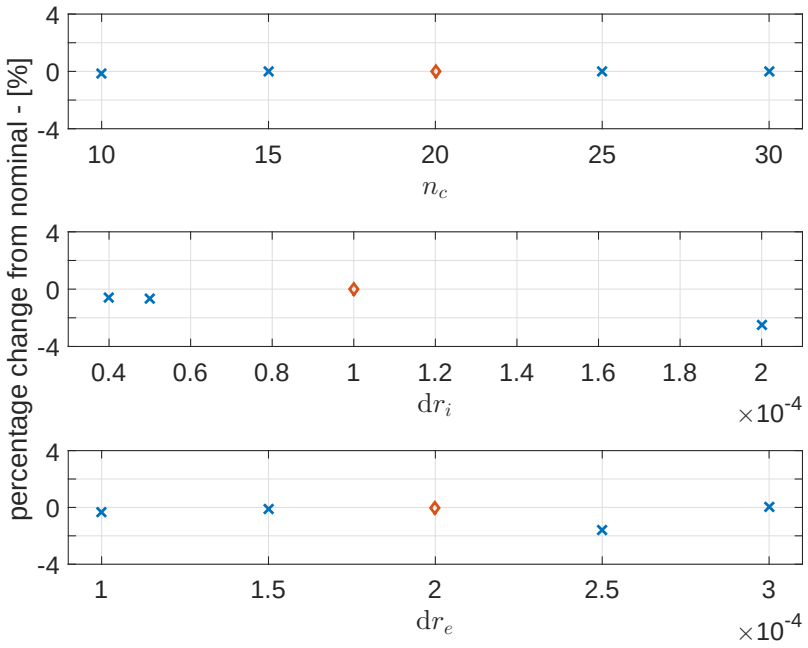

Fig. 5.5: Mesh sensitivity analysis; percentage variation of results as a function of the mesh parameters (n_c, $\mathrm{d}r_i$, $\mathrm{d}r_e$): orange diamonds mark the parameter values at which the simulation is performed (nominal), blue crosses show the percentage variation from nominal at different values of the size parameters

5.3 Boundary value problem

The actuator force, F, and the linear stroke, y, are determined with an iterative procedure based on a mathematical formulation similar to that presented in Sec. 5.1. In particular, a modified version of the approach proposed by He *et al.* [**he**] to the conic membrane boundary problem is implemented. Using the nomenclature introduced in Sec. 5.1, the following system of ordinary differential equations is defined

$$\begin{aligned} \frac{\mathrm{d}\rho}{\mathrm{d}P} &= \lambda_\rho \cos\beta \\ \frac{\mathrm{d}\zeta}{\mathrm{d}P} &= -\lambda_\rho \sin\beta \\ \frac{\mathrm{d}\beta}{\mathrm{d}P} &= -\frac{s_\phi}{s_\rho P}\sin\beta \end{aligned} \tag{5.10}$$

where β is the cone slope angle in deformed configuration defined as $\beta = \frac{\mathrm{d}\rho}{\mathrm{d}\zeta}$, while s_ϕ and s_ρ (see Sec. 4.1.2) are the nominal stresses in the membrane computed with the following derived from Eq. 4.29

$$\begin{aligned} s_\rho &= \frac{\partial \Psi}{\partial \lambda_\rho} \\ s_\phi &= \frac{\partial \Psi}{\partial \lambda_\phi} \end{aligned} \tag{5.11}$$

The system of differential equations in Eq. 5.10 has to be solved under the boundary conditions presented in Eq. 5.3 and recalled here

$$\begin{aligned}\rho(P_A) &= \lambda_e P_A = \frac{D}{2}\\ \rho(P_B) &= \lambda_e P_B = \frac{d}{2}\\ \zeta(P_A) &= a\\ \zeta(P_B) &= 0\end{aligned} \tag{5.12}$$

and the following additional equation has to be satisfied at all values of P to ensure equilibrium of forces

$$2\pi \frac{t}{\lambda_\rho \lambda_\phi} \rho \sigma_\rho(\lambda_\rho, \lambda_\phi, V) \sin\beta - F_c = 0 \tag{5.13}$$

where V is the voltage applied to the elastomer, F_c is the unknown force that ensures the desired cone deformation and is to be determined iteratively. The solution is found considering that $\lambda_\phi = \frac{\rho}{P}$ and that λ_ρ can be determined by solving 5.13 for a given value of F_c by means of numerical methods. The main steps of the solver algorithm developed in MATLAB® are:

1. choose an initial value of F_c ;
2. compute λ_ρ by solving Eq. 5.13 numerically (Trust-Region Dogleg);
3. try to solve the boundary value problem given in Eq. 5.10 (for example by implementing a Runge-Kutta implicit method like the Lobatto IIIa formula);
4. if the boundary conditions in Eq. 5.12 cannot be met, update the value of F_c and go back to point #1; otherwise the process ends.

The solution output are the $\rho(P)$ and $\zeta(P)$ functions and the value of F_c, which is a function of the cone height, a, and the applied voltage V. The actuator axial force at zero stroke, $F_{y=0}$, for a given value of applied voltage $V^\star$ can be computed with the following equation after solving the iterative process for $V = 0$ and $V = V^\star$ obtaining (knowing that $F_c = F_c(V,a)$)

$$F_{y=0} = F_c(0,a) - F_c(V^\star, a) \tag{5.14}$$

Eq. 5.14 comes from the assumption that the actuator axial force depends on the unbalanced equilibrium between the elastic forces of the upper and lower membranes of the device. For the upper membrane $V = V^\star$, while for the lower membrane $V = 0$. The equilibrium of forces allows to write Eq. 5.14.

The linear stroke, y, is computed by solving numerically the balanced equilibrium of forces similar to Eq. 5.14 and presented here

$$0 = F_c(0, a-y) - F_c(V^\star, a+y) \tag{5.15}$$

The obtained value of y corresponds to the free stroke of the actuator, $y_{F=0}$.

Again, a parametric study has been conducted and the force and stroke values at steady state have been computed for a large number (860) of different geometries. The design parameters have been selected within the following variability ranges (the model depends only on parameter a and not on c)

$$\begin{aligned} d &= \{60 \;\; 80 \;\; 120\} \text{ mm} \\ D &= \{10 \;\; 12 \;\; 14\} \text{ mm} \\ a &= \{15 \;\; 20 \;\; 25\} \text{ mm} \\ \delta_{re} &= \{0 \;\; 1 \;\; 10\} \,\% \\ \lambda_0 &= \{3 \;\; 3.5 \;\; 4\} \end{aligned} \tag{5.16}$$

5.4 Numeric results interpolation

Interpolating empirical relations are extrapolated from the data collected with the numerical methods described in Sec. 5.2 and Sec. 5.3. The procedure adopted is a common least squares interpolation method. The results data on the actuator performances ($T_{\theta=0}$, $\theta_{T=0}$, $F_{y=0}$ and $y_{F=0}$) are estimated by means of relations in the following form

$$\begin{aligned} \tilde{\theta}_{T=0} &= f_\theta(\vec{w}) \; V^2 \\ \tilde{T}_{\theta=0} &= f_T(\vec{w}) \; V^2 \\ \tilde{y}_{F=0} &= f_y(\vec{w}) \; V^2 \\ \tilde{F}_{y=0} &= f_F(\vec{w}) \; V^2 \end{aligned} \tag{5.17}$$

where $\vec{w} = \left\{ d \quad D \quad a \quad c \quad \delta_{re} \quad n \quad t \quad \lambda_0 \right\}^{\mathrm{T}}$ is the vector of geometric parameters considered and the tilde symbol, $\tilde{\cdot}$, denotes the estimated quantity values. Once expressions for the performance gains (f_T, f_θ, f_F, f_y) are determined, the interpolation procedure finds the numeric coefficients of such relations by minimizing the square root of the sum of squares of relative error, defined as follows for a generic quantity Q

$$s = \sqrt{\frac{1}{N} \sum_{i=1}^{N} \left(\frac{\left| Q_i - \tilde{Q}_i \right|}{Q_i} \right)^2} \tag{5.18}$$

where N is the number of samples collected from simulations. The minimization algorithm adopted is a Nelder-Mead simplex method. The quality of the fit is estimated by the standard

deviation, σ_s, of the percentage residual errors on the N samples. The best fits are presented below

$$
\begin{aligned}
f_\theta &= k_1 \left(\frac{D}{d}\right)^{\eta_2} \left(\frac{a}{d}+\alpha_3\right)\left(\frac{a}{c}\right)^{\eta_4} \left(\mathrm{e}^{-\delta_{re}}+1\right) \varepsilon_v \varepsilon_r \frac{\bar{\lambda}_\rho^2}{t^2} \\
f_T &= k_5\, n\, (\alpha_6 - D)^{-1} \frac{1+\gamma_7 (d-0.05)\log_{10}(\delta_{re}+0.5)}{d^2+\alpha_8 d+\beta_8}\, c^{\eta_9}\, (\mathrm{e}^{-\delta_{re}}+1)\, \varepsilon_v \varepsilon_r \frac{\bar{\lambda}_\rho^2}{t} \\
f_y &= k_{10}\, \bar{\lambda}_\rho^{\eta_{11}+2}\, d^{\eta_{12}}\, D^{\eta_{13}}\, a^{\eta_{14}}\, \mathrm{e}^{-\eta_{15}\delta_{re}} \varepsilon_v \varepsilon_r \frac{\lambda_0^2}{t^2} \\
f_F &= k_{16}\, d^{\eta_{17}}\, D^{\eta_{18}}\, a^{\eta_{19}}\, n\, \mathrm{e}^{-\frac{\delta_{re}}{100}} \varepsilon_v \varepsilon_r \frac{\lambda_0^2}{t}
\end{aligned}
\tag{5.19}
$$

Tab. 5.1: Model coefficients for $\theta_{T=0}$ (expressed in [deg]), $T_{\theta=0}$, $y_{F=0}$ and $F_{y=0}$

Coefficient	Value	Coefficient	Value
k_1	3.441×10^{-4}	k_5	3.876×10^{-5}
η_2	-0.9876	α_6	0.0675
α_3	0.9149	γ_7	3.752
η_4	2.271	α_8	-0.2676
		β_8	0.0276
		η_9	1.05
Coefficient	**Value**	**Coefficient**	**Value**
k_{10}	1.564×10^{-5}	k_{16}	16.55
η_{11}	-1.693	η_{17}	-0.5434
η_{12}	0.07183	η_{18}	0.6029
η_{13}	0.1286	η_{19}	1.103
η_{14}	0.8369	η_{20}	
η_{15}	1.253×10^{-2}		

The numerical values of model interpolation coefficients in Eq. 5.19 are listed in Tab. 5.1. The standard deviations (interpolation errors) for the relations shown in Eq. 5.17 with the form given in Eq. 5.19 are

$$
\begin{aligned}
\sigma_\theta &= 7.3\% \qquad \sigma_T = 7.5\% \\
\sigma_y &= 2.7\% \qquad \sigma_F = 3.8\%
\end{aligned}
\tag{5.20}
$$

Literature works [63] and experimental verification confirm that the dependency of cone actuators torque on rotation is linear. Eq. 5.21 presents the relation that describes this dependency at a given value of applied voltage.

$$\begin{aligned} T(\theta)\Big|_V &= T_{\theta=0}\Big|_V + m_\theta \cdot \theta \\ &= T_{\theta=0}\Big|_V - \frac{f_T}{f_\theta} \cdot \theta \end{aligned} \tag{5.21}$$

Also the dependency on stroke of the actuator force is linear. Eq. 5.22 presents the relation that describes this dependency at a given value of applied voltage.

$$\begin{aligned} F(y)\Big|_V &= F_{y=0}\Big|_V + m_y \cdot y \\ &= F_{y=0}\Big|_V - \frac{f_F}{f_y} \cdot y \end{aligned} \tag{5.22}$$

5.5 Steady state tests

The performance values estimated with the relations presented in Sec. 5.4 are compared with experimental values and presented in this section. Three different actuators have been tested in order to verify the dependency of the performances on design parameters.

5.5.1 Test apparatus

The power supply used in laboratory tests is a single channel Stanford Research Systems PS375; step output voltages are commanded. Force/torque measurements are taken with 0.1 kg load cells (Robotshop) read by means of a Yokogawa WE7245 100 kS/s strain module. Videos of the actuator displacements are recorded with a Nikon D3200 camera with 25 fps frame rate and 18-105 mm lens; the videos are post-processed with a dedicated MATLAB® code.

The force measure is computed with the following equation

$$\check{F} = k_c v g \tag{5.23}$$

where k_c is the load cell constant, v is the signal read by the acquisition system and $g = 9.8065855$ m/s^2 is the gravity acceleration value (in Padova, Italy). The torque measure is based on the following equation

$$\check{T} = (k_{c_1} v_1 + k_{c_2} v_2) g b_T \tag{5.24}$$

where b_T is the moment arm and the indexes 1 and 2 refer to different load cells (two sensors required for torque measurements). To estimate the uncertainty on the measures, the relation in Eq. 5.24 can be simplified by assuming that $k_{c_1} \approx k_{c_2}$ and $v_1 \approx v_2$

$$\check{T} = 2k_c v g b_T \tag{5.25}$$

Load cells are calibrated to measure mass so that $m = k_c v$. The uncertainty on $\check{F}$ and $\check{T}$ is determined by multiple sources which are combined according to the Kline-McKlintock approach. The considered uncertainty sources are:

- u_v [mV/V] is the uncertainty on the signal, v, measured by the acquisition system: it is estimated statistically by acquiring a large number of static measures; the distribution is normal with (triple) standard deviation $u_v = 3\sigma_v = 6.3 \times 10^{-3}$ mV/V;
- u_m [kg] is the uncertainty on the mass measure, $k_c v$, given by the intrinsic load cell error: it is provided by the sensor manufacturer, $u_m = 9 \times 10^{-5}$ kg;
- u_{b_T} [m] is the uncertainty on the measure of the moment arm, b_T: it depends not only on the length of the actuator central shaft but also on its position w.r.t. the actuator structure, by the dimensions of the interface that guarantee the contact between the shaft and the load cell and by the actual position of the load cell itself. For this reason a conservative value of $u_{b_T} = 2 \times 10^{-3}$ m is considered.

The value of combined uncertainty on force measurement is given by

$$u_F = \sqrt{\left(\frac{\partial F}{\partial m} u_m\right)^2 + \left(\frac{\partial F}{\partial v} u_v\right)^2} = 1.4 \times 10^{-2} \text{ N} \tag{5.26}$$

while the combined uncertainty on torque measurement is computed with

$$u_T = \sqrt{\left(\frac{\partial T}{\partial m} u_m\right)^2 + \left(\frac{\partial T}{\partial v} u_v\right)^2 + \left(\frac{\partial T}{\partial b_T} u_b\right)^2} \tag{5.27}$$

where the expressions of the partial derivatives can be derived from Eq. 5.23 and Eq. 5.25 obtaining

$$\begin{aligned} \frac{\partial F}{\partial m} &= g \\ \frac{\partial F}{\partial v} &= k_c g \end{aligned} \tag{5.28}$$

$$\begin{aligned} \frac{\partial T}{\partial m} &= gb \\ \frac{\partial T}{\partial v} &= k_c g b \\ \frac{\partial T}{\partial b_T} &= k_c v g \end{aligned} \tag{5.29}$$

From Eq. 5.29 it is clear that u_T is a function of the measured values and, therefore, it is not constant.

Stroke and rotation measurements are taken by determining the displacement of a green marker attached to the tip of the actuator central shaft: when the y stroke is measured, the camera points at the xy plane of the actuator (i.e. z-axis is perpendicular to the camera plane); when the z rotation (θ) is measured, the camera points at the xz plane (i.e. y-axis is perpendicular to the camera plane). The mentioned camera is used to record videos of the marker motion as a consequence of actuation. The main steps of the image processing are the following:

1. load RGB image
2. convert to gray-scale image
3. subtract green channel from gray-scale image (green regions become bright, other regions become dark)
4. convert to binary image via threshold (regions with value above the threshold become white, other become black)
5. delete white regions if too small
6. determine centroid of the remaining white region (marker)
7. determine the displacement of the centroids in pixels

A reference length object, l_r, is located close to the marker, captured during video recording and used as a standard to determine the pixel-to-m ratio, $\frac{l_r}{n_r}$, of the vision system (the reference length corresponds to the reference number of pixels, l_r, in the image, measured manually). Once the marker pixel displacement in x and y directions, n_x and n_y, relative to the initial position is known, the measured stroke, $\check{y}$, is computed with the following equations

$$\check{y} = \sqrt{n_x^2 + n_y^2}\frac{l_r}{n_r} \tag{5.30}$$

while the rotation angle is computed with the following equation

$$\check{\theta} = \arcsin\left(\frac{\sqrt{n_x^2 + n_y^2}}{b_\theta}\frac{l_r}{n_r}\right) \tag{5.31}$$

where b_θ is the distance between the marker position and the center of rotation of the actuator shaft. Again, the uncertainty on $\check{y}$ and $\check{\theta}$ is determined by multiple sources which are combined according to the Kline-McKlintock approach. The considered uncertainty sources are:

- u_n [pix] is the uncertainty on the x and y positions of the marker centroid, n_x and n_y: it is estimated statistically by acquiring a large number of video frames with static actuator; the distribution is normal with (triple) standard deviation $u_n = 3\sigma_v = 0.55$ pix;
- u_{b_θ} [m] is the uncertainty on the measure of the rotation arm b_θ: it depends not only on the length of the actuator central shaft, but also on the position of the center of rotation,

whose determination is not easy. For this reason a conservative value of $u_{b_\theta} = 10^{-3}$ m is considered;

- u_l [m] is the uncertainty on the measure of the reference length l_r: it is equal to the caliper resolution, $u_l = 5 \times 10^{-5}$ m;
- u_{n_r} [pix] is the uncertainty on the reference length in pixels, n_r, which is determined manually from example video frames; a value of $u_{n_r} = 2$ pix is considered.

The value of combined uncertainty on force measurement is given by

$$u_y = \sqrt{\left(\frac{\partial y}{\partial n_x} u_n\right)^2 + \left(\frac{\partial y}{\partial n_y} u_n\right)^2 + \left(\frac{\partial y}{\partial l_r} u_l\right)^2 + \left(\frac{\partial y}{\partial n_r} u_{n_r}\right)^2} \tag{5.32}$$

while the combined uncertainty on torque measurement is computed with

$$u_\theta = \sqrt{\left(\frac{\partial \theta}{\partial n_x} u_n\right)^2 + \left(\frac{\partial \theta}{\partial n_y} u_n\right)^2 + \left(\frac{\partial \theta}{\partial l_r} u_l\right)^2 + \left(\frac{\partial \theta}{\partial n_r} u_{n_r}\right)^2 + \left(\frac{\partial \theta}{\partial b_\theta} u_{b_\theta}\right)^2} \tag{5.33}$$

where the expressions of the partial derivatives can be derived from Eq. 5.30 and Eq. 5.31 obtaining

$$\begin{aligned}
\frac{\partial y}{\partial n_x} &= \frac{n_x l_r}{n_r \sqrt{n_x^2 + n_y^2}} \\
\frac{\partial y}{\partial n_y} &= \frac{n_y l_r}{n_r \sqrt{n_x^2 + n_y^2}} \\
\frac{\partial y}{\partial l_r} &= \frac{\sqrt{n_x^2 + n_y^2}}{n_r} \\
\frac{\partial y}{\partial n_r} &= -\frac{l_r \sqrt{n_x^2 + n_y^2}}{n_r^2}
\end{aligned} \tag{5.34}$$

$$\begin{aligned}
\Xi &= b_\theta n_r \sqrt{1 - \frac{n_x^2 + n_y^2}{2 b_\theta^2} \frac{l_r^2}{n_r^2}} \\
\frac{\partial \theta}{\partial n_x} &= \frac{n_x l_r}{\sqrt{n_x^2 + n_y^2}\,\Xi} \\
\frac{\partial \theta}{\partial n_y} &= \frac{n_y l_r}{\sqrt{n_x^2 + n_y^2}\,\Xi} \\
\frac{\partial \theta}{\partial l_r} &= \frac{\sqrt{n_x^2 + n_y^2}}{\Xi} \\
\frac{\partial \theta}{\partial n_r} &= -\frac{l_r \sqrt{n_x^2 + n_y^2}}{n_r \Xi} \\
\frac{\partial \theta}{\partial b_\theta} &= -\frac{l_r \sqrt{n_x^2 + n_y^2}}{b_\theta \Xi}
\end{aligned} \tag{5.35}$$

The values of u_y and u_θ depend on the measured quantity, thus depending on the tested prototype and its design parameters.

Performance evaluation tests have been performed on three prototypes with the dimensions and parameters listed in Tab. 5.2.

Tab. 5.2: Geometric and design parameters of tested prototypes

#	d [mm]	D [mm]	c [mm]	a [mm]	λ_0	δ_{re} [%]
1	120	12	25	24	3.5	2
2	80	12	25	23	3.4	0.13
3	60	12	20	18	3	0.13

5.5.2 Test results

The model relations described in Eq. 5.17 and Eq. 5.19 are verified by means of laboratory tests. The rotational stroke and torque values for prototypes #1, #2 and #3 are presented as functions of applied voltage, V, in Fig. 5.6 and Fig. 5.7. The model prediction capabilities are confirmed by the good accordance with experimental results with mean prediction error of 6.1% and 10.6% on rotation and torque respectively.

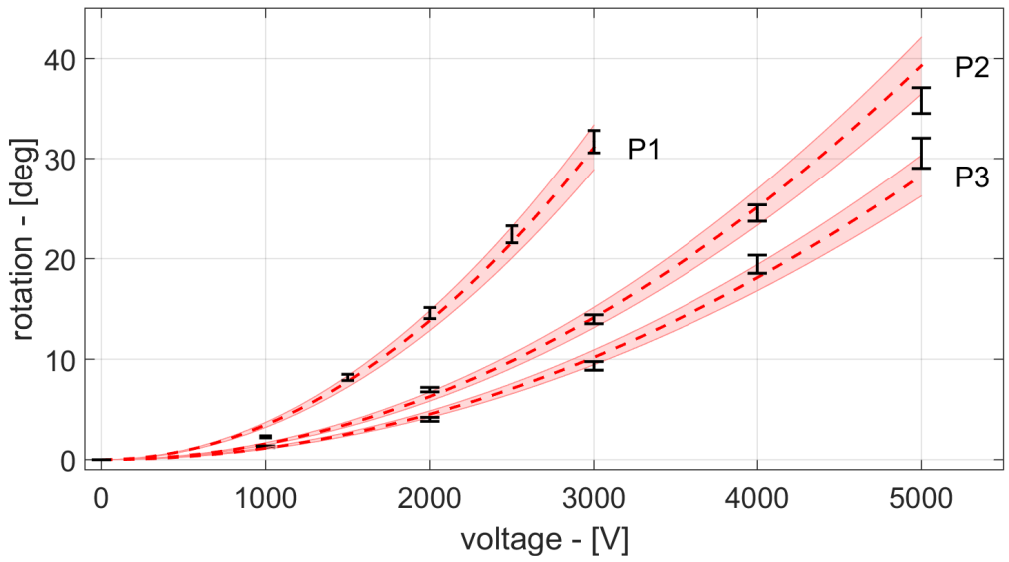

Fig. 5.6: Comparison between steady state rotation test results (black w/ error bars) and parametric model from Eq. 5.17 (red dashed w/ error band) for the three tested actuators (P1, P2 and P3)

Fig. 5.8 and Fig. 5.9 compares experimental results to validate model prediction. Stroke prediction is not as good as in other cases and, in general, the model overestimates the actuator stroke. In particular, tests on prototype #2 do not match with model output; a possible

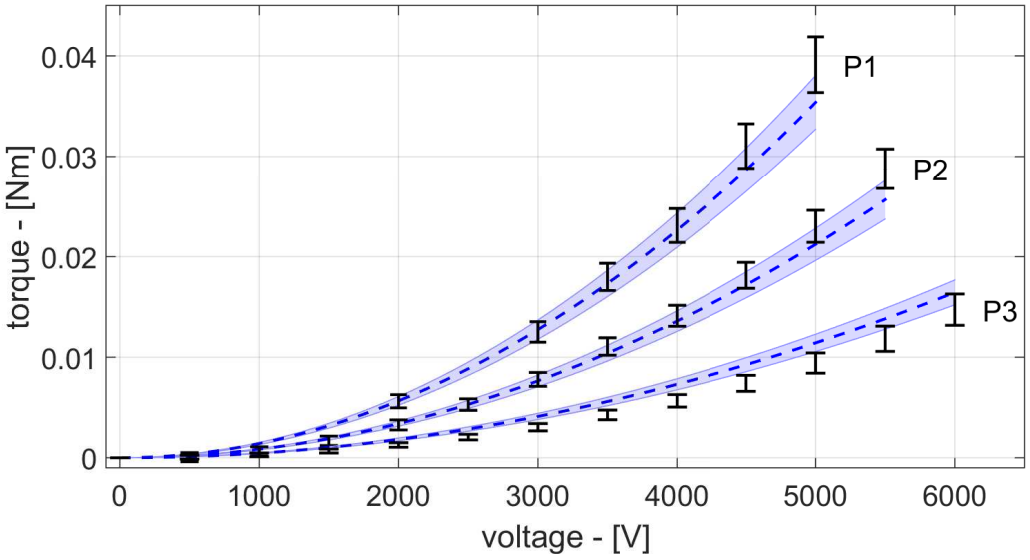

Fig. 5.7: Comparison between steady state torque test results (black w/ error bars) and parametric model from Eq. 5.17 (blue dashed w/ error band) for the three tested actuators (P1, P2 and P3)

reason for this inconsistency is that prototype #2 is flawed by some unrecognized manufacturing imperfection. All prototypes are hand manufactured and, therefore, they are likely to be affected by defects. The mean prediction error is 11.8% on force; error on translational stroke is 22.5% (considering only prototype #1 and #3).

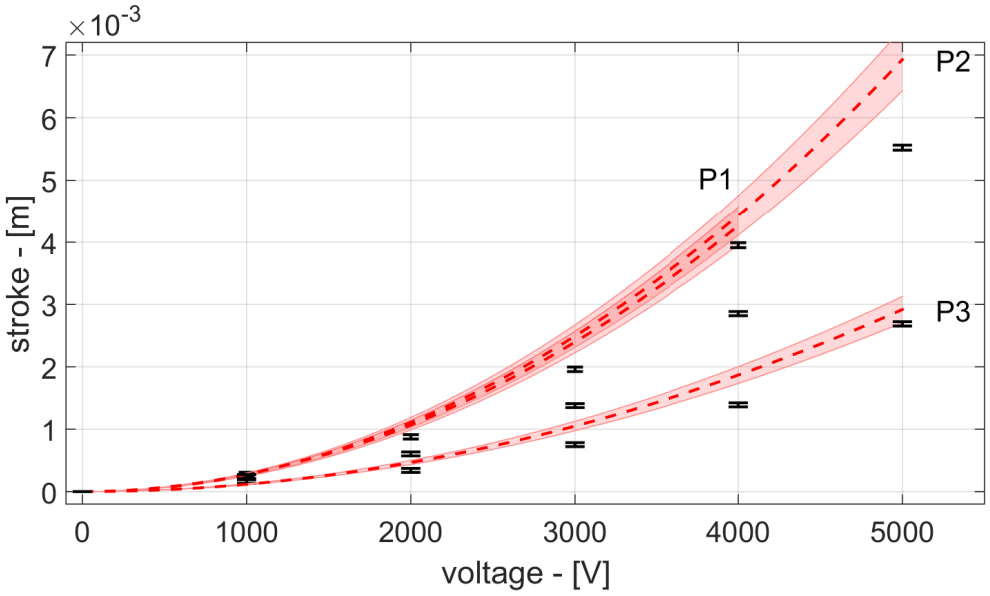

Fig. 5.8: Comparison between steady state stroke test results (black w/ error bars) and parametric model from Eq. 5.17 (red dashed w/ error band) for the three tested actuators (P1, P2 and P3)

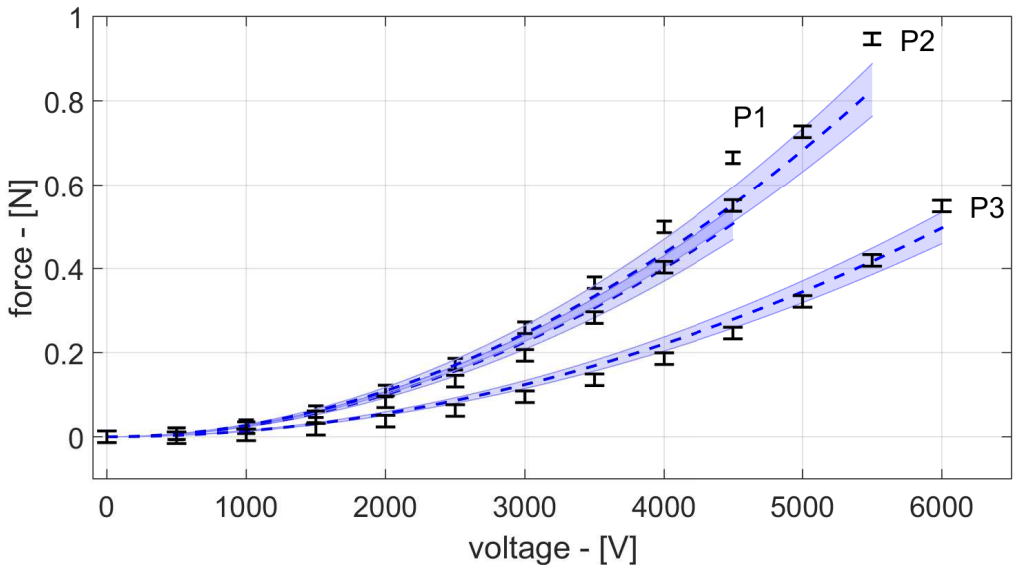

Fig. 5.9: Comparison between steady state force test results (black w/ error bars) and parametric model from Eq. 5.17 (blue dashed w/ error band) for the three tested actuators (P1, P2 and P3)

5.6 Transient behavior

The actuator is characterized by fairly slow dynamics in all degrees of freedom and this influences considerably the device time response. The most significant contribution to this behavior is due to the viscoelastic nature of dielectric elastomers. Other components are also present accounting for the electric performance of the power supply or the actuator, for the electromechanical conversion in the elastomer and for the inertial mechanics of the actuator. In particular, experimental evidence shows that an initial fast response is present in the timescale of one second, but the full steady state response is reached only after hundreds of seconds, due to slower dynamics components. Long time tests have been conducted and presented in Sec. 5.6.1. From the experimental results exponential and transfer function models are derived and proposed to predict the time behavior of the actuator.

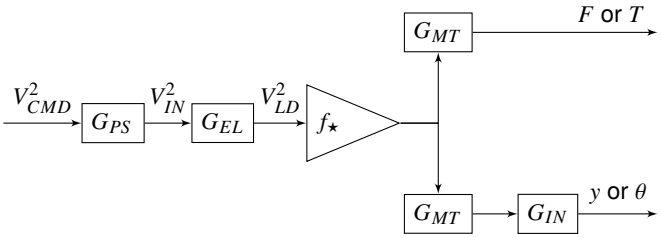

Fig. 5.10: Transfer function chain that describes all the different dynamic components of the actuator behavior providing the input/output relation, from the commanded squared voltage, V^2_{CMD}, to deformation, y or θ

Fig. 5.10 shows how all the different contributions to the actuator dynamics can be described as transfer functions (identified with G in this work) to be multiplied together. The voltage

command, V_{CMD}, is fed to the high voltage power supply that provides the input voltage, V_{IN}, to the actuator. The power supply used in the experimental set-up and mentioned in Sec. 5.5.1 has the experimentally determined second-order transfer function, $\frac{V_{IN}}{V_{CMD}}$, described in Eq. 5.36 with natural frequency $\omega_{PS} = 8.165$ rad/s and complex variable s. The actual transfer function, $G_{PS}(s)$, that comes into play in the actuator dynamics links the squared values of commanded and input voltage (see Fig. 5.10). Eq. 5.36 presents the best estimate of $G_{PS}(s)$ computed by interpolation of the squared value of measured voltage step signal.

$$\begin{aligned} \frac{V_{IN}}{V_{CMD}} &= \frac{1}{0.015s^2 + 0.25s + 1} \\ G_{PS} = \frac{V_{IN}^2}{V_{CMD}^2} &= \frac{0.00047s^2 - 0.0238s + 1}{0.0012s^3 + 0.0334s^2 + 0.3207s + 1} \end{aligned} \tag{5.36}$$

The electric behavior of the actuator is described by a planar capacitor transfer function in Eq. 5.37, which allows to calculate the actual load voltage, V_{LD}, from V_{IN}. The capacitor load time constant can be computed from resistance, R_{EL}, and capacitance, C_{EL}, of the electrodes and, assuming typical values for the considered geometries, the natural frequency is reasonably $\omega_n > 100$ rad/s. Once again, the actual transfer function $G_{EL}(s)$ links the squared voltages (as shown in Eq. 5.37). Consequently, for the purposes of this work, $G_{EL}(s) \approx 1$ given the much slower dynamics of the overall system.

$$\begin{aligned} \frac{V_{LD}}{V_{IN}} &= \frac{1}{1 + R_{EL}C_{EL}s} \approx 1 \\ G_{EL}(s) &= \frac{V_{LD}^2}{V_{IN}^2} \approx 1 \end{aligned} \tag{5.37}$$

The conversion from squared load voltage, V_{LD}^2, to electrostatic pressure, p_{EL}, has negligible time dependence; it derives from the conversion presented in Eq. 4.44. The electromechanical conversion from voltage to steady state performances is modeled here by a constant gain, $f_\star$, that matches amplitudes and units; in the different cases $f_\star$ equals the convenient steady state constant (f_θ, f_T, f_y and f_F).

Differently, the material deformation is strongly time dependent due to the intrinsic relaxation properties of elastomers. The related time function can be described by a sum of exponential terms with multiple time constants and can be transformed into a transfer function, $G_{MT}(s)$ (see Sec. 5.6.1). The influence of $G_{MT}(s)$ on the actuator performances depends on the amount of deformation that occurs in the different cases (i.e. blocked or free actuator). $G_{MT}(s)$ allows to calculate generalized forces, F and T, while, to compute generalized deformations, y or θ, the inertial properties of the actuator have to be considered with the $G_{IN}(s)$ transfer function. If an unloaded actuator is considered it is easy to compute a typical value of the inertial natural frequency with Eq. 5.38 for the considered geometries.

$$\omega_{IN} = \sqrt{\frac{K}{m}} > 25 \text{ rad/s} \tag{5.38}$$

where K and m are generalized rigidity and mass respectively (the values of K are estimated from FEM simulations). The natural frequency value is high compared to other dynamic components and for the characterization of the actuator it is possible to assume that $G_{IN}(s) \approx 1$. Note that $G_{IN}(s)$ is dependent on the inertial properties of the mechanical load connected to the actuator.

In summary, the complex time behavior of double-cone DE actuators can be described by the simplified diagram in Fig. 5.11 which accounts only for the significant transfer function terms (i.e. $G_{PS}(s)$ and $G_{MT}(s)$), since all the others are close or equal to one. The constant gain $f_\star$ is required to match amplitude and input/output units.

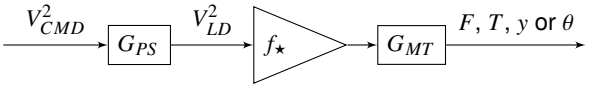

Fig. 5.11: Simplified transfer function chain of the system.

5.6.1 Test results

By interpolation of long duration tests (see Fig. 5.12 - 5.17) on the actuator performances, it is possible to estimate the device transfer functions. In particular, the material relaxation component of the dynamic response is a sum of exponential terms as shown in Eq. 5.39 that fits the obtained time response to step input, $g_{MT_\theta}(t)$. The time constants are comparable to material relaxation time constants available in literature [97].

$$g_{MT_\theta}(t) = \theta_{T=0} \cdot \Big[0.339\ (1-\mathrm{e}^{-\frac{t}{0.035}}) + 0.247\ (1-\mathrm{e}^{-\frac{t}{2.45}}) + 0.186\ (1-\mathrm{e}^{-\frac{t}{38.6}}) + 0.228\ (1-\mathrm{e}^{-\frac{t}{584.6}})\Big] \tag{5.39}$$

z-axis rotation dynamic behavior is modeled with $G_\theta(s)$ that is formed by the power supply contribution, $G_{PS}(s)$, and the material related component, $G_{MT_\theta}(s)$. The latter comes from the knowledge of $g_{MT_\theta}(t)$ and of the step input, through Laplace transform.

$$G_\theta(s) = f_\theta \cdot G_{PS}(s) \cdot G_{MT_\theta}(s) \quad \text{with} \quad f_\theta = \frac{\theta_{T=0}}{V^2_{CMD}}$$
$$G_{MT_\theta}(s) = \frac{43544s^3 + 15442s^2 + 429s + 1}{11046s^4 + 105247s^3 + 24909s^2 + 543s + 1} \tag{5.40}$$

Denote the 70% rise-time[1] with t_r. From comparison with test results, $G_\theta(s)$ (Eq. 5.40) is capable to predict the behavior of all prototypes at various voltages with a mean error on t_r of 15% and a maximum amplitude error below 4% of steady-state value for $t > t_r$ (see Fig. 5.12-5.13).

[1] The 70% rise time is defined as $t_r = \min\{t \geq 0 : |w_{-1}(t) - W(0)| \leq 0.3\,|W(0)|\}$.

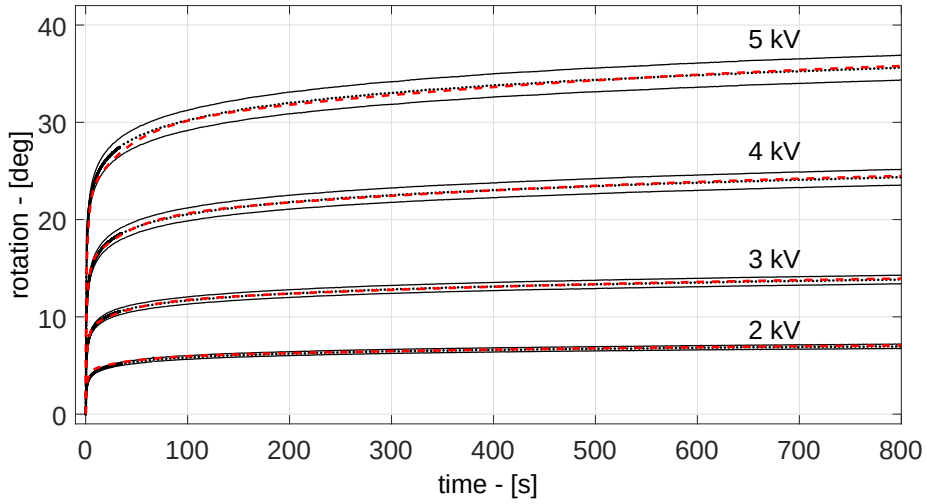

Fig. 5.12: Long duration tests of z-axis rotation for prototype 2 at different voltages; measured values (black dots) with estimated error bands (thin black lines) and estimated time response from $G_\theta(s)$ (red dashed lines)

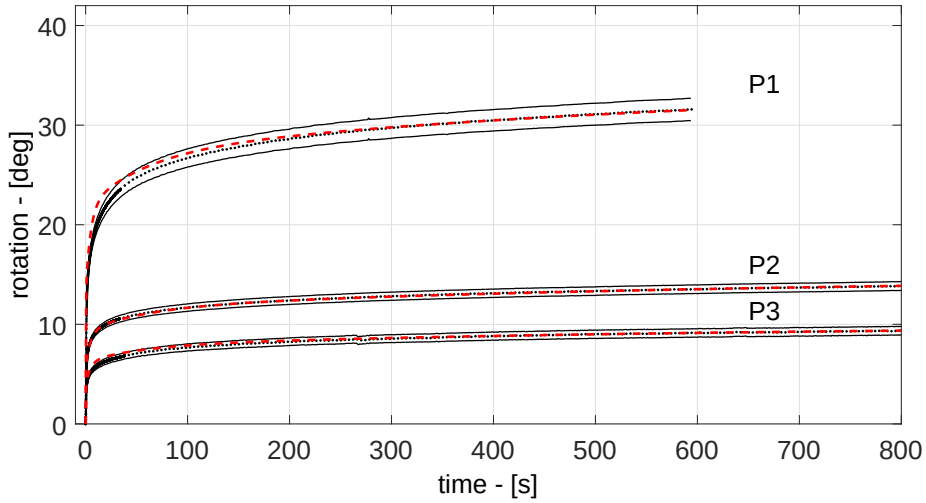

Fig. 5.13: Long duration tests of z-axis rotation at $3\ \mathrm{kV}$ applied voltage on all three prototypes (P1, P2 and P3); measured values (black dots) with estimated error bands (thin black lines) and estimated time response from $G_\theta(s)$ (red dashed lines)

Torque measurements are performed by blocking the actuator, thus leading to a much smaller material deformation. This gives a faster response of the actuator, with reduced relaxation. In this case the time response to step, $g_{MT_T}(t)$, becomes Eq. 5.41.

$$g_{MT_T}(t) = T_{\theta=0} \cdot \Big[\, 0.820\ (1 - \mathrm{e}^{-\frac{t}{0.01}}) + 0.113\ (1 - \mathrm{e}^{-\frac{t}{2.98}}) + 0.067\ (1 - \mathrm{e}^{-\frac{t}{43.78}}) \Big] \tag{5.41}$$

while $G_T(s)$ and $G_{MT_T}(s)$ are

$$G_T(s) = f_T \cdot G_{PS}(s) \cdot G_{MT_T}(s) \quad \text{with} \quad f_T = \frac{T_{\theta=0}}{V_{CMD}^2}$$
$$G_{MT_T}(s) = \frac{107.1s^2 + 43.48s + 1}{1.305s^3 + 130.9s^2 + 46.77s + 1} \tag{5.42}$$

$G_T(s)$ (Eq. 5.42) predicts the behaviour of prototypes with a mean error on t_r of 9.5% and a maximum amplitude error below 4% of steady-state value for $t > t_r$ (see Fig. 5.14-5.15).

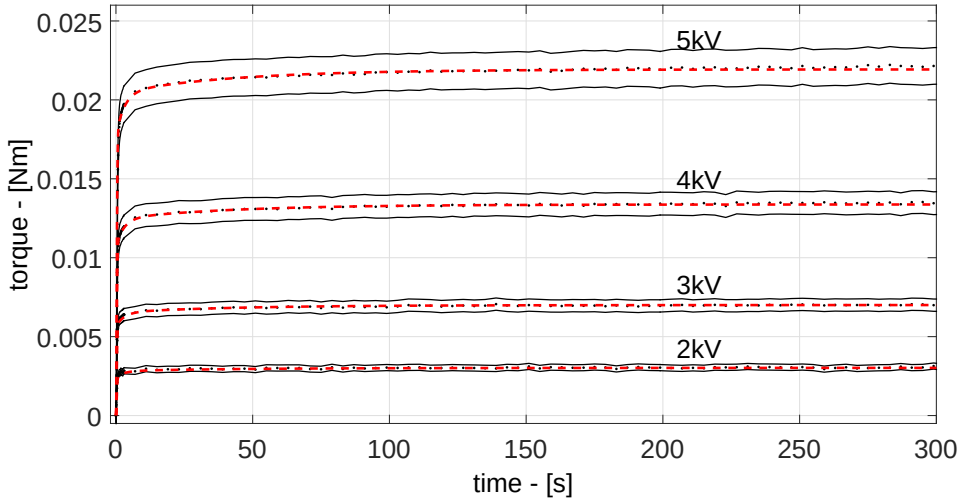

Fig. 5.14: Long duration tests of z-axis torque for prototype #2 at different voltages; measured values (black dots) with estimated error bands (thin black lines) and estimated time response $G_T(s)$ (red dashed lines).

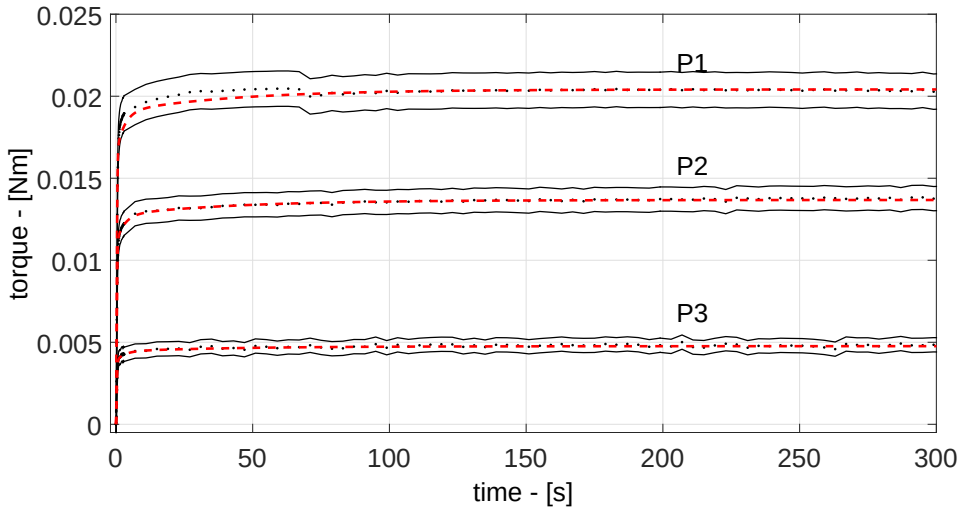

Fig. 5.15: Long duration tests of z-axis torque at $4\ \mathrm{kV}$ applied voltage on all three prototypes (P1, P2 and P3); measured values (black dots) with estimated error bands (thin black lines) and estimated time response from $G_T(s)$ (red dashed lines).

The material deformation in y-axis translation cases is less relevant than in z-axis rotation. The dynamic response is, in general, faster in y-axis cases. Eq. 5.43 is the time response to step

$$g_{MT_y}(t) = y_{F=0} \cdot \Big[\, 0.746\,(1-\mathrm{e}^{-\frac{t}{0.027}}) + 0.120\,(1-\mathrm{e}^{-\frac{t}{4.28}}) + 0.078\,(1-\mathrm{e}^{-\frac{t}{103.9}}) + 0.056\,(1-\mathrm{e}^{-\frac{t}{1864}}) \Big] \tag{5.43}$$

while $G_y(s)$ and $G_{MT_y}(s)$ are

$$G_y(s) = f_y \cdot G_{PS}(s) \cdot G_{MT_y}(s) \quad \text{with} \quad f_y = \frac{y_{F=0}}{V_{CMD}^2}$$
$$G_{MT_y}(s) = \frac{2922s^2 + 242s + 1}{904s^3 + 3586s^2 + 264s + 1} \tag{5.44}$$

$G_y(s)$ (Eq. 5.44) predicts the behavior of prototypes with a mean error on t_r of 14% and a maximum amplitude error below 9% of steady-state value for $t > t_r$ (see Fig. 5.16-5.17).

Force measurements are performed with blocked actuator and applying voltage to the whole surface of one membrane. The material is therefore in a hydrostatic pressure condition and deformation is negligible. For this reason, the actuator response is very close to the power supply response becoming $G_F(s) = f_F \cdot G_{PS}(s)$, with $f_F = \dfrac{F_{y=0}}{V_{CMD}^2}$. In Fig. 5.18-5.19 the time response to step input is shown: $G_F(s)$ predicts the behavior of prototypes with a mean error on t_r of 14% and a maximum amplitude error below 11% of steady-state value for $t > t_r$.

5.7 Frequency response

In Sec. 5.6 the slow actuator dynamics is discussed. In this section, the frequency behaviour of the actuator is presented by means of experimental results. In particular, the transfer functions proposed in Sec. 5.6.1 are used to predict the actuator response when excited at variable frequencies (from 50 mHz to 1 Hz). Sinusoidal waves for frequency response tests are generated with an Array Electronic 3400A functions generator.

Tests are executed on prototype #2 with sinusoidal load voltage oscillating between 0 and 4 kV at variable frequencies, namely 50 mHz, 100 mHz, 300 mHz, 500 mHz and 1 Hz. The amplitude of all outputs (i.e. rotation and translation, torque and force) is measured and related to the steady state values at 4 kV. The obtained values of normalized amplitude (i.e. the ratio between the steady state value and the value at given frequency) are presented in Fig. 5.20 - 5.23 in comparison to the curve of the transfer functions seen in Sec. 5.6.1. The first cut-off frequency is always below 0.8 Hz (~ 5 rad/s). In all cases good prediction is provided by the computed transfer functions.

Rotation presents a strong long term relaxation, consequently Fig. 5.20 shows a considerable attenuation at very low frequencies. The cut-off frequency is around 4 mHz (~ 0.024 rad/s), but the strongest attenuation is around 0.6 Hz (~ 4 rad/s).

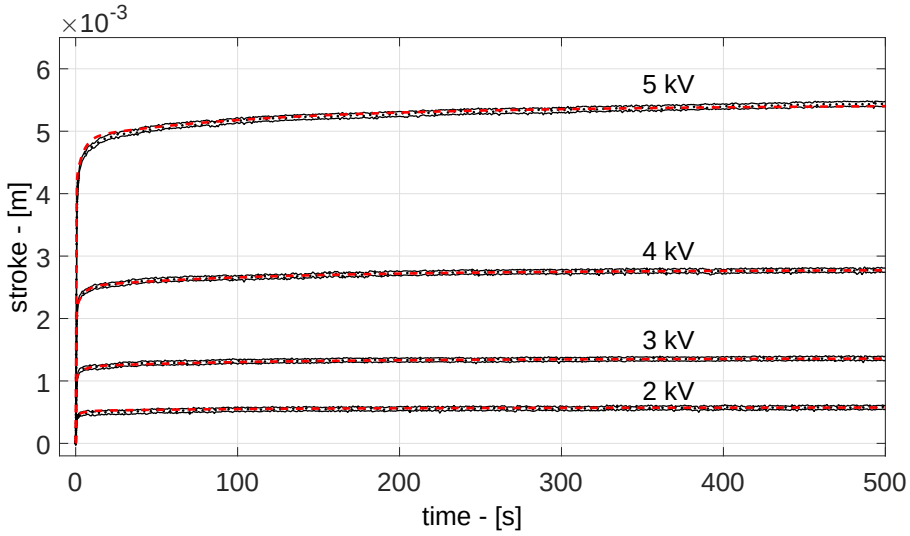

Fig. 5.16: Long duration tests of y-axis stroke for prototype #2 at different voltages; measured values (black dots) with estimated error bands (thin black lines) and estimated time response $G_y(s)$ (red dashed lines).

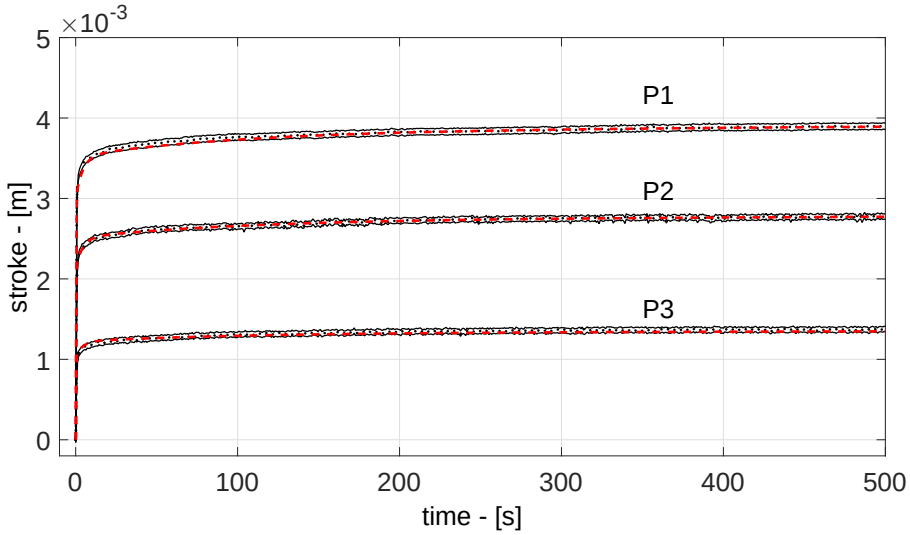

Fig. 5.17: Long duration tests of y-axis stroke at $4\ \mathrm{kV}$ applied voltage on all three prototypes (P1, P2 and P3); measured values (black dots) with estimated error bands (thin black lines) and estimated time response from $G_y(s)$ (red dashed lines).

Torque frequency response is less affected by material long term relaxation. The cut-off frequency is around $0.5\ \mathrm{Hz}$ ($\sim 3\ \mathrm{rad/s}$).

In y-axis translation the material deformation is less important, leading to a slightly faster response of the actuator. Translation response shows a cut-off frequency at $0.3\ \mathrm{Hz}$ ($\sim 1.8\ \mathrm{rad/s}$). Force response is almost unaffected by material deformation and relaxation, thus it is very close to the power supply response with $0.75\ \mathrm{Hz}$ ($\sim 4.7\ \mathrm{rad/s}$) cut-off frequency.

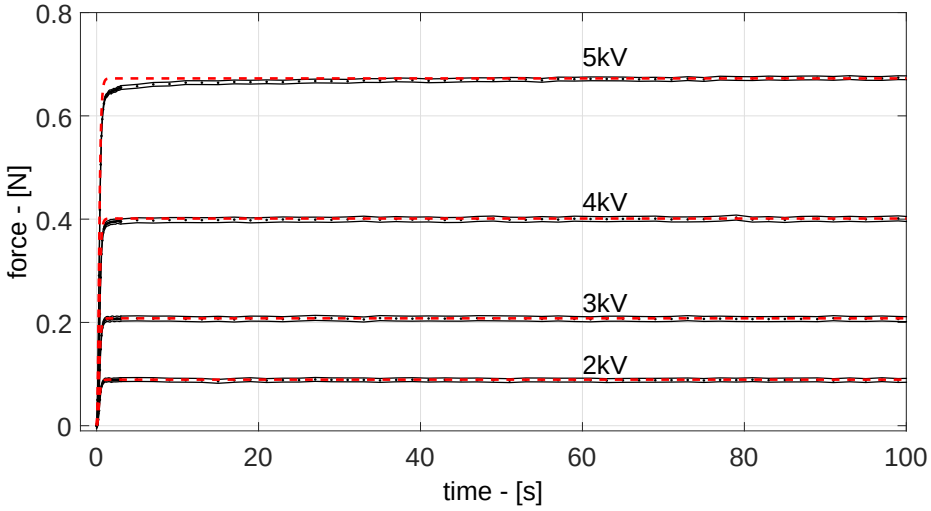

Fig. 5.18: Long duration tests of y-axis force for prototype #2 at different voltages; measured values (black dots) with estimated error bands (thin black lines) and estimated time response $G_F(s)$ (red dashed lines).

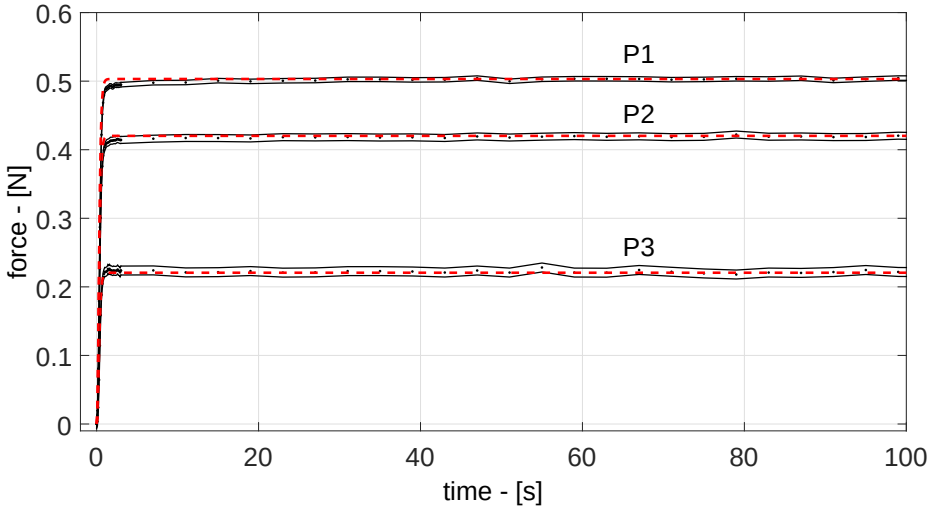

Fig. 5.19: Long duration tests of y-axis force at $4\ \mathrm{kV}$ applied voltage on all three prototypes (P1, P2 and P3); measured values (black dots) with estimated error bands (thin black lines) and estimated time response from $G_F(s)$ (red dashed lines).

5.8 Controlled motion

The dynamic model developed in Sec. 5.6 is in a form that can be easily exploited for control purposes. Single Input / Single Output (SISO) compensators have been designed to control the DoFs of the actuator (y and θ) one at a time. The objective is to improve the step response of the actuator for a given set-point by commanding a proper voltage to the power supply. The developed compensator calculate the control voltage on the basis of the error between the set-point and the measured control variable.

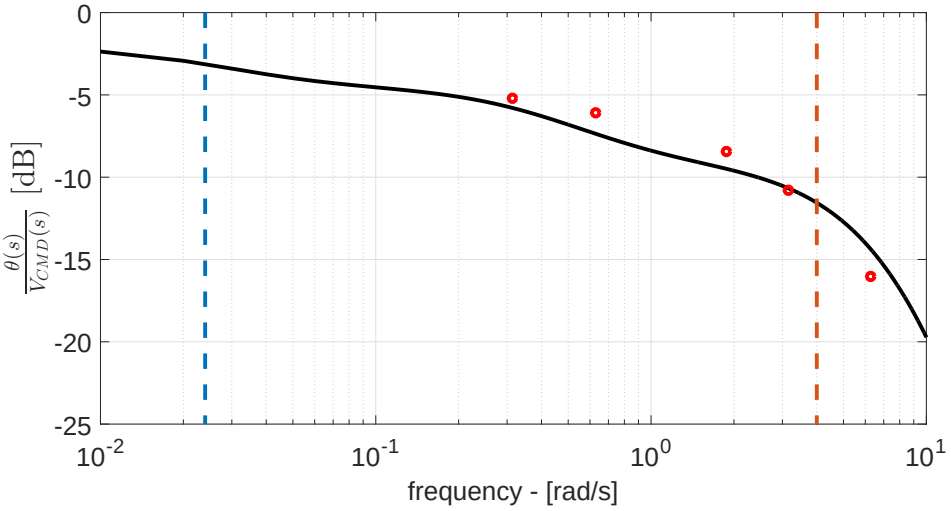

Fig. 5.20: Frequency response of the actuator in z-axis rotation. Measured response (red dots) and predicted with $G_\theta(s)$ (black line, Eq. 5.40); cut-off frequency at ~ 0.024 rad/s (blue dashed) strong attenuation at ~ 4 rad/s (red dashed).

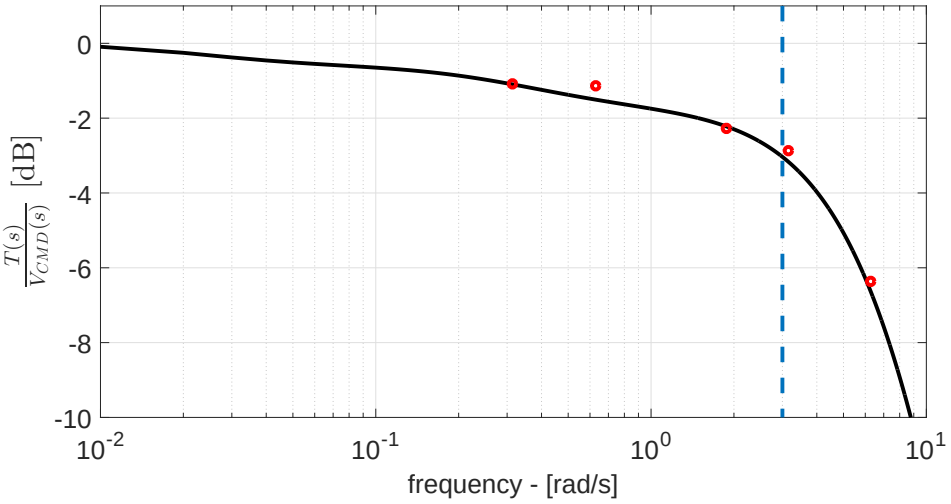

Fig. 5.21: Frequency response of the actuator in z-axis torque. Measured response (red dots) and predicted with $G_T(s)$ (black line, Eq. 5.42); cut-off frequency at ~ 3 rad/s (blue dashed)

5.8.1 Controller design

The controller design is based on the scheme presented in Fig. 5.11 with the following static and dynamic requirements:

- (static) steady-state error[2]: $e_{ss} = 0$
- (dynamic) 90% rise time[3]: $t_r^{(0.9)} = 4$ s

[2]For an arbitrary system $W(s) = \mathscr{L}[w(t)]$ (Laplace transform), the steady-state error is defined here as $e_{ss} = \lim_{t\to+\infty}[\delta_{-1}(t) - w_{-1}(t)]$, where $\delta_{-1}(t)$ is a step input and $w_{-1}(t)$ is the system time response to the step input.

[3]The 90% rise time is defined as $t_r = \min\{t \geq 0 : |w_{-1}(t) - W(0)| \leq 0.1\,|W(0)|\}$.

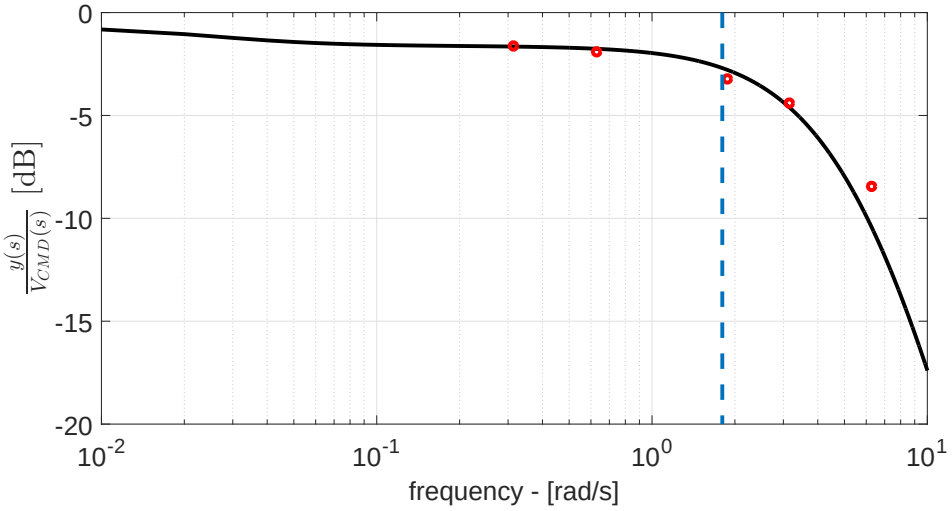

Fig. 5.22: Frequency response of the actuator in y-axis translation. Measured response (red dots) and predicted with $G_y(s)$ (black line, Eq. 5.44); cut-off frequency at ~ 1.8 rad/s (blue dashed).

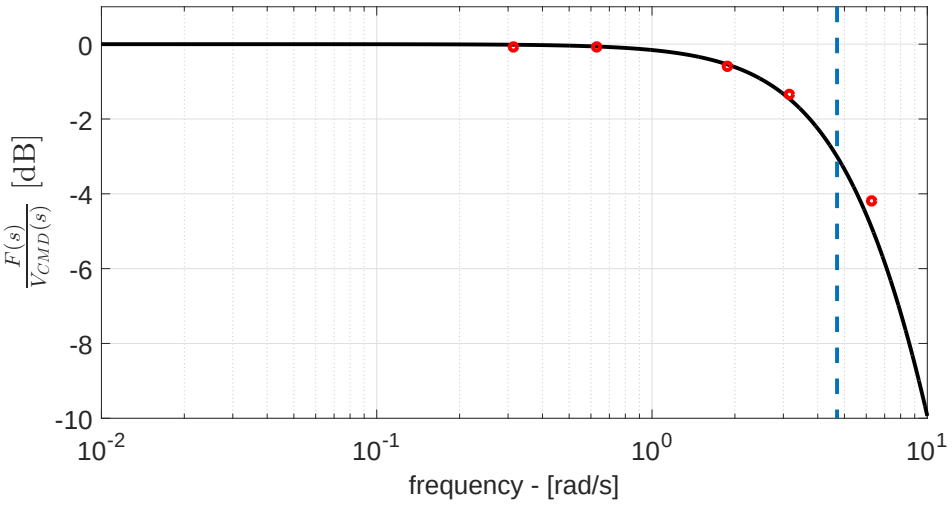

Fig. 5.23: Frequency response of the actuator in y-axis force. Measured response (red dots) and predicted with $G_F(s)$ (black line); cut-off frequency at ~ 4.7 rad/s (blue dashed).

- (dynamic) limited overshoot[4]: $s_o < 10\%$

The transfer function of the compensator to be designed is $C(s)$ and appears in the closed loop transfer function block diagram of the controlled actuator shown in Fig. 5.24. For a desired set point of the control variable, either y_r or θ_r, the controller computes the voltage command, V_{CMD}, to the power supply, which applies the voltage load, V_{LD}, to the actuator. The actual control variable is measured by a vision system and fed back to the controller. From Fig. 5.24 the closed loop transfer function of the system, $W_\star(s)$ (where $\star$ denotes either y or θ), is determined

$$W_\star(s) = \frac{C_\star(s)G_{PS}(s)G_{MT_\star}(s)}{1 + C_\star(s)G_{PS}(s)G_{MT_\star}(s)} \tag{5.45}$$

[4]The percentage overshoot is defined as: $s_o = \left(\sup_{t>0} \frac{w_{-1}(t) - W(0)}{W(0)}\right) \cdot 100$

which is valid for both y and θ. It is useful to define the open-loop transfer function of the system as $\tilde{G}_\star(s) = C_\star(s)G_{PS}(s)G_{MT_\star}(s)$, leading to

$$W_\star(s) = \frac{\tilde{G}_\star(s)}{1+\tilde{G}_\star(s)} \tag{5.46}$$

The mentioned design requirements are defined for the closed-loop system. The rise time is related to the closed loop system 3-dB passband[5], B_p, as follows

$$B_p \approx \frac{\ln 10}{t_r^{(0.9)}} \tag{5.47}$$

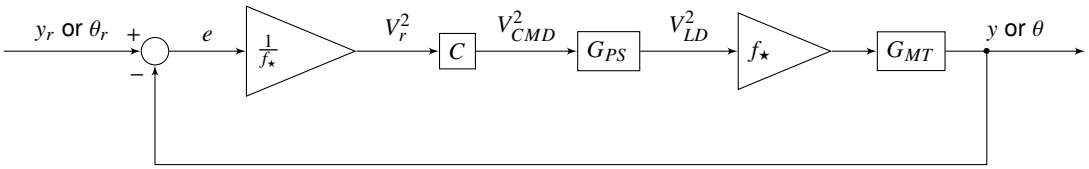

Fig. 5.24: Closed loop block diagram of controlled actuator

It is useful to adapt the dynamic requirements to the open loop transfer function:

- the cut-off frequency[6], ω_A, of the open-loop system is approximately equal to the pass-band of the closed-loop system: $\omega_A \approx B_p \approx \frac{\ln 10}{t_r^{(0.9)}}$
- limited overshoot and good stability can be achieved if the phase margin[7], m_ψ, of the open-loop transfer function is large enough: $m_\psi \geq 60$ deg

In addition, the steady-state error goes to zero if the open-loop transfer function, $\tilde{G}(s)$, has a pole in zero like when an integral term in the control scheme is adopted. The compensators are designed by trial and error obtaining the following purely Integral (I) control schemes for both y and θ

$$\begin{aligned} C_y &= \frac{0.6871}{s} \\ C_\theta &= \frac{1.266}{s} \end{aligned} \tag{5.48}$$

Fig. 5.25-5.26 show that the time responses to step input of the closed-loop system satisfy the requirements.

5.8.2 Test apparatus

An actuator with the following design parameters is tested (refer to Sec. 4.5): $d = 80$ mm, $D = 14$ mm, $a = 23$ mm, $c = 25$ mm, $t = 1$ mm, $n = 1$, $\delta_{re} = 2\%$ and $\lambda_0 = 3.5$.

[5] The 3-dB passband is defined as (ω denotes frequency in rad/s):
$B_p = \max\{\hat{\omega} > 0 : \forall\omega \in [0,\hat{\omega}]\ |W(j\omega)|_{dB} \geq |W(0)|_{dB} - 3\text{ dB}\}$.

[6] The cut-off frequency of $\tilde{G}(s)$ is defined as $\omega_A : \tilde{G}(\omega_A) = 0$ dB

[7] The phase margin of $\tilde{G}(s)$ is defined as $m_\psi = 180\,\text{deg} + \arg(\tilde{G}(\omega_A))$

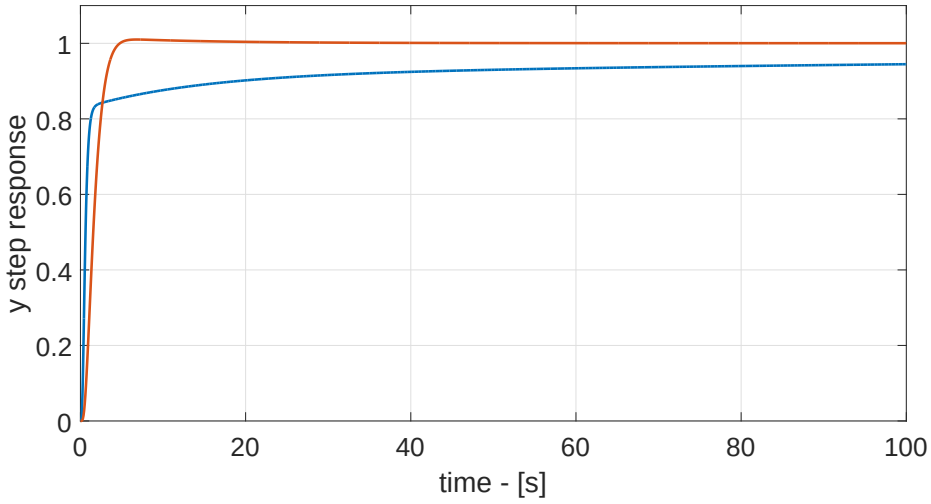

Fig. 5.25: Time response to unitary step input for linear stroke y: uncontrolled (blue) and controlled actuator (orange)

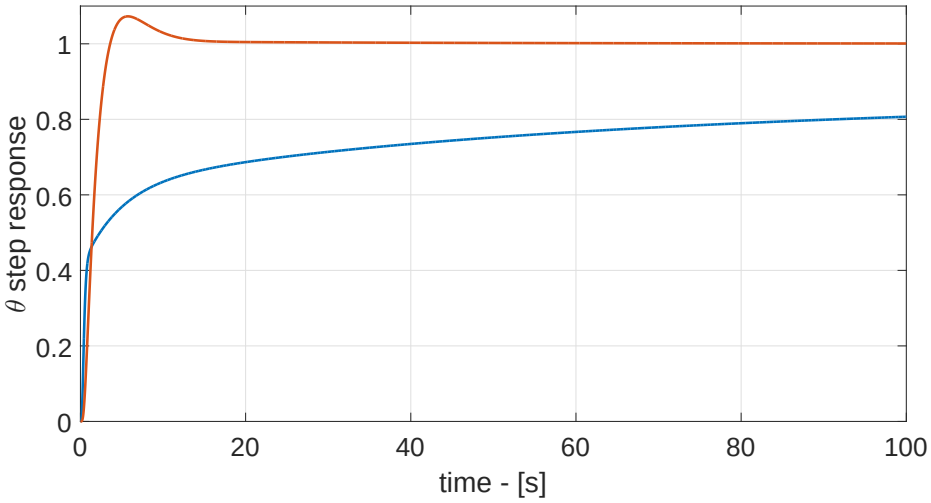

Fig. 5.26: Time response to unitary step input for rotation θ: uncontrolled (blue) and controlled actuator (orange)

The DEAs power supply is composed by a set of HV converters (EMCO^{TM} C50) powered by an AC/DC power supply (TRACOPOWER^{TM} TXM 035-112) and programmed via PC through a USB analog output board (Measurement Computing^{TM} USB-3112). Two HV channels are required to actuate one DoF (four electrodes, one channel for each couple of electrodes). Also in this case, the $G_{PS}(s)$ transfer function is estimated from measured step response of voltage signal resulting in:

$$G_{PS}(s) = \frac{V_{IN}^2}{V_{CMD}^2} \approx \frac{1}{0.063s+1} \tag{5.49}$$

A vision system based on a HD webcam (Logitech^{TM} C310) measures the position of two optical markers located on the tip of the central shaft. Again, when the y stroke is measured,

the camera points at the xy plane of the actuator (i.e. z-axis is perpendicular to the camera plane); when the z rotation (θ) is measured, the camera points at the xz plane (i.e. y-axis is perpendicular to the camera plane). A custom designed MATLAB® code acquires the RGB image of the optical markers (two red squares at a fixed distance, see Fig. 5.27), extracts the red channel and performs some image manipulation in order to identify the centers of the markers. The system takes a measure of the relative position (displacement), p, of the shaft tip. Once the position in pixels of the two red squares is known, the pixel measure of their distance is used to determine the pixel-to-mm ratio and to estimate the displacement of the shaft tip from its initial position. The measure is taken at a fixed frame rate that can be set to 5 fps or 10 fps ($5-10$ Hz sampling frequency). The shaft tip displacement information is than converted to the measured variable, $\breve{y}$ or $\breve{\theta}$, with the following equations (subscripts u and v denote the horizontal and vertical dimensions in the image reference frame):

$$\begin{aligned} p_u &= \frac{n_{1_u} + n_{2_u} - 2n_{0_u}}{2} \frac{d_{ref}}{d_{pix}} \\ p_v &= \frac{n_{1_v} + n_{2_v} - 2n_{0_v}}{2} \frac{d_{ref}}{d_{pix}} \\ \breve{y} &= \operatorname{sgn}(p_u) \sqrt{p_u^2 + p_v^2} \\ \breve{\theta} &= \operatorname{sgn}(p_u) \arcsin\left(\frac{\sqrt{p_u^2 + p_v^2}}{b_m} \right) \end{aligned} \tag{5.50}$$

where n_{i_j} are the pixel position of marker #1 or #2 ($i = 1,2$) in the u or v direction ($j = u,v$), $d_{ref} = 10$ mm is the reference distance between the markers in millimeters, $b_m = 42$ mm is the distance of the optical markers from the actuator center of rotation, $\operatorname{sgn}(p_j)$ returns the sign of p_j (the camera is oriented in a way that gives positive p_u for positive stroke or rotation), d_{pix} is the measured distance between markers in pixels, n_{0_j} is the initial average x or y position of the markers

$$\begin{aligned} d_{pix} &= \sqrt{(n_{1_u} - n_{2_u})^2 + (n_{1_v} - n_{2_v})^2} \\ n_{0_j} &= \left. \frac{n_{1_j} + n_{2_j}}{2} \right|_{t=0} \end{aligned} \tag{5.51}$$

The main steps of the image analysis and measurement process are the following:

1. acquire RGB image
2. convert to gray-scale image
3. subtract red channel from gray-scale image (red regions become bright, other regions become dark)
4. convert to binary image via threshold (regions with value above the threshold become white, other become black)
5. delete white regions if too small
6. determine centroid, area, solidity and bounding box of the remaining white regions

7. identify the markers among other areas on the basis of size, solidity and similarity to square shape
8. compute the position in millimeters of the central point between the markers by averaging the position of their centroids
9. compute the value of the control variable ($\check{y}$ of $\check{\theta}$)
10. return to step 1

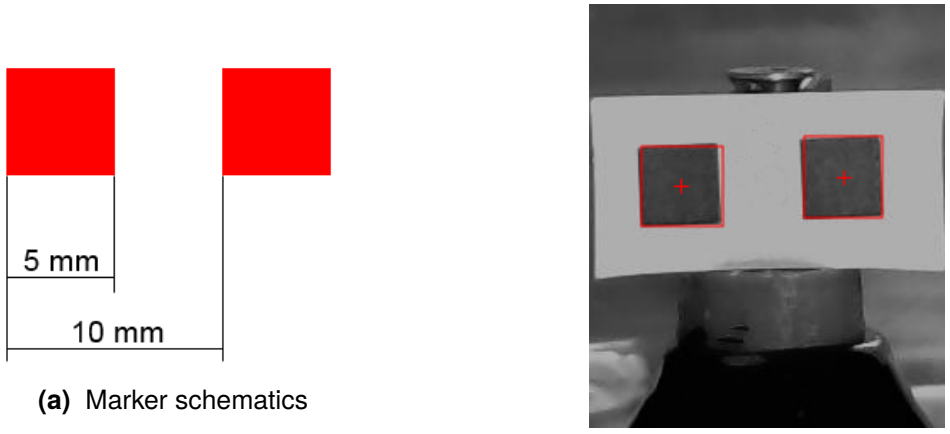

(a) Marker schematics

(b) Video frame with marker recognition

Fig. 5.27: Optical marker applied to the manipulator end-effector: the calibration distance between the centers of the red squares is 10 mm

The uncertainty analysis of the measurement system is performed from Eq. 5.50. The uncertainty sources and their distribution are listed here:

- u_n [pix] is the uncertainty on the pixel position of the marker centroids: it depends on the vision algorithm used to detect the marker position and is estimated statistically by acquiring a large number of static measures (600) of the shaft tip position; the distribution is normal with standard deviation $\sigma_{n_j} = 0.1$ pix on both horizontal and vertical direction;
- u_d [mm] is the uncertainty on the measure of the reference distance d_{ref}; the distribution is uniform with total interval width $w_d = 0.1$ mm and standard deviation $\sigma_d = \frac{w_d}{\sqrt{12}} = 0.029$ mm;
- u_b [mm] is the uncertainty on the measure of the rotation arm length b_m; the distribution is uniform with total interval width $w_b = 2$ mm and standard deviation $\sigma_b = \frac{w_b}{\sqrt{12}} = 0.58$ mm.

Uncertainty sources are combined with a Monte Carlo approach. A large number (3000) of values of a reference measurement, $\check{y}^\star$ or $\check{\theta}^\star$, are computed by inserting in Eq. 5.50 random values, $u^\star_{n_i}$, $u^\star_d$ and $u^\star_b$, of uncertainty picked from their probability distributions.

$$
\begin{aligned}
n^\star_{1_j} &= n_{1_j} + u^\star_{n_1} \\
n^\star_{2_j} &= n_{2_j} + u^\star_{n_2} \\
d^\star_{ref} &= d_{ref} + u^\star_d \\
b^\star_m &= b_m + u^\star_b \\
d^\star_{pix} &= \sqrt{(n^\star_{1_x} - n^\star_{2_x})^2 + (n^\star_{1_y} - n^\star_{2_y})^2} \\
p^\star_u &= \frac{n^\star_{1_u} + n^\star_{2_u} - 2n_{0_u}}{2} \frac{d^\star_{ref}}{d^\star_{pix}} \\
p^\star_v &= \frac{n^\star_{1_v} + n^\star_{2_v} - 2n_{0_v}}{2} \frac{d^\star_{ref}}{d^\star_{pix}} \\
\check{y}^\star &= \operatorname{sgn}(p^\star_u) \sqrt{p^{\star 2}_u + p^{\star 2}_v} \\
\check{\theta}^\star &= \operatorname{sgn}(p^\star_u) \arcsin\left(\frac{\sqrt{p^{\star 2}_u + p^{\star 2}_v}}{b^\star_m} \right)
\end{aligned}
\tag{5.52}
$$

If the number of values of $\check{y}^\star$ or $\check{\theta}^\star$ is large enough, they will have statistical distributions around the real value. The standard deviation, σ_y and σ_θ, of such distributions can be used to compute the uncertainty of the whole measure, u_y and u_θ, for example with $u_y = 2\sigma_y$ and $u_\theta = 2\sigma_\theta$. The standard deviation for test results presented in the following section (Sec. 5.8.3) is not constant and depends on the value of the measured variable:

$$
\begin{aligned}
\sigma_y &= \max \begin{cases} 6.2 \times 10^{-6} \text{ m} \\ 2.6 \times 10^{-3} \check{y} + 3.6 \times 10^{-6} \text{ m} \end{cases} \\
\sigma_\theta &= \max \begin{cases} 1.2 \times 10^{-2} \text{ deg} \\ 1.5 \times 10^{-2} \check{\theta} \text{ deg} \end{cases}
\end{aligned}
\tag{5.53}
$$

5.8.3 Test results

Fig. 5.28 and Fig. 5.29 show the results from controlled motion experiments for the mentioned double cone actuator. The results in terms of control variables are compared to the simulated behavior shown in Fig. 5.25 and Fig. 5.26. The results are presented in normalized form w.r.t. the step value imposed as a set point, which is 3 mm for stroke tests and 10 deg for rotation tests. The results show that the dynamic model described in Sec. 5.6 is accurate and allows to implement traditional control techniques on DE double-cone actuators, considerably improving their performances. In particular, the rotation test (Fig. 5.26) resulted in a better accordance to the simulated model compared to the stroke test (Fig. 5.25). This is due to

the better prediction capabilities of the model (Eq. 5.19) on steady-state values of $\theta_{T=0}$ than $y_{F=0}$. The model generally overestimates the actuator stroke (see Fig. 5.9), resulting in a delayed motion of the controlled actuator; in other words, the overestimation of steady-state deformations has the same effect as a positive gain smaller than one.

Voltages supplied during tests are shown in Fig. 5.30 and Fig. 5.31. In order to achieve a faster actuator dynamics, higher values of command voltages are required, possibly leading to temporary saturation of the power supply when larger values of the control variable, y or θ are desired. If saturation occurs, the actuation computed by the control system cannot be achieved, thus leading to degraded performances. Fig. 5.32 is an example of saturated motion during rotation tests with a set point of $15\ \mathrm{deg}$: the motion (rotation) of the actuator is shown and appears to be significantly slower compared the data reported in Fig. 5.29. Fig. 5.33 shows the saturated supply voltages.

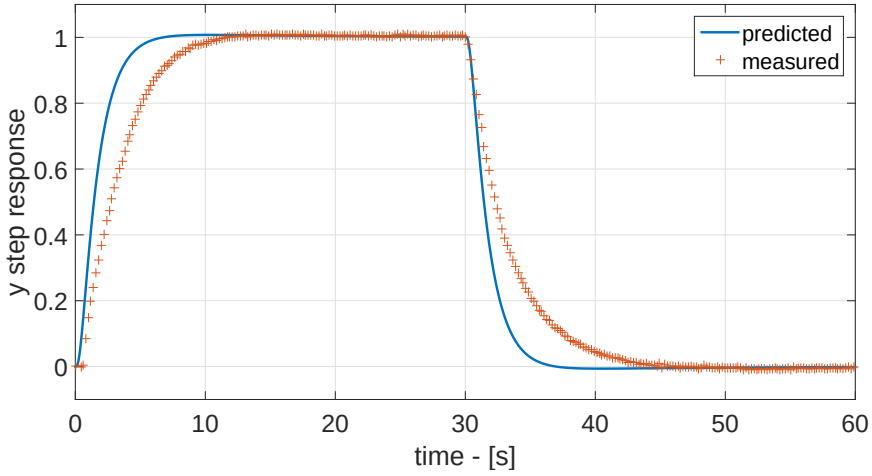

Fig. 5.28: Normalized experimental response to step input for linear stroke y: predicted (blue) and measured (orange crosses)

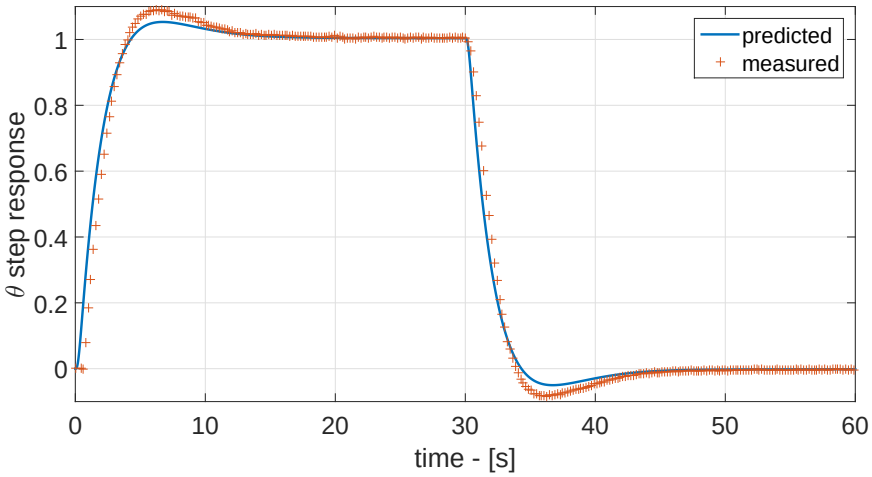

Fig. 5.29: Normalized experimental response to step input for rotation θ: predicted (blue) and measured (orange crosses)

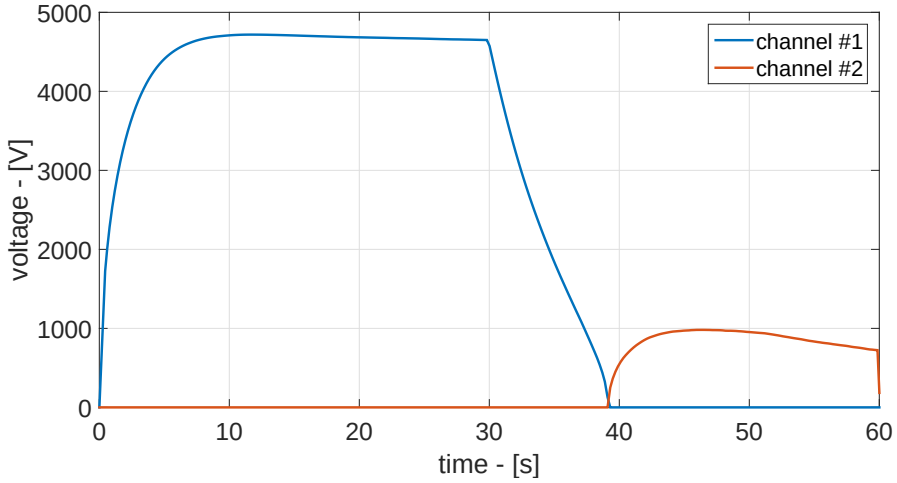

Fig. 5.30: Voltage supplied in controlled stroke y test: channel #1 (blue) and channel #2 (orange)

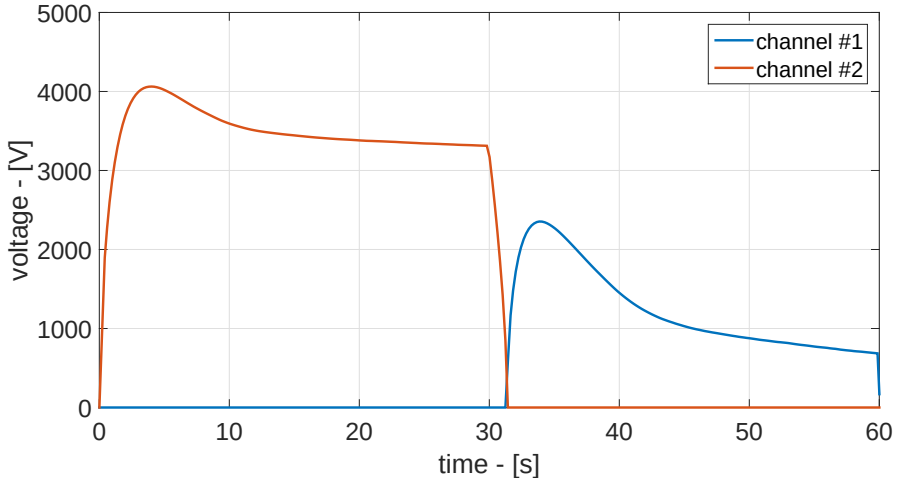

Fig. 5.31: Voltage supplied in controlled rotation θ test: channel #1 (blue) and channel #2 (orange)

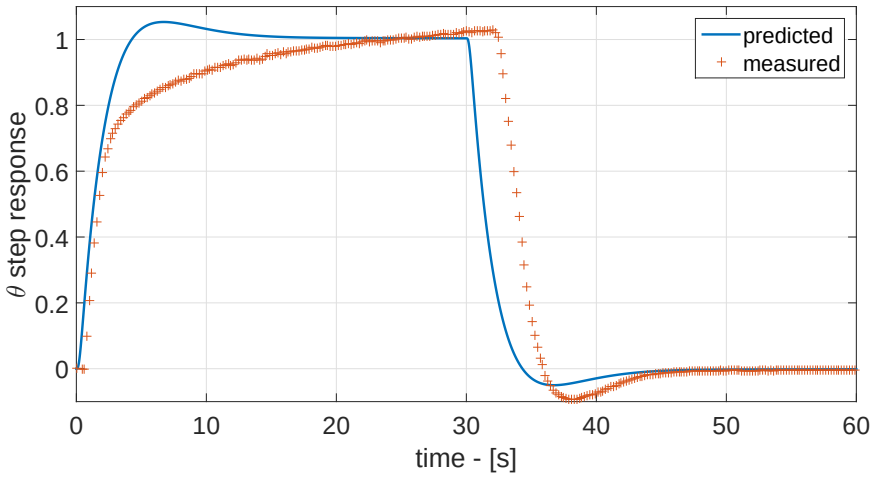

Fig. 5.32: Saturated (normalized) response to step input for rotation θ: predicted (blue) and measured (orange crosses)

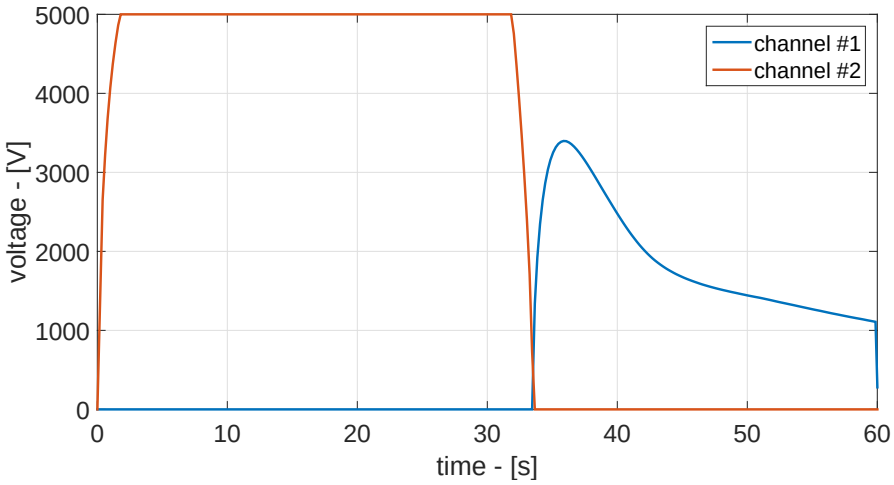

Fig. 5.33: Saturated voltage output in controlled rotation θ test: channel #1 (blue) and channel #2 (orange)

DE robotic manipulator

6

In this chapter the design, simulation and testing of a simple robotic application of double-cone DEAs are described. The objective is the preliminary validation of DE robotic systems, aiming to propose them for space implementation. A 4-DoF manipulator prototype is conceived, designed, simulated and tested.

The considered actuators are double-cone actuators, with two DoFs each: one translational and one rotational. For robot design purposes, each device is kinematically modeled as two joints, one for each DoF; the first joint is prismatic (translational DoF), the second is rotoidal (rotational DoF). Between the two joints a fictitious link is considered, with no mass and null dimensions. This is a technical mean that allows to use the classical approach to multi-body mechanics commonly adopted for robotic systems. In other words, the double motion provided by each actuator is here seen as the sum of the action of two different actuators, one in series to the other and with the same center of mass. From experimental evidence on a single actuator, it appears somehow more accurate to consider the translational motion as first, while the rotational motion as second. This method introduces some approximation, since the actual motion of double-cone DEAs is not a simple linear combination of the translational and rotational motion; nevertheless, the introduced approximation appears to be reasonable.

Generated force and torque are arguably the biggest limit of DEAs. For this reason, orbital applications are appealing for the reduced external loads acting on mechanisms. As a matter of fact, the zero-gravity environment eliminates the robot weight forces which cannot be sustained by most DE systems, including double-cone actuators. The prototype proposed here aims at simulating the behavior of a simple DE robotic system in low-gravity condition: the system is free to move only in the horizontal plane to avoid working against gravity and weight is compensated by a suspension system.

6.1 Manipulator configuration

The proposed manipulator is composed by two double-cone DEAs with two DoFs each (see Fig. 6.1). The actuators are mounted in series and connected through the central shafts. The system moves in the horizontal plane, also called motion plane. The rotational DoF axes are perpendicular to the motion plane, while the translational DoFs move horizontally. The ring support structure of the first joint is connected rigidly to the laboratory bench; a rigid beam connects the shafts of the actuators into a single element; the ring frame of the second actuator holds a light-weight structure that acts as the end-effector. The described robotic arm configuration is an open chain manipulator.

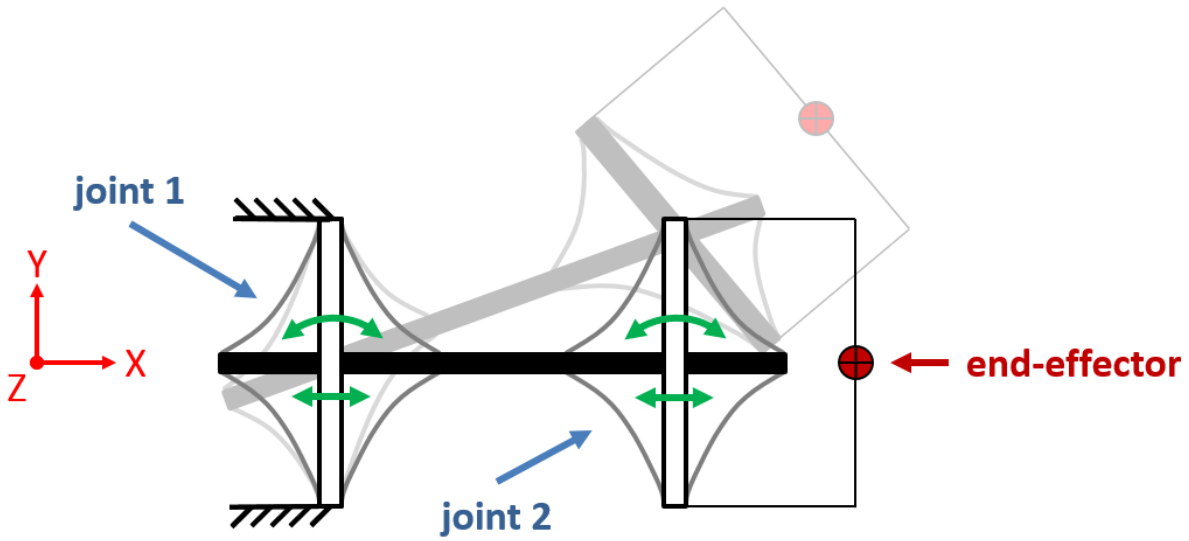

Fig. 6.1: Schematic drawing of the prototype manipulator: world reference frame (red), joints (blue), joint variables (green),degrees of freedom (green), end-effector (red)

Fig. 6.2 is the kinematic scheme of the manipulator prototype. An orthonormal reference frame is defined for each manipulator link (including the fictitious links) and the world (fixed reference frame). Each reference frame is denoted by O_i where $i = 0, 1, \ldots, n$ (where n is the number of joint variables) and is composed by a set of three orthonormal axes described by the unit vectors $\hat{e}_{i_x}$, $\hat{e}_{i_y}$, $\hat{e}_{i_z}$. In order to compute the kinematics of the system, a special convention is adopted for reference frame definition:

- the origin of frame i is located at joint $i+1$, where L_i is coupled with L_{i+1};
- the z-axis of each frame is perpendicular to the motion plane;
- the xX-axis of i-th frame passes through frame $i-1$.

Fig. 6.2 shows a kinematic scheme of the manipulator with the notable elements: the world reference frame (red), the joint reference frames (blue), joint variables (d_1, θ_2, d_3, θ_4), the link numbers ($L_{1,\ldots,4}$) and geometric parameters (b_1, b_2). The world reference frame, O_0, is inertial and fixed; the origin is located at the center of the first joint before actuation. The first reference frame, O_1, is originally coincident with O_0, but translates with L_1 along the first joint variable, d_1 (translational), which is parallel to $\hat{e}_{1_x}$; L_1 is a fictitious link. The second reference frame, O_2, rotates with L_2 around $\hat{e}_{1_z}$ of an angle equal to the second joint variable, θ_2 (rotational), and is located at a constant distance, b_1, form O_1; L_2 has a cylindrical shape with the axis parallel to $\hat{e}_{2_x}$. The third reference frame, O_3, is originally coincident with O_2, but translates with L_3 along the third joint variable, d_3 (translational), which is parallel to $\hat{e}_{3_x}$; L_3 is a fictitious link. The fourth reference frame, O_4, is coincident with the end-effector; rotates with L_4 around $\hat{e}_{3_z}$ of an angle equal to the fourth joint variable, θ_4 (rotational), and is located at a constant distance, b_2, form O_3; L_4 has a ring shape with the axis parallel to $\hat{e}_{4_x}$.

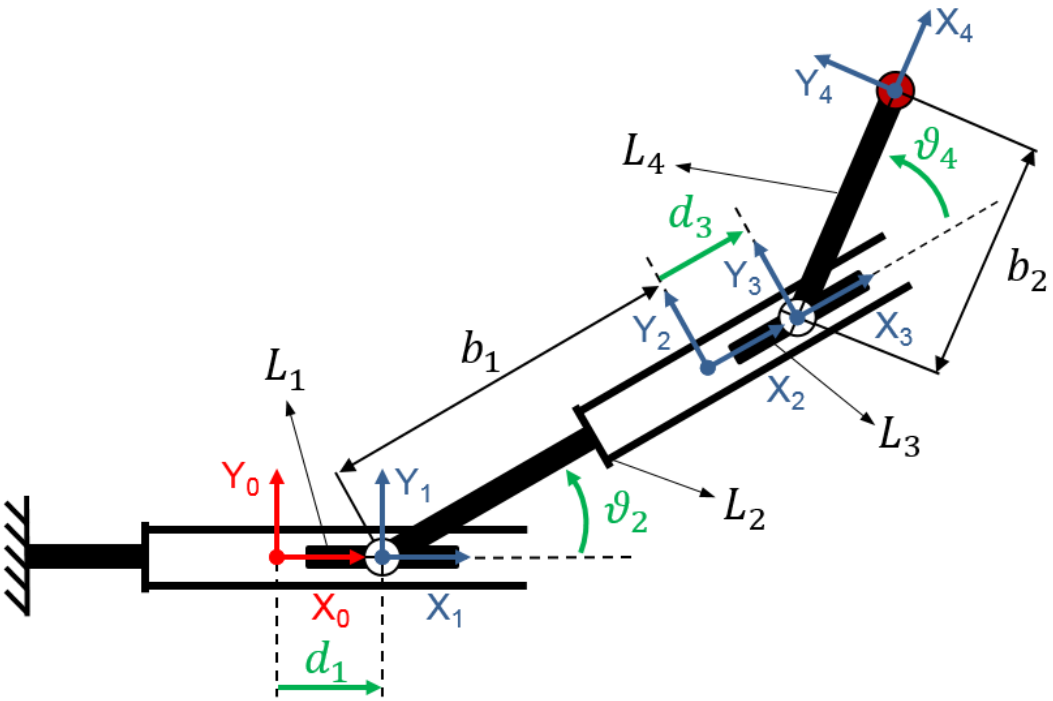

Fig. 6.2: Kinematic scheme of the manipulator: world reference frame (red), joint reference frames (blue), joint variables (green), link numbers and geometric parameters (black)

6.2 Kinematics

Direct kinematic is a relation that expresses the pose (position and orientation) of the end-effector (i.e. of the O_4 reference frame) as a function of the joint variables $\vec{q} = \{d_1\ \theta_2\ d_3\ \theta_4\}^{\mathrm{T}}$. The joint variables uniquely determine the posture of the manipulator (i.e. the pose of each link in the chain). Direct kinematics allows to compute the pose of the end-effector for a given set of joint variables; it is expressed by the homogeneous roto-translation matrix $\mathbf{T}_4^0(\vec{q})$ from the world reference frame, O_0, to the end-effector reference frame, O_4

$$\mathbf{T}_4^0(\vec{q}) = \begin{bmatrix} \hat{e}_{4_x}^0 & \hat{e}_{4_y}^0 & \hat{e}_{4_z}^0 & \vec{p}_4^{\,0} \\ 0 & 0 & 0 & 1 \end{bmatrix} \tag{6.1}$$

where $\hat{e}_{4_j}^0$ are the unit vectors of O_4 expressed in O_0 and $\vec{p}_4^{\,0}$ is the position vector of the origin of O_4 expressed in O_0. The matrix $\mathbf{T}_4^0$ is obtained recursively from systematic products between the homogeneous transformation matrices $\mathbf{A}_i^{i-1}(q_i)$ (with $i = 1, \ldots, n$) that transform vectors from O_i to O_{i-1}

$$\mathbf{T}_4^0(\vec{q}) = \mathbf{A}_1^0(d_1)\mathbf{A}_2^1(\theta_2)\mathbf{A}_3^2(d_3)\mathbf{A}_4^3(\theta_4) \tag{6.2}$$

The single transformation matrices are

$$\begin{aligned}
\mathbf{A}_1^0(d_1) &= \begin{bmatrix} 1 & 0 & 0 & d_1 \\ 0 & 1 & 0 & 0 \\ 0 & 0 & 1 & 0 \\ 0 & 0 & 0 & 1 \end{bmatrix} \\
\mathbf{A}_2^1(\theta_2) &= \begin{bmatrix} \cos\theta_2 & -\sin\theta_2 & 0 & b_1\cos\theta_2 \\ \sin\theta_2 & \cos\theta_2 & 0 & b_1\sin\theta_2 \\ 0 & 0 & 1 & 0 \\ 0 & 0 & 0 & 1 \end{bmatrix} \\
\mathbf{A}_3^2(d_3) &= \begin{bmatrix} 1 & 0 & 0 & d_3 \\ 0 & 1 & 0 & 0 \\ 0 & 0 & 1 & 0 \\ 0 & 0 & 0 & 1 \end{bmatrix} \\
\mathbf{A}_4^3(\theta_4) &= \begin{bmatrix} \cos\theta_4 & -\sin\theta_4 & 0 & b_2\cos\theta_4 \\ \sin\theta_4 & \cos\theta_4 & 0 & b_2\sin\theta_4 \\ 0 & 0 & 1 & 0 \\ 0 & 0 & 0 & 1 \end{bmatrix}
\end{aligned} \tag{6.3}$$

resulting in

$$\mathbf{T}_4^0(\vec{q}) = \begin{bmatrix} \cos(\theta_2+\theta_4) & -\sin(\theta_2+\theta_4) & 0 & d_1+(b_1+d_3)\cos(\theta_2)+b_2\cos(\theta_2+\theta_4) \\ \sin(\theta_2+\theta_4) & \cos(\theta_2+\theta_4) & 0 & (b_1+d_3)\sin(\theta_2)+b_2\sin(\theta_2+\theta_4) \\ 0 & 0 & 1 & 0 \\ 0 & 0 & 0 & 1 \end{bmatrix} \tag{6.4}$$

As already mentioned, last column of $\mathbf{T}_4^0(\vec{q})$ contains the position vector of the end-effector (i.e. frame O_4) w.r.t. the world reference frame O_0. The information about the orientation of O_4 is contained in the first three columns of $\mathbf{T}_4^0(\vec{q})$, but it is simply a rotation about the world z-axis of an angle equal to $\theta_2+\theta_4$. The pose of the end-effector can be expressed in a minimal number of coordinates, $\vec{c}_e$, in the task space of the manipulator, with p_{e_x} and p_{e_y} being the first two elements of $\vec{p}_4^0$, and ϕ_{e_z} being the rotation about $\hat{e}_{0_z} \equiv \hat{e}_{4_z}$ of O_4 w.r.t. O_0. The direct kinematics relation, $\vec{k}(\vec{q})$, provides the relationship between the joint variables and the task space variables

$$\vec{c}_e = \vec{k}(\vec{q}) = \begin{Bmatrix} p_{e_x} \\ p_{e_y} \\ \phi_{e_z} \end{Bmatrix} = \begin{Bmatrix} d_1+(b_1+d_3)\cos(\theta_2)+b_2\cos(\theta_2+\theta_4) \\ (b_1+d_3)\sin(\theta_2)+b_2\sin(\theta_2+\theta_4) \\ \theta_2+\theta_4 \end{Bmatrix} \tag{6.5}$$

This minimal representation ignores the position along the Z-axis, p_{e_z}, which is constantly null, since the motion of the manipulator is confined in the horizontal plane. The end-effector pose (position and orientation) is expressed by three task space variables (p_{e_x}, p_{e_y}, ϕ_{e_z}) meaning

that the operational space of the robot is of size $\mathbb{R}^m$ with $m = 3$, while the manipulator posture is given by four joint variables $(d_1, \theta_2, d_3, \theta_4)$ with joint space belonging to $\mathbb{R}^n$ with $n = 4$. Since the dimension of the operational space is smaller than the dimension of the task space (i.e. $m < n$) the manipulator is kinematically redundant. The redundancy in manipulators provides dexterity[1] to the system and is exploited in this work to tackle the intrinsic limits of DE mechanisms. The physical meaning of kinematic redundancy is that the same end-effector pose can nominally be reached by an infinite number of manipulator postures. In other words, an infinite number of joint variables combinations will result in the same task space variables.

The relationship between the joint velocities, $\dot{\vec{q}} = \left\{\dot{d}_1\ \dot{\theta}_2\ \dot{d}_3\ \dot{\theta}_4\right\}^{\mathrm{T}}$, and the corresponding end-effector linear and angular velocities, $\dot{\vec{c}}_e = \left\{\dot{p}_{e_x}\ \dot{p}_{e_y}\ \dot{\phi}_{e_z}\right\}^{\mathrm{T}}$, is given by the differential kinematics through the Jacobian matrix, $\mathbf{J}(\vec{q})$. The end-effector velocities are expressed as a function of the joint velocities with

$$\dot{\vec{c}}_e = \mathbf{J}_A(\vec{q})\dot{\vec{q}} \tag{6.6}$$

In the case studied, it is possible to compute the (analytical) Jacobian, $\mathbf{J}_A$, via differentiation of the direct kinematics $\vec{k}(\vec{q})$

$$\begin{aligned}\mathbf{J}_A(\vec{q}) = \frac{\partial \vec{k}(\vec{q})}{\partial \vec{q}} &= \begin{bmatrix} \frac{\partial k_1(\vec{q})}{\partial d_1} & \frac{\partial k_1(\vec{q})}{\partial \theta_2} & \frac{\partial k_1(\vec{q})}{\partial d_3} & \frac{\partial k_1(\vec{q})}{\partial \theta_4} \\ \frac{\partial k_2(\vec{q})}{\partial d_1} & \frac{\partial k_2(\vec{q})}{\partial \theta_2} & \frac{\partial k_2(\vec{q})}{\partial d_3} & \frac{\partial k_2(\vec{q})}{\partial \theta_4} \\ \frac{\partial k_3(\vec{q})}{\partial d_1} & \frac{\partial k_3(\vec{q})}{\partial \theta_2} & \frac{\partial k_3(\vec{q})}{\partial d_3} & \frac{\partial k_3(\vec{q})}{\partial \theta_4} \end{bmatrix} \\ &= \begin{bmatrix} 1 & -(b_1+d_3)\sin(\theta_2) - b_2\sin(\theta_2+\theta_4) & \cos(\theta_2) & -b_2\sin(\theta_2+\theta_4) \\ 0 & (b_1+d_3)\cos(\theta_2) + b_2\cos(\theta_2+\theta_4) & \sin(\theta_2) & b_2\cos(\theta_2+\theta_4) \\ 0 & 1 & 0 & 1 \end{bmatrix}\end{aligned} \tag{6.7}$$

In the proposed experiment, the control variables are the end-effector positions, p_{e_x} and p_{e_y}, neglecting its orientation which is useless for the proposed task (see Sec. 6.4.2). Considering only two task space variables increases the number of degrees of redundancy, which now become two. The increased manipulator redundancy provides the system with more dexterity and widens the workspace. The task space variables $\vec{c}_e$ and their time derivatives $\dot{\vec{c}}_e$ are now reduced to

$$\vec{x}_e = \begin{Bmatrix} p_{e_x} \\ p_{e_y} \end{Bmatrix} \qquad \dot{\vec{x}}_e = \begin{Bmatrix} \dot{p}_{e_x} \\ \dot{p}_{e_y} \end{Bmatrix} \tag{6.8}$$

and the Jacobian is reduced to

$$\mathbf{J}(\vec{q}) = \begin{bmatrix} 1 & -(b_1+d_3)\sin(\theta_2) - b_2\sin(\theta_2+\theta_4) & \cos(\theta_2) & -b_2\sin(\theta_2+\theta_4) \\ 0 & (b_1+d_3)\cos(\theta_2) + b_2\cos(\theta_2+\theta_4) & \sin(\theta_2) & b_2\cos(\theta_2+\theta_4) \end{bmatrix} \tag{6.9}$$

From now on, when mentioning the task space variables, velocities or accelerations, as well as the Jacobian matrix, it will refer to their reduced version.

[1] Among other definitions, Klein and Blaho [110] argue that dexterity measures the kinematic extent to which the manipulator can reach all orientations; in other words, dexterous manipulators must have kinematic redundancy.

The inverse relation between joint velocities and task space velocities is based on the (generalized) inverse of $\mathbf{J}(\vec{q})$ denoted by $\mathbf{J}^g(\vec{q})$:

$$\dot{\vec{q}} = \mathbf{J}^g(\vec{q})\dot{\vec{x}}_e \tag{6.10}$$

Such relation is used to understand what joint velocities has to be commanded to the manipulator in order to obtain a given motion at the end-effector. In redundant manipulators the Jacobian matrix is not a square matrix and, therefore, not invertible. Special algorithms can be exploited to compute generalized inverse matrices, $\mathbf{J}^g$, that satisfy some properties of the inverse matrix, but not necessarily all of them. An infinite number of generalized inverse matrices exists to compute the joint variables from the task space variables. Each generalized inverse corresponds to a different manipulator posture and it is possible to apply optimization techniques in order to achieve optimal solutions given a proper cost functional. The problem can be formulated as a constrained linear optimization, that can be solved using the Lagrange multipliers approach. The constrained cost functional is

$$g(\dot{\vec{q}}, \vec{\lambda}) = \frac{1}{2}\dot{\vec{q}}^{\mathrm{T}}\mathbf{W}\dot{\vec{q}} + \vec{\lambda}^{\mathrm{T}}(\dot{\vec{x}}_e - \mathbf{J}\dot{\vec{q}}) \tag{6.11}$$

where $\vec{\lambda}$ is a $[m \times 1]$ vector of unknown multipliers (m is the number of task space variables) and $\mathbf{W}$ is a proper weight matrix. The first term on the right-hand side of Eq. 6.11 is the cost to be minimized, while the second term is the constraint to be satisfied (i.e. the result has to be a solution to the differential kinematics problem). The solution to the problem comes from the necessary conditions

$$\left(\frac{\partial g}{\partial \dot{\vec{q}}}\right)^{\mathrm{T}} = 0 \qquad \left(\frac{\partial g}{\partial \vec{\lambda}}\right)^{\mathrm{T}} = 0 \tag{6.12}$$

leading to the optimal solution

$$\dot{\vec{q}} = \mathbf{W}^{-1}\mathbf{J}^{\mathrm{T}}(\mathbf{J}\mathbf{W}^{-1}\mathbf{J}^{\mathrm{T}})^{-1}\dot{\vec{x}}_e \tag{6.13}$$

and $\mathbf{J}^{\dagger}_W = \mathbf{W}^{-1}\mathbf{J}^{\mathrm{T}}(\mathbf{J}\mathbf{W}^{-1}\mathbf{J}^{\mathrm{T}})^{-1}$ is the weighted pseudo-inverse of $\mathbf{J}$. If the weight matrix $\mathbf{W}$ is the identity matrix $\mathbb{I}$, the Moore-Penrose pseudo-inverse, $\mathbf{J}^{\dagger}$, is obtained

$$\mathbf{J}^{\dagger} = \mathbf{J}^{\mathrm{T}}(\mathbf{J}\mathbf{J}^{\mathrm{T}})^{-1} \tag{6.14}$$

This particular generalized inverse minimizes the norm of the joint variables vector $\vec{q}$. If the weight matrix is the mass matrix of the manipulator, $\mathbf{B}$ (see Sec. 6.3), the mass matrix weighted Moore-Penrose pseudo-inverse, $\mathbf{J}^{\dagger}_B$, is obtained. $\mathbf{J}^{\dagger}_B$ minimizes the kinetic energy of the multi-body system.

$$\mathbf{J}^{\dagger}_B = \mathbf{B}^{-1}\mathbf{J}^{\mathrm{T}}(\mathbf{J}\mathbf{B}^{-1}\mathbf{J}^{\mathrm{T}})^{-1} \tag{6.15}$$

More inverse kinematic solutions can be obtained by adding constraints to the problem. This is achieved by means of some linear algebra.

Having the vector space of joint velocities, $\mathcal{Q}$, and the vector space of the end-effector velocities, $\mathcal{X}$, the differential kinematics is the map $g : \mathcal{Q} \to \mathcal{X}$. In redundant manipulators, such map has a null space (kernel) which is a subspace of $\mathcal{Q}$ and whose elements $\dot{\vec{q}}_k$ mapped onto $\mathcal{X}$ give the null vector $\vec{0}$

$$g(\dot{\vec{q}}) = \vec{0} \tag{6.16}$$

In other words, all the vectors of joint velocities belonging to the null space of g are null when mapped onto $\mathcal{X}$.

In the differential kinematics case the kernel of g corresponds to the kernel of $\mathbf{J}$. Practically, a set of joint velocities belonging to the null space of $\mathbf{J}$ results in an internal motion of the manipulator with no effects on the task space (i.e. the joints and links move, the end-effector does not move). It is possible to project any arbitrary vector of joint velocities $\dot{\vec{q}}_0$ onto the null space of $\mathbf{J}$ through pre-multiplication by the orthogonal projector $\mathbf{P} = \mathbb{I} - \mathbf{J}^g\mathbf{J}$ where $\mathbf{J}^g$ refers to any of the pseudo-inverses proposed above (i.e. $\mathbf{J}^\dagger$, $\mathbf{J}_W^\dagger$ or $\mathbf{J}_B^\dagger$). In addition, it can be proven that if $\dot{\vec{q}}^\star$ is a solution to the differential kinematics problem, than also $\dot{\vec{q}}^\star + \mathbf{P}\dot{\vec{q}}_0$ is a solution. This conclusion allows to define additional constraints to the inverse differential kinematics problem in terms of an arbitrary vector, $\dot{\vec{q}}_0$, to be minimized, leading to the solution

$$\dot{\vec{q}} = \mathbf{J}^g \dot{\vec{x}}_e + (\mathbb{I} - \mathbf{J}^g\mathbf{J})\dot{\vec{q}}_0 \tag{6.17}$$

Instantaneous joint variables at time t for a given end-effector motion are obtained via integration of the joint velocities from initial time t_0

$$\vec{q} = \int_{t_0}^{t} \dot{\vec{q}}\, \mathrm{d}t \tag{6.18}$$

The end-effector accelerations are obtained via time differentiation of Eq. 6.6 leading to

$$\ddot{\vec{x}}_e = \dot{\mathbf{J}}(\vec{q}, \dot{\vec{q}})\dot{\vec{q}} + \mathbf{J}(\vec{q})\ddot{\vec{q}} \tag{6.19}$$

where the time derivative of the Jacobian matrix becomes (denoting $\sin(\cdot)$ with $\mathrm{s}(\cdot)$, $\cos(\cdot)$ with $\mathrm{c}(\cdot)$, $(\theta_2 + \theta_4)$ with θ_{24} and $(\dot{\theta}_2 + \dot{\theta}_4)$ with $\dot{\theta}_{24}$)

$$\dot{\mathbf{J}}(\vec{q}, \dot{\vec{q}}) = \begin{bmatrix} 0 & -\dot{d}_3\,\mathrm{s}(\theta_2) - \dot{\theta}_2(b_1 + d_3)\,\mathrm{c}(\theta_2) - b_2(\dot{\theta}_{24})\,\mathrm{c}(\theta_{24}) & -\dot{\theta}_2\,\mathrm{s}(\theta_2) & -b_2(\dot{\theta}_{24})\,\mathrm{c}(\theta_{24}) \\ 0 & \dot{d}_3\,\mathrm{c}(\theta_2) - \dot{\theta}_2(b_1 + d_3)\,\mathrm{s}(\theta_2) - b_2(\dot{\theta}_{24})\,\mathrm{s}(\theta_{24}) & \dot{\theta}_2\,\mathrm{c}(\theta_2) & -b_2(\dot{\theta}_{24})\,\mathrm{s}(\theta_{24}) \\ 0 & 0 & 0 & 0 \end{bmatrix} \tag{6.20}$$

The joint accelerations are computed with

$$\ddot{\vec{q}} = \mathbf{J}^g \left[\ddot{\vec{x}}_e - \dot{\mathbf{J}}(\vec{q}, \dot{\vec{q}})\dot{\vec{q}} \right] \tag{6.21}$$

or, in the case the constrained pseudo-inverse based on the projector $\mathbf{P}$ is employed, with

$$\ddot{\vec{q}} = \mathbf{J}^g \left[\ddot{\vec{x}}_e - \dot{\mathbf{J}}(\vec{q}, \dot{\vec{q}})\dot{\vec{q}} \right] - (\mathbb{I} - \mathbf{J}^g \mathbf{J})\ddot{\vec{q}}_0 \tag{6.22}$$

Again, the $\mathbf{J}^g$ symbol is used here with a general meaning and can refer to any of the mentioned pseudo-inverses (i.e. $\mathbf{J}^\dagger$, $\mathbf{J}_W^\dagger$ or $\mathbf{J}_B^\dagger$)

Since the vectors $\dot{\vec{q}}_0$ or $\ddot{\vec{q}}_0$ are arbitrary, they can be equal and can be defined in a way that depends on the value of joint variables, thus its minimization mitigates the issue of actuators saturation. For example

$$\dot{\vec{q}}_0 = \ddot{\vec{q}}_0 = k_0 \begin{Bmatrix} \frac{q_1}{2q_{1_{max}}} \\ \frac{q_2}{2q_{2_{max}}} \\ \frac{q_3}{2q_{3_{max}}} \\ \frac{q_4}{2q_{4_{max}}} \end{Bmatrix} \tag{6.23}$$

The arbitrary vectors are always minimized, regardless if the kinematics is inverted at the velocity or acceleration level. A number of different kinematics and dynamics inversion approaches will be compared in Sec. 6.5.1.

6.3 Dynamics

The equation of motion of the manipulator allows to compute the manipulator motion under known joint actuation. In Lagrange formulation the equation of motion is obtained by derivation from the Lagrangian function $\mathcal{L}$ which depends on the total kinetic energy T and total potential energy U

$$\mathcal{L}(\vec{q}, \dot{\vec{q}}) = T(\vec{q}, \dot{\vec{q}}) - U(\vec{q}) \tag{6.24}$$

The generalized joint forces vector $\vec{f}$ is computed from the Lagrangian $\mathcal{L}$ with

$$\frac{\mathrm{d}}{\mathrm{d}t}\left(\frac{\partial \mathcal{L}}{\partial \dot{\vec{q}}}\right)^{\mathrm{T}} - \left(\frac{\partial \mathcal{L}}{\partial \vec{q}}\right)^{\mathrm{T}} = \vec{f} \tag{6.25}$$

In the proposed experiment, the potential term is neglected introducing some approximation. Since the manipulator moves in the horizontal plane, gravity effects are very small; in addition, intrinsic elasticity of the joints is considered (later) in the actuator response model. This leads to

$$\frac{\mathrm{d}}{\mathrm{d}t}\left(\frac{\partial T}{\partial \dot{\vec{q}}}\right)^{\mathrm{T}} - \left(\frac{\partial T}{\partial \vec{q}}\right)^{\mathrm{T}} = \vec{f} \tag{6.26}$$

The first step in the dynamics analysis of a multi-body system is the definition of the inertial properties. The experiment proposed is composed by two real links L_2 and L_4 (with masses m_2 and m_4, and inertia tensors $\mathbf{I_2}$ and $\mathbf{I_4}$ relative to the centers of mass of the links and expressed in the world frame O_0) and two mass-less and inertia-less fictitious links L_1 and L_3. Since the manipulator moves in the horizontal plane, the axis of rotation of each link is perpendicular

to such plane (i.e. parallel to the z-axis of the world frame O_0). Both links L_2 and L_4 have an axial symmetry about the x-axis of O_2 and O_4 respectively; consequently, the unit vectors $\hat{e}_{2_z}$ and $\hat{e}_{4_z}$ identify a principal axis of inertia for L_2 and L_4 respectively. Define $O_2^{(c)}$ and $O_4^{(c)}$ as the reference frames parallel to O_2 and O_4, but translated at the center of mass of L_2 and L_4 respectively. From axial symmetry, the inertia tensors $\mathbf{I}_2^{(c)}$ and $\mathbf{I}_4^{(c)}$ computed at $O_2^{(c)}$ and $O_4^{(c)}$ are principal and diagonal. To express $\mathbf{I}_2^{(c)}$ and $\mathbf{I}_4^{(c)}$ in the world frame O_0 and obtain $\mathbf{I_2}$ and $\mathbf{I_4}$ the multiplication by rotation matrices is required. Nevertheless, such rotation does not affect the rotation perpendicular to the motion plane and from Fig. 6.2 it is true that $\hat{e}_{0_z} \parallel \hat{e}_{2_z} \parallel \hat{e}_{4_z}$; it results that $I^{(c)}_{(3,3)_2} = I_{(3,3)_2} = I_{zz_2}$ and $I^{(c)}_{(3,3)_4} = I_{(3,3)_4} = I_{zz_4}$, where the subscript $(3,3)$ denotes the third element of the third row of the tensor and the subscripts 2 and 4 identify the link number.

The inertia information of the manipulator is contained in the mass matrix, $\mathbf{B}$. The system kinetic energy T is computed with the following equation

$$\begin{aligned} T &= \sum_{i=1}^{n} T_i \\ &= \sum_{i=1}^{n} \left[\frac{1}{2} m_i \dot{\vec{q}}^{\mathrm{T}} \mathbf{J}_P^{(i)\mathrm{T}} \mathbf{J}_P^{(i)} \dot{\vec{q}} + \frac{1}{2} \dot{\vec{q}}^{\mathrm{T}} \mathbf{J}_O^{(i)\mathrm{T}} \mathbf{I}_i \mathbf{J}_O^{(i)} \dot{\vec{q}} \right] \\ &= \frac{1}{2} \dot{\vec{q}}^{\mathrm{T}} \mathbf{B}(\vec{q}) \dot{\vec{q}} \end{aligned} \tag{6.27}$$

$\mathbf{J}_P^{(i)}$ and $\mathbf{J}_O^{(i)}$ are the parts of the Jacobian matrix computed at the center of mass of the i-th link that relate the joint velocities to the linear and angular velocities of the i-th link respectively. Although $n = 4$, it is true that $T_1 = T_3 = 0$ since the first and third links are massless. In the considered case

$$\begin{aligned} \mathbf{J}^{(2)} = \begin{bmatrix} \mathbf{J}_P^{(2)} \\ \mathbf{J}_O^{(2)} \end{bmatrix} &= \begin{bmatrix} \begin{bmatrix} 1 & -\frac{b_1}{2}\sin(\theta_2) & 0 & 0 \\ 0 & \frac{b_1}{2}\cos(\theta_2) & 0 & 0 \end{bmatrix} \\ \begin{bmatrix} 0 & 1 & 0 & 0 \end{bmatrix} \end{bmatrix} \\ \mathbf{J}^{(4)} = \begin{bmatrix} \mathbf{J}_P^{(4)} \\ \mathbf{J}_O^{(4)} \end{bmatrix} &= \begin{bmatrix} \begin{bmatrix} 1 & -(b_1+d_3)\sin(\theta_2) & \cos(\theta_2) & 0 \\ 0 & (b_1+d_3)\cos(\theta_2) & \sin(\theta_2) & 0 \end{bmatrix} \\ \begin{bmatrix} 0 & 1 & 0 & 1 \end{bmatrix} \end{bmatrix} \end{aligned} \tag{6.28}$$

These relations are computed assuming that the center of mass of link L_2 is located at half-length of L_2 and that the end-effector structure (see Fig. 6.2) is very lightweight and the center of mass of link L_4 is coincident with the origin of O_3.

The symmetric mass matrix $\mathbf{B}$ is computed from Eq. 6.27 and Eq. 6.28 and becomes

$$\mathbf{B}(\vec{q}) = \begin{bmatrix} m_2 + m_4 & -\left(\frac{1}{2}m_2 b_1 + m_4 b_1 + m_4 d_3\right) \mathrm{s}(\theta_2) & m_4\,\mathrm{c}(\theta_2) & 0 \\ \cdots & I_{zz_2} + I_{zz_4} + \left(\frac{1}{4}m_2 + m_4\right) b_1^2 + 2 b_1 d_3 m_4 & 0 & I_{zz_4} \\ \cdots & \cdots & m_4 & 0 \\ \cdots & \cdots & \cdots & I_{zz_4} \end{bmatrix} \tag{6.29}$$

which is computed assuming that the z-axes perpendicular to the manipulator motion plane and passing through the centers of mass of L_2 and L_4 are principal axes of inertia and that I_{zz_i} is the third element of principal-axes, diagonal inertia matrix of the i-th link.

The equation of motion of the multi-body system comes from Eq. 6.26

$$\mathbf{B}(\vec{q})\ddot{\vec{q}} + \vec{n}(\vec{q},\dot{\vec{q}}) = \vec{f} \tag{6.30}$$

where $\vec{n}(\vec{q},\dot{\vec{q}})$ is the centrifugal term and contains all the fictitious forces and the contributions that depend on the joint velocities

$$\begin{aligned}\vec{n}(\vec{q},\dot{\vec{q}}) &= \dot{\mathbf{B}}(\vec{q})\dot{\vec{q}} - \frac{1}{2}\left[\frac{\partial}{\partial \vec{q}}\left(\dot{\vec{q}}^{\mathrm{T}}\mathbf{B}(\vec{q})\dot{\vec{q}}\right)\right]^{\mathrm{T}} \\ &= \begin{Bmatrix} -\left(\frac{1}{2}b_1 m_2 + b_1 m_4 + d_3 m_4\right)\dot{\theta}_2^2\cos(\theta_2) - 2m_4\dot{d}_3\dot{\theta}_2\sin(\theta_2) \\ 2m_4\dot{d}_3\dot{\theta}_2(b_1 + d_3) \\ -m_4\dot{\theta}_2^2(b_1 + d_3) \\ 0 \end{Bmatrix}\end{aligned} \tag{6.31}$$

It is always possible to explicitly write the joint accelerations from Eq. 6.30 obtaining

$$\ddot{\vec{q}} = \mathbf{B}^{-1}(\vec{q})\left[\vec{f} - \vec{n}(\vec{q},\dot{\vec{q}})\right] \tag{6.32}$$

6.4 Manipulator control

The main control scheme implemented in the manipulator is an operational space (task space) control and is based on the inverse dynamics rather than the inverse kinematics. In other words, the actuation commanded by the control algorithm is expressed in terms of joint force/torque rather than joint variables, which cannot be measured directly. The control variables are the end-effector positions $\vec{x}_e = \{p_{e_x}\ p_{e_y}\}^{\mathrm{T}}$ which are measured via a vision system (see Sec. 6.6.1). The measured variables are used to compute the position and velocity errors used in the control law, as well as the inverted dynamics.

The control scheme used was proposed by Nakanishi *et al.* [111] as the simplified acceleration based control, with null-space premultiplication of $\mathbf{B}$ when the projector $\mathbf{P}$ is used. Since the actuator model is known from Ch. 5, it is possible to introduce an additional component to the command torques to account for the DEAs internal elastic forces; a simple proportional compensator, $\mathbf{K}_k$, is introduced that estimates the required torques to reach the desired joint variables on the basis of the steady state DEAs model presented in Sec 5.4. The generalized joint torques commanded to the manipulator are

$$\vec{\tau} = \mathbf{B}\mathbf{J}^g(\ddot{\vec{x}}_r - \dot{\mathbf{J}}\dot{\vec{q}}) + \vec{n} + \mathbf{K}_k\mathbf{J}^g\vec{x}_e \tag{6.33}$$

or in the case the projector $\mathbf{P}$ is used

$$\vec{\tau} = \mathbf{B}\mathbf{J}^g(\ddot{\vec{x}}_r - \dot{\mathbf{J}}\dot{\vec{q}}) + \vec{n} + \mathbf{K}_k\mathbf{J}^g\vec{x}_e + \mathbf{B}(\mathbb{I} - \mathbf{J}^g\mathbf{J})\ddot{\vec{q}}_0 \tag{6.34}$$

where $\ddot{\vec{x}}_r$ is computed from the control law which, in this work, can either be a Proportional-Derivative (PD) or a Proportional-Integral-Derivative (PID) law

$$\begin{aligned} \ddot{\vec{x}}_r^{\text{PD}} &= \ddot{\vec{x}}_d + \mathbf{K}_d(\dot{\vec{x}}_d - \dot{\vec{x}}_e) + \mathbf{K}_p(\vec{x}_d - \vec{x}_e) \\ \ddot{\vec{x}}_r^{\text{PID}} &= \ddot{\vec{x}}_d + \mathbf{K}_d(\dot{\vec{x}}_d - \dot{\vec{x}}_e) + \mathbf{K}_p(\vec{x}_d - \vec{x}_e) + \mathbf{K}_i\int_0^t(\vec{x}_d - \vec{x}_e)\mathrm{d}t \end{aligned} \tag{6.35}$$

where $\mathbf{K}_d$, $\mathbf{K}_p$ and $\mathbf{K}_i$ are proper gain matrices. The joint elasticity gain matrix $\mathbf{K}_k$ is diagonal and its elements are the ratios, $f_1 = \frac{f_F}{f_y}$ and $f_2 = \frac{f_T}{f_\theta}$, of the model constants

$$\mathbf{K}_k = \begin{bmatrix} f_1 & 0 & 0 & 0 \\ 0 & f_2 & 0 & 0 \\ 0 & 0 & f_1 & 0 \\ 0 & 0 & 0 & f_2 \end{bmatrix} \tag{6.36}$$

The control scheme is implemented with an algorithm that allows the computation of all the elements in Eq. 6.33-6.34. The commands are fed to the actuators at discrete time intervals given by the sample time of the measurement system. The end-effector positions $\vec{x}_e$ are measured and used to estimate the joint variables $\vec{q}$ at every time instant. The joint variables are, then, involved in the computation of the $\mathbf{B}$, $\mathbf{J}$, $\mathbf{J}^g$ and, consequently, $\dot{\vec{q}}$ and $\dot{\mathbf{J}}$. This finally leads to the computation of torques, $\vec{\tau}$, to be commanded to the manipulator joints. One algorithm iteration at time t_k (at the k-th time step) is composed by the following steps:

1. acquisition of $\vec{x}_e^{(k)}$
2. derivation of $\dot{\vec{x}}_e^{(k)}$
3. computation of $\mathbf{J}(\vec{q}^{(k-1)})$
4. computation of $\mathbf{B}(\vec{q}^{(k-1)})$
5. computation of $\mathbf{J}^g(\vec{q}^{(k-1)})$
6. computation of $\dot{\vec{q}}^{(k)} = \mathbf{J}^g\dot{\vec{x}}_e^{(k)}$
7. integration of $\vec{q}^{(k)} = \sum_{i=1}^{k}\dot{\vec{q}}^{(i)}\Delta t_i$
8. computation of $\dot{\mathbf{J}}(\vec{q}^{(k)}, \dot{\vec{q}}^{(k)})$
9. computation of $\vec{n}(\vec{q}^{(k)}, \dot{\vec{q}}^{(k)})$
10. computation of $\ddot{\vec{q}}_0(\vec{q}^{(k)})$ (when applicable)
11. computation of $\ddot{\vec{x}}_r(\vec{x}_e^{(k)}, \dot{\vec{x}}_e^{(k)})$ via PD/PID controller from a given trajectory
12. computation of $\vec{\tau}^{(k)}$

The described algorithm is repeated at every time step, with a frequency given by the sampling time of the vision system. Initial conditions on joint variables are provided at the first step.

6.4.1 Gaussian regression control

In addition to the main control scheme described above, an alternative solution was implemented with the introduction of a feedforward compensator (Fig. 6.8), in which the inverse dynamics is estimated using Gaussian regression.

Feedforward is based on the knowledge of the inverse dynamics of the system that allows to calculate the torques needed to reach a given robot configuration. With this approach it is possible to directly drive the manipulator from an initial to a final end-effector position. In order to overcome robustness issues in the feedforward scheme, it is good practice to close the loop with a low-gain PD controller to reject possible disturbances. A key point in this control scheme is the knowledge of the inverse dynamics. In this work the dynamics is inverted with the procedure described in Sec. 6.3 that provides one of the infinite solutions to the redundant problem. Although the inverse dynamics is known, the model is affected by non-negligible inaccuracies compared to the real system (see Sec. 4 and Sec. 6.5) mainly due to the difficulties in modeling the highly non-linear DE actuators. A way to improve the performances of the feedforward algorithm in the presence of model uncertainties is to use a learning algorithm. In this work a Gaussian regression technique is implemented.

Given a reference trajectory in terms of position, $\vec{x}_d$, velocity, $\dot{\vec{x}}_d$, and acceleration, $\ddot{\vec{x}}_d$, and assuming that N consecutive measurements of system inputs and outputs are available, then the regressor algorithm inputs are:

1. the vector, $\vec{\tau}_k,\ k = 1,\dots,N$, of generalized torques necessary to track the reference trajectory and obtained from the described inverse dynamics (see Sec. 6.4);
2. the vector of positions, velocities and accelerations, $\vec{p}_k = \{x_e\ y_e\ \dot{x}_e\ \dot{y}_e\ \ddot{x}_e\ \ddot{y}_e\}_k^T,\ k = 1,\dots,N$, obtained applying the torques, $\vec{\tau}$, to the robot.

Indicating with $Z_N = (\vec{p}_k, \vec{\tau}_k),\ k = 1,\dots,N$, the regressor is capable to estimate the inverse map $\mu(\vec{p}) : \vec{p} \to \vec{\tau}$. The unknown $\mu : \mathbb{R}^6 \to \mathbb{R}^4$ is modeled as realization of a zero-mean Gaussian field with covariance $K : \mathbb{R}^6 \times \mathbb{R}^6 \to \mathbb{R}$. K is assumed to be a Gaussian kernel, i.e $K(\vec{p}_i, \vec{p}_j) = e^{-\frac{\|\vec{p}_i - \vec{p}_j\|}{\sigma^2}}$ with $\sigma \in \mathbb{R}_+$. Under the framework of the regularization theory[112], a standard result is the form of the optimal estimate $\hat{\mu}(\vec{p})$, which in this case is given by

$$\hat{\mu}(\vec{p}) = \mathbb{E}[\mu(\vec{p})|Z_N] = \sum_{i=1}^{N} c_i K(\vec{p}_i, \vec{p}) \tag{6.37}$$

where $\mathbb{E}[\cdot]$ denotes the expected value, with

$$\begin{bmatrix} c_1 \\ \vdots \\ c_N \end{bmatrix} = (\bar{\mathbf{K}} + \sigma^2 \mathbb{I})^{-1} \begin{bmatrix} \vec{\tau}_1 \\ \vdots \\ \vec{\tau}_N \end{bmatrix} \tag{6.38}$$

and

$$\bar{\mathbf{K}} = \begin{bmatrix} K(\vec{p}_1, \vec{p}_1) & \dots & K(\vec{p}_1, \vec{p}_N) \\ \vdots & & \vdots \\ K(\vec{p}_N, \vec{p}_1) & \dots & K(\vec{p}_N, \vec{p}_N) \end{bmatrix} \tag{6.39}$$

6.4.2 Trajectory task

The task that has to be accomplished by the manipulator is a given trajectory of the end-effector in the horizontal plane. The trajectory is described by time laws that provide the instantaneous value of desired position, $\vec{x}_d$, velocity, $\dot{\vec{x}}_d$, and acceleration, $\ddot{\vec{x}}_d$. Fifth order polynomial time laws are implemented in order to be able to impose null initial velocity and acceleration. The geometric trajectory in the x-y plane is traveled by a (curvilinear) coordinate $s(t)$ and it first, $\dot{s}(t)$, and second derivatives, $\ddot{s}(t)$

$$\begin{aligned} s(t) &= 6\frac{s_f - s_i}{t_f^5}t^5 - 15\frac{s_f - s_i}{t_f^4}t^4 + 10\frac{s_f - s_i}{t_f^3}t^3 + s_i \\ \dot{s}(t) &= 30\frac{s_f - s_i}{t_f^5}t^4 - 60\frac{s_f - s_i}{t_f^4}t^3 + 30\frac{s_f - s_i}{t_f^3}t^2 \\ \ddot{s}(t) &= 120\frac{s_f - s_i}{t_f^5}t^3 - 180\frac{s_f - s_i}{t_f^4}t^2 + 60\frac{s_f - s_i}{t_f^3}t \end{aligned} \tag{6.40}$$

where s_i and s_f are the initial and final curvilinear coordinates along the trajectory, and t_f is the total time required to travel the whole trajectory. An example of graphic representation of these time laws is presented in Fig. 6.3. At $t = 0$ and $t = t_f$ it results that

$$\begin{aligned} &\text{if } \; t = 0 \Rightarrow s(t) = s_i, \;\; \dot{s}(t) = \ddot{s}(t) = 0 \\ &\text{if } \; t = t_f \Rightarrow s(t) = s_f, \;\; \dot{s}(t) = 0, \;\; \ddot{s}(t) = 0 \end{aligned} \tag{6.41}$$

The time laws in terms of curvilinear coordinate are then converted into positions, velocities and accelerations of the end-effector via the geometric trajectory law (e.g. rectilinear or circular trajectory). In the case of linear trajectory the initial curvilinear coordinate is zero ($s_i = 0$)

$$\begin{aligned} \vec{x}_d &= \begin{cases} p_{d_x} = \dfrac{p_{d_{x_f}} - p_{d_{x_i}}}{s_f} s(t) + p_{d_{x_i}} \\ p_{d_y} = \dfrac{p_{d_{y_f}} - p_{d_{y_i}}}{s_f} s(t) + p_{d_{y_i}} \end{cases} \\ \dot{\vec{x}}_d &= \begin{cases} \dot{p}_{d_x} = \dfrac{p_{d_{x_f}} - p_{d_{x_i}}}{s_f} \dot{s}(t) \\ \dot{p}_{d_y} = \dfrac{p_{d_{y_f}} - p_{d_{y_i}}}{s_f} \dot{s}(t) \end{cases} \\ \ddot{\vec{x}}_d &= \begin{cases} \ddot{p}_{d_x} = \dfrac{p_{d_{x_f}} - p_{d_{x_i}}}{s_f} \ddot{s}(t) \\ \ddot{p}_{d_y} = \dfrac{p_{d_{y_f}} - p_{d_{y_i}}}{s_f} \ddot{s}(t) \end{cases} \end{aligned} \tag{6.42}$$

In the case of circular trajectory, the curvilinear coordinate is the angle spanned by the trajectory. The coordinates of the center of the circular trajectory are c_x and c_y, while r is the radius. In general we have that $s_i \neq 0$

$$\vec{x}_d = \begin{cases} p_{d_x} = r\cos(s(t)) + c_x \\ p_{d_y} = r\sin(s(t)) + c_y \end{cases}$$
$$\dot{\vec{x}}_d = \begin{cases} \dot{p}_{d_x} = -r\dot{s}(t)\sin(s(t)) \\ \dot{p}_{d_y} = r\dot{s}(t)\cos(s(t)) \end{cases} \tag{6.43}$$
$$\ddot{\vec{x}}_d = \begin{cases} \ddot{p}_{d_x} = -r\ddot{s}(t)\sin(s(t)) - r\dot{s}^2(t)\cos(s(t)) \\ \ddot{p}_{d_y} = r\ddot{s}(t)\cos(s(t)) - r\dot{s}^2(t)\sin(s(t)) \end{cases}$$

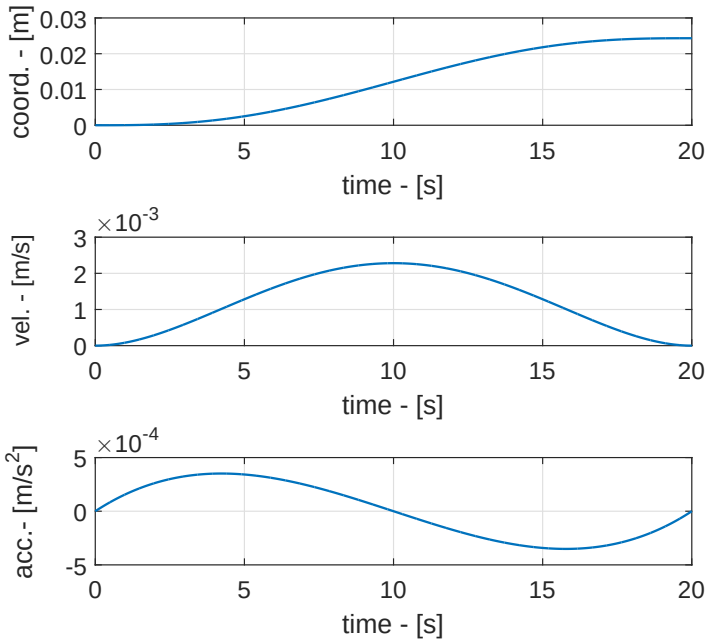

Fig. 6.3: Time evolution of curvilinear coordinate, velocity and acceleration in the case of an example rectilinear trajectory

6.5 Numerical simulations

The proposed robotic arm is simulated by means of a MATLAB® Simulink® numerical model to preliminarily verify its behavior. The numerical simulations are performed by applying the control algorithm described in Sec. 6.4 to the dynamic model of the manipulator prototype coupled with the dynamics of DE actuators as described in Sec. 5. Fig. 6.4 is the simplified block diagram of the numerical model implemented. A preliminary version of the results presented here has been published in [113].

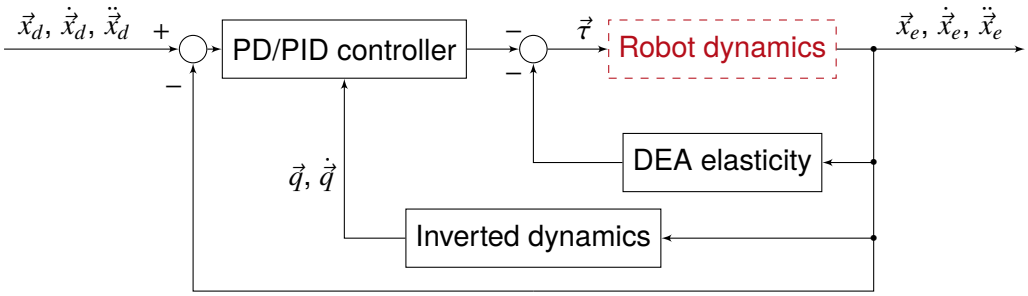

Fig. 6.4: Simplified block diagram of the arm prototype simulation model: joint torques are computed by the controller from the desired trajectory through the inverted dynamics algorithm (Sec. 6.4) and fed to the robot dynamics model

The DEA model implemented assesses the actuator behavior as a single device. In order to implement the actuators inside the multi-body model it is necessary to develop a further approximated model derived from the transfer functions in Eq. 5.40 and Eq. 5.44. This model is depicted in Fig. 6.5 in terms of block diagram and in Fig. 6.6 where the model accordance with measured response for both rotation (Fig. 6.6a) and translation (Fig. 6.6b) is presented. In Fig. 6.5 the actuator model for the rotational degree of freedom is described, but something similar can be developed for translation. The squared value of input voltage, V^2, becomes the single actuator torque, T, through the voltage-to-torque transfer function $G_T(s)$ and the Bode gain f_θ. This torque is summed to a component depending on the rotational velocity, $Q(\dot{\theta})$, and becomes the input of the actuator dynamics described by Eq. 6.44. The function $Q(\dot{\theta})$ is estimated considering the responses of $G_T(s)$ and $G_\theta(s)$.

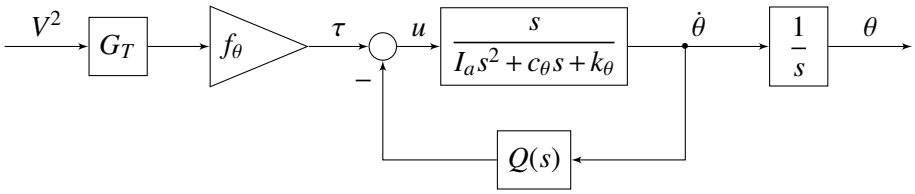

Fig. 6.5: Block diagram used in simulations for the approximate modeling of the actuator

$$\dot{\theta} = \frac{s}{I_a s^2 + c_\theta s + k_\theta} T \tag{6.44}$$

where I_a is the actuator rotor inertia, k_θ describes the elastic behavior, while c_θ is a properly tuned damping coefficient necessary to guarantee stability. The latter has to be introduced artificially in the actuator model and is the main responsible for the model inaccuracies shown in Fig. 6.5-6.6a. The adopted approximation is reasonable for the purpose of this work.

The modified actuator model is implemented inside the multi-body system model depicted in Fig. 6.7. The presented diagram is a single block in the complete simulation diagram and computes the time evolution of the end-effector position, $\vec{x}_e$, for given values of joint (generalized) torques, $\vec{\tau}$.

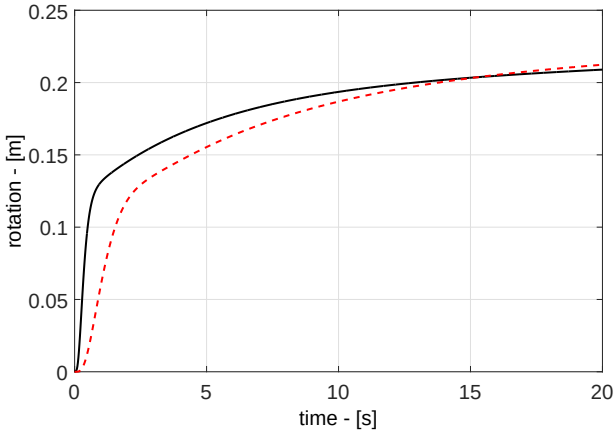

(a) Rotation response to 10 mNm commanded input: comparison between measured (black) and simulated response (red dashed)

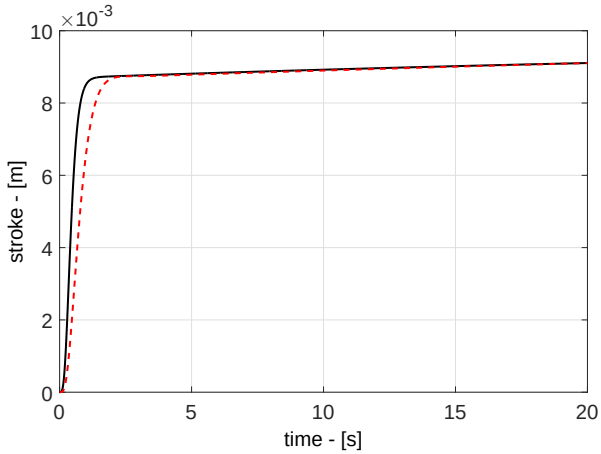

(b) Stroke response to 1 N commanded input: comparison between measured (black) and simulated response (red dashed).

Fig. 6.6: Simulation oriented model adopted for the response prediction of a single actuator. Some error between response from TF in Eq. 6.44 and the simulated response is present; the approximation is reasonable for the purpose of simulation

Introducing the Gaussian regression feedforward algorithm proposed in Sec. 6.4.1 modifies the control block diagram (Fig. 6.4) slightly as presented in Fig. 6.8.

As already mentioned, the actuator model described above and implemented in simulations is based on the available data reported in Sec. 5.6. The influence of power supply dynamics is considered based on the test setup described in Sec. 5.6.1: the power supply is a single-channel Stanford Research Systems™ PS375. Tests on the manipulator prototype require multi-channel HV supply, thus making PS375 unsuitable for the purpose. A different power supply will have a different transient behavior, introducing discrepancy between the simulated model and the actual prototype. Nevertheless, the multi-channel HV electronics described in Sec. 6.6.1 has a fast dynamics with time constant similar or smaller than PS375: the adoption of the PS375 transfer function in simulations results in a worse case compared to the actual experimental setup. Model uncertainties will be small or, if not negligible, will

slightly underestimate the system performances; therefore, uncertainties due to this aspect are considered acceptable.

In the results presented in Sec. 6.5.2, a limitation to the maximum voltage (4500 V) available from the power supply is considered, thus modeling the typical saturation limits of DE actuators (see Sec. 4.7).

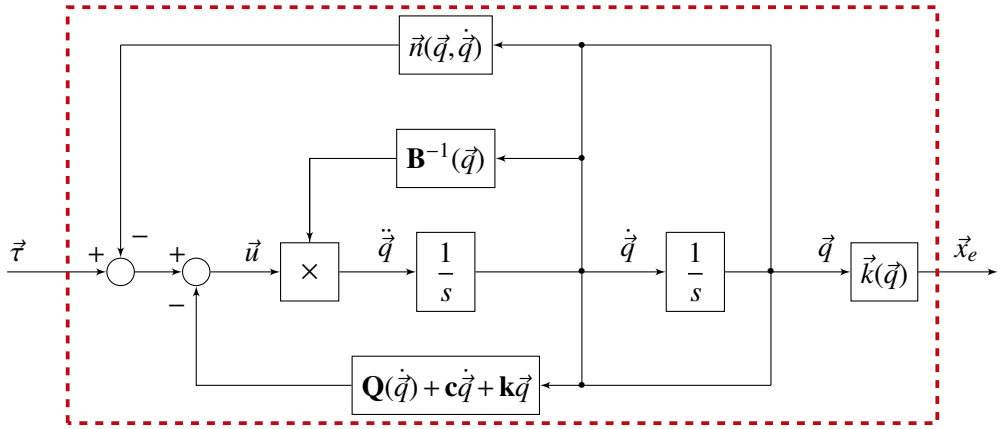

Fig. 6.7: Block diagram of the robotic system model embedded in simulations diagram

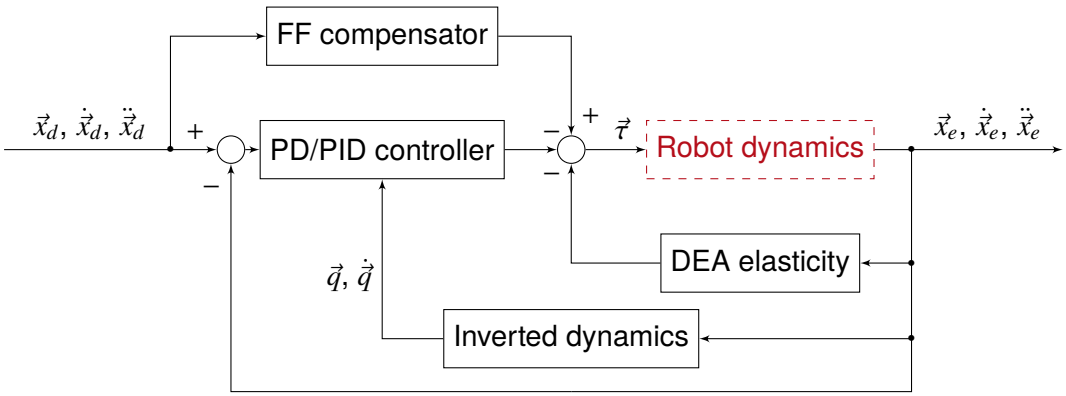

Fig. 6.8: Block schematics of system controlled with the feedforward and PD/PID scheme

6.5.1 Comparison of Jacobian inversion approaches

The kinematics inversion approaches mentioned in Sec. 6.2 are compared here. A 180-deg circular, 10-s trajectory is tested (see Fig. 6.9). In the following, a set of plots shows the simulation results for all the considered cases in terms of x-y trajectory $\vec{x}_e$ (Fig. 6.9), norm of position error w.r.t. desired trajectory $\|\vec{e}\| = \|\vec{x}_d - \vec{x}_e\|$ (Fig. 6.10), norm of the vector of joint variables $\|\vec{q}\|$ (Fig. 6.11), norm of the vector of reaction forces at manipulator base $\|\vec{r}\| = \| \begin{array}{ccc} f_x & f_y & m_z \end{array} \|$ (Fig. 6.12), the manipulator kinetic energy T from Eq. 6.27 (Fig. 6.13) and the absolute values of the single joint variables $|q_i|$ with $i = 1,\ldots,4$ (Fig. 6.14). For the

purpose of this section, the DEAs saturation limits are not implemented, but considered in the discussion. The PID controller gain matrices are:

$$\mathbf{K}_d = \begin{bmatrix} 160 & 0 \\ 0 & 160 \end{bmatrix} \qquad \mathbf{K}_p = \begin{bmatrix} 600 & 0 \\ 0 & 600 \end{bmatrix} \qquad \mathbf{K}_i = \begin{bmatrix} 0 & 0 \\ 0 & 0 \end{bmatrix} \tag{6.45}$$

Four different simulation cases are presented on the bases of different inversion approaches:

1. Kinematic inversion via the Moore-Penrose pseudo-inverse of Jacobian, $\mathbf{J}^{\dagger}$: this approach is simple, performs good in terms of position error (see Fig. 6.10) and minimizes the norm of the joint variables vector (see Fig. 6.11); nevertheless, the value of linear stroke of joints #1 and #3 is very high (see Fig. 6.14a and Fig. 6.14b) certainly leading to actuator saturation.
2. Kinematic inversion via the weighted pseudo-inverse of Jacobian, $\mathbf{J}_W^{\dagger}$: this approach introduces an arbitrary matrix of weights $\mathbf{W}$ aiming at reducing the amount of linear stroke required to joint #1 and #3. This objective is partially achieved, although position error norm is increased (see Fig. 6.10). The adopted matrix has the following arbitrary values:

$$\mathbf{W} = \begin{bmatrix} 10^5 & 0 & 0 & 0 \\ 0 & 10 & 0 & 0 \\ 0 & 0 & 10^5 & 0 \\ 0 & 0 & 0 & 10 \end{bmatrix} \tag{6.46}$$

3. Kinematic inversion via the mass-matrix weighted pseudo-inverse of Jacobian, $\mathbf{J}_B^{\dagger}$: this approach minimizes the kinetic energy of the manipulator over the trajectory (see Fig. 6.13) and, also, limits the stroke of joint #1 and #3; the position error norm is slightly increased (see Fig. 6.10) and the joint variables vector norm is not minimal (see Fig. 6.11).
4. Kinematic inversion at acceleration level via the mass-matrix weighted pseudo-inverse of Jacobian, $\mathbf{J}_B^{\dagger}$ and the addition of a null-space projected arbitrary vector, $\vec{q}_0$, to be minimized: this is the most sophisticated approach among those cited here. The vector $\vec{q}_0$ has the form of Eq. 6.23 (with $k_0 = 320$) and, consequently, it has the best performances in terms of minimization of the joint variables (see Fig. 6.14c and Fig. 6.14d). Error performance is slightly worse (see Fig. 6.10).

Joint saturation is one of the most limiting aspects for the application of DEAs to robotic system (see Sec. 4.7). For this reason, the last approach described above will be implemented in the manipulator experimental evaluation.

6.5.2 Simulation results

Dynamic simulations of the manipulator system have been performed with two 10-s trajectories, one linear and one circular. Both control schemes described in Sec. 6.4 are simulated and their results are compared, also in the presence of inaccurate measurements of the output

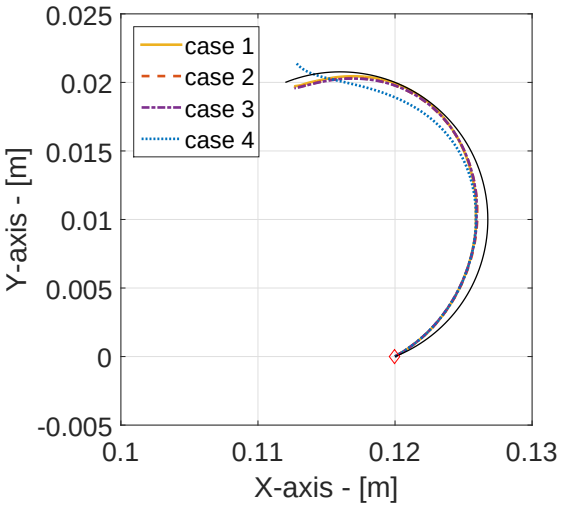

Fig. 6.9: Arc trajectory

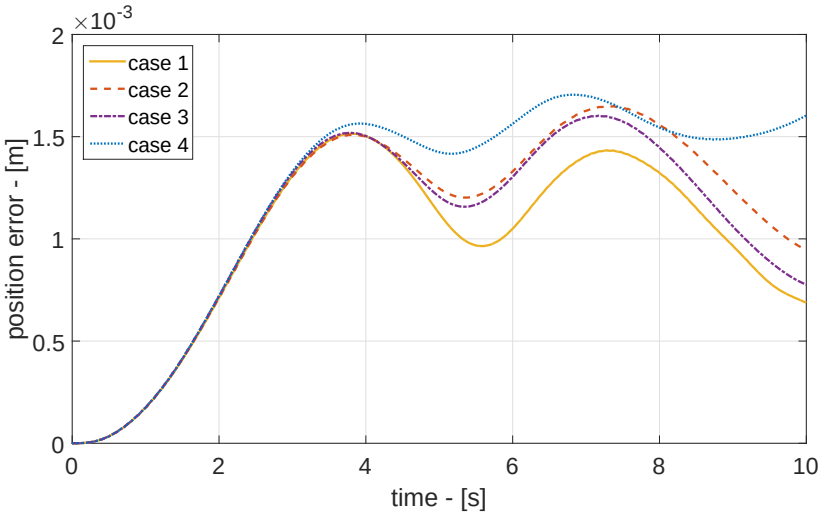

Fig. 6.10: Position error norm

variables. The results of linear trajectory simulations are shown in Fig. 6.16-6.17, while those for the circular trajectory are shown in Fig. 6.18-6.19.

The actuator parameters considered in the simulations are (refer to Sec. 4.5): $d = 100$ mm, $D = 12$ mm, $a = 23$ mm, $c = 25$ mm, $t = 1$ mm, $n = 1$, $\delta_{re} = 2\%$ and $\lambda_0 = 3.5$. The manipulator geometric parameters are $b_1 = b_2 = b = 60$ mm. The simulated manipulator workspace is computed on the basis of the direct kinematics relation (Eq. 6.5) and the considerations presented in Sec. 4.7. The theoretical workspace is presented in Fig. 6.15 based on the maximum stroke and rotation values computed considering that steady state condition cannot be reached in 10s; attenuation on rotation and stroke amplitude at 0.1 Hz can be estimated from Fig. 5.20 and Fig. 5.22 to obtain $y_{max} = 5$ mm and $\theta_{max} = 19.2$ deg.

The comparison of the two control schemes is based on the robustness to output measurements inaccuracies. Such inaccuracies are modeled as uniform noise on the end-effector position

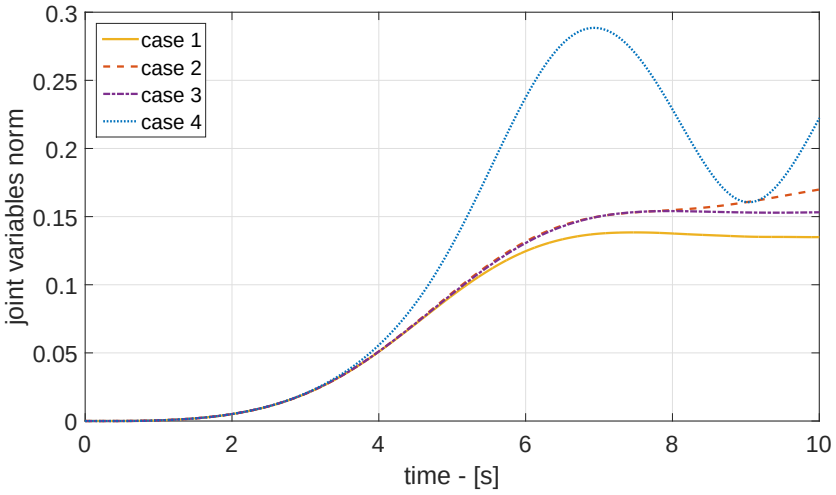

Fig. 6.11: Joint variables vector norm

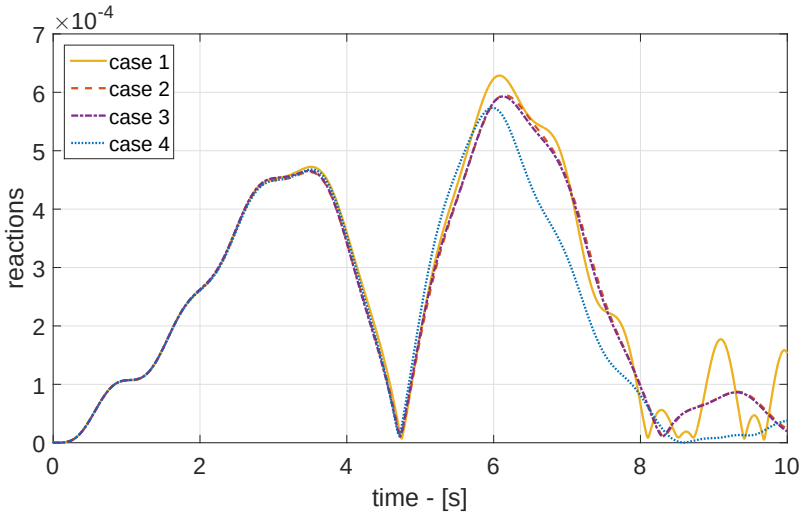

Fig. 6.12: Base reactions (forces and torques) norm

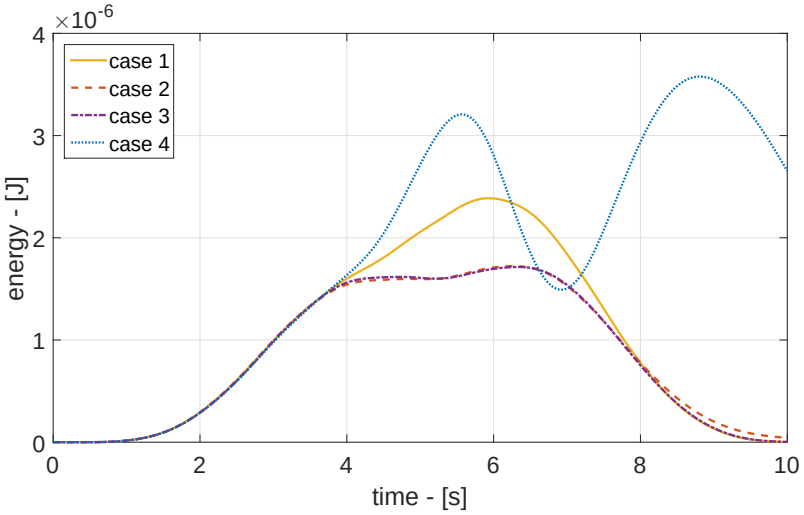

Fig. 6.13: Manipulator kinetc energy

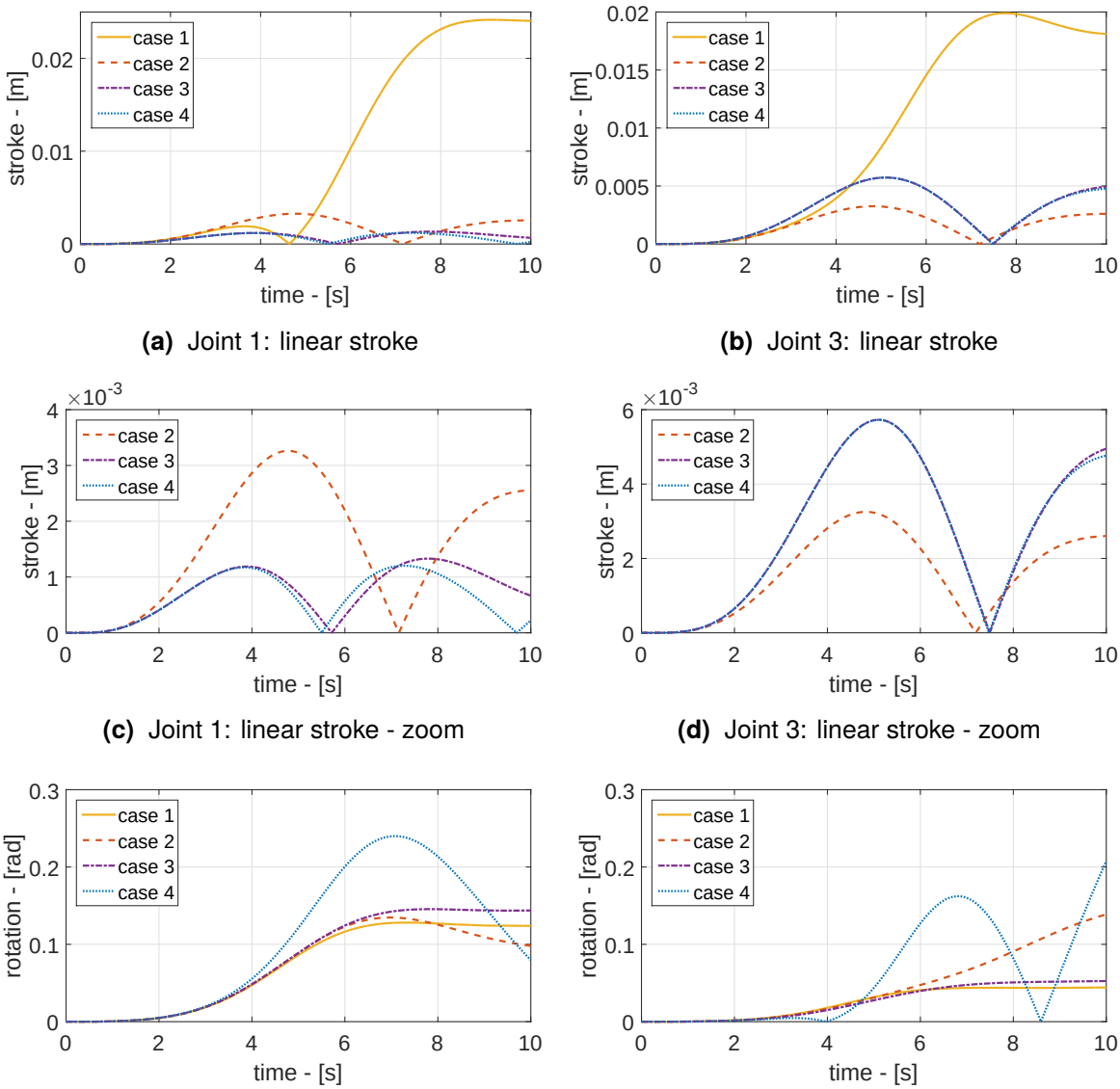

(a) Joint 1: linear stroke

(b) Joint 3: linear stroke

(c) Joint 1: linear stroke - zoom

(d) Joint 3: linear stroke - zoom

(e) Joint 2: rotation

(f) Joint 4: rotation

Fig. 6.14: Absolute value of joint variables

with an amplitude range of ± 0.01 m. The feedforward compensator performs better than the PD controller and, therefore, it is more suitable for application to DE systems, whose model is known with non-negligible parameter uncertainties (see Ch. 4). In particular, the maximum position error with FF compensator is roughly half than with PD for both trajectories considered (see Fig. 6.16b and Fig. 6.18b). Moreover, the simulations performed including noise show that the system controlled with PD becomes unstable and diverges (results not shown), while the FF compensator is still capable to control the system with some performances degradation. Tab. 6.1 summarizes the simulations results as absolute position errors and as relative errors w.r.t. the trajectory overall length. The desired trajectories are traveled with a maximum error of 9.9 mm equivalent to 12.9% of the distance traveled by the end-effector. If noise on output is

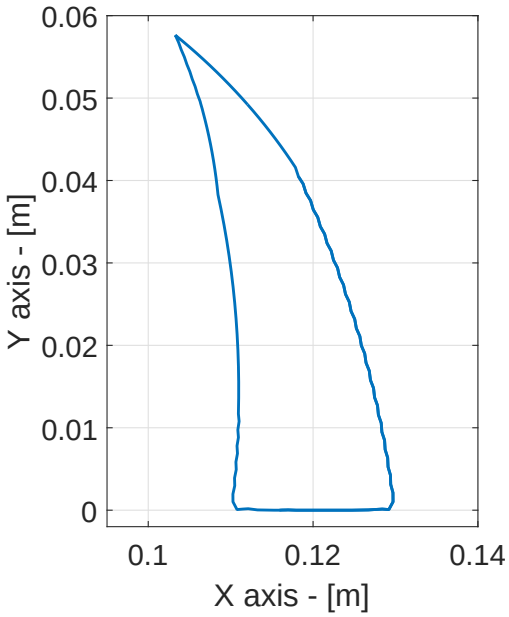

Fig. 6.15: Theoretical workspace of the simulated manipulator (the negative-Y half-plane is not shown for simmetry)

neglected, the trajectories are followed with a maximum error as low as 1.8 mm equivalent to 2.1% of path length.

Tab. 6.1: Manipulator simulations results: absolute error and relative error (w.r.t. trajectory length) for both trajectories and control schemes.

Trajectory	Control	Absolute error [mm]	Relative error [%]
Linear	PD	4.8	5.6
	FF	1.8	2.1
	FF w/ noise	8.1	9.5
Circular	PD	6.7	8.8
	FF	3.3	4.3
	FF w/ noise	9.9	12.9

6.6 Laboratory tests

The prototype performances are verified by means of laboratory experiments. The system has been manufactured and assembled in a proper laboratory setup described in Sec. 6.6.1 and the capability to accomplish the trajectory tracking task was compared with simulation results in Sec. 6.6.2.

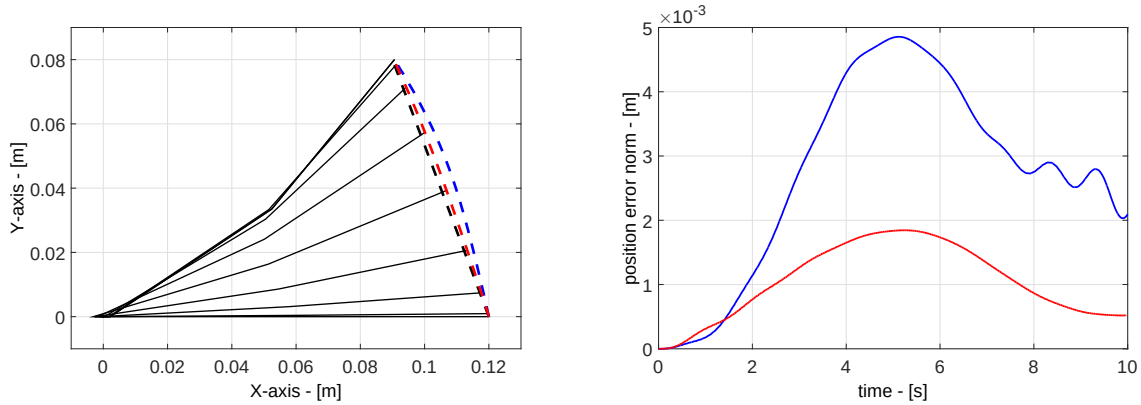

(a) Desired trajectory (black dashed) and actual trajectory (FF in red and PD in blue)

(b) Position error norm

Fig. 6.16: Linear trajectory w/o noise; FF compensator (red) and PD controller (blue)

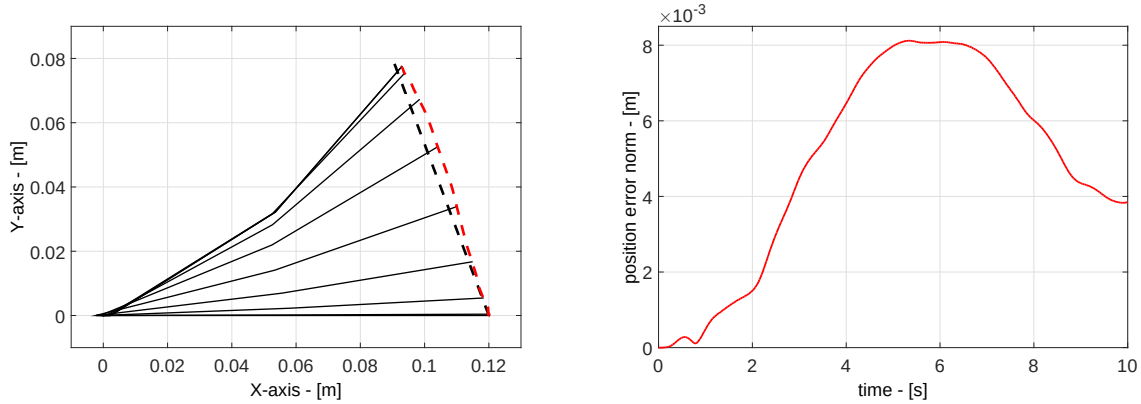

(a) Desired trajectory (black) and FF compensator actual trajectory (red)

(b) Position error norm

Fig. 6.17: Linear trajectory w/ noise (FF compensator only)

6.6.1 Test apparatus

The DE manipulator prototype is tested with a proper test setup (see Fig. 6.21-6.22). Two actuators with the following parameters are employed (refer to Sec. 4.5): $d = 80$ mm, $D = 14$ mm, $a = 23$ mm, $c = 25$ mm, $t = 1$ mm, $n = 1$, $\delta_{re} = 2\%$ and $\lambda_0 = 3.5$. The manipulator base (structure of the first DE actuator) is fixed. The prototype is a planar arm that moves in the horizontal plane and a flexible support system is implemented in order to counteract the effects of gravity and simulate the orbital weightlessness. A polyethylene cable (ultra-high-molecular-weight polyethilene, UHMWPE, Dyneema®) is employed for its rigidity and light weight. The cable suspends the second link, L_2, vertically w.r.t. its center of mass and allows the manipulator motion in the x-y plane, but prevents any vertical displacement. The DEAs power supply is the same involved in the tests presented in Sec. 5.8 and is composed by a set of HV converters (EMCO™ C50) powered by an AC/DC power supply (TRACOPOWER™ TXM 035-112) and programmed via PC through a USB analog output board (Measurement Computing™ USB-

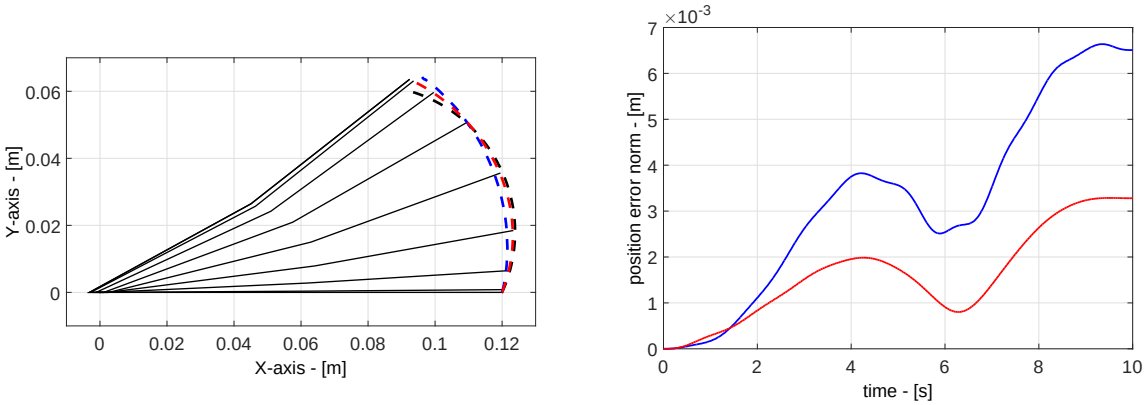

(a) Desired trajectory (black dashed) and actual trajectory (FF in red and PD in blue)

(b) Position error norm

Fig. 6.18: Arc trajectory w/o noise; FF compensator (red) and PD controller (blue).

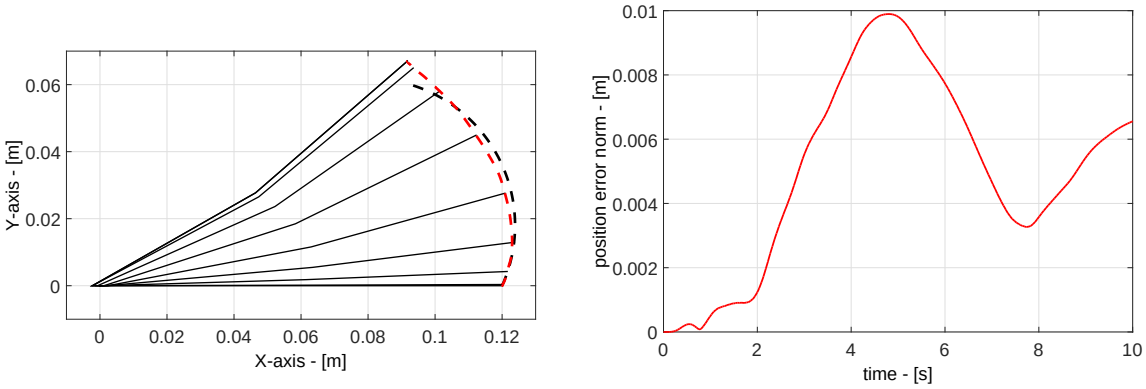

(a) Desired trajectory (black) and FF compensator actual trajectory (red).

(b) Position error norm.

Fig. 6.19: Arc trajectory w/ noise (FF compensator only)

3112). Eight HV channels are required to actuate two 2-DoF actuators (two electrodes for each DoF). A vision system is used to measure the control variables (i.e. end-effector postion).

The gravity compensation achieved by the proposed system allows to perform significant tests on the prototype, although some perturbations to the x-y motion are introduced by the suspending system due to the pendulum effect of the cables: gravity acting on the suspended prototype tends to bring it back to the original rest position when displaced. The entity of such recovery force depends on the angular rotation of the cable w.r.t. to the local vertical. In particular, the longer the suspending cables the lower the perturbations. It is possible to estimate the horizontal forces introduced by the suspending system and design the setup to reduce them within acceptable limits. In the considered case, assuming 2.5 m long cables the maximum perturbing horizontal forces are on the order of $4 \div 5 \times 10^{-2}$ N, while the torques are below 7×10^{-3} Nm: maximum disturbances are on the order of $5 \div 10\%$ of nominal actuator force and $15 \div 20\%$ of nominal actuator torque. The torques due to the suspending system are acceptable and are not the main perturbations in the proposed laboratory setup.

Other perturbations to the ideal motion of the manipulator are due to the electrical wirings of the DEAs. In particular, the power supply of the second actuator (the suspended one) is achieved by means of loose cables that run vertically, parallel to the suspending system. When the robotic arm moves, such cables resist to the displacement due to their mass and residual rigidity. The resulting forces are difficult to estimate, but exert an important disturbance. The manipulator assembly and mountings have been manually tuned in order to minimize the effects of this perturbation. Nevertheless, the elastic forces due to the power supply cables are considerable and limit the actual workspace w.r.t. the theoretical one computed on the basis of the direct kinematics relation (Eq. 6.5) and the considerations presented in Sec. 4.7. Fig. 6.20 shows a comparison of the theoretical and measured workspace of the manipulator prototype (the negative-y half-plane is not shown for symmetry). The theoretical maximum values of stroke and rotation are $y_{max} = 5$ mm and $\theta_{max} = 17.2$ deg computed considering the attenuation at 0.05 Hz (the trajectory is traveled in 20 s, see Sec. 6.6.2).

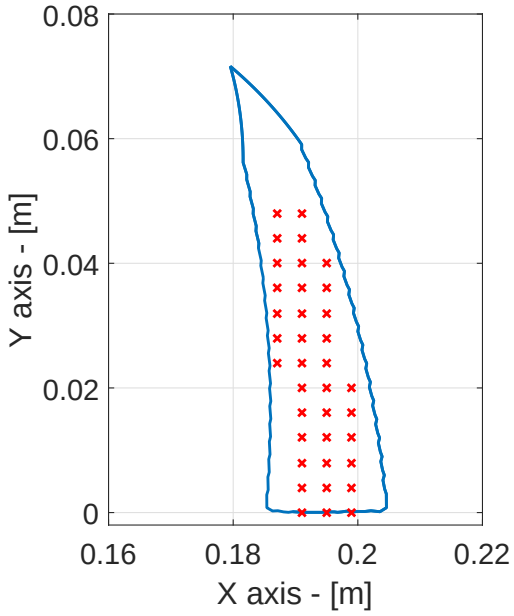

Fig. 6.20: Comparison between theoretical (blue envelope) and measured (red crosses) workspace of the tested manipulator (the negative-y half-plane is not shown for simmetry)

Although the described effects are significant, they are neglected in the prototype model since the feedback control system takes care of additional actuation that is required to minimize tracking errors. Control gains will be different from those simulated numerically also due to these uncertainties. Good results in terms of trajectory tracking are achieved, the trajectory length is limited and, therefore, the experiments below are not completely significant for the performance evaluation of the system. The experimental results presented in Sec. 6.6.2 derive from preliminary tests that aim at proving the feasibility of a complex multi-DoF system based on DEAs and controlled in feedback to achieve specific tracking tasks; the full performances

of such system, especially in terms of operational envelope, need to be investigated in depth by means of tests within a more sophisticated laboratory setup.

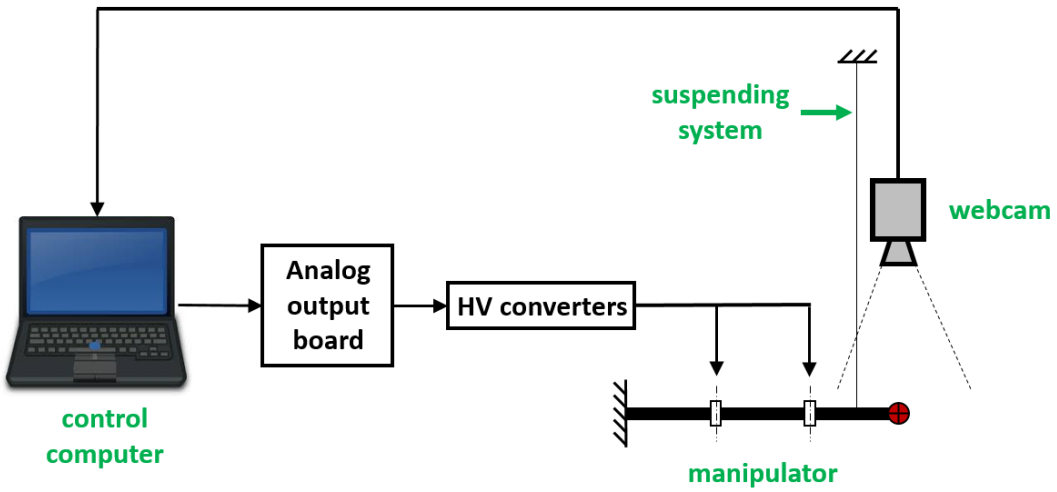

Fig. 6.21: Schematic representation of the laboratory setup for manipulator tests: a control computer commands the voltages to the HV converters through an analog output board, a flexible suspending system holds the manipulator, the position of the end-effector is measured via a vision system which feeds the information back to the controller

6.6.1.1 Vision system

The vision system described in Sec. 5.8.2 measures the x-y position of the end-effector (i.e. optical markers). A custom designed MATLAB® code similar to that described in the referenced section takes a measure of the displacement of two optical markers (see Fig. 5.27). Sampling frequency is 5 or 10 Hz. The relative position measure is computed with the following equations:

$$\begin{aligned} \check{p}_{e_x} &= \frac{n_{1_x} + n_{2_x} - 2n_{0_x}}{2} \frac{d_{ref}}{d_{pix}} \\ \check{p}_{e_y} &= \frac{n_{1_y} + n_{2_y} - 2n_{0_y}}{2} \frac{d_{ref}}{d_{pix}} \end{aligned} \tag{6.47}$$

where n_{i_j} are the pixel position of marker 1 or 2 ($i = 1,2$) in the x or y direction ($j = x,y$), $d_{ref} = 10$ mm is the reference distance between the markers in millimeters, d_{pix} is the measured distance between markers in pixels, n_{0_j} is the initial average x or y position of the markers

$$\begin{aligned} d_{pix} &= \sqrt{(n_{1_x} - n_{2_x})^2 + (n_{1_y} - n_{2_y})^2} \\ n_{0_j} &= \left. \frac{n_{1_j} + n_{2_j}}{2} \right|_{t=0} \end{aligned} \tag{6.48}$$

The uncertainty analysis of the measurement system is performed from Eq. 6.47. The uncertainty sources and their distribution are

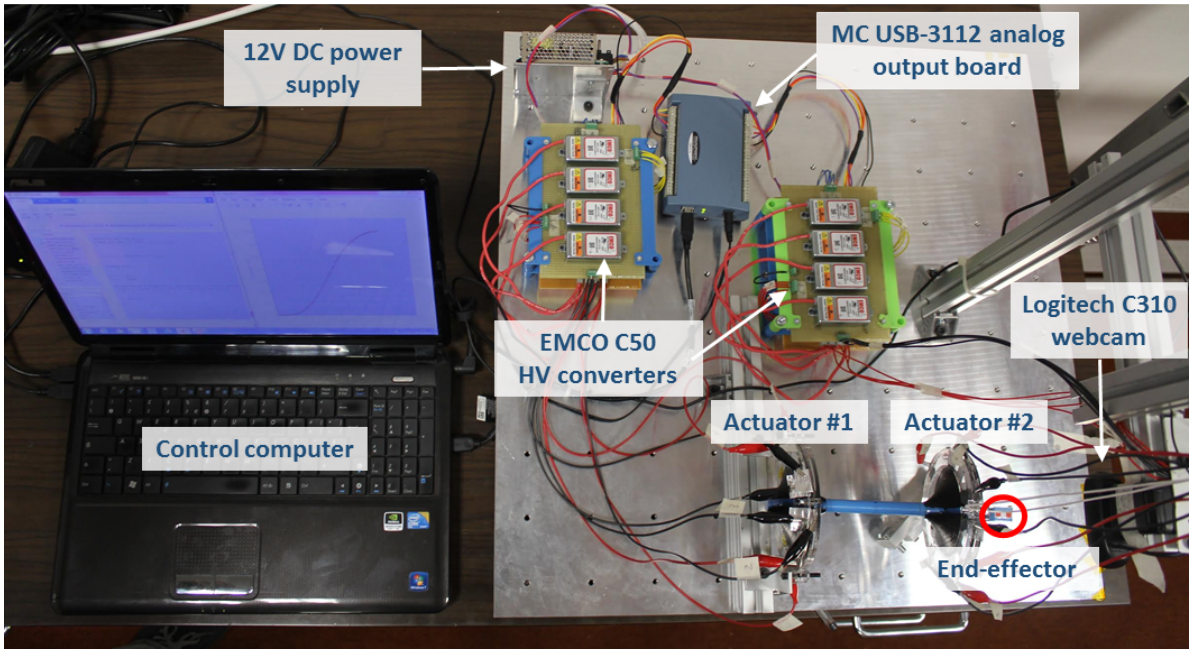

Fig. 6.22: Picture of the laboratory setup for manipulator tests; main components are: manipulator (bottom-right), power supply electronics (top-center), control PC (left)

- u_n [pix] is the uncertainty on the pixel position of the marker centroids: it depends on the vision algorithm used to detect the marker position and is estimated statistically by acquiring a large number of static measures (600) of the end-effector; the distribution is normal with standard deviation $\sigma_{n_x} = 0.067$ pix on the x direction and $\sigma_{n_y} = 0.08$ pix on the y direction;
- u_d [mm] is the uncertainty on the measure of the reference distance d_{ref}; the distribution is uniform with total interval width $w_d = 0.1$ mm and standard deviation $\sigma_d = \frac{w_d}{\sqrt{12}} = 0.029$ mm.

Uncertainty sources are combined with a Monte Carlo approach. A large number of values of a reference measurement $p^\star_{e_j}$ are computed by inserting in Eq. 6.49 random values, $u^\star_{n_i}$ and $u^\star_d$, of uncertainty picked from their probability distributions.

$$
\begin{aligned}
n^\star_{1_j} &= n_{1_j} + u^\star_{n_1} \\
n^\star_{2_j} &= n_{2_j} + u^\star_{n_2} \\
d^\star_{ref} &= d_{ref} + u^\star_d \\
d^\star_{pix} &= \sqrt{(n^\star_{1_x} - n^\star_{2_x})^2 + (n^\star_{1_y} - n^\star_{2_y})^2} \\
p^\star_{e_j} &= \frac{n^\star_{1_j} + n^\star_{2_j} - 2n_{0_j}}{2} \frac{d^\star_{ref}}{d^\star_{pix}}
\end{aligned}
\tag{6.49}
$$

If the number of values of $p^\star_{e_j}$ is large enough, they will have a statistical distribution around the real value. The standard deviation, σ_{p_j}, of such distribution can be used to compute the uncertainty of the whole measure, u_{p_j}, for example with $u_{p_j} = 2\sigma_{p_j}$. The standard deviation for the test results presented in the following Sec. 6.6.2 is $\sigma_{p_x} = 1.5 \times 10^{-5}$ m, while $\sigma_{p_y} = 1.8 \times 10^{-5}$ m.

6.6.2 Test results

This section presents the preliminary experimental results obtained for three trajectory cases and compare them to dynamic simulations. A preliminary version of these results have been presented in [114].

The commanded manipulator tasks are three: two rectilinear trajectories and one arc trajectory; all the trajectories are traveled in 20 s. The commanded time laws are fifth order polynomials (see Sec. 6.4.2). The length varies in the $0.025 \div 0.045$ m range approximately. Trajectory #1 is rectilinear and perpendicular to the manipulator axis, with a total length of 0.04 m. Trajectory #2 is rectilinear, slightly inclined w.r.t. the manipulator axis with a total length of 0.046 m. Trajectory #3 is a 30-deg arc trajectory with 0.045 m of radius, total length 0.026 m. The dynamic inversion algorithm presented in Eq. 6.34 is adopted. The model gain matrices in simulations are:

$$\mathbf{K}_d = \begin{bmatrix} 60 & 0 \\ 0 & 60 \end{bmatrix} \qquad \mathbf{K}_p = \begin{bmatrix} 250 & 0 \\ 0 & 250 \end{bmatrix} \qquad \mathbf{K}_i = \begin{bmatrix} 0 & 0 \\ 0 & 0 \end{bmatrix} \qquad (6.50)$$
$$k_0 = 5$$

while in experimental tests are:

$$\mathbf{K}_d = \begin{bmatrix} 0 & 0 \\ 0 & 0 \end{bmatrix} \qquad \mathbf{K}_p = \begin{bmatrix} 130 & 0 \\ 0 & 130 \end{bmatrix} \qquad \mathbf{K}_i = \begin{bmatrix} 250 & 0 \\ 0 & 250 \end{bmatrix} \qquad (6.51)$$
$$k_0 = 200$$

The simulations are performed with the numerical model described in Sec. 6.5. The actual dimensions of the actuators and other geometric parameters of the prototype manipulator tested are: $d = 80$ mm, $D = 12$ mm, $a = 23$ mm, $c = 25$ mm, $t = 1$ mm, $n = 1$, $\delta_{re} = 2\%$ and $\lambda_0 = 3.5$; $b_1 = 143$ mm and $b_2 = 52$ mm. Discrepancies between the actual test setup and the simulated system exist and include the disturbing effects due to the suspension system and to power cabling. In the following, the simulation results in the three mentioned trajectory cases are presented in comparison to laboratory results.

Test results are presented in Fig. 6.23-6.25 as x-y position in comparison to desired trajectory and simulated motion. The position error norm over time is presented for each test case in Fig. 6.26. Experimental results are summarized in Tab. 6.2. The maximum position error norm never exceeds 3×10^{-3} m or 7% of total trajectory length. Position error norm from simulations is, in general, roughly comparable to the experimental error, exept for trajectory #1.

The experimental results presented in this section give a preliminary feasibility prove of feedback-controlled, multi-DoF systems based on DE technology and their capability to accurately track given trajectories. The laboratory setup adopted for tests is characterized by limitations in terms of disturbances transmitted to the test prototype; for this reason the workspace of the robotic arm is much more limited than the theoretical one. Tests in more

sophisticated low-gravity experimental setups need to be implemented in order to fully characterize the overall system behavior.

Tab. 6.2: Manipulator test results: absolute error and relative error (w.r.t. trajectory length) for all tested trajectories.

Trajectory	Length [mm]	Max error [mm]	Max error [%]
#1	0.04	1.95	4.9%
#2	0.046	2.95	6.4%
#3	0.026	1.78	6.8%

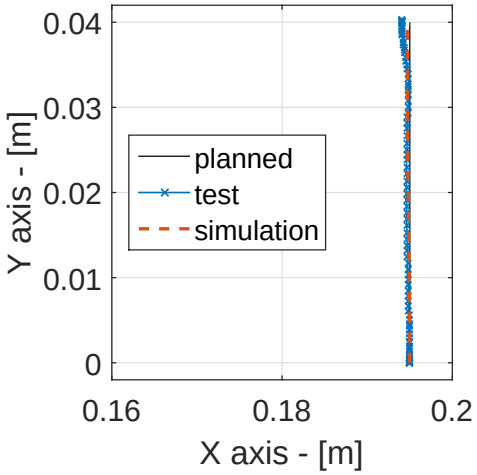

Fig. 6.23: Trajectory #1, rectilinear and perpendicular to arm axis.Planned trajectory (black), test results (blue w/ crosses) and simulation results (yellow dashed)

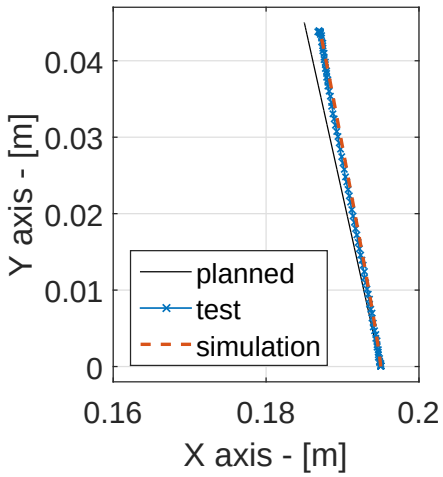

Fig. 6.24: Trajectory #2, rectilinear. Planned trajectory (black), test results (blue w/ crosses) and simulation results (yellow dashed)

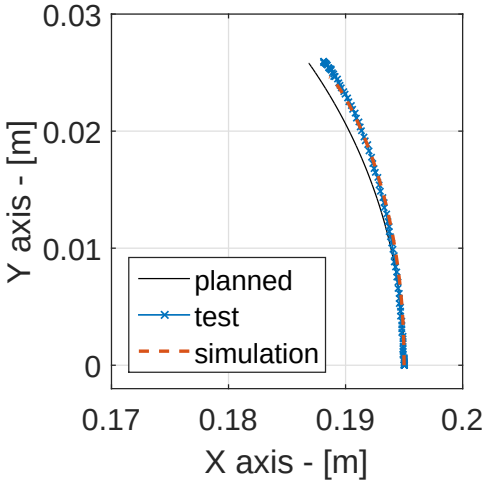

Fig. 6.25: Trajectory #3, arc. Planned trajectory (black), test results (blue w/ crosses) and simulation results (yellow dashed)

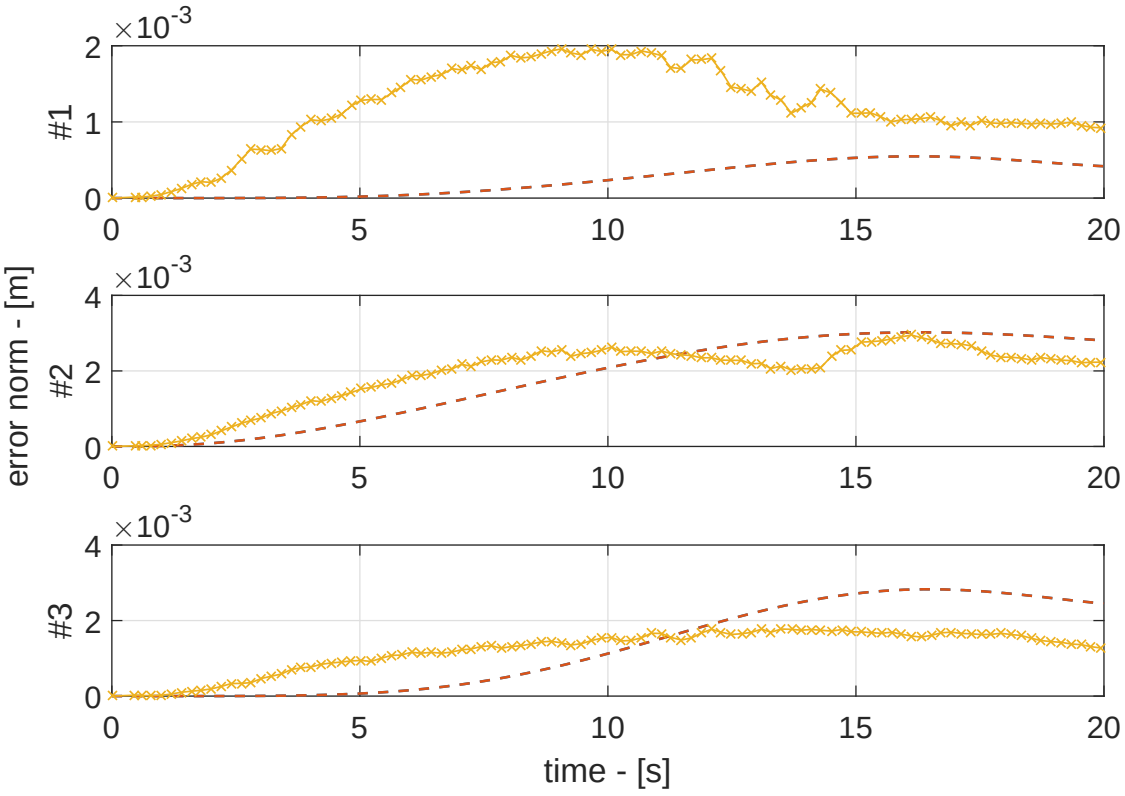

Fig. 6.26: Position error norm for the three tested trajectories: experimental data in blue, simulation result in yellow. Maximum experimental error is below 3×10^{-3} m in all cases

7 Conclusion

In this work, Dielectric Elastomer Actuators (DEAs) have been investigated as possible alternative to traditional motors in space robotics applications. The research activity focused on double-cone DEAs leading to the development of predictive models for the static and dynamic performances of such devices. In accordance to the general aim to study automated space systems, the developed models are compatible with the implementation of control algorithms in laboratory prototypes.

This section briefly presents the thesis contents recalling all the meaningful results achieved. A discussion on how the initial expectations and requirements are met is presented. In addition, possible future developments are envisaged.

7.1 Thesis outcome

The general objective of the thesis is to evaluate innovative actuation technologies for space robotics; the main expected output of the research is the feasibility proof of a robotic manipulator prototype based on low-TRL (Technology Readiness Level) devices. This objective is achieved by fulfilling two secondary goals:

1. development and validation of models to predict the actuator performances and ready-to-use tools for the design of robotic systems;
2. experimental validation in laboratory environment of a multi-body manipulator prototype.

The motivation on which this work is founded, comes from the wide interest on robotics that recently grew among the space community. A large variety of space missions can benefit from the implementation of automated systems reducing risks, costs, delays and errors deriving from human interaction (i.e. astronauts or ground operators) with space vehicles and structures. Future effective and efficient exploitation of space is strongly dependent on the development of key technologies to support existing and planned orbital assets, aiming to extend spacecraft operational life and to boost mission flexibility. Investigation on innovative actuation technologies is critical to improve space robotics performances and enable new applications. The TRL advancement of young technologies is at the basis of the development of new systems.

The most common actuators in space systems are conventional DC drives. Innovative technologies, like smart materials, are rarely adopted mainly due to reliability and heritage reasons. Nevertheless, implementation examples of smart technologies in space exist and it is worth mentioning the most notable: piezo-electric actuators and motors; shape memory devices; bimetallic actuators; Electro-Active Polymers (EAPs). The latter have not been employed in

space systems yet, although interest is growing around them on the basis of the appealing capabilities proved in many laboratory tests. Dielectric Elastomer Actuators are a promising branch of EAPs family, whose TRL is currently 2-3. DEAs have been selected to be investigated in this work for three main reasons:

1. good compromise performances in terms of stroke/deformation, force/torque and time response;
2. interesting characteristics like low mass and low power consumption, possibility to improve performances through design flexibility and modularity, multi-DoF configurations, simple manufacturing process, low costs, solid state actuation (no friction), self-sensing capability;
3. highly innovative technology with low TRL.

Double-cone actuators have been selected for their good performances and multi-DoF architecture.

The thesis activities and main results are reported schematically in the following:

- *Actuator steady-state performances estimation*
  Once a set of geometric and manufacturing parameters have been identified, numerical simulations based on literature as well as newly developed FEM models have been performed in order to collect a large number of performance data. Interpolating relations have been obtained from the collected data and allow to estimate the steady-state performances of the actuator. The mean error on estimations is 6.1% for angular rotation, 10.6% for torque, 22.5% for linear stroke and 11.8% for force.

- *Actuator time response estimation*
  A different approach has been adopted to model the dynamic behavior of DEAs: transfer function (TF) based models have been developed on the basis of time dependent data from long term tests. The prediction capabilities of TF models have been evaluated by comparison with experimental step response. The mean error on the 70% rise time is 15% for angular rotation, 9.5% for torque, 14% for linear stroke and 14% for force; the mean error on amplitude for $t > t_r$ is 4% for angular rotation, 4% for torque, 9% for linear stroke and 11% for force.

- *Feedback control of double-cone actuator*
  The developed models are suitable for the implementation of control algorithms and, consequently, for robotic applications. The capability to control the actuator have been experimentally proven by developing Single Input / Single Output compensators to actuate both DoF independently. Good accordance has been obtained between the simulated and the experimentally measured time behavior with errors compatible with the prediction inaccuracies of the mentioned models.

- *Robotic arm prototype testing*
  A multi-body application of double-cone actuators have been designed, manufactured and tested along with a proper control algorithm. The robotic arm is composed by two

DEAs mounted in series. Each actuator has two DoFs and the manipulator moves in the plane. Two degrees of kinematic redundancy are achieved in the manipulator by controlling only the in plane position of the end-effector. The arm is suspended by an inextensible cable that reduces the effects of gravity on the motion. The experimental task is the tracking of simple trajectories. A vision system monitors the position of the end-effector (optical marker) and feeds the position information to a control computer that commands the voltage actuation to the joints through a properly designed control algorithm. The kinematic redundancy is exploited by the controller to optimize the end-effector trajectory to achieve a given objective like, for example, joint limits avoidance. The system performs well and the maximum position error norm is 6.4% of total path length for linear trajectory and 6.8% for arc trajectory.

In view of the results achieved, the requirements defined initially from an Active Debris Removal (ADR) mission simulation have been met partially. Tab. 3.2 summarizes the expected forces and torques at manipulator joints: in the best cases, torque is ~ 5 Nm and normal force is ~ 7 N. Test results on actuators presented in Fig. 5.7 and Fig. 5.9, as well as the relations shown in Eq. 5.19 allow to infer that the force requirement can be easily satisfied, for example by implementing a multi-layer actuator with a number of elastomer layers ranging between 5 and 10. Differently, the torque requirement is harder to meet, since even a 10-layer actuator can reasonably output only 0.5 Nm of force. Nevertheless, by slightly relaxing the requirements it is possible to reach a compromise situation. An acceptable level of expected joint torque can be achieved by exploiting the quadratic relation between the debris angular momentum and the reaction forces/torques; in particular, if angular momentum does not exceed 500 kg m^2 rad/s the 10-layer actuator is capable to provide the required torque. Such relaxed requirement turns in a reduced debris angular velocity (maximum 0.02 rad/s) or mass (maximum 280 kg). Although the requirements have to be relaxed in order to be completely satisfied, this work proves that DEA technology can be potentially applied to ADR missions and other OOS scenarios.

7.2 Research impact

Relevant advancements in the modeling of DE double-cone actuators as well as in the experimental validation of DE robotic systems are presented in this thesis. The work aims at studying the feasibility of space applications based on this young technology. The research impact can be summarized in four main points:

1. the improved knowledge on double-cone DE actuators mainly represented by the predictive models for the actuator performances;
2. the tested robotic arm manipulator is among the most complex multi-DoF, multi-body robotic systems based on DE devices and controlled in feedback;
3. the experimental activity conducted successfully validated the robotic system in laboratory environment pushing the TRL to 3-4;

4. the thesis results consolidate the technology and allow to consider a number of terrestrial and space applications particularly referring to compliant systems and soft manipulation.

Although a few multi-DoF and multi-actuator systems based on DEAs are available in literature, the presented redundant manipulator is innovative as it implements a feedback control and trajectory optimization algorithms, reaching a considerable level of complexity. Furthermore, the prototype was evaluated with good results in laboratory environment, matching the requirements for TRL 3-4. The work results are promising for the future development of innovative robotic systems; the technology is particularly suitable for robots that operate in critical environments, interacting with brittle objects or human operators. Smooth motion, absence of vibrations and compliance due to soft materials allow to safely perform tasks reducing collision and other risks.

7.3 Future developments

Future developments of the research activities include the implementation of integrated feedback sensors as well as embedded wiring for power supply, and a thorough assessment of survivability of DE technology to the space environment.

The self-sensing capability of DE devices can be exploited to directly measure the manipulator joint variables, thus avoiding to use of the feedback vision system which is bulky, heavy and requires considerable computational power. Self-sensing in DEAs has been demonstrated and allows to determine the actuator stroke/rotation by directly measuring the material deformation. Improvements are required in the power supply wiring: high voltages require extreme caution in the operation of DE devices in order to avoid short circuits. Great advantages would come from the embedding of cables inside the actuators support structures which are usually made of non-conductive, plastic materials.

A critical development required for space application of DEAs is to verify the compatibility with the space environment. Although some elastomers can withstand the thermal loads and wide temperature ranges experimented by spacecraft on orbit and outgassing due to vacuum can be mitigated, the effects of radiation and atomic oxygen on the dielectric membrane need to be evaluated experimentally. In addition, the interaction of charged electrodes with the plasma environment needs to be assessed to understand risks of arching.

Bibliography

[1] A. Flores-Abad, O. Ma, K. Pham, and S. Ulrich. „A review of space robotics technologies for on-orbit servicing“. In: *Progress in Aerospace Sciences* 68 (2014), pp. 1–26. DOI: 10.1016/j.paerosci.2014.03.002 (cit. on p. 5).

[2] R. Rembala and C. Ower. „Robotic assembly and maintenance of future space stations based on the ISS mission operations experience“. In: *Acta Astronautica* 65.7-8 (2009), pp. 912–920. DOI: 10.1016/j.actaastro.2009.03.064 (cit. on p. 5).

[3] C. Sallaberger. „Robotic assembly and maintenance of future space stations based on the ISS mission operations experience“. In: *Acta Astronautica* 41.4-10 (1997), pp. 239–246. DOI: 10.1016/S0094-5765(98)00082-4 (cit. on p. 5).

[4] N. Sato and S. Doi. „JEM remote manipulator system (JEMRMS) human-in-the-loop test“. In: *Proc. The 22nd international symposium on space technology and science*. 2000, pp. 1195–1199 (cit. on p. 5).

[5] G. Didot, M. Oort, J. Kouwen, and P. Verzijden. „The ERA system: control architecture and performance results“. In: *Proc. International symposium on artificial intelligence, robotics and automation in space*. 2001 (cit. on p. 5).

[6] G. Hirzinger, B. Brunner, J. Dietrich, and J. Heindl. „ROTEX - the first remotely controlled robot in space“. In: *Proc. IEEE international conference on robotics and automation*. 1994, pp. 2604–2611 (cit. on p. 6).

[7] G. Hirzinger, K. Landzettel, D. Reintsema, C. Preusche, A. Albu-Schäffer, and B. Rebele. „ROKVISS - robotics component verification on ISS“. In: *Proc. International symposium on artificial intelligence, robotics and automation in space*. ESA, 2005 (cit. on p. 6).

[8] C. Borst, C. Ott, T. Wimbock, B. Brunner, B. B. Franziska Zacharias, U. Hillenbrand, S. Haddadin, A. Albu-Schäffer, and G. Hirzinger. „A humanoid upper body system for two-handed manipulation“. In: *Proc. IEEE International Conference on Robotics and Automation*. 2007 (cit. on pp. 6, 8).

[9] W. Bluethmann, R. Ambrose, M. Diftler, S. Askew, E. Huber, M. Goza, F. Rehnmark, C. Lovchik, and D. Magruder. „Robonaut: A Robot Designed to Work with Humans in Space“. In: *Autonomous Robots* 14.2 (2003), pp. 179–197. DOI: 10.1023/A:1022231703061 (cit. on p. 7).

[10] M. Diftler, J. Mehling, M. Abdallah, N. Radford, L. Bridgwater, A. Sanders, R. Askew, D. Linn, J. Yamokoski, F. Permenter, B. Hargrave, R. Platt, R. Savely, and R. Ambrose. „Robonaut 2 – The First Humanoid Robot in Space“. In: *Proc. IEEE International Conference on Robotics and Automation*. 2011 (cit. on p. 7).

[11] M. Oda, K. Kibe, and F Yamagata. „ETS-VII, Space Robot In-Orbit Experiment Satellite“. In: *Proc. IEEE International Conference on Robotics and Automation*. 1996 (cit. on p. 8).

[12] K. Yoshida. „Contact dynamics and control strategy based on impedance matching for robotic capture of a non-cooperative satellite“. In: *Proc. The 15th CISM-IFToMM symposium on robot design, dynamics and control - ROMANSY*. 2004 (cit. on p. 8).

[13] T. Mulder. „Orbital express autonomous rendezvous and capture flight operations.“ In: *Proc. AIAA/AAS astrodynamics specialist conference and exhibit*. 2008 (cit. on p. 8).

[14] R. B. Friend. „Orbital express program summary and mission overview“. In: *Proc. SPIE defense and security symposium*. 2008 (cit. on p. 8).

[15] B. Kelm, J. Angielski, S. Butcher, N.G.Creamer, K. Harris, C. Henshaw, J. Lennon, W. E. Purdy, F. A. Tasker, W. S. Vincent, and B. Whalen. „FREND: Pushing the Envelope of Space Robotics“. In: *NRL Review - Space Research and Satellite Technology* (2008), pp. 239–241 (cit. on p. 8).

[16] T. J. Debus and S. P. Dougherty. „Overview and performance of the front-end robotics enabling near-term demonstration (FREND) robotic arm“. In: *Proc. AIAA infotech@ aerospace conference*. 2009 (cit. on p. 8).

[17] T. Rumford. „Demonstration of autonomous rendezvous technology (DART) project summary“. In: *Proc. SPIE defense and security symposium*. 2003 (cit. on p. 9).

[18] D. Reintsema, B. Sommer, T. Wolf, J. Theater, A. Radthke, J. Sommer, W. Naumann, and P. Rank. „DEOS - the in-flight technology demonstration of Germans robotics approach to dispose malfunctioned satellites“. In: *Proc. ESA workshop on advanced space technologies for robotics and automation*. 2011 (cit. on p. 9).

[19] D. Wingo. „Orbital recovery's responsive commercial space tug for life extension missions“. In: *Proc. AIAA second responsive space conference*. 2004 (cit. on p. 10).

[20] K. Yoshida. „Achievements in space robotics“. In: *Robotics & Automation Magazine, IEEE* 16.4 (2009), pp. 20–28 (cit. on p. 10).

[21] J. Andión, C Burgui, and G Migliorero. „Rotary actuator for space applications“. In: *11th European Space Mechanisms and Tribology Symposium, ESMATS 2005*. Vol. 591. 2005, pp. 317–322 (cit. on pp. 11, 12).

[22] A. Ledoux. „Theory of piezoelectric materials and their applications in civil engineering“. PhD thesis. Massachusetts Institute of Technology, 2011 (cit. on p. 14).

[23] F. Claeyssen, R. L. Letty, E. F. Barillot, E. N. Lhermet, and E. G. Rajeev. „Amplified Piezoelectric Actuators for Air & Space Applications“. In: *www.cedrat.com*. 2003 (cit. on pp. 15, 18).

[24] F. Barillot, R. L. Letty, F. Claeyssen, N. Lhermet, M. Yorck, and S. Ikoss. „Design and functional tests of a XY piezoelectric stage for the ROSETTA/MIDAS“. In: *European Space Agency Publications* SP438 (1999), pp. 121–126 (cit. on p. 16).

[25] F. Burger and J. Eder. „High-precision pointing device for the LASCO instrument on SOHO“. In: *Proc. 6th European Space Mechanisms & Tribology Symposium*. Vol. SP-374. 1995 (cit. on p. 16).

[26] R. Le Letty, F. Barillot, H. Fabbro, F. Claeyssen, P. Guay, and L. Cadiergues. „Miniature Piezo mechanisms for optical and space applications“. In: *Proc. 9th International Conference on New Actuators*. 2004, pp. 177–180 (cit. on p. 17).

[27] M. Meftah, A. Irbah, R Le Letty, A Bataille, E. Ducourt, G. Poiet, M Privat, et al. „The PICARD/SODISM Pointing Mechanism: From the Design to the Flight Performances“. In: *Proc. 14th European Space Mechanisms & Tribology Symposium (ESMATS)*. 2011 (cit. on p. 17).

[28] L. Cadiergues, C. Bourdit, D. Trouchet, V. Larchet, P. Sugranes, R. Le Letty, and F. Barillot. „A mirror control mechanism for space telescope“. In: *Proc. 10th European Space Mechanisms & Tribology Symposium (ESMATS), SP-524*. 2003, pp. 24–26 (cit. on p. 17).

[29] N. Rijnveld and J. A. C. M. Pijnenburg. „Picometer stable scan mechanism for gravitational wave detection in space“. In: *Proc. SPIE*. Vol. 7734. 2010. DOI: 10.1117/12.857040 (cit. on pp. 17, 18).

[30] F. Bourgain, O. Sosnicki, F. Barillot, F. Claeyssen, J. P. Lelay, E. Prevost, T. Pain, and B. Germain. „Beam steering mechanism for earthcare atmospheric LIDAR instrument - an improved piezoelectric tip-tilt mechanism“. In: *15th European Space Mechanisms and Tribology Symposium - ESMATS 2013*. 2013 (cit. on pp. 17, 18).

[31] D. Blake, D. Vaniman, C. Achilles, R. Anderson, D. Bish, T. Bristow, C. Chen, S. Chipera, J. Crisp, D. Des Marais, et al. „Characterization and calibration of the CheMin mineralogical instrument on Mars Science Laboratory“. In: *Space Science Reviews* 170.1-4 (2012), pp. 341–399 (cit. on pp. 17, 18).

[32] G. Noci, G. Matticari, P. Siciliano, L. Fallerini, L. Boschini, and V. Vettorello. „Cold Gas Micro Propulsion System for Scientific Satellites fine pointing: Review of Development and Qualification activities at Thales Alenia Space Italia“. In: *45th AIAA/ASME/SAE/ASEE Joint Propulsion Conference and Exhibit. Reston, VA, USA: AIAA*. 2009 (cit. on p. 17).

[33] L. Vaillon and C. Philippe. „Passive and active microvibration control for very high pointing accuracy space systems“. In: *Smart materials and structures* 8.6 (1999), pp. 719–728 (cit. on p. 17).

[34] A. A. Hanieh, A Preumont, and N Loix. „Piezoelectric Stewart platform for general purpose active damping interface and precision control“. In: *European Space Agency Publications - ESA SP* 480 (2001), pp. 331–334 (cit. on p. 17).

[35] E. Courau, P. Guay, and P. Bousquet. „CASTOR experiment results“. In: *42nd AIAA/ASME/ASCE/-AHS/ASC Structures, Structural Dynamics, and Materials Conference and Exhibit*. 2001 (cit. on p. 18).

[36] A. Neukom, R. Romano, and P. M. Nellen. „Testing and lessons learnt of LISA GPRM“. In: *13th European Space Mechanisms and Tribology Symposium - ESMATS 2009*. 2009, p. 23 (cit. on p. 19).

[37] J. M. Jani, M. Leary, A. Subic, and M. A. Gibson. „A review of shape memory alloy research, applications and opportunities“. In: *Materials & Design* 56 (2014), pp. 1078–1113 (cit. on p. 20).

[38] D. J. Hartl and D. C. Lagoudas. „Aerospace applications of shape memory alloys“. In: *Proc. of the Institution of Mechanical Engineers, Part G: Journal of Aerospace Engineering* 221.4 (2007), pp. 535–552 (cit. on p. 21).

[39] W. Huang and W. Toh. „Training two-way shape memory alloy by reheat treatment“. In: *Journal of materials science letters* 19.17 (2000), pp. 1549–1550 (cit. on p. 21).

[40] R. Edeson, M. Whalley, B. Kent, S. Canfer, and E. Sawyer. „SMA gas release mechanism for the Rosetta Lander’s Ptolemy instrument“. In: *Acta Astronautica* 58.11 (2006), pp. 576–582 (cit. on pp. 22, 23).

[41] W. Purdy and M. Hurley. „The Clementine Mechanisms“. In: *29th Aerospace Mechanisms Symposium, NASA Johnson Space Center*. 1995 (cit. on p. 23).

[42] D. B. Carte, N. K. Inamdar, M. P. Jones, and R. A. Masterson. „Design and Test of a Deployable Radiation Cover for the REgolith X-ray imaging Spectrometer“. In: *42nd MEA Aerospace Mechanisms Symposium*. 2014 (cit. on p. 23).

[43] B. Fleck, E. Marsch, R. Schwenn, E. Antonucci, P. Bochsler, J.-L. Bougeret, R. Harrison, R. Marsden, and J.-C. Vial. „Solar Orbiter - A High Resolution Mission to the Sun and Inner Heliosphere“. In: *Bulletin of the American Astronomical Society*. Vol. 32. 2000, p. 828 (cit. on p. 23).

[44] B. Carpenter and J. Lyons. *Lightweight flexible solar array experiment summary*. Tech. rep. Technical report, Preliminary Technology and Science Validation Report, NASA Goddard Space Flight Center.(Cited on page 36.), 2002 (cit. on p. 23).

[45] S. Montminy, E. Dupuis, and H. Champliaud. „Mechanical design of a hopper robot for planetary exploration using SMA as a unique source of power“. In: *Acta Astronautica* 62.6 (2008), pp. 438–452 (cit. on p. 24).

[46] P. P. Jenkins and G. A. Landis. „A rotating arm using shape-memory alloy“. In: *Proc. 29th Aerospace Symposium, NASA CP-3293*. 1995, pp. 167–171 (cit. on p. 24).

[47] D. W. Hengeveld, M. M. Mathison, J. E. Braun, E. A. Groll, and A. D. Williams. „Review of modern spacecraft thermal control technologies“. In: *HVAC&R Research* 16.2 (2010), pp. 189–220 (cit. on p. 25).

[48] P. Muller, H. Henkel, and S. Klinkner. „Miniaturized Single-Shot Valve and its Application to the ExoMars Pasteur Payload“. In: (cit. on p. 26).

[49] Y. Bar-Cohen. „Electro-active polymers: current capabilities and challenges“. In: *Proc. of SPIE, the International Society for Optical Engineering*. Vol. 4695. SPIE. 2002, pp. 1–7 (cit. on p. 26).

[50] R. Pelrine, R. D. Kornbluh, Q. Pei, and J. Joseph. „High-speed electrically actuated elastomers with strain greater than 100%“. In: *Science* 287.5454 (2000), pp. 836–839. DOI: 10.1126/science.287.5454.836 (cit. on p. 26).

[51] R. D. Kornbluh, R. Pelrine, Q. Pei, R. Heydt, S. Stanford, S. Oh, and J. Eckerle. „Electroelastomers: applications of dielectric elastomer transducers for actuation, generation, and smart structures“. In: *Proc. SPIE Smart Structures and Materials 2002: Industrial and Commercial Applications of Smart Structures Technologies*. Vol. 4698. 2002. DOI: 10.1117/12.475072 (cit. on p. 27).

[52] J. Rossiter, P. Walters, and B. Stoimenov. „Printing 3D dielectric elastomer actuators for soft robotics“. In: *Proc. SPIE Electroactive Polymers and Devices (EAPAD)*. Vol. 7287. 2009. DOI: 10.1117/12.815746 (cit. on p. 27).

[53] Q. Pei, M. Rosenthal, S. Stanford, H. Prahlad, and R. Pelrine. „Multiple-degrees-of-freedom electroelastomer roll actuators“. In: *Smart Materials and Structures* 13.5 (2004), N86. DOI: 10.1088/0964-1726/13/5/N03 (cit. on pp. 27, 29, 30, 33, 34).

[54] K. Jung, K. J. Kim, and H. R. Choi. „A self-sensing dielectric elastomer actuator“. In: *Sensors and Actuators A* 143 (2008), pp. 343–351. DOI: 10.1016/j.sna.2007.10.076 (cit. on pp. 27, 63, 64).

[55] F. Carpi and D. D. Rossi. „Dielectric elastomer cylindrical actuators: electromechanical modelling and experimental evaluation“. In: *Materials Science and Engineering C* 24 (2004), pp. 555–562. DOI: 10.1016/j.msec.2004.02.005 (cit. on pp. 27, 29, 36).

[56] M. T. Wissler and E. Mazza. „Modeling of a pre-strained circular actuator made of dielectric elastomers“. In: *Sensors and Actuators A* 120 (2005), pp. 184–192. DOI: 10.1016/j.sna.2004.11.015 (cit. on p. 27).

[57] F. Carpi, C. Salaris, and D. D. Rossi. „Folded dielectric elastomer actuators“. In: *Smart Materials and Structures* 16.2 (2007), S300. DOI: 10.1088/0964-1726/16/2/S15 (cit. on pp. 27, 30, 31).

[58] R. Vertechy, G. Berselli, V. P. Castelli, and G. Vassura. „Optimal Design of Lozenge-shaped Dielectric Elastomer Linear Actuators: Mathematical Procedure and Experimental Validation“. In: *Journal of Intelligent Material Systems and Structures* 21.5 (2009), pp. 836–839. DOI: 10.1177/1045389X09356608 (cit. on pp. 27, 29).

[59] I. A. Anderson, T. C. H. Tse, T. Inamura, B. M. O'Brien, T. McKay, and T. Gisby. „A soft and dexterous motor“. In: *Applied Physics Letters* 98 (2011), p. 123704. DOI: 10.1063/1.3565195 (cit. on pp. 27, 29, 30, 36).

[60] J. C. Koo, H. R. Choi, M. Y. Jung, K. M. Jung, J. D. Nam, and Y. K. Lee. „Design and Control of Three-DOF Dielectric Polymer Actuator“. In: *Key Engineering Materials* 297-300 (2005), pp. 665–670. DOI: 10.4028/www.scientific.net/KEM.297-300.665 (cit. on p. 27).

[61] P. Chouinard and J.-S. Plante. „Bistable Antagonistic Dielectric Elastomer Actuators for Binary Robotics and Mechatronics“. In: *IEEE/ASME Transactions on Mechatronics* 17.5 (2011), pp. 857–865. DOI: 10.1109/TMECH.2011.2135862 (cit. on p. 27).

[62] A. T. Conn and J. Rossiter. „Antagonistic dielectric elastomer actuator for biologically-inspired robotics“. In: *Proc. SPIE Electroactive Polymers and Devices (EAPAD)*. Vol. 7976. 2011. DOI: 10.1117/12.880438 (cit. on p. 27).

[63] A. T. Conn and J Rossiter. „Towards holonomic electro-elastomer actuators with six degrees of freedom“. In: *Smart Materials and Structures* 21.3 (2012), p. 035012. DOI: 10.1088/0964-1726/21/3/035012 (cit. on pp. 27, 32, 36, 41, 64, 83).

[64] M. Wissler and E. Mazza. „Modeling of a pre-strained circular actuator made of dielectric elastomers“. In: *Sensors and Actuators A: Physical* 120.1 (2005), pp. 184–192 (cit. on pp. 27, 28).

[65] A. M. Tews, K. L. Pope, and A. J. Snyder. „Pressure-volume characteristics of dielectric elastomer diaphragms“. In: *Proc. SPIE*. Vol. 5051. 2003, pp. 159–169. DOI: 10.1117/12.484305 (cit. on p. 28).

[66] J.-S. Plante, L. M. Devita, and S. Dubowsky. „A road to practical dielectric elastomer actuators based robotics and mechatronics: discrete actuation“. In: *Proc. SPIE*. Vol. 6524. 2007, pp. 652406–652406–15. DOI: 10.1117/12.715236 (cit. on pp. 28, 33, 34).

[67] N. Bonwit, J. Heim, M. Rosenthal, C. Duncheon, and A. Beavers. „Design of commercial applications of EPAM technology“. In: *Proc. SPIE*. Vol. 6168. 2006, pp. 616805–616805–10. DOI: 10.1117/12.658775 (cit. on pp. 28, 29).

[68] P Chakraborti, H. K. Toprakci, P Yang, N Di Spigna, P Franzon, and T Ghosh. „A compact dielectric elastomer tubular actuator for refreshable Braille displays“. In: *Sensors and Actuators A: Physical* 179 (2012), pp. 151–157 (cit. on p. 29).

[69] F. Carpi, A. Migliore, G. Serra, and D. De Rossi. „Helical dielectric elastomer actuators“. In: *Smart Materials and Structures* 14.6 (2005), p. 1210 (cit. on pp. 29, 30).

[70] G. Kovacs, L. Düring, S. Michel, and G. Terrasi. „Stacked dielectric elastomer actuator for tensile force transmission“. In: *Sensors and Actuators A: Physical* 155.2 (2009), pp. 299–307 (cit. on pp. 30, 31).

[71] P. Lochmatter and G. Kovacs. „Design and characterization of an active hinge segment based on soft dielectric EAPs“. In: *Sensors and Actuators A: Physical* 141.2 (2008), pp. 577–587 (cit. on p. 31).

[72] R. Zhang. „Development of dielectric elastomer actuators and their implementation in a novel force feedback interface“. PhD thesis. Department of Mechanical Engineering, Swiss Federal Institute of Technology, Zurich, Switzerland, 2006 (cit. on p. 31).

[73] H. Wang and C. Li. „A linear dielectric EAP actuator with large displacement output“. In: *Measuring Technology and Mechatronics Automation, 2009. ICMTMA'09. International Conference on*. Vol. 1. IEEE. 2009, pp. 73–76 (cit. on p. 32).

[74] G. Berselli, R. Vertechy, G. Vassura, and V. Parenti-Castelli. „Optimal Synthesis of Conically Shaped Dielectric Elastomer Linear Actuators: Design Methodology and Experimental Validation“. In: *IEEE/ASME Transactions on Mechatronics* 16.1 (2011), pp. 67–79. DOI: 10.1109/TMECH.2010.2090664 (cit. on pp. 32, 53, 56, 57).

[75] H. Wang and J. Zhu. „Implementation and simulation of a cone dielectric elastomer actuator“. In: *International Symposium on Optomechatronic Technologies*. SPIE. 2008 (cit. on p. 32).

[76] P. Chouinard and J.-S. Plante. „Bistable antagonistic dielectric elastomer actuators for binary robotics and mechatronics“. In: *Mechatronics, IEEE/ASME Transactions on* 17.5 (2012), pp. 857–865 (cit. on p. 33).

[77] A. Wingert, M. D. Lichter, and S. Dubowsky. „On the design of large degree-of-freedom digital mechatronic devices based on bistable dielectric elastomer actuators“. In: *Mechatronics, IEEE/ASME Transactions on* 11.4 (2006), pp. 448–456 (cit. on p. 33).

[78] J. Shintake, S. Rosset, B. Schubert, S. Mintchev, D. Floreano, and H. R. Shea. „DEA for soft robotics: 1-gram actuator picks up a 60-gram egg“. In: *Proc. SPIE*. Vol. 9430. 2015, 94301S–94301S–6. DOI: 10.1117/12.2084043 (cit. on pp. 33, 34).

[79] S. Cho, S. Ryew, J. Jeon, H. Kim, J. Nam, and H. Choi. „Development of micro inchworm robot actuated by electrostrictive polymer actuator“. In: *SPIE 8th Annual International Symposium on Smart Structures and Materials*. SPIE. 2001, pp. 466–474 (cit. on pp. 33, 34).

[80] K. Jung, J. Nam, Y. Lee, and H. Choi. „Micro inchworm robot actuated by artificial muscle actuator based on nonprestrained dielectric elastomer“. In: *Smart Structures and Materials*. 2004, pp. 357–367 (cit. on pp. 33, 34).

[81] M. Artusi, M. Potz, J. Aristizabal, C. Menon, S. Cocuzza, and S. Debei. „Electroactive elastomeric actuators for the implementation of a deformable spherical rover“. In: *Mechatronics, IEEE/ASME Transactions on* 16.1 (2011), pp. 50–57 (cit. on pp. 33, 34).

[82] Y Bar-Cohen, S Leary, A Yavrouian, K Oguro, S Tadokoro, J Harrison, J Smith, and J Su. „Challenges to the transition of IPMC artificial muscle actuators to practical application“. In: *MRS Symposium Proc.* Citeseer. 1999 (cit. on p. 34).

[83] C. Menon and D. Izzo. „Satellite Pointing System based on EAP actuators“. In: *Proc. of TAROS*. 2005 (cit. on p. 34).

[84] C. Menon, F. Carpi, and D. De Rossi. „Concept design of novel bio-inspired distributed actuators for space applications“. In: *Acta Astronautica* 65.5 (2009), pp. 825–833 (cit. on p. 34).

[85] F. Carpi, P. Sommer-Larsen, D. De Rossi, P. Gaudenzi, L. Lampani, F. Campanile, E. Pfeiffer, G. Neri, and S. Baldacci. „Electroactive polymers: new materials for spacecraft structures“. In: *Spacecraft Structures, Materials and Mechanical Testing 2005*. Vol. 581. 2005, p. 153 (cit. on p. 34).

[86] F. Branz, L. Savioli, A. Francesconi, F. Sansone, C. Menon, and J. Krahn. „Soft-Docking System for Capture of Irregularly Shaped, Uncontrolled Space Objects“. In: *Proc. Sixth European Conference on Space Debris*. ESA. 2013 (cit. on p. 37).

[87] J.-C. Liou and N. L. Johnson. „A sensitivity study of the effectiveness of active debris removal in LEO“. In: *Acta Astronautica* 64.2 (2009), pp. 236–243 (cit. on p. 38).

[88] J.-C. Liou, N. L. Johnson, and N. Hill. „Controlling the growth of future LEO debris populations with active debris removal“. In: *Acta Astronautica* 66.5 (2010), pp. 648–653 (cit. on p. 38).

[89] L. DeLuca, F Bernelli, F Maggi, P Tadini, C Pardini, L Anselmo, M Grassi, D Pavarin, A Francesconi, F Branz, et al. „Active space debris removal by a hybrid propulsion module“. In: *Acta Astronautica* 91 (2013), pp. 20–33 (cit. on p. 38).

[90] H Cowardin, G Ojakangas, M Mulrooney, S Lederer, and J. Liou. „Optical signature analysis of tumbling rocket bodies via laboratory measurements“. In: *Advanced Maui Optical and Space Surveillance Technologies Conference*. Vol. 1. 2012, p. 61 (cit. on p. 39).

[91] L. Savioli, A. Francesconi, F. Maggi, L. Olivieri, E. Lorenzini, and C. Pardini. „Space debris removal using multi-mission modular spacecraft“. In: *Proc. of the 6th European Conference on Space Debris* (cit. on p. 39).

[92] J. R. Wertz and W. J. Larson. „Space mission analysis and design“. In: *MicrocosmPress, Torrance* (1999) (cit. on p. 39).

[93] F. Fan and J. Szpunar. „Characterization of Viscoelasticity and Self-Healing Ability of VHB 4910“. In: *Macromolecular Materials and Engineering* 300.1 (2015), pp. 99–106. DOI: 10.1002/mame.201400122 (cit. on pp. 45, 57).

[94] G. A. Holzapfel. *Nonlinear solid mechanics*. Vol. 24. Wiley Chichester, 2000 (cit. on p. 45).

[95] O. Yeoh. „Characterization of elastic properties of carbon-black-filled rubber vulcanizates“. In: *Rubber chemistry and technology* 63.5 (1990), pp. 792–805 (cit. on p. 52).

[96] Y.-C. Fung. *Biomechanics: mechanical properties of living tissues*. Springer Science & Business Media, 2013 (cit. on p. 54).

[97] M. T. Wissler. „Modeling dielectric elastomer actuators“. PhD thesis. Swiss Federal Institute of Technology in Zurich, 2007 (cit. on pp. 54, 57, 91).

[98] X. Zhang, M. Wissler, B Jaehne, R. Breonnimann, and G. Kovacs. „Effects of crosslinking, prestrain, and dielectric filler on the electromechanical response of a new silicone and comparison with acrylic elastomer“. In: *Smart Structures and Materials*. SPIE. 2004, pp. 78–86 (cit. on p. 56).

[99] R. Sahu, K Patra, S Bhaumik, A. Pandey, and D. Setua. „Stress-Strain Behaviour of Dielectric Elastomer for Actuators“. In: *Applied Mechanics and Materials*. Vol. 789. Trans Tech Publ. 2015, pp. 837–841 (cit. on p. 57).

[100] P. Lochmatter, G. Kovacs, and M. Wissler. „Characterization of dielectric elastomer actuators based on a visco-hyperelastic film model“. In: *Smart Materials and Structures* 16.2 (2007) (cit. on p. 57).

[101] M. Hossain, D. K. Vu, and P. Steinmann. „Experimental study and numerical modelling of VHB 4910 polymer“. In: *Computational Materials Science* 59 (2012), pp. 65–74 (cit. on p. 57).

[102] V. Tagarielli, R Hildick-Smith, and J. Huber. „Electro-mechanical properties and electrostriction response of a rubbery polymer for EAP applications“. In: *International Journal of Solids and Structures* 49.23 (2012), pp. 3409–3415 (cit. on p. 57).

[103] S. Michel, X. Q. Zhang, M. Wissler, C. Löwe, and G. Kovacs. „A comparison between silicone and acrylic elastomers as dielectric materials in electroactive polymer actuators“. In: *Polymer international* 59.3 (2010), pp. 391–399 (cit. on p. 57).

[104] J.-S. Plante and S. Dubowsky. „Large-scale failure modes of dielectric elastomer actuators“. In: *International journal of solids and structures* 43.25 (2006), pp. 7727–7751 (cit. on pp. 57, 60, 62).

[105] R. E. Pelrine, R. D. Kornbluh, and J. P. Joseph. „Electrostriction of polymer dielectrics with compliant electrodes as a means of actuation“. In: *Sensors and Actuators A: Physical* 64.1 (1998), pp. 77–85 (cit. on p. 57).

[106] T. Vu-Cong, N. Nguyen-Thi, C. Jean-Mistral, and A. Sylvestre. „How does static stretching decrease the dielectric constant of VHB 4910 elastomer?“ In: *Proc. SPIE Electroactive Polymer Actuators and Devices (EAPAD)*. Vol. 9056. 2014. DOI: 10.1117/12.2045042 (cit. on pp. 58, 59).

[107] X. Zhao and Z. Suo. „Method to analyze electromechanical stability of dielectric elastomers“. In: *Applied Physics Letters* 91.6 (2007), p. 061921 (cit. on p. 59).

[108] J. D. Vogan. „Development of dielectric elastomer actuators for MRI devices“. PhD thesis. Massachusetts Institute of Technology, 2004 (cit. on pp. 60, 61).

[109] R. H. C. Bonser, W. S. Harwin, W. Hayes, G. Jeronimidis, G. R. Mitchell, and C. Santulli. *EAP-based artificial muscles as an alternative to space mechanisms*. Tech. rep. The University of Reading, UK, 2004 (cit. on p. 62).

[110] C. A. Klein and B. E. Blaho. „Dexterity measures for the design and control of kinematically redundant manipulators“. In: *The International Journal of Robotics Research* 6.2 (1987), pp. 72–83 (cit. on p. 111).

[111] J. Nakanishi, R. Cory, M. Mistry, J. Peters, and S. Schaa. „Comparative Experiments on Task Space Control with Redundancy Resolution“. In: *IEEE/RSJ International Conference on Intelligent Robots and Systems*. 2005, pp. 3901 –3908 (cit. on p. 116).

[112] A. Tikhonov and V. Arsenin. *Solutions of Ill-Posed Problems*. Washington, D.C.: Winston/Wiley, 1977 (cit. on p. 118).

[113] F. Branz, A. Antonello, A. Carron, R. Carli, and A. Francesconi. „Kinematics and control of redundant robotic arm based on dielectric elastomer actuators“. In: *Proc. SPIE Smart Structures and Materials+ Nondestructive Evaluation and Health Monitoring*. SPIE. 2015 (cit. on p. 120).

[114] F. Branz, A. Carron, A. Antonello, R. Carli, and A. Francesconi. „Dielectric Elastomer Space Manipulator: Design and Testing“. In: *Proc. 66th International Astronautical Congress*. IAF. 2015 (cit. on p. 134).

List of Figures

List of Tables

This thesis was typeset with LaTeX 2_ε. It uses the *Clean Thesis* style developed by Ricardo Langner and edited by the author.